ISSN 1605-2730
E-ISSN 1605-8119

MATERIALS PHYSICS AND MECHANICS

Vol. 49, No. 1, 2022

MATERIALS PHYSICS AND MECHANICS

Principal Editors:

Dmitrii Indeitsev
Institute of Problems of Mechanical Engineering
of the Russian Academy of Science (RAS), Russia

Andrei Rudskoi
Peter the Great St.Petersburg Polytechnic University, Russia

Founder and Honorary Editor: Ilya Ovid'ko (1961-2017)
Institute of Problems of Mechanical Engineering
of the Russian Academy of Sciences (RAS), Russia

Associate Editors:

Anna Kolesnikova
Institute of Problems of Mechanical Engineering
of the Russian Academy of Sciences (RAS), Russia

Alexander Nemov
Peter the Great St.Petersburg Polytechnic University, Russia

Editorial Board:

E.C. Aifantis
Aristotle University of Thessaloniki, Greece
K.E. Aifantis
University of Florida, USA
U. Balachandran
Argonne National Laboratory, USA
A. Bellosi
Research Institute for Ceramics Technology, Italy
A.K. Belyaev
Institute of Problems of Mechanical Engineering (RAS), Russia
S.V. Bobylev
Institute of Problems of Mechanical Engineering (RAS), Russia
A.I. Borovkov
Peter the Great St.Petersburg Polytechnic University, Russia
G.-M. Chow
National University of Singapore, Singapore
Yu. Estrin
Monash University, Australia
A.B. Freidin
Institute of Problems of Mechanical Engineering (RAS), Russia
Y. Gogotsi
Drexel University, USA
I.G. Goryacheva
Institute of Problems of Mechanics (RAS), Russia
D. Hui
University of New Orleans, USA
G. Kiriakidis
IESL/FORTH, Greece
D.M. Klimov
Institute of Problems of Mechanics (RAS), Russia
G.E. Kodzhaspirov
Peter the Great St.Petersburg Polytechnic University, Russia
S.A. Kukushkin
Institute of Problems of Mechanical Engineering (RAS), Russia
T.G. Langdon
University of Southampton, U.K.
V.P. Matveenko
Institute of Continuous Media Mechanics (RAS), Russia
A.I. Melker
Peter the Great St.Petersburg Polytechnic University, Russia
Yu.I. Meshcheryakov
Institute of Problems of Mechanical Engineering (RAS), Russia
N.F. Morozov
St.Petersburg State University, Russia
R.R. Mulyukov
Institute for Metals Superplasticity Problems (RAS), Russia
Yu.V. Petrov
St.Petersburg State University, Russia
N.M. Pugno
Politecnico di Torino, Italy
B.B. Rath
Naval Research Laboratory, USA
A.E. Romanov
Ioffe Physico-Technical Institute (RAS), Russia
A.M. Sastry
University of Michigan, Ann Arbor, USA
B.A. Schrefler
University of Padua, Italy
N.V. Skiba
Institute of Problems of Mechanics (RAS), Russia
A.G. Sheinerman
Institute of Problems of Mechanics (RAS), Russia
R.Z. Valiev
Ufa State Aviation Technical University, Russia
K. Zhou
Nanyang Technological University, Singapore

"Materials Physics and Mechanics" Editorial Office:
Phone: +7(812)552 77 78, ext. 224 **E-mail:** mpmjournal@spbstu.ru **Web-site:** http://www.mpm.spbstu.ru

International scientific journal "**Materials Physics and Mechanics**" is published by Peter the Great St.Petersburg Polytechnic University in collaboration with Institute of Problems of Mechanical Engineering of the Russian Academy of Sciences in both hard copy and electronic versions.

The journal provides an international medium for the publication of reviews and original research papers written in English and focused on the following topics:

- Mechanics of composite and nanostructured materials.
- Physics of strength and plasticity of composite and nanostructured materials.
- Mechanics of deformation and fracture processes in conventional materials (solids).
- Physics of strength and plasticity of conventional materials (solids).
- Physics and mechanics of defects in composite, nanostructured, and conventional materials.
- Mechanics and physics of materials in coupled fields.

Owner organizations: Peter the Great St. Petersburg Polytechnic University; Institute of Problems of Mechanical Engineering RAS.

Materials Physics and Mechanics is indexed in Chemical Abstracts, Cambridge Scientific Abstracts, Web of Science Emerging Sources Citation Index (ESCI) and Elsevier Bibliographic Databases (in particular, SCOPUS).

© 2022, Peter the Great St. Petersburg Polytechnic University
© 2022, Institute of Problems of Mechanical Engineering RAS

МЕХАНИКА И ФИЗИКА МАТЕРИАЛОВ

Materials Physics and Mechanics

Том 49, номер 1, 2022 год

Proceedings of the Nineteenth International Workshop on Nano–Design, Technology and Computer Simulations dedicated to A.L. Sanin

28-29 October, 2021, Minsk, Belarus

Organized by
Belarusian State University of Informatics and Radioelectronics
(Belarus)
St. Petersburg Academy of Sciences on Strength Problems
(Russia)

Edited by
Vladimir A. Labunov and Alexander I. Melker

Учредители:
ФГАОУ ВО «Санкт-Петербургский политехнический университет Петра Великого»
ФГБУН «Институт проблем машиноведения Российской Академии Наук»

Редакционная коллегия журнала

Главные редакторы:

д.ф.-м.н., чл.-корр. РАН **Д.А. Индейцев**
Институт проблем машиноведения Российской Академии Наук (РАН)

д.т.н., академик РАН **А.И. Рудской**
Санкт-Петербургский политехнический университет Петра Великого

Основатель и почетный редактор: д.ф.-м.н. **И.А. Овидько (1961-2017)**
Институт проблем машиноведения Российской Академии Наук (РАН)

Ответственные редакторы

д.ф.-м.н. **А.Л. Колесникова**
Институт проблем машиноведения Российской Академии Наук (РАН)

к.т.н. **А.С. Немов**
Санкт-Петербургский политехнический университет Петра Великого

Международная редакционная коллегия:

д.ф.-м.н., проф. **А.К. Беляев**
Институт проблем машиноведения РАН, Россия
д.ф.-м.н. **С.В. Бобылев**
Институт проблем машиноведения РАН, Россия
к.т.н., проф. **А.И. Боровков**
Санкт-Петербургский политехнический у-т Петра Великого, Россия
д.ф.-м.н., проф. **Р.З. Валиев**
Уфимский государственный технический университет, Россия
д.ф.-м.н., академик РАН **И.Г. Горячева**
Институт проблем механики РАН, Россия
д.ф.-м.н., академик РАН **Д.М. Климов**
Институт проблем механики РАН, Россия
д.т.н., проф. **Г.Е. Коджаспиров**
Санкт-Петербургский политехнический у-т Петра Великого, Россия
д.ф.-м.н., проф. **С.А. Кукушкин**
Институт проблем машиноведения РАН, Россия
д.ф.-м.н., академик РАН **В.П. Матвеенко**
Институт механики сплошных сред РАН, Россия
д.ф.-м.н., проф. **А.И. Мелькер**
Санкт-Петербургский политехнический у-т Петра Великого, Россия
д.ф.-м.н., проф. **Ю.И. Мещеряков**
Институт проблем машиноведения РАН, Россия
д.ф.-м.н., академик РАН **Н.Ф. Морозов**
Санкт-Петербургский государственный университет, Россия
д.ф.-м.н., чл.-корр. РАН **Р.Р. Мулюков**
Институт проблем сверхпластичности металлов РАН, Россия
д.ф.-м.н., чл.-корр. РАН **Ю.В. Петров**
Санкт-Петербургский государственный университет, Россия
д.ф.-м.н., проф. **А.Е. Романов**
Физико-технический институт им. А.Ф. Иоффе РАН, Россия
д.ф-м.н. **Н.В. Скиба**
Институт проблем машиноведения РАН, Россия
д.ф.-м.н., проф. **А.Б. Фрейдин**
Институт проблем машиноведения РАН, Россия
д.ф-м.н. **А.Г. Шейнерман**
Институт проблем машиноведения РАН, Россия

Prof., Dr. **E.C. Aifantis**
Aristotle University of Thessaloniki, Greece
Dr. **K.E. Aifantis**
University of Florida, USA
Dr. **U. Balachandran**
Argonne National Laboratory, USA
Dr. **A. Bellosi**
Research Institute for Ceramics Technology, Italy
Prof., Dr. **G.-M. Chow**
National University of Singapore, Singapore
Prof., Dr. **Yu. Estrin**
Monash University, Australia
Prof., Dr. **Y. Gogotsi**
Drexel University, USA
Prof., Dr. **D. Hui**
University of New Orleans, USA
Prof., Dr. **G. Kiriakidis**
IESL/FORTH, Greece
Prof., Dr. **T.G. Langdon**
University of Southampton, UK
Prof., Dr. **N.M. Pugno**
Politecnico di Torino, Italy
Dr. **B.B. Rath**
Naval Research Laboratory, USA
Prof., Dr. **A.M. Sastry**
University of Michigan, Ann Arbor, USA
Prof., Dr. **B.A. Schrefler**
University of Padua, Italy
Prof. Dr. **K. Zhou**
Nanyang Technological University, Singapore

Тел.: +7(812)552 77 78, доб. 224 **E-mail:** mpmjournal@spbstu.ru **Web-site:** http://www.mpm.spbstu.ru

Тематика журнала

Международный научный журнал "Materials Physics and Mechanics" издается Санкт-Петербургским политехническим университетом Петра Великого в сотрудничестве с Институтом проблем машиноведения Российской Академии Наук в печатном виде и электронной форме. Журнал публикует обзорные и оригинальные научные статьи на английском языке по следующим тематикам:

- Механика композиционных и наноструктурированных материалов.
- Физика прочности и пластичности композиционных и наноструктурированных материалов.
- Механика процессов деформации и разрушения в традиционных материалах (твердых телах).
- Физика прочности и пластичности традиционных материалов (твердых тел).
- Физика и механика дефектов в композиционных, наноструктурированных и традиционных материалах.
- Механика и физика материалов в связанных полях.

Редколлегия принимает статьи, которые нигде ранее не опубликованы и не направлены для опубликования в другие научные издания. Все представляемые в редакцию журнала "Механика и физика материалов" статьи рецензируются. Статьи могут отправляться авторам на доработку. Не принятые к опубликованию статьи авторам не возвращаются.

Журнал "Механика и физика материалов" ("Materials Physics and Mechanics") включен в систему цитирования Web of Science Emerging Sources Citation Index (ESCI), SCOPUS и РИНЦ.

© 2022, Санкт-Петербургский политехнический университет Петра Великого
© 2022, Институт проблем машиноведения Российской Академии Наук

Contents

A4

PREFACE

The Nineteenth International Workshop on Nano-Design, Technology and Computer Simulations (NDTCS-2021) took place on October 28-29, 2021 in Minsk, Belarus. The workshop NDTCS-2021 was organized jointly by the Belarusian State University of Informatics and Radioelectronics and the St. Petersburg Academy of Sciences on Strength Problems (Russia). More than 70 participants including scientists, teachers, graduate students, and undergraduates from Azerbaijan, Belarus, India, Kazakhstan, Russian Federation, The United Kingdom and Vietnam prepared and delivered more than 60 reports. The Nineteenth Workshop was focused on nanomaterials and nanotechnology, especially in electronics.

LG Electronics and Joint Stock Company 'Integral' acted as the partners and supporters of the Workshop.

Workshop NDTCS-2021 is a continuation of the previous workshops, which were held in:

- Russia (9), *St. Petersburg* 1997-2005
- Belarus (5), *Minsk* 2008, 2013, 2017, *Grodno* 2015, *Brest* 2019
- Poland, *Olsztyn* 2006
- Germany, *Bayreuth* 2007
- Lithuania, *Vilnius* 2009
- Finland, *Espoo* 2011

The first nine workshops, which took place in Russia, had the name "Nondestructive Testing and Computer Simulations in Science and Engineering." In due course, the focus of the meetings gradually moved towards Nanoscience and Nanotechnology, so the following workshops (2007-2021) had the new name "International Workshop on New Approaches to High-Tech: Nano-Design, Technology and Computer Simulations" what reflects better their profile.

All the contributions to the Workshops were published in English:

- Modelling and Computer Simulation in Materials Science and Engineering, **6** (4) 1998
- Proceedings of St. Petersburg Academy of Sciences on Strength Problems (SPAS), vols. **2-11,** 1998–2007
- Proceedings of the International Society for Optical Engineering (SPIE), vols. 3345, 3687, 4064, 4348, 4627, 5127, 5400, 5831, 6253, 6597, 7377; 1998–2008
- Proceedings of NDTCS, 2008, 2009, 2011, 2013, 2015, 2017, 2019, 2021
- Reviews on Advanced Materials Science, **20** (1, 2) 2009
- Materials Physics and Mechanics (MPM), **9** (1-3) 2010; **13** (1-2) 2012; **20** (1-2) 2014; **34** (1) 2017, **39** (1) 2018, **41** (1) 2019, **45** (1) 2020
- St. Petersburg State Polytechnical Journal. Physics and Mathematics, **2** (242), **3** (248), **4** (253) 2016; **10** (1) 2017

This issue of MPM contains some selected papers presented at the Workshop. All the papers have been peer-reviewed prior to publication. The issue will be of interest to researchers and graduate students in the field of nanotechnology, physics, chemistry, and mechanics.

The workshop is dedicated to the memory of Andrey Leonardovich Sanin. He was for a long time the Professor of Theoretical Physics (Physics-Mechanics Faculty, Peter the Great St. Petersburg Polytechnic University) and an active member of NDTCS Workshops.

Alexander I. Melker, Vladimir A. Labunov

Andrey Leonardovich SANIN
(1935-2020)

The outstanding scientist in the field of theoretical physics, Doctor of Physical-Mathematical Sciences, Professor Sanin A.L. was born on the 13th October 1935 in Leningrad. After finishing secondary school, he did military service in the Baltic region of the USSR (1954-1957, 1963), and thereafter in 1957 he went to Leningrad Polytechnical Institute (now Peter the Great St. Petersburg Polytechnic University) and graduated from the Radio Electronics Faculty in 1962; his speciality having been Physical Electronics. From 1964 to 1971 A.L. Sanin worked at the Department of Electronics Devices of the North-West Polytechnical Institute. After graduating from the Post-graduate School, (the Department of Theoretical Physics, Leningrad Polytechnical Institute) in 1972 he worked in this department at first as a junior research assistant (1972-73), then as Assistant Professor (1973-76), as an Associated Professor (Dozent, 1976-98) and as a Full Professor (1998-2020).

His outstanding academic career is tightly connected with his scientific achievements. A.L. Sanin defended PhD thesis (Physics & Mathematics) in 1973 and his DSc thesis (Physics & Mathematics) in 1998. Under his direction, there is done plenty of scientific research works such as the space resonances and structures of electronic current in heterogeneous media, as well as the problems of nonlinearity and self-organization in physics.

In addition to intensive research activities, teaching was an important part of Sanin's life. Being an excellent lecturer, he lectured classical courses on Analytical Mechanics, Electrodynamics, Quantum Mechanics, and Statistical Physics. Moreover, he developed and lectured original courses: Nonequilibrium Phenomena in Solids, Synergy, etc. On the basis of these courses, A.L. Sanin has written the monograph "Electronic Synergy" which was published in Russian, Leningrad State University Publishing House, 1989. As a result of his great activity both in the scientific and educational fields, several of his disciples have become PhD and now they are working with success in science, industry, and education.

A.L. Sanin was widely known as an outstanding scientist not only in our country but also among the international community of physicists. In the USSR and Russia, he was many years an active member of the all-Union Society "Knowledge", he entered into the Editorial Board of the International Workshop "New Approaches to High-Tech: Nano-design, Technology, Computer Simulations". Andrey L. Sanin was in close collaboration with the leading physicists of China, Mexico, Poland, etc. He visited some countries as an Inviting Lecturer.

It should be emphasized that in spite of his great achievements, A.L. Sanin was a very modest person. Contrary to the widespread manner, he never tried to get registered in the activities even if his role was decisive but preferred to give preference to his pupils.

Andrey L. Sanin was a cheerful person. He liked football and especially swimming.

There is no doubt that A.L. Sanin was a splendid, sincere, decent, and noble person with a great sense of responsibility for any problem he dealt with. He was a very hard-working person with high standards for himself as well as for his colleagues.

We will hold Andrey Leonardovich Sanin as an eminent person, scientist, and teacher in our hearts forever.

Colleagues and Friends

Materials Physics and Mechanics. 2022;49(1): 1-16
Conference materials
http://dx.doi.org/10.18149/MPM.4912022_1

Maxwell electrodynamics in media, geometry effect on constitutive relations

N.G. Krylova[1], **E.M. Ovsiyuk**[2], **A.V. Ivashkevich**[3], **V.M. Red'kov**[3]✉

[1]Belarusian State Agrarian Technical University, Minsk, Republic of Belarus

[2]Mozyr State Pedagogical University named after I.P. Shamyakin, Republic of Belarus

[3]B.I. Stepanov Institute of Physics, Minsk, Republic of Belarus

✉ v.redkov@ifanbel.bas-net.by

Abstract. The problem of constitutive relations in Maxwell electrodynamics, their possible form and role in physical manifestation of electromagnetic fields, its behavior under the motion of the reference frame and its connection with Special Relativity theory, interplay between electrodynamics constitutive relations and gravity theory, and so on, has a long history. The main accent in our treatment is the known possibility to simulate material media by geometrical methods. This review includes the following items: Riemannian geometry and Maxwell theory; Maxwell equations in Riemannian space and effective media; metrical tensor $g_{\alpha\beta}(x)$ and constitutive relations; inverse constitutive equations; geometric simulation of inhomogeneous media; geometrical simulation of uniform media; geometrical modeling of anisotropic uniform media; the moving medium and anisotropy; geometry effect on material equations in arbitrary linear media; the plane wave in the Lobachevsky space, simulating a special medium; arbitrary metrics, etc.

Keywords: constitutive relations, gravity theory, Lobachevsky space, Maxwell electrodynamics, plane waves, Riemannian geometry

***Acknowledgements**. No external funding was received for this study.*

Citation: Krylova NG, Ovsiyuk EM, Ivashkevich AV, Red'kov VM. Maxwell electrodynamics in media, geometry effect on constitutive relations. *Materials Physics and Mechanics*. 2022;49(1): 1-16. DOI: 10.18149/MPM.4912022_1.

1. Introduction

We can track interest in the problem of geometry effect on the constitutive relations in Maxwell electrodynamics, for instance, see the references [1-30]. Note that Gordon [2] was first largely interested in trying to describe dielectric media by effective metrics. Gordon tried to use a gravitational field to simulate a dielectric medium. The idea was taken up and developed by Tamm and Mandelstam [3,4], and by many others.

Let us start with the Maxwell equations in Minkowski space for the uniform medium:

$$\mathrm{div}\mathbf{B} = 0, \quad \mathrm{rot}\,\mathbf{E} = -\frac{\partial \mathbf{B}}{\partial t}, \quad \epsilon\epsilon_0\,\mathrm{div}\mathbf{E} = \rho, \quad \frac{1}{\mu\mu_0}\mathrm{rot}\mathbf{B} = \mathbf{J} + \epsilon\epsilon_0\frac{\partial \mathbf{E}}{\partial t}. \tag{1}$$

Using the constitutive relations

$$\mathbf{H} = \frac{\mathbf{B}}{\mu\mu_0}, \quad \mathbf{D} = \epsilon\epsilon_0\,\mathbf{E} \tag{2}$$

Publisher: Peter the Great St. Petersburg Polytechnic University

eqs. (1) can be written with the use of four vectors $\mathbf{E},\mathbf{B},\mathbf{D},\mathbf{H}$:

$$\mathrm{div}c\mathbf{B}=0,\quad \mathrm{rot}\mathbf{E}=-\frac{\partial c\mathbf{B}}{\partial x^0},\quad \mathrm{div}\mathbf{D}=j^0,\quad \mathrm{rot}\frac{\mathbf{H}}{c}=\frac{\mathbf{J}}{c}+\frac{\partial\mathbf{D}}{\partial x^0}\ \ (x^0=ct). \tag{3}$$

We represent the electric displacement $\mathbf{D}$ and the magnetic field $\mathbf{H}$ by the antisymmetric tensor H^{ik}, the electric $\mathbf{E}$ and the magnetic induction $\mathbf{B}$ are accounted for by the tensor F^{ik}:

$$(F^{\alpha\beta})=\begin{vmatrix}0 & -E^1 & -E^2 & -E^3\\ E^1 & 0 & -cB^3 & cB^2\\ E^2 & cB^3 & 0 & -cB^1\\ E^3 & -cB^2 & cB^1 & 0\end{vmatrix},\quad (H^{\alpha\beta})=\begin{vmatrix}0 & -D^1 & -D^2 & -D^3\\ D^1 & 0 & -H^3/c & H^2/c\\ D^2 & H^3/c & 0 & -H^1/c\\ D^3 & -H^2/c & H^1/c & 0\end{vmatrix};$$

here we apply the notations

$$E^i=-E_i,\ D^i=-D_i,\ B^i=+B_i,\ H^i=+H_i,\ j^a=(\rho,\mathbf{J}/c).$$

Then eqs. (3) can be presented in tensor form

$$\partial_a F_{bc}+\partial_b F_{ca}+\partial_c F_{ab}=0,\quad \partial_b H^{ba}=j^a. \tag{4}$$

For the vacuum case, the constitutive relations $\mathbf{D}=\epsilon_0\mathbf{E},\ \mathbf{H}=\frac{1}{\mu_0}\mathbf{B},$ are read in the tensor form as follows

$$H^{ab}(x)=\epsilon_0 F^{ab}(x), \tag{5}$$

so eqs. (4) contain only one tensor

$$\partial_a F_{bc}+\partial_b F_{ca}+\partial_c F_{ab}=0,\quad \partial_b F^{ba}=\frac{1}{\epsilon_0}j^a. \tag{6}$$

The situation is quite different in the presence of media. Even for the simplest case of the uniform medium, relativizing the above constitutive equations

$$\mathbf{D}=\epsilon_0\epsilon\mathbf{E},\quad \mathbf{H}=\frac{1}{\mu_0\mu}\mathbf{B}$$

requires the subsidiary (4×4)-matrix with the presumed properties of the 2-rank tensor:

$$\eta^{am}=\sqrt{\epsilon}\begin{vmatrix}1/k & 0 & 0 & 0\\ 0 & -k & 0 & 0\\ 0 & 0 & -k & 0\\ 0 & 0 & 0 & -k\end{vmatrix},\quad k=\frac{1}{\sqrt{\epsilon\mu}},\quad H^{ab}=\epsilon_0\eta^{am}\eta^{bn}F_{mn}. \tag{7}$$

We may postulate the class of linear inhomogeneous electromagnetic media characterized by the 4-rank tensor [3,4]:

$$H^{ab}(x)=\epsilon_0\Delta^{abmn}(x)F_{mn}(x), \tag{8}$$

where the relativistic symmetry presumes the evident symmetry constraints:

$$\Delta^{abmn}(x)=-\Delta^{bamn}(x)=-\Delta^{abnm}(x), \tag{9}$$

and, in general, the tensor $\Delta^{abmn}(x)$ depends upon 36 parameters.

When extending Maxwell's theory to space-time with non-Euclidean geometry, which describes gravity according to General Relativity, one must change previous equations to a more general form. In particular, the vacuum Maxwell equations are given as

$$\nabla_\alpha f_{\beta\gamma}+\nabla_\beta f_{\gamma\alpha}+\nabla_\gamma f_{\alpha\beta}=0,\quad \nabla_\beta h^{\beta\alpha}=j^\alpha,\quad h_{\alpha\beta}=\epsilon_0 f_{\alpha\beta}, \tag{10}$$

where ∇_β stands for the covariant derivative. In order to distinguish formulas referring to flat and curved models we will use small letters for designating the electromagnetic tensors in curved model, f_{ab} and h^{ab}.

2. Maxwell equations in Riemannian space and effective media

Let us discuss the possibility to consider the vacuum Maxwell equations in a curved space-time as Maxwell equations in a flat space-time but specified for an effective medium, the properties of which are determined by the metrical structure of the initial curved model $g_{\alpha\beta}(x)$. We will restrict ourselves to the case of curved space-time models which are parameterized by some quasi-Cartesian coordinates.

Vacuum Maxwell equations in a Riemannian space-time, parameterized by some quasi-Cartesian coordinates, can be brought to the form [5]

$$\partial_a f_{bc} + \partial_b f_{ca} + \partial_c f_{ab} = 0, \quad \frac{1}{\sqrt{-g}} \partial_b \sqrt{-g}\, f^{ba} = \frac{1}{\epsilon_0} j^a . \tag{11}$$

Indeed, one can immediately see that after introducing the new variables

$$\sqrt{-g}\, j^a \text{™}\, j^a, \quad f_{ab} \text{™}\, F_{ab}, \quad \epsilon_0 \sqrt{-g}\, g^{am}(x) g^{bn}(x) f_{mn}(x) \text{™}\, H^{ba}, \tag{12}$$

eqs. (11) in the curved space can be re-written as Maxwell equations for the flat space but in the medium:

$$\partial_a F_{bc} + \partial_b F_{ca} + \partial_c F_{ab} = 0, \quad \partial_b H^{ba} = \frac{1}{\epsilon_0} j^a . \tag{13}$$

Relations playing the role of constitutive equations are determined by the metrical structure of the geometrical model:

$$H^{\beta\alpha}(x) = \epsilon_0 \left[\sqrt{-g(x)}\, g^{\alpha\rho}(x) g^{\beta\sigma}(x) \right] F_{\rho\sigma}(x). \tag{14}$$

There exists one special case; namely, if $g(x)$ does not depend on coordinates, then the factor $\sqrt{-g(x)} = \sqrt{-g}$ can be omitted from the above formulas.

3. Metrical tensor and constitutive relations

Let us consider the material equations for electromagnetic fields which are generated by the metrical structure of the space-time model. For an arbitrary metrical tensor $g_{\alpha\beta}(x)$ we may obtain a 3-dimensional form of relation (14):

$$D^i = \epsilon_0 \epsilon^{ik}(x) E_k + \epsilon_0 c \alpha^{ik}(x) B_k , \quad H^i = \epsilon_0 c \beta^{ik}(x) E_k + \mu_0^{-1} (\mu^{-1})^{ik}(x) B_k . \tag{15}$$

Four dimensionless (3×3)-matrices $\epsilon^{ik}(x)$, $\alpha^{ik}(x)$, $\beta^{ik}(x)$, $(\mu^{-1})^{ik}(x)$ are not independent because they are bilinear functions of only 10 components of the symmetrical tensor $g_{\alpha\beta}(x)$.

After simple calculation, for these tensors one produces expressions

$$\epsilon^{ik}(x) = \sqrt{-g}\left(g^{00}(x) g^{ik}(x) - g^{0i}(x) g^{0k}(x) \right), \quad (\mu^{-1})^{ik}(x) = \frac{1}{2}\sqrt{-g}\, \epsilon_{imn}\, g^{ml}(x) g^{nj}(x) \epsilon_{ljk} ,$$

$$\alpha^{ik}(x) = +\sqrt{-g}\, g^{ij}(x) g^{0l}(x) \epsilon_{ljk} , \quad \beta^{ik}(x) = -\sqrt{-g}\, g^{0j}(x) \epsilon_{jil}\, g^{lk}(x).$$

The tensor $\epsilon^{ik}(x)$ is evidently symmetrical; it is easy to demonstrate the same property for $(\mu^{-1})^{ik}(x)$. Indeed, we have

$$(\mu^{-1})^{ki}(x) = \frac{1}{2} \epsilon_{kmn} g^{ml}(x) g^{nj}(x) \epsilon_{lji} ,$$

here making changes in mute indices, $m \leftrightarrow j, n \leftrightarrow l$, we get

$$(\mu^{-1})^{ki}(x) = \frac{1}{2} \epsilon_{kjl} g^{jn}(x) g^{lm}(x) \epsilon_{nmi} \epsilon_{imn} g^{lm}(x) g^{jn}(x) \epsilon_{ljk} = (\mu^{-1})^{ik}(x).$$

In the same manner, one can prove the identity $\beta^{ki}(x) = +\alpha^{ik}$:

$$\beta^{ki} = -g^{0j}(x) \epsilon_{jkl} g^{li}(x) = g^{il}(x) g^{0j}(x) \epsilon_{jlk} = +\alpha^{ik} .$$

So, the above tensors obey the following symmetry constraints:

$$\epsilon^{ik}(x) = +\epsilon^{ki}(x), \quad (\mu^{-1})^{ik}(x) = +(\mu^{-1})^{ki}(x), \quad \beta^{ki}(x) = \alpha^{ik} ;$$

that means the (6×6)-matrix defining constitutive equations is symmetrical

$$\begin{vmatrix} D^i(x) \\ H^i(x) \end{vmatrix} = \begin{vmatrix} \epsilon_0\epsilon^{ik}(x) & \epsilon_0 c\alpha^{ik}(x) \\ \epsilon_0 c\beta^{ik}(x) & \mu_0^{-1}(\mu^{-1})^{ik}(x) \end{vmatrix} \begin{vmatrix} E_k(x) \\ B_k(x) \end{vmatrix}. \tag{16}$$

Making $(3+1)$-splitting in the metrical tensor

$$g^{\alpha\beta}(x) = \begin{vmatrix} g^{00} & (g^{0i}) = \bar{g} \\ (g^{i0}) = \bar{g} & (g^{ik}) = g \end{vmatrix}, \quad (\bar{g}^{\times})_{jk} \equiv g^{0l}(x)\epsilon_{ljk} = g^{l}(x)\epsilon_{ljk}, \tag{17}$$

tensors $(\epsilon^{ik}),(\alpha^{ik})$, (β^{ik}) can be written in the form

$$\epsilon(x) = \sqrt{-g}\,[g^{00}(x)g(x) - \bar{g}(x)\cdot\bar{g}(x)],$$

$$\alpha(x) = \sqrt{-g}\, g(x)\bar{g}^{\times}(x), \quad \beta(x) = -\sqrt{-g}\,\bar{g}^{\times}(x)g(x). \tag{18}$$

In doing so, one can produce a more convenient representation for matrix $(\mu^{-1})^{ik}(x)$. Indeed, with the notation $(\tau_i)_{mn} = \epsilon_{imn}$, we get

$$(\mu^{-1})^{ik}(x) = -\frac{1}{2}\sqrt{-g}\ \mathrm{Sp}[\tau_i\, g(x)\tau_k\, g(x)]. \tag{19}$$

The metrical tensors, which are the most interesting in the context of General relativity [5], have a quasi-diagonal structure, so the effective constitutive relations are simplified:

$$g^{\alpha\beta}(x) = \begin{vmatrix} g^{00} & 0 & 0 & 0 \\ 0 & g^{11} & g^{12} & g^{13} \\ 0 & g^{21} & g^{22} & g^{23} \\ 0 & g^{31} & g^{32} & g^{33} \end{vmatrix}, \quad \alpha(x) = 0, \quad \beta(x) = 0,$$

$$\epsilon(x) = \sqrt{-g}\, g^{00}(x)g(x), \quad (\mu^{ik})(x) = -\frac{1}{2}\sqrt{-g}\ \mathrm{Sp}[\tau_i\, g(x)\tau_k\, g(x)]. \tag{20}$$

The explicit expressions for tensors $\epsilon^{ik}(x)$ and $(\mu^{-1})^{ik}(x)$ given by (20) are

$$(\epsilon^{ik}) = \sqrt{-g}\, g^{00} \begin{vmatrix} g^{11} & g^{12} & g^{13} \\ g^{21} & g^{22} & g^{23} \\ g^{31} & g^{32} & g^{33} \end{vmatrix}, \quad ((\mu^{-1})^{ik}) = \sqrt{-g} \begin{vmatrix} G^{11} & G^{12} & G^{13} \\ G^{21} & G^{22} & G^{23} \\ G^{31} & G^{32} & G^{33} \end{vmatrix}, \tag{21}$$

where $G^{ik}(x)$ stand for (algebraic) co-factors to the elements $g^{ik}(x)$:

$$G^{ik}(x) = \begin{vmatrix} (g^{22}g^{33} - g^{23}g^{32}) & (g^{31}g^{23} - g^{21}g^{33}) & (g^{21}g^{32} - g^{22}g^{31}) \\ (g^{32}g^{13} - g^{33}g^{12}) & (g^{33}g^{11} - g^{31}g^{13}) & (g^{31}g^{12} - g^{32}g^{11}) \\ (g^{12}g^{23} - g^{13}g^{22}) & (g^{13}g^{21} - g^{11}g^{23}) & (g^{11}g^{22} - g^{12}g^{21}) \end{vmatrix}. \tag{22}$$

Therefore, two constitutive matrices, $\epsilon(x)$ and $\mu^{-1}(x)$, are not independent and obey the following constraint:

$$\epsilon(x)\mu^{-1}(x) = \frac{-g^{00}g_{00}}{\det g_{ik}} \begin{vmatrix} g^{11} & g^{12} & g^{13} \\ g^{21} & g^{22} & g^{23} \\ g^{31} & g^{32} & g^{33} \end{vmatrix} \begin{vmatrix} (g^{22}g^{33} - g^{23}g^{32}) & (g^{31}g^{23} - g^{21}g^{33}) & (g^{21}g^{32} - g^{22}g^{31}) \\ (g^{32}g^{13} - g^{33}g^{12}) & (g^{33}g^{11} - g^{31}g^{13}) & (g^{31}g^{12} - g^{32}g^{11}) \\ (g^{12}g^{23} - g^{13}g^{22}) & (g^{13}g^{21} - g^{11}g^{23}) & (g^{11}g^{22} - g^{12}g^{21}) \end{vmatrix} = -I. \tag{23}$$

Thus, the metric tensors with the quasi-diagonal structure effectively describe the media with the following constitutive relations (note that the sign minus may be eliminated by changing the notation)

$$\mathbf{D} = -\epsilon_0\,\epsilon(x)\mathbf{E}, \quad \mathbf{B} = \mu_0\mu(x)\mathbf{H}, \quad \mu(x) = -\epsilon(x), \quad (\epsilon^{ik})(x) = \sqrt{-g(x)}\, g^{00}(x) \begin{vmatrix} g^{11}(x) & g^{12}(x) & g^{13}(x) \\ g^{21}(x) & g^{22}(x) & g^{23}(x) \\ g^{31}(x) & g^{32}(x) & g^{33}(x) \end{vmatrix}. \tag{24}$$

For the general case of an arbitrary metrical tensor, four constitutive tensors may be given explicitly as follows (we use notation $g^{i}(x) = g^{i0}(x)$)

$$[\epsilon^{ik}(x)] = \sqrt{-g}\, g^{00} \begin{vmatrix} g^{11} & g^{12} & g^{13} \\ g^{21} & g^{22} & g^{23} \\ g^{31} & g^{32} & g^{33} \end{vmatrix} - \sqrt{-g} \begin{vmatrix} g^1 g^1 & g^1 g^2 & g^1 g^3 \\ g^2 g^1 & g^2 g^2 & g^2 g^3 \\ g^3 g^1 & g^3 g^2 & g^3 g^3 \end{vmatrix},$$

$$(\mu^{-1})^{ik}(x) = (\sqrt{-g} \begin{vmatrix} (g^{22}g^{33} - g^{23}g^{32}) & (g^{31}g^{23} - g^{21}g^{33}) & (g^{21}g^{32} - g^{22}g^{31}) \\ (g^{32}g^{13} - g^{33}g^{12}) & (g^{33}g^{11} - g^{31}g^{13}) & (g^{31}g^{12} - g^{32}g^{11}) \\ (g^{12}g^{23} - g^{13}g^{22}) & (g^{13}g^{21} - g^{11}g^{23}) & (g^{11}g^{22} - g^{12}g^{21}) \end{vmatrix}, \tag{25}$$

$$\alpha^{ik}(x) = \sqrt{-g} \begin{vmatrix} (-g^{12}g^3 + g^{13}g^2) & (g^{11}g^3 - g^{13}g^1) & (-g^{11}g^2 + g^{12}g^1) \\ (-g^{22}g^3 + g^{23}g^2) & (g^{21}g^3 - g^{23}g^1) & (-g^{21}g^2 + g^{22}g^1) \\ (-g^{32}g^3 + g^{33}g^2) & (g^{31}g^3 - g^{33}g^1) & (-g^{31}g^2 + g^{32}g^1) \end{vmatrix} = \beta^{ki}(x).$$

4. Inverse constitutive equations

The tensor relationship

$$H^{\rho\sigma}(x) = \epsilon_0 \sqrt{-g(x)}\, g^{\rho\alpha}(x) g^{\sigma\beta}(x) F_{\alpha\beta}(x)$$

in 3-vector form reads

$$D^i = \epsilon_0 \epsilon^{ik} E_k + \epsilon_0 c \alpha^{ik} B_k, \quad H^i = \epsilon_0 c \beta^{ik} E_k + \frac{1}{\mu_0} (\mu^{-1})^{ik} B_k;$$

let us derive inverse constituents

$$F_{\rho\sigma} = \frac{1}{\epsilon_0} \frac{1}{\sqrt{-g(x)}} g_{\rho\alpha}(x) g_{\sigma\beta}(x) H^{\alpha\beta}, \; E_i = \frac{1}{\epsilon_0} (\epsilon^{-1})_{ik} D^k + \frac{1}{\epsilon_0 c} (\alpha^{-1})_{ik} H^k, \quad B_i = \frac{1}{\epsilon_0 c} (\beta^{-1})_{ik} D^k + \mu_0 \mu_{ik} H^k. \tag{26}$$

One does not need to make new calculations in addition to those given in Section IV. Expressions for the inverse constitutive tensors are

$$(\epsilon^{-1})_{ik} = \frac{1}{\sqrt{-g(x)}} [g_{00}(x) g_{ik}(x) - g_i(x) g_k(x)], \quad \mu_{ik} = \frac{1}{2} \frac{1}{\sqrt{-g(x)}} \epsilon_{imn} g_{ml}(x) g_{nj}(x) \epsilon_{ljk},$$

$$(\alpha^{-1})_{ik} = +\frac{1}{\sqrt{-g(x)}} g_{ij}(x) g_l(x) \epsilon_{ljk}, \quad (\beta^{-1})_{ik} = -\frac{1}{\sqrt{-g(x)}} g_j(x) \epsilon_{jil}\, g_{lk}(x), \tag{27}$$

with symmetry

$$(\epsilon^{-1})_{ik}(x) = +(\epsilon^{-1})_{ki}(x), \quad \mu_{ik}(x) = +\mu_{ki}(x), \quad (\beta^{-1})_{ki}(x) = +(\alpha^{-1})_{ik}. \tag{28}$$

Therefore, the (6×6)-matrix, determining the inverse material equations, is symmetrical as well

$$\begin{vmatrix} E_k \\ B_k \end{vmatrix} = \begin{vmatrix} \epsilon_0^{-1} (\epsilon^{-1})_{kl} & \epsilon_0^{-1} c^{-1} (\alpha^{-1})_{kl} \\ \epsilon_0^{-1} c^{-1} (\beta^{-1})_{kl} & \mu_0 \mu_{kl} \end{vmatrix} \begin{vmatrix} D^l \\ H^l \end{vmatrix}. \tag{29}$$

5. Geometrical modeling of inhomogeneous media

Let us consider a special form of the diagonal metrical tensor

$$g_{\alpha\beta} = \begin{vmatrix} a^2(x) & 0 & 0 & 0 \\ 0 & -b^2(x) & 0 & 0 \\ 0 & 0 & -b^2(x) & 0 \\ 0 & 0 & 0 & -b^2(x) \end{vmatrix}. \tag{30}$$

In this case, relations (24) take the form

$$\mathbf{D} = -\epsilon_0\, \epsilon(x) \mathbf{E}, \quad \mathbf{B} = \mu_0 \mu(x) \mathbf{H}, \quad \mu(x) = -\epsilon(x) = \frac{b(x)}{a(x)}. \tag{31}$$

For the diagonal anisotropic metrics

$$g_{\alpha\beta} = \begin{vmatrix} a^2(x) & 0 & 0 & 0 \\ 0 & -b_1^2(x) & 0 & 0 \\ 0 & 0 & -b_2^2(x) & 0 \\ 0 & 0 & 0 & -b_3^2(x) \end{vmatrix}, \tag{32}$$

relations (24) lead to

$$\mathbf{D} = -\epsilon_0\,\epsilon(x)\mathbf{E}, \quad \mathbf{B} = \mu_0\mu(x)\mathbf{H}, \quad \mu(x) = -\epsilon(x) = \begin{vmatrix} b_2 b_3 / a b_1 & 0 & 0 \\ 0 & b_3 b_1 / a b_2 & 0 \\ 0 & 0 & b_1 b_2 / a b_3 \end{vmatrix}. \tag{33}$$

6. Geometrical modeling of uniform media

Let us consider one special form of the metrical tensor

$$g_{\alpha\beta} = \begin{vmatrix} a^2 & 0 & 0 & 0 \\ 0 & -b^2 & 0 & 0 \\ 0 & 0 & -b^2 & 0 \\ 0 & 0 & 0 & -b^2 \end{vmatrix}, \tag{34}$$

where a^2 and b^2 are numerical parameters. This is a special case mentioned in connection with eq. (14): if $g(x)$ does not depend on coordinates, then the factor $\sqrt{-g}$ can be omitted from the formulas. In this way we get the following constitutive equations:

$$(\epsilon^{ik}) = \frac{1}{a^2 b^2} \begin{vmatrix} -1 & 0 & 0 \\ 0 & -1 & 0 \\ 0 & 0 & -1 \end{vmatrix}, \quad ((\mu^{-1})^{ik}) = \frac{1}{b^4} \begin{vmatrix} 1 & 0 & 0 \\ 0 & 1 & 0 \\ 0 & 0 & 1 \end{vmatrix}, \tag{35}$$

or

$$D^i = -\frac{\epsilon_0}{a^2 b^2} E_i, \quad H^i = \frac{1}{\mu_0 b^4} B_i, \tag{36}$$

whence it follows

$$b^2 = \sqrt{\mu}, \quad a^2 = \frac{1}{\epsilon} \frac{1}{\sqrt{\mu}}. \tag{37}$$

The corresponding metrical tensor (34) can be presented as follows

$$g_{\alpha\beta} = \frac{1}{\sqrt{\epsilon}} \begin{vmatrix} 1/\sqrt{\epsilon\mu} & 0 & 0 & 0 \\ 0 & -\sqrt{\epsilon\mu} & 0 & 0 \\ 0 & 0 & -\sqrt{\epsilon\mu} & 0 \\ 0 & 0 & 0 & -\sqrt{\epsilon\mu} \end{vmatrix}. \tag{38}$$

Such possibilities will exist in all other cases considered below.

7. Geometrical modeling of anisotropic media

Let us extend the previous analysis and consider the metrical tensor

$$g_{\alpha\beta} = \begin{vmatrix} a^2 & 0 & 0 & 0 \\ 0 & -b_1^2 & 0 & 0 \\ 0 & 0 & -b_2^2 & 0 \\ 0 & 0 & 0 & -b_3^2 \end{vmatrix}, \tag{39}$$

where a^2, b_i^2 are arbitrary numerical parameters. The constitutive equations generated by this geometry have the form

$$D^i = \epsilon_0 \epsilon^{ik} E_k\,, \quad H^i = \mu_0^{-1} \mu^{ik} B_k\,,$$

$$(\epsilon^{ik}) = a^{-2} \begin{vmatrix} -b_1^{-2} & 0 & 0 \\ 0 & -b_2^{-2} & 0 \\ 0 & 0 & -b_3^{-2} \end{vmatrix}, \quad (\mu^{ik}) = \begin{vmatrix} b_2^{-2} b_3^{-2} & 0 & 0 \\ 0 & b_3^{-2} b_1^{-2} & 0 \\ 0 & 0 & b_1^{-2} b_2^{-2} \end{vmatrix}, \tag{40}$$

or differently

$$D^1 = -\frac{\epsilon_0 E_1}{a^2 b_1^2}, D^2 = -\frac{\epsilon_0 E_2}{a^2 b_2^2}, D^3 = -\frac{\epsilon_0 E_3}{a^2 b_3^2}, \qquad H^1 = \frac{B_1}{\mu_0 b_2^2 b_3^2}, H^2 = \frac{B_2}{\mu_0 b_3^2 b_1^2}, H^3 = \frac{B_3}{\mu_0 b_1^2 b_2^2}.$$

Being compared these equations with the physical ones

$$D^1 = -\epsilon_0 \epsilon_1 E_1, D^2 = -\epsilon_0 \epsilon_2 E_2, D^3 = -\epsilon_0 \epsilon_3 E_3, \qquad H^1 = \frac{B_1}{\mu_0 \mu_1}, H^2 = \frac{B_2}{\mu_0 \mu_2}, H^3 = \frac{B_3}{\mu_0 \mu_3},$$

one obtains

$$\epsilon_1 = \frac{1}{a^2 b_1^2}, \quad \epsilon_2 = \frac{1}{a^2 b_2^2}, \quad \epsilon_3 = \frac{1}{a^2 b_3^2}, \quad \mu_1 = b_2^2 b_3^2, \quad \mu_2 = b_3^2 b_1^2, \quad \mu_3 = b_1^2 b_2^2. \tag{41}$$

It follows that

$$\frac{\mu_1}{\epsilon_1} = \frac{\mu_2}{\epsilon_2} = \frac{\mu_3}{\epsilon_3} = (a^2 b_1^2 b_2^2 b_3^2) = -g, \quad -g = \sqrt{\frac{\mu_1^2 + \mu_2^2 + \mu_3^2}{\epsilon_1^2 + \epsilon_2^2 + \epsilon_2^2}}, \qquad \frac{\mu_i}{\sqrt{\mu_1^2 + \mu_2^2 + \mu_3^2}} = \frac{\epsilon_i}{\sqrt{\epsilon_1^2 + \epsilon_2^2 + \epsilon_2^2}}. \tag{42}$$

The latter means that one can use four independent parameters ϵ, μ, n_i:

$$\epsilon_i = \epsilon n_i\,, \quad \mu_i = \mu n_i\,, \quad \mathbf{n}^2 = 1. \tag{43}$$

One can express b_i^2 in terms of μ_i:

$$b_1^2 = \sqrt{\frac{\mu_2 \mu_3}{\mu_1}} = \sqrt{\mu}\sqrt{\frac{n_2 n_3}{n_1}}, \quad b_2^2 = \sqrt{\frac{\mu_3 \mu_1}{\mu_2}} = \sqrt{\mu}\sqrt{\frac{n_3 n_1}{n_2}}, \quad b_3^2 = \sqrt{\frac{\mu_1 \mu_2}{\mu_3}} = \sqrt{\mu}\sqrt{\frac{n_1 n_2}{n_3}}. \tag{44}$$

In its turn, from $a^2 b_1^2 b_2^2 b_3^2 = \mu / \epsilon$ it follows

$$a^2 = \frac{\mu}{\epsilon} \frac{1}{b_1^2 b_2^2 b_3^2} = \frac{1}{\epsilon \sqrt{\mu}} \frac{1}{\sqrt{n_1 n_2 n_3}}. \tag{45}$$

The formulas (44), (45) provide us with the anisotropic metrical tensor

$$g_{ab}(x) = \frac{1}{\sqrt{\epsilon}} \begin{vmatrix} \frac{1}{\sqrt{\epsilon\mu}} \frac{1}{\sqrt{n_1 n_2 n_3}} & 0 & 0 & 0 \\ 0 & -\sqrt{\epsilon\mu}\sqrt{\frac{n_2 n_3}{n_1}} & 0 & 0 \\ 0 & 0 & -\sqrt{\epsilon\mu}\sqrt{\frac{n_3 n_1}{n_2}} & 0 \\ 0 & 0 & 0 & -\sqrt{\epsilon\mu}\sqrt{\frac{n_1 n_2}{n_3}} \end{vmatrix}. \tag{46}$$

8. Moving medium and anisotropy

A more complicated example of an effective anisotropic medium is provided by the constitutive equations for the uniform media in a moving reference frame. Following the initial Minkowski investigation [1], this problem was considered by many authors. The starting point is that, in Minkowski approach to electrodynamics, the constitutive relations explicitly depend on the 4-velocity of the reference frame motion under a medium. Gordon [2], Tamm, and Mandelstam [3,4] noticed that for a moving observer, the constitutive relations can be expressed with the help of effective metric as follows:

$$H^{ab}(x) = \epsilon_0 \Delta^{abmn} F_{mn}, \quad \Delta^{abmn} = \epsilon_0 \frac{1}{\sqrt{\mu}} [g^{am} + (\epsilon\mu - 1) u^a u^m] \frac{1}{\sqrt{\mu}} [g^{bn} + (\epsilon\mu - 1) u^b u^n], \tag{47}$$

where $g^{ab} = \text{diag}(+1,-1,-1,-1)$. Corresponding constitutive 3-dimensional tensors are (let us use the notation $\epsilon\mu - 1 = \gamma$)

$$\epsilon^{ik} = \frac{1}{\mu} \begin{vmatrix} (-1+\gamma u^1 u^1 - \gamma u^0 u^0) & \gamma u^1 u^2 & \gamma u^1 u^3 \\ \gamma u^1 u^2 & (-1+\gamma u^2 u^2 - \gamma u^0 u^0) & \gamma u^2 u^3 \\ \gamma u^3 u^1 & \gamma u^3 u^2 & (-1+\gamma u^3 u^3 - \gamma u^0 u^0) \end{vmatrix},$$

$$(\mu^{-1})^{ik} = \frac{1}{\mu} \begin{vmatrix} (1-\gamma u^2 u^2 - \gamma u^3 u^3) & \gamma u^1 u^2 & \gamma u^1 u^3 \\ \gamma u^1 u^2 & (1-\gamma u^3 u^3 - \gamma u^1 u^1) & \gamma u^2 u^3 \\ \gamma u^3 u^1 & \gamma u^3 u^2 & (1-\gamma u^1 u^1 - \gamma u^2 u^2) \end{vmatrix}, \tag{48}$$

$$\alpha^{ik} = \frac{1}{\mu} \begin{vmatrix} 0 & -\gamma u^0 u^3 & +\gamma u^0 u^2 \\ +\gamma u^0 u^3 & 0 & -\gamma u^0 u^1 \\ -\gamma u^0 u^2 & +\gamma u^0 u^1 & 0 \end{vmatrix}, \quad \beta^{ik} = \frac{1}{\mu} \begin{vmatrix} 0 & +\gamma u^0 u^3 & -\gamma u^0 u^2 \\ -\gamma u^0 u^3 & 0 & +\gamma u^0 u^1 \\ +\gamma u^0 u^2 & -\gamma u^0 u^1 & 0 \end{vmatrix}.$$

Let us deduce 3-dimensional form of these relations. For the vector D^i we have

$$D^1 = \frac{\epsilon_0}{\mu} \Big[(-1+\gamma u^1 u^1 - \gamma u^0 u^0) E_1 + \gamma u^1 u^2 E_2 + \gamma u^1 u^3 E_3 \Big] + \frac{\epsilon_0 c}{\mu} (-\gamma u^0 u^3 B_2 + \gamma u^0 u^2 B_3),$$

$$D^2 = \frac{\epsilon_0}{\mu} \Big[+\gamma u^1 u^2 E_1 + (-1+\gamma u^2 u^2 - \gamma u^0 u^0) E_2 + \gamma u^2 u^3 E_3 \Big] + \frac{\epsilon_0 c}{\mu} (\gamma u^0 u^3 B_1 - \gamma u^0 u^1 B_3),$$

$$D^1 = \frac{\epsilon_0}{\mu} \Big[+\gamma u^1 u^3 E_1 + \gamma u^2 u^3 E_2 + (-1+\gamma u^3 u^3 - \gamma u^0 u^0) E_3 \Big] + \frac{\epsilon_0 c}{\mu} (-\gamma u^0 u^2 B_1 + \gamma u^0 u^1 B_2),$$

and further, we obtain

$$D^1 = -\frac{\epsilon_0}{\mu} E_1 + \frac{\epsilon_0 \gamma}{\mu} [-u^0 u^0 E_1 + (u^1 E_1 + u^2 E_2 + u^3 E_3) u^1] + \frac{\epsilon_0 c \gamma}{\mu} u^0 (u^2 B_3 - u^3 B_2),$$

$$D^2 = -\frac{\epsilon_0}{\mu} E_2 + \frac{\epsilon_0 \gamma}{\mu} [-u^0 u^0 E_2 + (u^1 E_1 + u^2 E_2 + u^3 E_3) u^2] + \frac{\epsilon_0 c \gamma}{\mu} u^0 (u^3 B_1 - u^1 B_3),$$

$$D^3 = -\frac{\epsilon_0}{\mu} E_3 + \frac{\epsilon_0 \gamma}{\mu} [-u^0 u^0 E_3 + (u^1 E_1 + u^2 E_2 + u^3 E_3) u^3] + \frac{\epsilon_0 c \gamma}{\mu} u^0 (u^1 B_2 - u^2 B_1).$$

Using the notations

$$V = v / c, \quad u^0 = \frac{1}{\sqrt{1-V^2}}, \quad u^i = \frac{V^i}{\sqrt{1-V^2}}$$

the previous relations can be written as follow

$$D^1 = -\frac{\epsilon_0}{\mu} E_1 + \frac{\epsilon_0 \gamma}{\mu} \frac{[-E_1 + (V^1 E_1 + V^2 E_2 + V^3 E_3) V^1]}{1-V^2} + \frac{\epsilon_0 c \gamma}{\mu} \frac{(V^2 B_3 - V^3 B_2)}{1-V^2},$$

$$D^2 = -\frac{\epsilon_0}{\mu} E_2 + \frac{\epsilon_0 \gamma}{\mu} \frac{[-E_1 + (V^1 E_1 + V^2 E_2 + V^3 E_3) V^2]}{1-V^2} + \frac{\epsilon_0 c \gamma}{\mu} \frac{(V^3 B_1 - V^1 B_3)}{1-V^2},$$

$$D^3 = -\frac{\epsilon_0}{\mu} E_3 + \frac{\epsilon_0 \gamma}{\mu} \frac{[-E_3 + (V^1 E_1 + V^2 E_2 + V^3 E_3) V^3]}{1-V^2} + \frac{\epsilon_0 c \gamma}{\mu} \frac{(V^1 B_2 - V^2 B_1)}{1-V^2};$$

in the vector form, they can be rewritten as

$$\mathbf{D} = \frac{\epsilon_0}{\mu} \mathbf{E} + \frac{\epsilon_0 \gamma}{\mu} \frac{\mathbf{E} - (\mathbf{VE})\mathbf{V}}{1-V^2} + \frac{\epsilon_0 c \gamma}{\mu} \frac{\mathbf{V} \times \mathbf{B}}{1-V^2}. \tag{49}$$

Similarly, we obtain three relations for H^i:

$$H_1 = \frac{1}{\mu_0\mu}[(1-\gamma u^2u^2-\gamma u^3u^3)B_1+\gamma u^1u^2B_2+\gamma u^1u^3B_3]+\frac{\epsilon_0 c}{\mu}(\gamma u^0u^3E_2-\gamma u^0u^2E_3),$$

$$H_2 = \frac{1}{\mu_0\mu}[\gamma u^1u^2B_1+(1-\gamma u^3u^3-\gamma u^1u^1)B_2+\gamma u^2u^3B_3]+\frac{\epsilon_0 c}{\mu}(\gamma u^0u^3E_2-\gamma u^0u^2E_3),$$

$$H_3 = \frac{1}{\mu_0\mu}[\gamma u^3u^1B_1+\gamma u^3u^2B_3+(1-\gamma u^1u^1-\gamma u^2u^2)B_3]+\frac{\epsilon_0 c}{\mu}(\gamma u^0u^2E_1-\gamma u^0u^1E_2),$$

and then

$$H_1 = \frac{1}{\mu_0\mu}B_1+\frac{\gamma}{\mu_0\mu}(-u^2u^2B_1-u^3u^3B_1+u^1u^2B_2+u^1u^3B_3)+\frac{\epsilon_0 c\gamma}{\mu}u^0(u^3E_2-u^2E_3),$$

$$H_2 = \frac{1}{\mu_0\mu}B_2+\frac{\gamma}{\mu_0\mu}(+u^1u^2B_1-u^3u^3B_2-u^1u^1B_2+u^2u^3B_3)+\frac{\epsilon_0 c\gamma}{\mu}u^0(u^3E_2-u^2E_3),$$

$$H_3 = \frac{1}{\mu_0\mu}B_3+\frac{\gamma}{\mu_0\mu}(+u^3u^1B_1+u^3u^2B_2-u^1u^1B_3-u^2u^2B_3)+\frac{\epsilon_0 c\gamma}{\mu}u^0(u^2E_1-u^1E_2);$$

these relations are written in the vector form as follows:

$$\mathbf{H} = \frac{1}{\mu_0\mu}\mathbf{B}+\frac{\gamma}{\mu_0\mu}\frac{\mathbf{V}\times(\mathbf{V}\times\mathbf{B}))}{1-V^2}+\frac{\epsilon_0 c\gamma}{\mu}\frac{\mathbf{V}\times\mathbf{E}}{1-V^2}. \tag{50}$$

Relations (49), (50) provide us with the vector form of constitutive relations for the uniform medium moving with velocity $\mathbf{V}$. We may conclude that the motion is effectively equivalent to an anisotropic medium.

9. Constitutive equations for an arbitrary linear medium

Above, we started with Maxwell equations in vacuum and changed them to the Riemannian space-time. At that, the vacuum material equations $H_{\alpha\beta} = \epsilon_0 F_{\alpha\beta}$, due to the presence of metrical tensor $g^{\rho\alpha}(x)$, gave us the modified material equations

$$H^{\rho\sigma}(x) = \sqrt{-g}\, g^{\rho\alpha}(x) g^{\sigma\beta}(x)\epsilon_0 F_{\alpha\beta}(x). \tag{51}$$

As a first generalization, let us start with Maxwell equations in the uniform media. In this case, the material equations for the uniform media

$$H_{\alpha\beta}(x) = \epsilon_0 \eta_\alpha^{\ a}\eta_\beta^{\ b} F_{ab}(x) \tag{52}$$

will take the form

$$H^{\rho\sigma}(x)) = \sqrt{-g}\, g^{\rho\alpha}(x) g^{\sigma\beta}(x)\epsilon_0 \eta_\alpha^{\ a}\eta_\beta^{\ b} F_{ab}(x). \tag{53}$$

With the notation $\hat{F}_{\alpha\beta}(x) = \eta_\alpha^{\ a}\eta_\beta^{\ b} F_{ab}(x)$, they can be rewritten as follows

$$H^{\rho\sigma}(x)(x) = \sqrt{-g}\, g^{\rho\alpha}(x) g^{\sigma\beta}(x)\epsilon_0 \hat{F}_{\alpha\beta}(x), \quad \hat{F}_{\alpha\beta}(x) = \begin{vmatrix} 0 & \epsilon F_{0i} \\ \epsilon F_{i0} & F_{ik}/\mu \end{vmatrix}. \tag{54}$$

One should not make any additional calculation, it suffices to make one formal change $F_{\alpha\beta}(x) \longrightarrow \hat{F}_{\alpha\beta}(x)$, so the constitutive equations take the form

$$D^i = \epsilon_0 \epsilon \epsilon^{ik}(x) E_k + \epsilon_0 \epsilon c \alpha^{ik}(x) B_k, \quad H^i = \epsilon_0 \epsilon c \beta^{ik}(x) E_k + \frac{1}{\mu_0\mu}(\mu^{-1})^{ik}(x) B_k. \tag{55}$$

These relations provide us with the material equations for the uniform media modified by Riemannian geometry of the background space-time.

It is easy to make another extension: let us start with an anisotropic medium in Minkowski space

$$D_i = \epsilon_0 \epsilon_{(0)kl} E_l , \quad H_i = \mu_0^{-1} \mu_{(0)kl}^{-1} B_k ; \tag{56}$$

these equations will be modified as

$$D^i = \epsilon_0 \epsilon^{ik}(x) \epsilon_{(0)kl} E_l + \epsilon_0 c \alpha^{ik}(x) \mu_{(0)kl}^{-1} B_l , \quad H^i = \epsilon_0 c \beta^{ik}(x) \epsilon_{(0)kl} E_l + \mu_0^{-1} (\mu^{-1})^{ik}(x) \mu_{(0)kl} B_l . \tag{57}$$

Now we make the final extension: constitutive equations for an arbitrary linear medium, determined by 4-rank tensor $H_{\alpha\beta}(x) = \epsilon_0 \Delta_{\alpha\beta}{}^{ab} F_{ab}(x)$, will be transformed by the Riemannian geometry into the following ones

$$H^{\rho\sigma}(x)(x) = \sqrt{-g}\, g^{\rho\alpha}(x) g^{\sigma\beta}(x) \epsilon_0 \Delta_{\alpha\beta}{}^{ab} F_{ab}(x), \tag{58}$$

or in the 3-dimensional form

$$D^i = \epsilon_0 \Big[\epsilon^{ik}(x) \epsilon_{(0)kl} + \alpha^{ik}(x) \beta_{(0)kl} \Big] E_l + \epsilon_0 c \Big[\epsilon^{ik}(x) \alpha_{(0)kl} + \alpha^{ik}(x) \mu_{(0)kl}^{-1} \Big] B_l ,$$

$$H^i = \epsilon_0 c \Big[\beta^{ik}(x) \epsilon_{(0)kl} + (\mu^{-1})^{ik}(x) \beta_{(0)kl} \Big] E_l + \frac{1}{\mu_0} \Big[\beta^{ik}(x) \alpha_{(0)kl} + (\mu^{-1})^{ik}(x) \mu_{(0)kl}^{-1} \Big] B_l .$$

In the index-free form, they can be written as

$$\mathbf{D} = \epsilon_0 \Big[\epsilon(x) \epsilon_{(0)} + \alpha(x) \beta_{(0)} \Big] \mathbf{E} + \epsilon_0 c \Big[\epsilon(x) \alpha_{(0)} + \alpha(x) \mu_{(0)}^{-1} \Big] \mathbf{B},$$

$$\mathbf{H} = \epsilon_0 c \Big[\beta(x) \epsilon_{(0)} + \mu^{-1}(x) \beta_{(0)} \Big] \mathbf{E} + \frac{1}{\mu_0} \Big[\beta(x) \alpha_{(0)} + \mu^{-1}(x) \mu_{(0)}^{-1} \Big] \mathbf{B}. \tag{59}$$

These formulas can be presented symbolically as follow

$$\hat{\epsilon} = \epsilon(x) \epsilon_{(0)} + \alpha(x) \beta_{(0)} , \quad \hat{\alpha} = \epsilon(x) \alpha_{(0)} + \alpha(x) \mu_{(0)}^{-1} ,$$

$$\hat{\beta} = \beta(x) \epsilon_{(0)} + \mu^{-1}(x) \beta_{(0)} , \quad \hat{\mu}^{-1} = \beta(x) \alpha_{(0)} + \mu^{-1}(x) \mu_{(0)}^{-1} . \tag{60}$$

If the initial constitutive equations have only diagonal blocks $\epsilon_{(0)}, \alpha_{(0)} = 0, \beta_{(0)} = 0, \mu_{(0)}^{-1}$, relations (60) become simpler

$$\hat{\epsilon} = \epsilon(x) \epsilon_{(0)} , \quad \hat{\alpha} = +\alpha(x) \mu_{(0)} , \quad \hat{\beta} = \beta(x) \epsilon_{(0)} , \quad \hat{\mu}^{-1} = \mu(x) \mu_{(0)}^{-1} . \tag{61}$$

10. Plane wave in the Lobachevsky space

Let us study a simple example, the solutions of plane wave type for the Maxwell equations in 3-dimensional Lobachevsky space, with the use of the horospherical coordinates. We start with equations

$$(I) \quad \partial_\alpha F_{\beta\gamma} + \partial_\beta F_{\gamma\alpha} + \partial_\gamma F_{\alpha\beta} = 0, \quad (II) \quad \frac{1}{\sqrt{-g}} \partial_\beta \sqrt{-g}\, F^{\beta\alpha} = \epsilon_0^{-1} j^\alpha , \tag{62}$$

where $g(x) = \det[g_{\alpha\beta}(x)] < 0$. Eqs. (I) are equivalent to

$$(123) \quad \partial_1 F_{23} + \partial_2 F_{31} + \partial_3 F_{12} = 0, \quad (012) \quad \partial_0 F_{12} + \partial_1 F_{20} + \partial_2 F_{01} = 0,$$

$$(023) \quad \partial_0 F_{23} + \partial_2 F_{30} + \partial_3 F_{02} = 0, \quad (031) \quad \partial_0 F_{31} + \partial_3 F_{10} + \partial_1 F_{03} = 0. \tag{63}$$

In its turn, eqs. (II) in the detailed form are written as

$$\frac{1}{\sqrt{-g}} \partial_1 \sqrt{-g}\, F^{10} + \frac{1}{\sqrt{-g}} \partial_2 \sqrt{-g}\, F^{20} + \frac{1}{\sqrt{-g}} \partial_3 \sqrt{-g}\, F^{30} = \epsilon_0^{-1} j^0 ,$$

$$\frac{1}{\sqrt{-g}} \frac{\partial}{\partial x^0} \sqrt{-g}\, F^{01} - \frac{1}{\sqrt{-g}} \frac{\partial}{\partial x^2} \sqrt{-g}\, F^{12} + \frac{1}{\sqrt{-g}} \frac{\partial}{\partial x^3} \sqrt{-g}\, F^{31} = \epsilon_0^{-1} j^1 ,$$

$$\frac{1}{\sqrt{-g}} \frac{\partial}{\partial x^0} \sqrt{-g}\, F^{02} + \frac{1}{\sqrt{-g}} \frac{\partial}{\partial x^1} \sqrt{-g}\, F^{12} - \frac{1}{\sqrt{-g}} \frac{\partial}{\partial x^3} \sqrt{-g}\, F^{23} = \epsilon_0^{-1} j^2 ,$$

$$\frac{1}{\sqrt{-g}} \frac{\partial}{\partial x^0} \sqrt{-g}\, F^{03} - \frac{1}{\sqrt{-g}} \frac{\partial}{\partial x^1} \sqrt{-g}\, F^{31} + \frac{1}{\sqrt{-g}} \frac{\partial}{\partial x^2} \sqrt{-g}\, F^{23} = \epsilon_0^{-1} j^3 . \tag{64}$$

We will specify these equations in the absence of any sources, and in the horospherical coordinates of the hyperbolic model H_3:

$$u_1 = re^{-z}\cos\phi, \quad u_2 = re^{-z}\sin\phi, \quad u_3 = \sinh z + \frac{1}{2}r^2 e^{-z} = \frac{1}{2}[e^{+z} + (r^2 - 1)e^{-z}],$$

$$u_0 = \cosh z + \frac{1}{2}r^2 e^{-z} = \frac{1}{2}[e^{+z} + (r^2 + 1)e^{-z}], \quad u_1^2 + u_2^2 + u_3^2 - u_0^2 = -1, \quad u_0 = +\sqrt{1 + u_1^2 + u_2^2 + u_3^2} > 0,$$

$$dS^2 = c^2 dt^2 - e^{-2z}dr^2 - e^{-2z}r^2 d\phi^2 - dz^2; \tag{65}$$

here all the coordinates are dimensionless. In the limit of vanishing curvature, the given coordinates reduce to cylindrical ones. Using the notations $x^0, r = x^1, \phi = x^2, z = x^3$, eqs. (63) and (64) take the form

$$\partial_1 F_{23} + \partial_2 F_{31} + \partial_3 F_{12} = 0, \quad \partial_0 F_{12} + \partial_1 F_{20} + \partial_2 F_{01} = 0,$$

$$\partial_0 F_{23} + \partial_2 F_{30} + \partial_3 F_{02} = 0, \quad \partial_0 F_{31} + \partial_3 F_{10} + \partial_1 F_{03} = 0, \tag{66}$$

$$\frac{1}{r}\partial_r r F^{10} + \partial_\phi F^{20} + e^{2z}\partial_z e^{-2z}F^{30} = 0, \quad \partial_0 F^{01} - \partial_\phi F^{12} + e^{2z}\partial_z e^{-2z}F^{31} = 0,$$

$$\partial_0 F^{02} + \frac{1}{r}\partial_r r F^{12} - e^{2z}\partial_z e^{-2z}F^{23} = 0, \quad \partial_0 F^{03} - \frac{1}{r}\partial_r r F^{31} + \partial_\phi F^{23} = 0. \tag{67}$$

Let us impose the simplicity restrictions

$$F_{01} = 0, \quad F_{02} = F_{0\phi}(r, z) \neq 0, \quad F_{03} = 0, \tag{68}$$

then eqs. (66), (67) become simpler

$$\partial_r F_{23} + \partial_z F_{12} = 0, \partial_0 F_{12} + \partial_r F_{20} = 0, \partial_0 F_{23} + \partial_z F_{02} = 0, \tag{60}$$

$$F_{31} = 0, \quad \partial_0 F^{02} + \frac{1}{r}\partial_r r F^{12} - e^{2z}\partial_z e^{-2z}F^{23} = 0. \tag{70}$$

Note that in (69), the first equation follows from 2-nd and 3-rd ones, so only three equations are independent

$$\partial_0 F_{12} = \partial_r F_{02}, \quad \partial_0 F_{23} = -\partial_z F_{02}, \tag{71}$$

$$\partial_0^2 g^{22} F_{02} + \frac{1}{r}\partial_r r g^{11} g^{22}\partial_0 F_{12} - e^{2z}\partial_z e^{-2z} g^{22} g^{33}\partial_0 F_{23} = 0. \tag{72}$$

Differentiating the third equation with respect to x_0 and taking into account (71), we get

$$-\frac{e^{2z}}{r^2}\partial_0^2 F_{02} + \frac{1}{r}\partial_r \frac{e^{4z}}{r}\partial_r F_{02} + \frac{e^{2z}}{r^2}\partial_z^2 F_{02} = 0. \tag{73}$$

Let us search for solutions of eq. (73) in the form of a plane wave

$$F_{02} = E(r)\cos(k_0 x^0 - kz + \beta), \tag{74}$$

where the dimensionless quantities are used

$$k_0 = \frac{\omega\rho}{c}, \quad k = \pm\frac{\omega\rho}{c} = \pm k_0, \tag{75}$$

then eq. (73) leads to

$$\frac{k_0^2 e^{2z}}{r^2}E + \frac{e^{4z}}{r}\frac{d}{dr}\frac{1}{r}\frac{d}{dr}E - \frac{k_0^2 e^{2z}}{r^2}E = 0, \tag{76}$$

or

$$\frac{d}{dr}\frac{1}{r}\frac{d}{dr}E = 0, \tag{77}$$

so we arrive at two simple solutions

$$E = \text{const}\, r^2, \quad E = \text{const}. \tag{78}$$

Eq. (77) coincides with the similar equation arising in the flat space; correspondingly its solutions coincide with the known ones in the Minkowski space. The most interesting is the second solution $E = \text{const}$, so that

$$F_{02} = E\cos(k_0 x^0 - kz + \beta). \tag{79}$$

From (71) we readily find F_{12} and F_{23}:

$$\partial_0 F_{12} = \partial_r F_{02}, \quad \partial_0 F_{23} = -\partial_z F_{02} \quad \Rightarrow \quad F_{12} = 0, \quad F_{23} = E\frac{k}{k_0}\cos(k_0 x^0 - kz + \beta). \tag{80}$$

The following 4-potential corresponds to electromagnetic field (79), (80)

$$A_\phi = A_2 = \frac{E}{k_0}\sin(k_0 x^0 - kz + \beta). \tag{81}$$

It exactly coincides with the expression of the 4-potential for the simplest cylindrical wave in Minkowski space. Taking $\beta = 0, \pi/2$, we get two linearly independent solutions.

The above solution obtained in horospherical coordinates can be translated to quasi-Cartesian coordinates in H_3:

$$(x^1, x^2, x^3) = (r, \phi, z) \quad \Rightarrow \quad y^i = \frac{u_i}{u_0} = (q_1, q_2, q_3),$$

$$y^1 = \frac{2r\cos\phi}{e^{2z} + r^2 + 1}, \quad y^2 = \frac{2r\sin\phi}{e^{2z} + r^2 + 1}, \quad y^3 = \frac{e^{2z} + r^2 - 1}{e^{2z} + r^2 + 1}. \tag{82}$$

Allowing for the following identities

$$A_i(y) = \frac{\partial x^j}{\partial y^i} A_j = \frac{\partial \phi}{\partial y^i} A_\phi(x), \quad \frac{y^2}{y^1} = \tan\phi, \quad \frac{1}{\cos^2\phi} = \frac{(y^1)^2 + (y^2)^2}{(y^1)^2},$$

$$\frac{(y^1)^2 + (y^2)^2}{(y^1)^2}\frac{\partial \phi}{\partial y^1} = -\frac{y^2}{(y^1)^2} \quad \Rightarrow \quad \frac{\partial \phi}{\partial y^1} = -\frac{y^2}{(y^1)^2 + (y^2)^2},$$

$$\frac{(y^1)^2 + (y^2)^2}{(y^1)^2}\frac{\partial \phi}{\partial y^2} = \frac{1}{y^1} \quad \Rightarrow \quad \frac{\partial \phi}{\partial y^2} = \frac{y^1}{(y^1)^2 + (y^2)^2}, \tag{83}$$

we arrive at (for simplicity we use notation $y^j = q_j$)

$$A_1(q) = -\frac{q_2}{q_1^2 + q_2^2} A\sin(\omega t - kz + \beta), \quad A_2(q) = \frac{q_1}{q_1^2 + q_2^2} A\sin(\omega t - kz + \beta), \quad A_3(q) = 0. \tag{84}$$

Allowing for the formulas

$$e^z = \frac{\sqrt{1 - q_1^2 - q_2^2 - q_3^2}}{1 - q_3} \quad \Rightarrow \quad z = \ln\frac{\sqrt{1 - q_1^2 - q_2^2 - q_3^2}}{1 - q_3}, \tag{85}$$

we obtain the following expressions for these solutions:

$$A_1(q) = -\frac{q_2}{q_1^2 + q_2^2} A\sin\Big(\omega t - k\ln\frac{\sqrt{1 - q_1^2 - q_2^2 - q_3^2}}{1 - q_3} + \beta\Big),$$

$$A_2(q) = \frac{q_1}{q_1^2 + q_2^2} A\sin\Big(\omega t - k\ln\frac{\sqrt{1 - q_1^2 - q_2^2 - q_3^2}}{1 - q_3} + \beta\Big), \quad A_3(q) = 0. \tag{86}$$

It should be noted that the very similar and trivial form of solutions in horospherical coordinates turns out to be much more complicated in quasi-Cartesian coordinates. Let us specify the electromagnetic tensor for that solution (compare it with (79) and (80))

$$\varphi = \Big(\omega t - k\ln\frac{\sqrt{1 - q^2}}{1 - q_3} + \beta\Big), \quad q^2 = q_1^2 + q_2^2 + q_3^2,$$

$$E_1 = F_{01} = -\frac{q_2\,\omega}{q_1^2+q_2^2}A\cos\varphi,\quad E_2 = F_{02} = \frac{q_1\,\omega}{q_1^2+q_2^2}A\cos\varphi,\quad E_3 = F_{03} = 0,\quad -B_3 = F_{12} = Ak\frac{1}{1-q^2}\cos\varphi,$$

$$-B_1 = F_{23} = Ak\frac{q_1}{(q_1^2+q_2^2)}\frac{(1-q_3-q_1^2-q_2^2)}{(1-q_3)(1-q^2)}\cos\varphi = Ak\frac{q_1}{(q_1^2+q_2^2)}F\cos\varphi,$$

$$-B_2 = F_{31} = Ak\frac{q_2}{(q_1^2+q_2^2)}\frac{(1-q_3-q_1^2-q_2^2)}{(1-q_3)(1-q^2)}\cos\varphi = Ak\frac{q_2}{(q_1^2+q_2^2)}F\cos\varphi, \tag{87}$$

here the notation is used

$$F = \frac{(1-q_3-q_1^2-q_2^2)}{(1-q_3)(1-q^2)}.$$

For this wave, the electric vector is oriented along the circle in the plane $1-2$; whereas the magnetic vector has a projection on axis 3 and radial direction. The density of energy flow $\mathbf{S} = \mathbf{E}\times\mathbf{B}$ is described by the formulas

$$S_1 = E_2B_3 = -A^2k\omega\frac{q_1}{q_1^2+q_2^2}\frac{1}{1-q^2}\frac{1+\cos 2\varphi}{2},\quad S_2 = -E_1B_3 = -A^2k\omega\frac{q_2}{q_1^2+q_2^2}\frac{1}{1-q^2}\frac{1+\cos 2\varphi}{2},$$

$$S_3 = E_1B_2 - E_2B_1 = \frac{A^2\omega k}{(q_1^2+q_2^2)}F\frac{1+\cos 2\varphi}{2}; \tag{88}$$

therefore, the vector $\mathbf{S}$ has the structure $\mathbf{S} = \mathbf{S}_{\parallel} + \mathbf{S}\perp$. Let us detail the surface of a fixed phase

$$\omega t - k\ln\frac{\sqrt{1-q_1^2-q_2^2-q_3^2}}{1-q_3} = \lambda = \omega t_0,$$

whence it follows

$$\frac{1-q_1^2-q_2^2-q_3^2}{(1-q_3)^2} = a^2(t),\quad a^2(t) = e^{2\omega(t-t_0)}. \tag{89}$$

In the canonical form, it is recognized as an ellipsoid equation

$$\Big(q_3 - \frac{a^2}{1+a^2}\Big)^2 + \frac{q_1^2}{1+a^2} + \frac{q_2^2}{1+a^2} = \frac{1}{(1+a^2)^2}. \tag{90}$$

In the moment $t = t_0$, the parameter $a = 1$ and we have

$$\Big(q_3 - \frac{1}{2}\Big)^2 + \frac{q_1^2}{2} + \frac{q_2^2}{2} = \frac{1}{4} \quad\longrightarrow\quad q_3 \to +1.$$

When $a \to 0$ ($t \to -\infty$), we obtain $q_3^2 + q_1^2 + q_2^2 = 1.$ When $a \to \infty$ ($t \to +\infty$), we will have

$$(q_3-1)^2 + \frac{q_1^2}{\infty^2} + \frac{q_2^2}{\infty^2} = \frac{1}{\infty^4}.$$

The constructed solution can be considered as an exact solution for the Maxwell equations in Minkowski space-time but in the special effective medium.

11. Arbitrary metrical tensor, additional consideration

In the general case, four (3×3) constitutive tensors contain $6+6+9=21$ independent functions, but the metrical tensor $g^{\alpha\beta}(x)$ is determined only by 10 functions, so we must assume the existence of additional constraints on constitutive tensors. In the first place, note evident identity

$$\mathrm{Sp}\,\alpha = \mathrm{Sp}\,\beta = 0. \tag{91}$$

Besides, we can see two identities

$$\mathbf{g}\beta = 0 \quad \Rightarrow \quad (g^{01}, g^{02}, g^{03}) \begin{vmatrix} \beta^{11} & \beta^{12} & \beta^{13} \\ \beta^{21} & \beta^{22} & \beta^{23} \\ \beta^{31} & \beta^{32} & \beta^{33} \end{vmatrix} = 0, \tag{92}$$

$$\alpha \mathbf{g}^{+} = 0 \quad \Rightarrow \quad \begin{vmatrix} \alpha^{11} & \alpha^{12} & \alpha^{13} \\ \alpha^{21} & \alpha^{22} & \alpha^{23} \\ \alpha^{31} & \alpha^{32} & \alpha^{33} \end{vmatrix} \begin{vmatrix} g^{01} \\ g^{02} \\ g^{03} \end{vmatrix} = 0; \tag{93}$$

which are equivalent to each other. To proceed, let us rewrite expressions for $\epsilon^{ik}(x)$ and $(\mu^{-1})^{ik}(x)$ as follows

$$\frac{1}{g^{00}(x)}\Big(\frac{\epsilon^{ik}(x)}{\sqrt{-G(x)}} + (\mathbf{g}(x)\cdot\mathbf{g}(x))^{ik}\Big) = g^{ik}(x), \quad \frac{(\mu^{-1})^{ik}(x)}{\sqrt{-G(x)}} = \det(g^{ik}(x))\,(g^{ik}(x))^{-1} = \frac{1}{\det(g_{ik}(x))}(g_{ik}(x))$$

$$\Rightarrow \quad \mu^{ik}(x)\sqrt{-G(x)} = \det(g_{ik}(x))\, g^{ik}(x); \tag{94}$$

whence we derive the equation

$$\frac{1}{g^{00}(x)}\Big(\frac{\epsilon^{ik}(x)}{\sqrt{-G(x)}} + (\mathbf{g}(x)\cdot\mathbf{g}(x))^{ik}\Big) = \frac{\mu^{ik}(x)\sqrt{-G(x)}}{\det(g_{ik}(x))}, \tag{95}$$

or differently

$$\epsilon^{ik}(x) + \sqrt{-G(x)}[\mathbf{g}(x)\cdot\mathbf{g}(x)]^{ik} = -g^{00}(x)G(x)\frac{\mu^{ik}(x)}{\det(g_{ik}(x))}. \tag{96}$$

This relationship provides us with the needed additional constraint on $\epsilon^{ik}(x)$ and $\mu^{ik}(x)$. For the special form of metrical tensor

$$\mathbf{g}(x) = 0, \quad G(x) = g_{00}\det[g_{ij}(x)]; \tag{97}$$

we obtain the known result

$$\epsilon^{ik}(x) = -\frac{1}{g_{00}(c)}G(x)\frac{1}{\det[g_{ik})x)]}\mu^{ik}(x) = -\mu^{ik}(x). \tag{98}$$

References

1. Gordon W. Zur Lichtfortpanzungnach der Relativitätstheorie. *Annalen der Physik. (Leipzig).* 1923;72: 421-456.
2. Tamm IE. Electrodinamika anizotropnoi sredy v spetsialnonoi teorii otnositelnosti. *Zhurnal Russkogo Fiziko-Khimicheskogo Obschestva. Fizika.* 1924;56(2-3): 248-262. (In Russian)
3. Tamm IE. Kristallooptika teorii otnositelbnosti v svyazi s geometriei bikvadratichnoi formuy. *Zhurnal Russkogo Fiziko-Khimicheskogo Obschestva. Fizika.* 1925;54(3-4): 1. (In Russian)
4. Mandelstam LI, Tamm IE. Elektrodynamik der anisotropen Medien und der speziallen Relativitatstheorie. *Mathematische Annalen.* 1925;95: 154-160.
5. Landau LD, Lifsjitz EM. *Theoretical physics. Vol. 2. Field theory*. Moscow: Science; 1973.
6. Novacu V. *Introducere in Electrodinamica*. Bucharest: Editura Academiei; 1955.
7. Balazs NL. Effect of a gravitational field, due to a rotating body, on the plane of polarization of an electromagnetic wave. *Physical Review*. 1958;110(1): 236-239.
8. Quan PM. Sur les équations de l'électromagnetisme dans la materie. *Compt. Rend. Acad. Sci. Paris*. 1956;242: 465-467.
9. Quan PM. Projections des géodésiques de longuer nulle et rayons électromagnétiques dans un milieu en movement permanent. *Comptes rendus de l'Académie des Sciences. Paris.* 1956;242: 857.
10. Skrotskii GV. The influence of gravitation on the propagation of light. *Soviet Physics Doklady.* 1957;2: 226-229.

11. Tomil'chik LM, Fedorov FI. Magnetic anisotropy as metrical property of space. *Crystalography*. 1959;4(4): 498-504.
12. Plebanski J. Electromagnetic waves in gravitational fields. *Physical Review*. 1960;118(5): 1396-1408.
13. Post E. *Formal Structure of Electrodynamics. General Covariance and Electromagnetics*. Amsterdam: North-Holland; 1962.
14. Tonnelat MA. Sur la théorie du photon dans un espace de Riemann. *Annals of Physics. Phys. N.Y.* 1941;15: 144-224.
15. Ellis JR. *Maxwell's equations and theories of Maxwell form. Ph.D. thesis.* University of London; 1964.
16. De Felice F. On the gravitational field acting as an optical medium. *General Relaivity and Gravity*. 1971;2: 347-357.
17. Bolotovskiy BM, Stolyarov SN. Modern state of electrodynamics of moving media. *Uspekhi Fizicheskikh Nauk.* 1974;114(4):489-529.
18. Schleich W, Scully MO. General relativity and modern optics. In: Grynberg G, Stora R (eds.) *New Trends in Atomic Physics*. *Les Houches, Session XXXVIII, 1982.* Amsterdam: North-Holland; 1984.
19. Berezin AB, Tolkachev EA, Fedorov FI. Dual-invariant constitutive equations for gyrotropic media in rest. *Doklady AN BSSR*. 1985;29(7): 595-597.
20. Berezin AB, Tregubovich A, Tolkachev EA, Fedorov FI. Quaternion constitutive equations for moving gyrotropic media. *J. Appl. Spectroscopy.* 1987;47(1): 747-751.
21. Barykin VN, Tolkachev EA, Tomil’chik LM. On symmetry aspects for choosing constitutive relations in microscopic electrodynamics of moving media. *Vesti AN BSSR. Ser.Phys.-mat.* 1982;2: 96-98.
22. Antoci S. The electromagnetic properties of material media and Einstein's unified field theory. *Progress of Theor. Phys*. 1992;87: 1343-1357.
23. Antoci S, Mihich L. A forgotten argument by Gordon uniquely selects Abraham's tensor as the energy-momentum tensor for the electromagnetic field in homogeneous, isotropic matter. *Nuovo Cimento. B.* 1997;112: 991.
24. Hillion P. Spinor electromagnetism in isotropic chiral media. *Adv. Appl. Clifford Alg*. 1993;3: 107-120.
25. Hillion P. Constitutive relations and Clifford algebra in electromagnetism. *Advances in Applied Clifford Algebras* 1995;5: 141-158.
26. Leonhardt U, Piwnicki P. Optics of nonuniformly moving media. *Phyical Review. A.* 1999;60: 4301-4312.
27. Leonhardt U. Space-time geometry of quantum dielectrics. *Physical Review. A.* 2000;62(1): 012111.
28. De Lorenci WA, Klippert R, Obukhov YN. On optical black holes in moving dielectrics. *Physical Review. D.* 2003;68(6): 061502.
29. Hehl FW, Obukhov YN. Linear media in classical electrodynamics and the Post constraint. *Physics Letters. A.* 2005;334(4): 249-259.
30. Novello M, Salim JM. Effective electromagnetic geometry. *Physical Review. D.* 2001;63(8): 083511.
31. Novello M, Perez Bergliaffa S. Effective Geometry. *AIP Conf. Proc*. 2003;668(1): 288-300.
32. Novello M, Perez Bergliaffa S, Salim J. Analog black holes in flowing dielectrics. *Classical and Quantum Gravity*. 2003;20(5): 859-872.
33. De Lange OL, Raab RE. Post's constrain for electromagnetic constitutive relations. *Journal of Optics. A.* 2001;3(6): 23-26.

34. Raab RE, de Lange OL. Symmetry constrains for electromagnetic constitutive relations. *Journal of Optics. A.* 2001;3(6): 446-451.
35. Nandi KK, Zhang YZ, Alsing PM, Evans JC, Bhadra A. Analog of the Fizeau effect in an effective optical medium. *Physical Review. D.* 2003;67(2): 025002.
36. Boonserm P, Cattoen C, Faber T, Visser M, Weinfurtner S. Effective refractive index tensor for weak field gravity. *Classical and Quantum Gravity.* 2005;22(11): 1905-1915.
37. Red'kov V.M. *Particle fields in Riemannian space and the Lorentz Group.* Minsk: Belarusian Science; 2009.

THE AUTHORS

N.G. Krylova
e-mail: nina-kr@tut.by
ORCID: 0000-0002-9819-0556

E.M. Ovsiyuk
e-mail: e.ovsiyuk@mail.ru
ORCID: 0000-0002-7921-7960

A.V. Ivashkevich
e-mail: ivashkevich.alina@yandex.by
ORCID: 0000-0002-5029-7901

V.M. Red'kov
e-mail: v.redkov@ifan.bel.bas-net.by
ORCID: 0000-0001-5318-565X

Materials Physics and Mechanics. 2022;49(1): 17-43
Conference materials
http://dx.doi.org/10.18149/MPM.4912022_2

Maxwell electrodynamics, complex rotation group, media

A.V. Ivashkevich[1], E.M. Ovsiyuk[2], V.V. Kisel[3], V.M. Red'kov[1]✉

[1]B.I. Stepanov Institute of Physics, Minsk, Republic of Belarus

[2]Mozyr State Pedagogical University named after I.P. Shamyakin, Republic of Belarus

[3]Belarusian State University of Informatics and Radio-Electronics, Minsk, Republic of Belarus

✉ v.redkov@ifanbel.bas-net.by

Abstract. Our treatment will be with definite accents: the main attention is given to classical electrodynamics in material media, focusing on the structure of Minkowski constitutive relations, matrix complex form of Maxwell theory in the form of Riemann–Silberstein–Majorana–Oppenheimer, and the theory of complex rotation group $SO(3.C)$, isomorphic to the Lorentz group. This review includes the topics: introduction; matrix complex form of Maxwell theory in a vacuum; modified Lorentz symmetry in electrodynamics; Minkowski electrodynamics in moving bodies; Minkowski constitutive relations in the complex 3-vector form; symmetry properties of the matrix equation in any linear media; Dirac matrices and electromagnetic field.

Keywords: complex rotation group $SO(3.C)$, Dirac matrices, formalism Majorana–Oppenheimer, Maxwell theory, Minkovski constitutive equations

Acknowledgements. *No external funding was received for this study.*

Citation: Ivashkevich AV, Ovsiyuk EM, Kisel VV, Red'kov VM. Maxwell electrodynamics, complex rotation group, media. *Materials Physics and Mechanics*. 2022;49(1): 17-43. DOI: 10.18149/MPM.4912022_2.

1. Introduction

Special Relativity arose from the study of the symmetry properties of the Maxwell equations: Lorentz [1-3], Poincaré [4-10], and Einstein [11-13]. Naturally, an analysis of the Maxwell equations with respect to Lorentz transformations was the first object of relativity theory [14-21]. After discovering the relativistic equation for a particle with spin 1/2 – Dirac [22, 23] – much work was done to study spinors and vectors within the Lorentz group theory: Ivanenko–Landau [24], Neumann [25], van der Waerden [26], Juvet [27]. As was shown, any quantity which transforms linearly under Lorentz transformations is a spinor. For that reason, spinor quantities are considered fundamental in quantum field theory and basic equations for such quantities should be written in a spinor form. A spinor formulation of Maxwell equations was studied by Laporte and Uhlenbeck [28], see also Rumer [29]. In 1931, Majorana [30] and Oppenheimer [31] proposed to consider the Maxwell theory of electromagnetism as the wave mechanics of the photon. They introduced a complex 3-vector wave function satisfying the massless Dirac-like equations. Before Majorana and Oppenheimer, the most crucial steps were made by Silberstein [32]; he showed the possibility of formulating the Maxwell equations in the terms of complex 3-vector entities. Silberstein in his second paper [33] wrote that the complex form of Maxwell equations has been known before; he refers to the second

Publisher: Peter the Great St. Petersburg Polytechnic University

volume of the lecture notes on the differential equations of mathematical physics by Riemann which were edited and published by H. Weber in 1901 [34]. This not widely used fact is noted by Bialynicki-Birula [35,36].

The Maxwell equations in the matrix Dirac-like form were considered during long time by many authors; the interest to the Majorana–Oppenheimer formulation of electrodynamics has grown in recent years: Luis de Broglie [37-40], Mercier [41], Petiau [42], Proca [43, 44], Kemmer [45-47], Bhabha [48], Belinfante [49,50], Taub [51], Sakata and Taketani [52], Erikson [53], Schrödinger [54-56], Tonnelat [57], Stratton [58], Heitler [59], Einstain-bargnann [60], Harish-Chandra [61-62], Hoffmann [63], Utiyama [64], Schouten [65], Mercier [66], de Broglie and Tonnelat [67], Gupta [68], Bleuler [69], Brulin and Hjalmars [70], Rosen [71], Fujiwara [72], Gürsey [73], Gupta [74], Lichnerowicz [75], Ohmura [76], Borgardt [77,78], Fedorov [79], Kuohsien [80], Bludman [81], Good [82], Moses [83-85], Silveira [86,87], Lomont [88], Post [89], Bogush and Fedorov [90], Sachs and Schwebel [91], Ellis [92], Beckers and Pirotte [93], Casanova [94], Carmeli [95], Weingarten [96], Mignani, Recami and Baldo [97], Newmann [98], Frankel [99], Edmonds [100], Jena et al [101], Venuri [102], Chow [103], Fushchich and Nikitin [104], Cook [105,106], Giannetto [107], Nuez et al [108], Kidd et al [109], Recami [110], Hillion [111], Inagaki [112], Sipe [113], Ghose [114], Gersten [115], Esposito [116], Torres del Castill and Mercado-Perez [117], Dvoeglazov [118,119], Gsponer [120], Ivezic [121-125], Kravchenko [126], Varlamov [127], Khan [128].

In the present paper, the main attention is given to technical aspects of classical electrodynamics based on the theory of rotation complex group SO(3.C) which is isomorphic to the Lorentz group: Macfarlane [129], Fedorov [130].

2. Matrix complex form of Maxwell theory in a vacuum

Let us start with Maxwell equations in the homogeneous (ε, μ)-media in presence of external sources:

$$div\, cB = 0, \quad rot\, E = -\frac{\partial cB}{\partial ct}, \quad div\, E = \frac{\rho}{\varepsilon\varepsilon_0}, \quad rot\, cB = \mu\mu_0 cJ + \varepsilon\mu\frac{\partial E}{\partial ct}. \tag{1}$$

With the use of usual notation for current 4-vector

$$j^a = (\rho, J/c), \quad c^2 = 1/\varepsilon_0\mu_0, \tag{2}$$

eqs. (1) read

$$div\, cB = 0, \quad rot\, E = -\frac{\partial cB}{\partial ct}, \quad div\, E = \frac{\rho}{\varepsilon_0}, \quad rot\, cB = \frac{j}{\varepsilon_0} + \frac{\partial E}{\partial ct}, \tag{3}$$

or in an explicit component form (let $x_0 = ct, \partial_0 = c\partial_t$)

$$\begin{aligned} &\partial_1 cB^1 + \partial_2 cB^2 + \partial_3 cB^3 = 0, \quad \partial_2 E^3 - \partial_3 E^2 + \partial_0 cB^1 = 0, \\ &\partial_3 E^1 - \partial_1 E^3 + \partial_0 cB^2 = 0, \quad \partial_1 E^2 - \partial_2 E^1 + \partial_0 cB^3 = 0, \\ &\partial_1 E^1 + \partial_2 E^2 + \partial_3 E^3 = j^0/\varepsilon_0, \quad \partial_2 cB^3 - \partial_3 cB^2 - \partial_0 E^1 = j^1/\varepsilon_0, \\ &\partial_3 cB^1 - \partial_1 cB^3 - \partial_0 E^2 = j^2/\varepsilon_0, \quad \partial_1 cB^2 - \partial_2 cB^1 - \partial_0 E^3 = j^3/\varepsilon_0. \end{aligned} \tag{4}$$

Let us introduce 3-dimensional complex vector

$$\psi^k = E^k + icB^k, \tag{5}$$

with the help of which the above equations can be combined into the following ones:

$$\partial_1\Psi^1 + \partial_2\Psi^0 + \partial_3\Psi^3 = j^0/\varepsilon_0, \quad -i\partial_0\psi^1 + (\partial_2\psi^3 - \partial_3\psi^2) = i\, j^1/\varepsilon_0,$$

$$-i\partial_0\psi^2 + (\partial_3\psi^1 - \partial_1\psi^3) = i\,j^2 / \varepsilon_0, \quad -i\partial_0\psi^3 + (\partial_1\psi^2 - \partial_2\psi^1) = i\,j^3 / \varepsilon_0. \tag{6}$$

These four equations can be re-written in a matrix form; we use a 4-dimensional column ψ with one additional zero-element:

$$\left(-i\partial_0 \begin{vmatrix} a_0 & 0 & 0 & 0 \\ a_1 & 1 & 0 & 0 \\ a_2 & 0 & 1 & 0 \\ a_3 & 0 & 0 & 1 \end{vmatrix} + \partial_1 \begin{vmatrix} b_0 & 1 & 0 & 0 \\ b_1 & 0 & 0 & 0 \\ b_2 & 0 & 0 & -1 \\ b_3 & 0 & 1 & 0 \end{vmatrix} + \partial_2 \begin{vmatrix} c_0 & 0 & 1 & 0 \\ c_1 & 0 & 0 & 1 \\ c_2 & 0 & 0 & 0 \\ c_3 & -1 & 0 & 0 \end{vmatrix} \right.$$

$$\left. +\partial_3 \begin{vmatrix} d_0 & 0 & 0 & 1 \\ d_1 & 0 & -1 & 0 \\ d_2 & 1 & 0 & 0 \\ d_3 & 0 & 0 & 0 \end{vmatrix} \right) \begin{vmatrix} 0 \\ \psi^1 \\ \psi^2 \\ \psi^3 \end{vmatrix} = \frac{1}{\varepsilon_0} \begin{vmatrix} j^0 \\ i\,j^1 \\ i\,j^2 \\ i\,j^3 \end{vmatrix}.$$

Here, there arise four ambiguously determined matrices (parameters a_k, b_k, c_k, d_k are arbitrary):

$$(-i\alpha^0\partial_0 + \alpha^j\partial_j)\Psi = J, \quad \Psi = \begin{vmatrix} 0 \\ \psi^1 \\ \psi^2 \\ \psi^3 \end{vmatrix}, \quad \alpha^0 = \begin{vmatrix} a_0 & 0 & 0 & 0 \\ a_1 & 1 & 0 & 0 \\ a_2 & 0 & 1 & 0 \\ a_3 & 0 & 0 & 1 \end{vmatrix},$$

$$\alpha^1 = \begin{vmatrix} b_0 & 1 & 0 & 0 \\ b_1 & 0 & 0 & 0 \\ b_2 & 0 & 0 & -1 \\ b_3 & 0 & 1 & 0 \end{vmatrix}, \quad \alpha^2 = \begin{vmatrix} c_0 & 0 & 1 & 0 \\ c_1 & 0 & 0 & 1 \\ c_2 & 0 & 0 & 0 \\ c_3 & -1 & 0 & 0 \end{vmatrix}, \quad \alpha^3 = \begin{vmatrix} d_0 & 0 & 0 & 1 \\ d_1 & 0 & -1 & 0 \\ d_2 & 1 & 0 & 0 \\ d_3 & 0 & 0 & 0 \end{vmatrix}. \tag{7}$$

Consider the products of these matrices. Taking into account the identity

$$(\alpha^0)^2 = \begin{vmatrix} a_0 & 0 & 0 & 0 \\ a_1 & 1 & 0 & 0 \\ a_2 & 0 & 1 & 0 \\ a_3 & 0 & 0 & 1 \end{vmatrix} \begin{vmatrix} a_0 & 0 & 0 & 0 \\ a_1 & 1 & 0 & 0 \\ a_2 & 0 & 1 & 0 \\ a_3 & 0 & 0 & 1 \end{vmatrix} = \begin{vmatrix} a_0 a_0 & 0 & 0 & 0 \\ a_1 a_0 + a_1 & 1 & 0 & 0 \\ a_2 a_0 + a_2 & 0 & 1 & 0 \\ a_3 a_0 + a_3 & 0 & 0 & 1 \end{vmatrix},$$

and requiring that $(\alpha^0)^2 = +I$, we get equations

$$a_0 a_0 = 1, \quad a_1 a_0 + a_1 = 0, \quad a_2 a_0 + a_2 = 0, \quad a_3 a_0 + a_3 = 0;$$

their simple solution is

$$a_0 = \pm 1, \quad a_j = 0, \quad \alpha^0 = \begin{vmatrix} \pm 1 & 0 & 0 & 0 \\ 0 & 1 & 0 & 0 \\ 0 & 0 & 1 & 0 \\ 0 & 0 & 0 & 1 \end{vmatrix}, \quad (\alpha^0)^2 = I. \tag{8}$$

In the same manner, we obtain

$$\alpha^1 = \begin{vmatrix} 0 & 1 & 0 & 0 \\ -1 & 0 & 0 & 0 \\ 0 & 0 & 0 & -1 \\ 0 & 0 & 1 & 0 \end{vmatrix}, \quad (\alpha^1)^2 = -I; \tag{9}$$

$$\alpha^2 = \begin{vmatrix} 0 & 0 & 1 & 0 \\ 0 & 0 & 0 & 1 \\ -1 & 0 & 0 & 0 \\ 0 & -1 & 0 & 0 \end{vmatrix}, \quad (\alpha^2)^2 = -I; \tag{10}$$

$$\alpha^3 = \begin{vmatrix} 0 & 0 & 0 & 1 \\ 0 & 0 & -1 & 0 \\ 0 & 1 & 0 & 0 \\ -1 & 0 & 0 & 0 \end{vmatrix}, \quad (\alpha^3)^2 = -I. \tag{11}$$

For other products we have

$$\alpha^1\alpha^2 = -\alpha^2\alpha^1 = \alpha^3, \tag{12}$$

$$\alpha^2\alpha^3 = -\alpha^3\alpha^2 = \alpha^1, \tag{13}$$

$$\alpha^3\alpha^1 = -\alpha^1\alpha^3 = \alpha^2. \tag{14}$$

Let us turn to $\alpha^0\alpha^i$:

$$\delta = \pm 1, \quad \alpha^0\alpha^1 = \begin{vmatrix} 0 & \delta & 0 & 0 \\ -1 & 0 & 0 & 0 \\ 0 & 0 & 0 & -1 \\ 0 & 0 & 1 & 0 \end{vmatrix}, \quad \alpha^1\alpha^0 = \begin{vmatrix} 0 & 1 & 0 & 0 \\ -\delta & 0 & 0 & 0 \\ 0 & 0 & 0 & -1 \\ 0 & 0 & 1 & 0 \end{vmatrix}.$$

It should be noted that only at $\delta = +1$ we have a simple commutation rule:

$$\alpha^0 = I, \quad \alpha^i\alpha^0 = \alpha^0\alpha^i = \alpha^i. \tag{15}$$

Thus, the eight Maxwell equations are presented in the following matrix form:

$$(-i\partial_0 + \alpha^j\partial_j)\Psi = J, \quad \Psi = \begin{vmatrix} 0 \\ \psi^1 \\ \psi^2 \\ \psi^3 \end{vmatrix}, \quad J = \frac{1}{\varepsilon_0}\begin{vmatrix} j^0 \\ i\,j^1 \\ i\,j^2 \\ i\,j^3 \end{vmatrix},$$

$$\alpha^1 = \begin{vmatrix} 0 & 1 & 0 & 0 \\ -1 & 0 & 0 & 0 \\ 0 & 0 & 0 & -1 \\ 0 & 0 & 1 & 0 \end{vmatrix}, \quad \alpha^2 = \begin{vmatrix} 0 & 0 & 1 & 0 \\ 0 & 0 & 0 & 1 \\ -1 & 0 & 0 & 0 \\ 0 & -1 & 0 & 0 \end{vmatrix}, \quad \alpha^3 = \begin{vmatrix} 0 & 0 & 0 & 1 \\ 0 & 0 & -1 & 0 \\ 0 & 1 & 0 & 0 \\ -1 & 0 & 0 & 0 \end{vmatrix},$$

$$(\alpha^1)^2 = -I, \quad (\alpha^2)^2 = -I, \quad (\alpha^2)^2 = -I,$$

$$\alpha^1\alpha^2 = -\alpha^2\alpha^1 = \alpha^3, \quad \alpha^2\alpha^3 = -\alpha^3\alpha^2 = \alpha^1, \quad \alpha^3\alpha^1 = -\alpha^1\alpha^3 = \alpha^2. \tag{16}$$

Such a complex matrix form can be transformed to a real 8-dimensional presentation (see in [93]). Indeed, we have two conjugated equations:

$$(-i\partial_0 + \alpha^j \partial_j)\Psi = J, \quad (+i\partial_0 + \alpha^j \partial_j)\Psi^* = J^*, \tag{17}$$

$$E = (\psi + \psi^*)/2, \quad B = (\psi - \psi^*)/2i. \tag{18}$$

Summing and subtracting them we get

$$\partial_0 \frac{\Psi - \Psi^*}{2i} + \alpha^j \partial_j \frac{\Psi + \Psi^*}{2} = \frac{J + J^*}{2}, \quad -\partial_0 \frac{\Psi + \Psi^*}{2} + \alpha^j \partial_j \frac{\Psi - \Psi^*}{2i} = \frac{J - J^*}{2i};$$

that is

$$\partial_0 B + \alpha^j \partial_j E = Re(J), \quad -\partial_0 E + \alpha^j \partial_j B = Im(J).$$

These equations can be presented in a matrix 8-dimensional form

$$\begin{vmatrix} \alpha^j \partial_j & \partial_0 \\ -\partial_0 & \alpha^j \partial_j \end{vmatrix} \begin{vmatrix} E \\ B \end{vmatrix} = \begin{vmatrix} Re(J) \\ Im(J) \end{vmatrix}, \quad (\Gamma^0 \partial_0 + \Gamma^i \partial_i)\Psi = J, \tag{19}$$

where

$$\Gamma^0 = \begin{vmatrix} 0 & I \\ -I & 0 \end{vmatrix}, \quad \Gamma^i = \begin{vmatrix} \alpha^i & 0 \\ 0 & \alpha^i \end{vmatrix}, \tag{20}$$

with the properties

$$(\Gamma^0)^2 = -I, \quad (\Gamma^1)^2 = -I, \quad (\Gamma^1)^2 = -I, \quad (\Gamma^1)^2 = -I,$$

$$\Gamma^1\Gamma^2 = -\Gamma^2\Gamma^1 = \Gamma^3, \quad \Gamma^2\Gamma^3 = -\Gamma^3\Gamma^2 = \Gamma^1, \quad \Gamma^3\Gamma^1 = -\Gamma^1\Gamma^3 = \Gamma^2,$$

$$\Gamma^0\Gamma^i = \Gamma^i\Gamma^0 = \begin{vmatrix} 0 & \alpha^i \\ -\alpha^i & 0 \end{vmatrix} \neq \Gamma^i. \tag{21}$$

Now let us turn again to the 4-dimensional complex form as a more compact one and consider the problem of relativistic invariance of this equation. The lack of explicit invariance of 3-vector complex form of Maxwell theory has been intensively discussed in various aspects by Ivezic [114-118]. Let us start with the relations

$$(-i\partial_0 + \alpha^j \partial_j)\Psi = J, \quad \Psi = \begin{vmatrix} 0 \\ \psi^1 \\ \psi^2 \\ \psi^3 \end{vmatrix}, \quad J = \frac{1}{\varepsilon_0} \begin{vmatrix} j^0 \\ i\,j^1 \\ i\,j^2 \\ i\,j^3 \end{vmatrix}.$$

Arbitrary Lorentz transformation over the function Ψ is given by (take notice that one may introduce four undefined parameters $s_0, ..., s_3$, but we will take $s_0 = 1, s_j = 0$)

$$S = \begin{vmatrix} s_0 & 0 & 0 & 0 \\ s_1 & . & . & . \\ s_2 & . & O(k) & . \\ s_3 & . & . & . \end{vmatrix}, \quad \Psi' = S\Psi, \quad \Psi = S^{-1}\Psi', \tag{22}$$

where $O(k)$ stands for a (3×3)-rotation complex matrix from the group $SO(3,C)$, isomorphic to the Lorentz one, more detail see in the book by Fedorov [130]. Equation for a primed function Ψ' reads

$$(-i\partial_0 + S\alpha^j S^{-1}\partial_j)\Psi' = SJ. \tag{23}$$

When working with matrices α^j we will use vectors e_i and (3×3)-matrices τ_i; then the structure $S\alpha^j S^{-1}$ is presented as follows

$$S\alpha^j S^{-1} = \begin{vmatrix} 1 & 0 \\ 0 & O(k) \end{vmatrix} \begin{vmatrix} 0 & e_j \\ -e_j^t & \tau_j \end{vmatrix} \begin{vmatrix} 1 & 0 \\ 0 & O^{-1}(k) \end{vmatrix} = \begin{vmatrix} 0 & e_j O^{-1}(k) \\ -O(k)e_j^t & O(k)\tau_j O^{-1}(k) \end{vmatrix}.$$

This relationship can be rewritten with the help of indices

$$S\alpha^j S^{-1} = \begin{vmatrix} 0 & \delta_{ji} O^{-1}(k)_{in} \\ -O(k)_{ni}\delta_{ij} & \tau_n O(k)_{nj} \end{vmatrix} = \begin{vmatrix} 0 & O(k)_{nj} \\ -O(k)_{nj} & \tau_n O(k)_{nj} \end{vmatrix}$$

$$= \begin{vmatrix} 0 & (e_m)_n O(k)_{mj} \\ -(e_m)_n O(k)_{mj} & \tau_m O(k)_{mj} \end{vmatrix} = \alpha^m O_{mj}(k). \qquad (24)$$

Therefore, after the above transformation, the matrix equation is brought to

$$(-i\partial_0 + S\alpha^j S^{-1}\partial_j)\Psi' = SJ, \quad (-i\partial_0 + \alpha^m O_{mj}\partial_j)\Psi' = SJ, \quad O_{mj}\partial_j = \partial_m',$$

that is

$$(-i\partial_0 + \alpha^m \partial_m')\Psi' = SJ. \qquad (25)$$

Let us specify this result for simple cases when S looks as follows (to a real value a corresponds Euclidean rotation, to an imaginary value a corresponds a Lorentzian rotation):

Euclidean rotation $(1-2)$,

$$S\alpha^1 S^{-1} = \begin{vmatrix} 1 & 0 & 0 & 0 \\ 0 & \cos a & -\sin a & 0 \\ 0 & \sin a & \cos a & 0 \\ 0 & 0 & 0 & 1 \end{vmatrix} \begin{vmatrix} 0 & 1 & 0 & 0 \\ -1 & 0 & 0 & 0 \\ 0 & 0 & 0 & -1 \\ 0 & 0 & 1 & 0 \end{vmatrix} \begin{vmatrix} 1 & 0 & 0 & 0 \\ 0 & \cos a & +\sin a & 0 \\ 0 & -\sin a & \cos a & 0 \\ 0 & 0 & 0 & 1 \end{vmatrix}$$

$$= \cos a\alpha^1 + \sin a\alpha^2 = \alpha^j O_{j1}. \qquad (26)$$

$$S\alpha^2 S^{-1} = \begin{vmatrix} 1 & 0 & 0 & 0 \\ 0 & \cos a & -\sin a & 0 \\ 0 & \sin a & \cos a & 0 \\ 0 & 0 & 0 & 1 \end{vmatrix} \begin{vmatrix} 0 & 0 & 1 & 0 \\ 0 & 0 & 0 & 1 \\ -1 & 0 & 0 & 0 \\ 0 & -1 & 0 & 0 \end{vmatrix} \begin{vmatrix} 1 & 0 & 0 & 0 \\ 0 & \cos a & \sin a & 0 \\ 0 & -\sin a & \cos a & 0 \\ 0 & 0 & 0 & 1 \end{vmatrix}$$

$$= -\sin a\alpha^1 + \cos a\alpha^2 = \alpha^j O_{j2}. \qquad (27)$$

$$S\alpha^3 S^{-1} = \begin{vmatrix} 1 & 0 & 0 & 0 \\ 0 & \cos a & -\sin a & 0 \\ 0 & \sin a & \cos a & 0 \\ 0 & 0 & 0 & 1 \end{vmatrix} \begin{vmatrix} 0 & 0 & 0 & 1 \\ 0 & 0 & -1 & 0 \\ 0 & 1 & 0 & 0 \\ -1 & 0 & 0 & 0 \end{vmatrix} \begin{vmatrix} 1 & 0 & 0 & 0 \\ 0 & \cos a & \sin a & 0 \\ 0 & -\sin a & \cos a & 0 \\ 0 & 0 & 0 & 1 \end{vmatrix}$$

$$= \alpha^3 = \alpha^j O_{j3}. \qquad (28)$$

Now, one should give special attention to the fact that the symmetry properties given by (25) look satisfactory only at real values of parameter a; in this case, it describes the symmetry of the Maxwell equations under Euclidean rotations. However, if the values of a are imaginary, the above transformation S gives a Lorentzian boost:

$$a = ib,\, b^* = b,\, \sin a = i\, sinh b,\, \cos a = cosh b,\, S(a = ib) = \begin{vmatrix} 1 & 0 & 0 & 0 \\ 0 & cosh b & -i\, sinh b & 0 \\ 0 & i\, sinh b & cosh b & 0 \\ 0 & 0 & 0 & 1 \end{vmatrix}, \qquad (29)$$

and formulas (26) will take the form

$$S\alpha^1 S^{-1} = cosh b\alpha^1 + i\, sinh b\alpha^2, \quad S\alpha^2 S^{-1} = -i\, sinh b\alpha^1 + cosh b\alpha^2, \quad S\alpha^3 S^{-1} = \alpha^3. \qquad (30)$$

So the Maxwell matrix equation after transformations (29), (30) will look asymmetric

$$\left[(-i\partial_0 + \alpha^3\partial_3) + (cosh b\alpha^1 + i\, sinh b\alpha^2)\partial_2 + (-i\, sinh b\alpha^1 + cosh b\alpha^2)\partial_3\right]\Psi' = SJ. \qquad (31)$$

One can note the identity

$$(cosh b - i\, sinh b\alpha^3)(-i\partial_0 + \alpha^3\partial_3)$$

$$= -i(cosh b\partial_0 - sinh b\partial_3) + \alpha^3(-sinh b\partial_0 + cosh b\partial_3) = -i\partial_0' + \alpha^3\partial_3', \qquad (32)$$

where derivatives are changed in accordance with the Lorentzian symmetry. It remains to determine the action of the operator

$$\Delta = cosh b - i\, insh b\alpha^3 \qquad (33)$$

on two other terms in eq. (31); one might expect two relations:

$$(cosh b - i\, sinh b\alpha^3)(cosh b\alpha^1 + i\, sinh b\alpha^2) = \alpha^2,$$

$$(cosh b - i\, sinh b\alpha^3)(-i\, sinh b\alpha^1 + cosh b\alpha^2) = \alpha^3. \qquad (34)$$

As easily verified they hold indeed. We should determine the term $\Delta S\, J$. First, we have

$$S\, J = \varepsilon_0^{-1} \begin{vmatrix} 1 & 0 & 0 & 0 \\ 0 & cosh b & -i\, sinh b & 0 \\ 0 & i\, sinh b & cosh b & 0 \\ 0 & 0 & 0 & 1 \end{vmatrix} \begin{vmatrix} j^0 \\ ij^1 \\ ij^2 \\ ij^3 \end{vmatrix} = \begin{vmatrix} j^0 \\ i\, cosh b\, j^1 + sinh b\, j^2 \\ -sinh b\, j^1 + i\, cosh b\, j^2 \\ ij^3 \end{vmatrix},$$

and then

$$\Delta S\, J = \begin{vmatrix} cosh b\, j^0 + sinh b\, j^3 \\ i\, j^1 \\ i\, j^2 \\ i(sinh b\, j^0 + cosh b\, j^3) \end{vmatrix}; \qquad (35)$$

the right-hand side of (35) is what we need. Thus, the symmetry of the matrix Maxwell equation under the Lorentzian boost in the plane $(0-3)$ is described by the relations.

Pseudo-Euclidean rotation $(0-3)$

$$S(b) = \begin{vmatrix} 1 & 0 & 0 & 0 \\ 0 & cosh b & -i\, sinh b & 0 \\ 0 & i\, sinh b & cosh b & 0 \\ 0 & 0 & 0 & 1 \end{vmatrix}, \quad \Delta(b) = cosh b - i\, sinh b\alpha^3,$$

$$\Delta(b)(-i\partial_0 + S\alpha^j S^{-1}\partial_j)\Psi' = \Delta S\, J \equiv J' \quad \Rightarrow \quad (-i\partial_0' + \alpha^j\partial_j')\Psi' = J',$$

$$cosh b\partial_0 - sinh b\partial_3 = \partial_0', \quad -sinh b\partial_0 + cosh b\partial_3 = \partial_3'. \qquad (36)$$

The symmetry properties of this equation under two other boosts are similar.

Pseudo-Euclidean rotation $(0-1)$

$$S(a=b)=\begin{vmatrix} 1 & 0 & 0 & 0 \\ 0 & 0 & 0 & 0 \\ 0 & 0 & \cosh b & i\sinh b \\ 0 & 0 & -i\sinh b & \cosh b \end{vmatrix}, \quad \Delta(b) = \cosh b + i\sinh b\,\alpha^1,$$

$$\Delta(b)(-i\partial_0 + S\alpha^j S^{-1}\partial_j)\Psi' = \Delta S\,J \equiv J' \quad \Rightarrow \quad (-i\partial_0' + \alpha^j\partial_j')\Psi' = J',$$

$$\cosh b\,\partial_0 + \sinh b\,\partial_1 = \partial_0', \quad \sinh b\,\partial_0 + \cosh b\,\partial_1 = \partial_3'. \tag{38a}$$

Pseudo-Euclidean rotation $(0-2)$

$$S(ib)=\begin{vmatrix} 1 & 0 & 0 & 0 \\ 0 & \cosh b & 0 & i\sinh b \\ 0 & 0 & 1 & 0 \\ 0 & -i\sinh b & 0 & \cosh b \end{vmatrix}, \quad \Delta(b) = \cosh b - i\sinh b\,\alpha^2,$$

$$\Delta(b)(-i\partial_0 + S\alpha^j S^{-1}\partial_j)\Psi' = \Delta S\,J \equiv J' \quad \Rightarrow \quad (-i\partial_0' + \alpha^j\partial_j')\Psi' = J',$$

$$\cosh b\,\partial_0 - \sinh b\,\partial_2 = \partial_0', \quad -\sinh b\,\partial_0 + \cosh b\,\partial_2 = \partial_3'. \tag{38b}$$

For the general case, one can think that for an arbitrarily oriented boost the operator Δ should be of the form:

$$\Delta = \Delta_\alpha = \cosh b - i\sinh b\,n_j\alpha^j.$$

This can be verified by direct calculation, all details are omitted. Therefore, under general Lorentzian boost (take note that $x^a = (x^0, x)$ is a contra-variant 4-vector, whereas ∂_a is a covariant one)

$$t' = \cosh\beta\,t + \sinh\beta\,nx, \quad x' = +n\sinh\beta\,t + x + (\cosh\beta - 1)n(nx); \tag{39}$$

the matrix Maxwell equation transforms according to

$$(A_0 + \alpha^1 A_1 + \alpha^2 A_2 + \alpha^3 A_3)\Psi' = \Delta SJ, \tag{40}$$

where

$$\partial_0' \equiv A_0 = \cosh b\,\partial_0 - \sinh b(n_1\partial_1 + n_2\partial_2 + n_3\partial_3),$$

$$\partial_1' \equiv A_1 = -\sinh b\,n_1\partial_0 + [\partial_1 + (\cosh b - 1)n_1(n_1\partial_1 + n_2\partial_2 + n_3\partial_3)],$$

$$\partial_2' \equiv A_2 = -\sinh b\,n_2\partial_0 + [\partial_2 + (\cosh b - 1)n_2(n_1\partial_1 + n_2\partial_2 + n_3\partial_3)],$$

$$\partial_3' \equiv A_3 = -\sinh b\,n_3\partial_0 + [\partial_3 + (\cosh b - 1)n_2(n_1\partial_1 + n_2\partial_2 + n_3\partial_3)];$$

so that the transformed equation reads

$$(\partial_0' + \alpha^1\partial_1' + \alpha^2\partial_2' + \alpha^3\partial_3')\Psi' = \Delta SJ. \tag{41}$$

It remains to examine the term ΔSJ in the right-hand side. Using

$$\Delta = \cosh b - i\sinh b\,n_1\alpha^1 - i\sinh b\,n_2\alpha^2 - i\sinh b\,n_3\alpha^3$$

$$= \begin{vmatrix} \cosh b & -i\sinh b\,n_1 & -i\sinh b\,n_2 & -i\sinh b\,n_3 \\ i\sinh b\,n_1 & \cosh b & i\sinh b\,n_3 & -i\sinh b\,n_2 \\ i\sinh b\,n_2 & -i\sinh b\,n_3 & \cosh b & i\sinh b\,n_1 \\ i\sinh b\,n_3 & i\sinh b\,n_2 & -i\sinh b\,n_1 & \cosh b \end{vmatrix}, \tag{42}$$

and (for a time, the factor ε_0^{-1} is omitted; remember notation $f \equiv 1 - cosh b$):

$$SJ = \begin{vmatrix} 1 & 0 & 0 & 0 \\ 0 & 1 - f(n_2^2 + n_3^2) & -i sinh b n_3 + f n_1 n_2 & i sinh b n_2 + f n_1 n_3 \\ 0 & i sinh b n_3 + f n_1 n_2 & 1 - f(n_3^2 + n_1^2) & -i sinh b n_1 + f n_2 n_3 \\ 0 & -i sinh b n_2 + f n_1 n_3 & i sinh b n_1 + f n_2 n_3 & 1 - f(n_1^2 + n_2^2) \end{vmatrix} \begin{vmatrix} j^0 \\ ij^1 \\ ij^2 \\ ij^2 \end{vmatrix}$$

$$= \begin{vmatrix} j^0 \\ ij^1[1 - f(n_2^2 + n_3^2)] + ij^2[-i sinh b n_3 + f n_1 n_2] + ij^3[i sinh b n_2 + f n_1 n_3] \\ ij^1[i sinh b n_3 + f n_1 n_2] + ij^2[1 - f(n_3^2 + n_1^2)] + ij^3[-i sinh b n_1 + f n_2 n_3] \\ ij^1[-i sinh b n_2 + f n_1 n_3] + ij^2[i sinh b n_1 + f n_2 n_3] + ij^3[1 - f(n_1^2 + n_2^2)] \end{vmatrix} \qquad (43)$$

for ΔSJ, one should produce

$$\Delta SJ = \begin{vmatrix} j^{'0} \\ ij^{'1} \\ ij^{'2} \\ ij^{'3} \end{vmatrix}. \qquad (44)$$

First, we prove

$$j^{'0} = cosh b\, j^0 + sinh b (n_1 j^1 + n_2 j^2 + n_3 j^3) = cosh b\, j^0 + sinh b (nj). \qquad (45)$$

Now let us calculate the term

$$j^{'1} = + sinh b n_1 j^0 + j^1 + (cosh b - 1) n_1 (n_1 j^1 + n_2 j^2 + n_3 j^3). \qquad (46)$$

It is evidently the first component of the vector formula is (see (2.56))

$$j' = + sinh b n\, j^0 + j + (cosh b - 1) n (nj). \qquad (47)$$

Let us calculate the term $j^{'2}$:

$$j^{'2} = + sinh b n_2 j^0 + j^2 + (cosh b - 1) n_2 (n_1 j^1 + n_2 j^2 + n_3 j^3). \qquad (48)$$

In the same way, we prove the formula

$$j^{'3} = + sinh b n_3 j^0 + j^3 + (cosh b - 1) n_3 (n_1 j^1 + n_2 j^2 + n_3 j^3). \qquad (49)$$

Thus, the matrix Maxwell equation $(-i\partial_0 + \alpha^i \partial_i)\Psi = J$ is invariant under an arbitrary Lorentzian boost:

$$S(ib, n) = \begin{vmatrix} 1 & 0 \\ 0 & O(ib, n) \end{vmatrix},$$

$$t' = cosh \beta t + sinh \beta n x, \quad x' = + n\, sinh \beta t + x + (cosh \beta - 1) n (nx),$$

$$\Delta(-i\partial_0 + S\alpha^i S^{-1} \partial_i) S\Psi = \Delta SJ \quad \Rightarrow \quad (\partial_0' + \alpha^i \partial_i')\Psi' = J'; \qquad (50)$$

the derivatives and current transform by the rules:

$$\partial_0' = cosh b \partial_0 - sinh b (n\nabla), \quad \nabla' = - sinh b n \partial_0 + [\nabla + (cosh b - 1) n (n\nabla),$$

$$j^{'0} = cosh b\, j^0 + sinh b (nj), \quad j' = + sinh b n\, j^0 + j + (cosh b - 1) n (nj). \qquad (51)$$

Invariance of the matrix equation under Euclidean rotations is achieved in a simpler way:

$$(-i\partial_0 + \alpha^i \partial_i)\Psi = J,$$

$$S(a,n) = \begin{vmatrix} 1 & 0 \\ 0 & O(a,n) \end{vmatrix}, \quad t' = t, \quad x' = R(a,n)x,$$

$$(-i\partial_0 + S\alpha^i S^{-1}\partial_i)S\Psi = SJ \quad \Rightarrow \quad (-i\partial_0' + \alpha^i \partial_i')\Psi' = J', \tag{52}$$

$$\partial_0' = \partial_0, \quad \nabla' = R(a,-n)\nabla, \quad j'^0 = j^0, \quad j' = R(a,n)j. \tag{53}$$

3. Modified Lorentz symmetry

Let us start with Maxwell equations in the uniform medium:

$$div\, cB = 0, \quad rot\, E = -\frac{\partial cB}{\partial ct}, \quad div\, E = \frac{\rho}{\varepsilon\varepsilon_0}, \quad rot\, cB = \mu\mu_0 cJ + \varepsilon\mu \frac{\partial E}{\partial ct}. \tag{54}$$

The coefficient $\varepsilon\mu$ can be factorized as follows

$$\varepsilon\mu = \sqrt{\varepsilon\mu}\sqrt{\varepsilon\mu} = \frac{1}{k^2}, \quad c' = \frac{1}{\sqrt{\varepsilon_0 \varepsilon \mu_0 \mu}} = kc; \tag{55}$$

then the above system can be presented differently

$$div\, kcB = 0, \quad rot\, E = -\frac{\partial kcB}{\partial kct}, \quad div\, E = \frac{\rho}{\varepsilon\varepsilon_0}, \quad rot\, kcB = \frac{1}{\varepsilon\varepsilon_0}\frac{J}{kc} + \frac{\partial E}{\partial kct}. \tag{56}$$

Introducing new variables

$$x^a = (x^0 = kct, x^i), \quad j^a = (j^0 = \rho, j = \frac{J}{kc}), \tag{57}$$

previous equations can be rewritten as

$$div\, kcB = 0, \quad rot\, E = -\frac{\partial kcB}{\partial x^0}, \quad div\, E = \frac{1}{\varepsilon\varepsilon_0} j^0, \quad rot\, kcB = \frac{1}{\varepsilon\varepsilon_0} j + \frac{\partial E}{\partial x^0}, \tag{58}$$

or in explicit component form

$$\partial_1 c'B^1 + \partial_2 c'B^2 + \partial_3 c'B^3 = 0, \quad \partial_2 E^3 - \partial_3 E^2 + \partial_0 c'B^1 = 0,$$

$$\partial_3 E^1 - \partial_1 E^3 + \partial_0 c'B^2 = 0, \quad \partial_1 E^2 - \partial_2 E^1 + \partial_0 c'B^3 = 0,$$

$$\partial_1 E^1 + \partial_2 E^2 + \partial_3 E^3 = j^0 / \varepsilon\varepsilon_0, \quad \partial_2 cB^3 - \partial_3 cB^2 - \partial_0 E^1 = j^1 / \varepsilon\varepsilon_0,$$

$$\partial_3 cB^1 - \partial_1 cB^3 - \partial_0 E^2 = j^2 / \varepsilon\varepsilon_0, \quad \partial_1 cB^2 - \partial_2 cB^1 - \partial_0 E^3 = j^3 / \varepsilon\varepsilon_0. \tag{59}$$

Eqs. (58), (59) formally differ from eqs. (4) only in one change $c \Rightarrow c' = kc$ (and also $\varepsilon_0 \Rightarrow \varepsilon_0 \varepsilon$); therefore, all analysis performed in Section 2 is applicable here as well:

$$\psi^k = E^k + ic'B^k; \tag{60}$$

eqs. (59) are combined into

$$\partial_1 \Psi^1 + \partial_2 \Psi^0 + \partial_3 \Psi^3 = j^0 / \varepsilon\varepsilon_0, \quad -i\partial_0 \psi^1 + (\partial_2 \psi^3 - \partial_3 \psi^2) = i\, j^1 / \varepsilon\varepsilon_0,$$

$$-i\partial_0 \psi^2 + (\partial_3 \psi^1 - \partial_1 \psi^3) = i\, j^2 / \varepsilon\varepsilon_0, \quad -i\partial_0 \psi^3 + (\partial_1 \psi^2 - \partial_2 \psi^1) = i\, j^3 / \varepsilon\varepsilon_0. \tag{61}$$

These ones are rewritten in the matrix form

$$(-i\partial_0 + \alpha^i \partial_i)\Psi = J; \tag{62}$$

where the same matrices are used. The given matrix form of the Maxwell theory in the uniform media proves the existence of the theory symmetry under a modified Lorentz group (see Rosen [71]) in which instead of the vacuum speed of light we are to use the modified speed of light:

$$c' = kc, \quad c = \frac{1}{\sqrt{\varepsilon_0 \mu_0}}, \quad k = \frac{1}{\sqrt{\varepsilon \mu}}. \tag{63}$$

4. On Minkowski electrodynamics in moving bodies

In agreement with Minkowski approach [14-17], in the presence of the uniform media, we should introduce two electromagnetic tensors F^{ab} and H^{ab} that transform independently under the Lorentz group. At that, the known constitutive (or material) relations change their form in the moving reference frame.

In the rest reference frame the Maxwell equations are

$$F^{ab} = (E, cB), \quad div\, B = 0, \quad rot\, E = -\frac{\partial cB}{\partial ct}, \tag{64}$$

$$H^{ab} = (D, H/c), \quad div\, D = \rho, \quad rot \frac{H}{c} = \frac{J}{c} + \frac{\partial D}{\partial ct}, \tag{65}$$

with the constitutive relations

$$D = \varepsilon_0 \varepsilon E, \quad H = \frac{1}{\mu \mu_0} B. \tag{66}$$

The quantities with simple transformation properties under the Lorentz group are

$$f = E + icB, \quad h = \frac{1}{\varepsilon_0}(D + iH/c), \quad j^a = (j^0 = \rho, j = J/c); \tag{67}$$

where f, h are the complex 3-vector under complex orthogonal group $SO(3.C)$, the latter is isomorphic to the Lorentz group. One can combine eqs. (64), (65) into the following ones

$$div(\frac{D}{\varepsilon_0} + icB) = \frac{1}{\varepsilon_0}\rho, \quad -i\partial_0(\frac{D}{\varepsilon_0} + icB) + rot(E + i\frac{H/c}{\varepsilon_0}) = \frac{i}{\varepsilon_0} j. \tag{68}$$

Taking into account relationships

$$E = \frac{f + f^*}{2}, \quad i\frac{H/c}{\varepsilon_0} = \frac{h - h^*}{2}, \quad \frac{D}{\varepsilon_0} = \frac{h + h^*}{2}, \quad icB = \frac{f - f^*}{2}, \tag{69}$$

eqs. (68) can be rewritten in the form

$$div(\frac{h+h^*}{2} + \frac{f - f^*}{2}) = \frac{1}{\varepsilon_0}\rho, \quad -i\partial_0(\frac{h+h^*}{2} + \frac{f - f^*}{2}) + rot(\frac{f + f^*}{2} + \frac{h - h^*}{2}) = \frac{i}{\varepsilon_0} j. \tag{70}$$

Let us introduce two quantities

$$M = \frac{h + f}{2}, \quad N = \frac{h^* - f^*}{2}, \tag{71}$$

which are different 3-vectors under the group $SO(3.C)$:

$$M' = OM, \quad N' = O^* N; \tag{72}$$

with respect to Euclidean rotations, the identity $O^{*} = O$ holds; instead for Lorentzian boosts we have $O^{*} = O^{-1}$.

In terms of M and N eqs. (70) look as

$$div M + div N = \frac{1}{\varepsilon_0}\rho, \quad -i\partial_0 M + rot M - i\partial_0 N - rot N = \frac{i}{\varepsilon_0} j, \tag{73}$$

or in a matrix form

$$(-i\partial_0 + \alpha^i \partial_i) M + (-i\partial_0 + \beta^i \partial_i) N = J, \tag{74}$$

where

$$M = \begin{vmatrix} 0 \\ M \end{vmatrix}, \quad N = \begin{vmatrix} 0 \\ N \end{vmatrix}, \quad J = \frac{1}{\varepsilon_0} \begin{vmatrix} \rho \\ i\, j \end{vmatrix}.$$

The matrices α^i and β^i are taken in the form

$$\alpha^1 = \begin{vmatrix} 0 & 1 & 0 & 0 \\ -1 & 0 & 0 & 0 \\ 0 & 0 & 0 & -1 \\ 0 & 0 & 1 & 0 \end{vmatrix}, \quad \alpha^2 = \begin{vmatrix} 0 & 0 & 1 & 0 \\ 0 & 0 & 0 & 1 \\ -1 & 0 & 0 & 0 \\ 0 & -1 & 0 & 0 \end{vmatrix}, \quad \alpha^3 = \begin{vmatrix} 0 & 0 & 0 & 1 \\ 0 & 0 & -1 & 0 \\ 0 & 1 & 0 & 0 \\ -1 & 0 & 0 & 0 \end{vmatrix},$$

$$\beta^1 = \begin{vmatrix} 0 & 1 & 0 & 0 \\ -1 & 0 & 0 & 0 \\ 0 & 0 & 0 & 1 \\ 0 & 0 & -1 & 0 \end{vmatrix}, \quad \beta^2 = \begin{vmatrix} 0 & 0 & 1 & 0 \\ 0 & 0 & 0 & -1 \\ -1 & 0 & 0 & 0 \\ 0 & 1 & 0 & 0 \end{vmatrix}, \quad \beta^3 = \begin{vmatrix} 0 & 0 & 0 & 1 \\ 0 & 0 & 1 & 0 \\ 0 & -1 & 0 & 0 \\ -1 & 0 & 0 & 0 \end{vmatrix}. \tag{75}$$

It should be noted that the main idea of Minkowski – to divide the Maxwell equations into equations for tensors F^{ab} and H^{ab} transforming independently under the Lorentz group – should correspond to immiscible equations for f, f^{*} and h, h^{*} respectively. Such a form can be readily found. Indeed, let us start with eqs. (70) and their conjugated:

$$div(\frac{h+h^{*}}{2} + \frac{f-f^{*}}{2}) = \frac{1}{\varepsilon_0}\rho, \quad div(\frac{h+h^{*}}{2} - \frac{f-f^{*}}{2}) = \frac{1}{\varepsilon_0}\rho;$$

$$-i\partial_0(\frac{h+h^{*}}{2} + \frac{f-f^{*}}{2}) + rot(\frac{f+f^{*}}{2} + \frac{h-h^{*}}{2}) = \frac{i}{\varepsilon_0} j,$$

$$+i\partial_0(\frac{h+h^{*}}{2} - \frac{f-f^{*}}{2}) + rot(\frac{f+f^{*}}{2} - \frac{h-h^{*}}{2}) = -\frac{i}{\varepsilon_0} j.$$

From these, it follows

$$div\frac{h+h^{*}}{2} = \frac{1}{\varepsilon_0}\rho, \quad div\frac{f-f^{*}}{2} = 0;$$

$$-i\partial_0 \frac{f-f^{*}}{2} + rot\frac{f+f^{*}}{2} = 0, \quad -i\partial_0 \frac{h+h^{*}}{2} + rot\frac{h-h^{*}}{2} = \frac{i}{\varepsilon_0} j.$$

Thus the needed form is

$$div\frac{f-f^{*}}{2} = 0, \quad -i\partial_0 \frac{f-f^{*}}{2} + rot\frac{f+f^{*}}{2} = 0, \tag{76}$$

$$div \frac{h+h^*}{2} = \rho, \quad -i\partial_0 \frac{h+h^*}{2} + rot \frac{h-h^*}{2} = \frac{i}{\varepsilon_0} j. \qquad (77)$$

The quantities entering these equations behave under the Lorentz group in accordance with the rules:

$$f' = O f, \quad f^{*'} = O^* f^*, \quad h' = Oh, \quad h^{*'} = O^* h^*.$$

Comparing eqs. (76), (77) with eqs. (73), (74):

$$div M + div N = \frac{1}{\varepsilon_0}\rho, \quad -i\partial_0 M + rot M - i\partial_0 N - rot N = \frac{i}{\varepsilon_0} j,$$

$$(-i\partial_0 + \alpha^i \partial_i) M + (-i\partial_0 + \beta^i \partial_i) N = J,$$

and taking into account

$$div h + div h^* = \frac{1}{\varepsilon_0}\rho, \quad -i\partial_0 h + rot h - i\partial_0 h^* - rot h^* = \frac{i}{\varepsilon_0} j, \qquad (78)$$

$$div f - div f^* = 0, \quad -i\partial_0 f + rot f + i\partial_0 f^* + rot f^* = 0 \qquad (79)$$

we conclude that the matrix equations we need are

$$(-i\partial_0 + \alpha^i \partial_i) h + (-i\partial_0 + \beta^i \partial_i) h^* = J, \qquad (80)$$

$$(-i\partial_0 + \alpha^i \partial_i) f - (-i\partial_0 + \beta^i \partial_i) f^* = 0. \qquad (81)$$

In the following, we will work with the more simple matrix equation (74).

5. Minkowski relations in the complex 3-vector form

The symmetry of the matrix equation under the Lorentz transformations must exist because the symmetry exists for these equations written in the ordinary tensor form. Now, let us examine how the above constitutive relations behave under the Lorentz transformations.

Let us start with these relations in the rest reference frame

$$D = \varepsilon_0 \varepsilon E, \quad \frac{H}{c} = \frac{1}{\mu_0 \mu} \frac{1}{c^2} cB = \frac{\varepsilon_0}{\mu} cB. \qquad (82)$$

Allowing for (87), eqs. (82) can be rewritten as

$$\frac{h+h^*}{2} = \varepsilon \frac{f+f^*}{2}, \quad \frac{h-h^*}{2} = \frac{1}{\mu} \frac{f-f^*}{2}; \qquad (83)$$

whence it follows

$$2h = (\varepsilon + \frac{1}{\mu}) f + (\varepsilon - \frac{1}{\mu}) f^*, \quad 2h^* = (\varepsilon + \frac{1}{\mu}) f^* + (\varepsilon - \frac{1}{\mu}) f. \qquad (84)$$

This is a complex form of constitutive relations (82). It should be noted that eqs. (83) can be resolved under the variables f, f^* as well:

$$2f = (\frac{1}{\varepsilon} + \mu) h + (\frac{1}{\varepsilon} - \mu) h^*, \quad 2f^* = (\frac{1}{\varepsilon} + \mu) h^* + (\frac{1}{\varepsilon} - \mu) h; \qquad (85)$$

these are the same constitutive equations (84) but in other forms.

Now let us allow for the Lorentz transformations:

$$f' = O f, \quad f'^* = O^* f^*, \quad h' = Oh, \quad h'^* = O^* h^*,$$

then eqs. (83) become

$$\frac{O^{-1}h' + (O^{-1})^* h^{*\prime}}{2} = \varepsilon \frac{O^{-1} f' + (O^{-1})^* f^{*\prime}}{2}, \quad \frac{O^{-1}h' - (O^{-1})^* h^{*\prime}}{2} = \frac{1}{\mu} \frac{O^{-1} f' - (O^{-1})^* f^{*\prime}}{2}.$$

Multiplying both equations by O and summing (or subtracting) the results we get

$$h' = \varepsilon \frac{f' + O(O^{-1})^* f^{*\prime}}{2} + \frac{1}{\mu} \frac{f' - O(O^{-1})^* f^{*\prime}}{2}, \tag{86}$$

$$h^{*\prime} = \varepsilon \frac{O^* O^{-1} f' + f^{*\prime}}{2} - \frac{1}{\mu} \frac{O^* O^{-1} f' - f^{*\prime}}{2}. \tag{87}$$

Eqs. (86), (87) can be presented as

$$2h' = (\varepsilon + \frac{1}{\mu}) f' + (\varepsilon - \frac{1}{\mu}) O(O^{-1})^* f^{'*}, \quad 2h^{'*} = (\varepsilon + \frac{1}{\mu}) f^{'*} + (\varepsilon - \frac{1}{\mu}) O^* O^{-1} f^{'}. \tag{88}$$

Analogously, starting from eqs. (85) we can produce

$$2 f' = (\frac{1}{\varepsilon} + \mu) h' + (\frac{1}{\varepsilon} - \mu) O(O^{-1})^* h^{'*}, \quad 2 f^{'*} = (\frac{1}{\varepsilon} + \mu) h^{'*} + (\frac{1}{\varepsilon} - \mu) O^* O^{-1} h'. \tag{89}$$

Eqs. (88), (89) represent the constitutive relations after changing the reference frame. At this point, one should distinguish between two cases: Euclidean rotation and Lorentzian boosts. Indeed, for any Euclidean rotations, we have the identities

$$O^* = O, \quad \Rightarrow \quad O(O^{-1})^* = I, \quad O^* O^{-1} = I;$$

and therefore eqs. (88), (89) take the form of (84), (85); in other words, at Euclidean rotations, the constitutive relations do not change their form. However, for any pseudo-Euclidean rotations, we have different relations

$$O^* = O^{-1} \quad \Rightarrow \quad O(O^{-1})^* = 0^2, \quad O^* O^{-1} = O^{*2};$$

therefore eqs. (88), (89) look like

$$2h' = (\varepsilon + \frac{1}{\mu}) f' + (\varepsilon - \frac{1}{\mu}) O^2 f^{'*}, \quad 2h^{'*} = (\varepsilon + \frac{1}{\mu}) f^{'*} + (\varepsilon - \frac{1}{\mu}) O^2 f^{'}; \tag{90}$$

$$2 f' = (\frac{1}{\varepsilon} + \mu) h' + (\frac{1}{\varepsilon} - \mu) O^{*2} h^{'*}, \quad 2 f^{'*} = (\frac{1}{\varepsilon} + \mu) h^{'*} + (\frac{1}{\varepsilon} - \mu) O^{*2} h'. \tag{91}$$

In the complex 3-vector form these relations seem to be shorter than in the real 3-vector form:

$$D' + i\frac{H'}{c} = \varepsilon_0 \varepsilon \frac{(E' + icB') + O(O^{-1})^* (E' - icB')}{2} + \frac{\varepsilon_0}{\mu} \frac{(E' + icB') - O(O^{-1})^* (E' - icB')}{2},$$

$$D' - i\frac{H'}{c} = \varepsilon_0 \varepsilon \frac{(E' - icB') + O^* O^{-1} (E' + icB')}{2} + \frac{\varepsilon_0}{\mu} \frac{(E' - icB') - O^* O^{-1} (E' + icB')}{2},$$

or

$$2D' = \varepsilon_0 \varepsilon [E' + \frac{O(O^{-1})^* + O^* O^{-1}}{2} E' + \frac{O(O^{-1})^* - O^* O^{-1}}{2i} cB']$$

$$+ \frac{\varepsilon_0}{\mu} [E' - \frac{O(O^{-1})^* + O^* O^{-1}}{2} E' - \frac{O(O^{-1})^* - O^* O^{-1}}{2i} cB'], \tag{92}$$

$$2\frac{H'}{c} = \varepsilon_0 \varepsilon [cB' - \frac{O(O^{-1})^* + O^* O^{-1}}{2} cB' + \frac{O(O^{-1})^* - O^* O^{-1}}{2i} E']$$

$$+\frac{\varepsilon_0}{\mu}[cB'+\frac{O(O^{-1})^*+O^*O^{-1}}{2}cB'-\frac{O(O^{-1})^*-O^*O^{-1}}{2i}E']. \qquad (93)$$

These are the constitutive equations for electromagnetic field in the uniform media according to Minkowski in a moving reference frame. For any Euclidean rotation, $O^*=O$ and eqs. (92), (93) coincide with the initial ones

$$D'=\varepsilon_0\varepsilon E', \quad H'/c=\varepsilon_0\frac{1}{\mu}cB'\Rightarrow H'=\frac{1}{\mu_0\mu}B'.$$

For any Lorentzian boosts $O^*=O^{-1}$, eqs. (92), (93) read

$$2D'=\varepsilon_0\varepsilon[(I+\frac{OO+O^*O^*}{2})E'+\frac{OO-O^*O^*}{2i}cB']+\frac{\varepsilon_0}{\mu}[(I-\frac{OO+O^*O^*}{2})E'-\frac{OO-O^*O^*}{2i}cB'], \qquad (94)$$

$$2H'/c=\varepsilon_0\varepsilon[(I-\frac{OO+O^*O^*}{2})cB'+\frac{OO-O^*O^*}{2i}E']+\frac{\varepsilon_0}{\mu}[(I+\frac{OO+O^*O^*}{2})cB'-\frac{OO-O^*O^*}{2i}E']. \qquad (95)$$

They can be written differently

$$D'=\frac{\varepsilon_0}{2}\left\{[(\varepsilon+\frac{1}{\mu})+(\varepsilon-\frac{1}{\mu})Re\,O^2]E'+(\varepsilon-\frac{1}{\mu})Im\,O^2cB']\right\}, \qquad (96)$$

$$\frac{H'}{c}=\frac{\varepsilon_0}{2}\left\{[(\varepsilon+\frac{1}{\mu})-(\varepsilon-\frac{1}{\mu})Re\,O^2]cB'+(\varepsilon-\frac{1}{\mu})Im\,O^2E']\right\}. \qquad (97)$$

Lorentzian complex vector boosts are given by the matrix (remembering $f=1-cosh\,b$)

$$O=O(b,n)=\begin{vmatrix} 1-f(n_2^2+n_3^2) & -i\,sinh\,bn_3+fn_1n_2 & i\,sinh\,bn_2+fn_1n_3 \\ i\,sinh\,bn_3+fn_1n_2 & 1-f(n_3^2+n_1^2) & -i\,sinh\,bn_1+fn_2n_3 \\ -sinh\,bn_2+fn_1n_3 & i\,sinh\,bn_1+fn_2n_3 & 1-f(n_1^2+n_2^2) \end{vmatrix}. \qquad (98)$$

The square of O^2 is (let $F=1-cosh\,2b$)

$$O^2=\begin{vmatrix} cosh2b+(1-cosh2b)n_1^2 & Fn_1n_2-i\,sinh\,2bn_3 & Fn_3n_1+i\,sinh\,2bn_2 \\ Fn_1n_2+i\,sinh\,2bn_3 & cosh\,2b+Fn_2^2 & Fn_2n_3-i\,sinh\,2bn_1 \\ Fn_3n_1-i\,sinh\,2bn_2 & Fn_2n_3+i\,sinh\,2bn_1 & cosh\,2b+Fn_3^2 \end{vmatrix}. \qquad (99)$$

We have obtained the result that should be expected: eq. (99) differs from eq. (98) only in one change $b\to 2b$. These expressions for O^2 ought to be substituted into the formulas:

$$2h'=(\varepsilon+\frac{1}{\mu})f'+(\varepsilon-\frac{1}{\mu})O^2f'^*, \quad 2h'^*=(\varepsilon+\frac{1}{\mu})f'^*+(\varepsilon-\frac{1}{\mu})O^2f',$$

$$2f'=(\frac{1}{\varepsilon}+\mu)h'+(\frac{1}{\varepsilon}-\mu)O^{*2}h'^*, \quad 2f'^*=(\frac{1}{\varepsilon}+\mu)h'^*+(\frac{1}{\varepsilon}-\mu)O^{*2}h',$$

or

$$D'=\frac{\varepsilon_0}{2}\left\{[(\varepsilon+\frac{1}{\mu})+(\varepsilon-\frac{1}{\mu})Re\,O^2]E'+(\varepsilon-\frac{1}{\mu})Im\,O^2cB']\right\},$$

$$\frac{H'}{c}=\frac{\varepsilon_0}{2}\left\{[(\varepsilon+\frac{1}{\mu})-(\varepsilon-\frac{1}{\mu})Re\,O^2]cB'+(\varepsilon-\frac{1}{\mu})Im\,O^2E']\right\}.$$

All the formulas become much more simple for rotations in the planes $(0-1),(0-2),(0-3)$:

$$n=(1,0,0),\quad O^2=\begin{vmatrix}1 & 0 & 0\\ 0 & cosh\,2b & +i\,sinh\,2b\\ 0 & -i\,sinh\,2b & cosh\,2b\end{vmatrix},$$

$$n=(0,1,0),\quad O^2=\begin{vmatrix}cosh\,2b & 0 & -i\,sinh\,2b\\ 0 & 1 & 0\\ +i\,sinh\,2b & 0 & cosh\,2b\end{vmatrix}, \qquad (100)$$

$$n=(0,0,1),\quad O^2=\begin{vmatrix}cosh\,2b & +i\,sinh\,2b & 0\\ -i\,sinh\,2b & cosh\,2b & 0\\ 0 & 0 & 1\end{vmatrix}.$$

The previous results can be easily extended to more general media, let us restrict ourselves to linear media. Arbitrary linear media are characterized by the following constitutive equations:

$$D=\varepsilon_0\varepsilon(x)E+\varepsilon_0 c\alpha(x)B,\quad H=\varepsilon_0 c\beta(x)E+\frac{1}{\mu_0}\mu(x)B, \qquad (101)$$

where $\varepsilon(x),\mu(x),\alpha(x),\beta(x)$ are (3×3)-dimensionless matrices. Eqs. (101) should be rewritten in terms of complex vectors f,h:

$$\frac{h+h^*}{2}=\varepsilon(x)\frac{f+f^*}{2}+\alpha(x)\frac{f-f^*}{2i},\quad \frac{h-h^*}{2i}=\beta(x)\frac{f+f^*}{2}+\mu(x)\frac{f-f^*}{2i}. \qquad (102)$$

From (101), (102) it follows

$$h=[(\varepsilon(x)+\mu(x))+i(\beta(x)-\alpha(x))]f+[(\varepsilon(x)-\mu(x))+i(\beta(x)+\alpha(x))]f^*, \qquad (103)$$

$$h^*=[(\varepsilon(x)+\mu(x))-i(\beta(x)-\alpha(x))]f^*+[(\varepsilon(x)-\mu(x))-i(\beta(x)+\alpha(x))]f. \qquad (104)$$

Under Lorentz transformations, relations (5.20) will take the form

$$O^{-1}h'=\left[(\varepsilon(x)+\mu(x))+i(\beta(x)-\alpha(x))\right]O^{-1}f'+\left[(\varepsilon(x)-\mu(x))+i(\beta(x)+\alpha(x))\right](O^{-1})^*f'^*,$$

$$(O^{-1})^*h'^*=\left[(\varepsilon(x)+\mu(x))-i(\beta(x)-\alpha(x))\right](O^{-1})^*f'^*$$

$$+\left[(\varepsilon(x)-\mu(x))-i(\beta(x)+\alpha(x))\right](O^{-1})f', \qquad (105)$$

or

$$h'=\varepsilon_0\left[(\varepsilon(x)+\mu(x))+i(\beta(x)-\alpha(x))\right]f'+\left[(\varepsilon(x)-\mu(x))+i(\beta(x)+\alpha(x))\right][O(O^{-1})^*]f'^*,$$

$$h'^*=\varepsilon_0\left[(\varepsilon(x)+\mu(x))-i(\beta(x)-\alpha(x))\right]f'^*+\left[(\varepsilon(x)-\mu(x))-i(\beta(x)+\alpha(x))\right][O^*(O^{-1})]f'. \qquad (106)$$

For Euclidean rotation, we have

$$[O(O^{-1})^*]=I,\quad [O^*(O^{-1})]=I,$$

and the constitutive relations preserve their form. For Lorentz boosts we have

$$[O(O^{-1})^*]=O^2,\quad [O^*(O^{-1})]=O^{*2},$$

and the constitutive equations in a moving reference frame change their form in accordance with the relations

$$h' = \left[(\varepsilon(x)+\mu(x)) + i(\beta(x)-\alpha(x)) \right] f' + \left[(\varepsilon(x)-\mu(x)) + i(\beta(x)+\alpha(x)) \right] O^2 f'^{*},$$

$$h'^{*} = \left[(\varepsilon(x)+\mu(x)) - i(\beta(x)-\alpha(x)) \right] f'^{*} + \left[(\varepsilon(x)-\mu(x)) - i(\beta(x)+\alpha(x)) \right] O^{*2} f'. \qquad (107)$$

They are the constitutive relations for arbitrary linear media in the moving reference frame.

6. Symmetry properties of the matrix equation in media

Maxwell equations in media are written in two groups

$$F^{ab}, \quad div\, f - div\, f^{*} = 0, \quad -i\partial_0 f + rot\, f + i\partial_0 f^{*} + rot\, f^{*} = 0; \qquad (108)$$

$$H^{ab}, \quad div\, h + div\, h^{*} = \frac{1}{\varepsilon_0}\rho, \quad -i\partial_0 h + rot\, h - i\partial_0 h^{*} - rot\, h^{*} = i\frac{1}{\varepsilon_0} j. \qquad (109)$$

Their matrix forms respectively read

$$(-i\partial_0 + \alpha^i \partial_i) f - (-i\partial_0 + \beta^i \partial_i) f^{*} = 0, \qquad (110)$$

$$(-i\partial_0 + \alpha^i \partial_i) h + (-i\partial_0 + \beta^i \partial_i) h^{*} = J. \qquad (111)$$

Equations (108), (109) can be presented in a more short form (see (91), (92)):

$$div\, M + div\, N = \frac{1}{\varepsilon_0}\rho, \quad -i\partial_0 M + rot\, M - i\partial_0 N - rot\, N = \frac{i}{\varepsilon_0} j; \qquad (112)$$

with the corresponding matrix form

$$(-i\partial_0 + \alpha^i \partial_i) M + (-i\partial_0 + \beta^i \partial_i) N = J. \qquad (113)$$

The matrices α^i and β^i are given by

$$\alpha^1 = \begin{vmatrix} 0 & 1 & 0 & 0 \\ -1 & 0 & 0 & 0 \\ 0 & 0 & 0 & -1 \\ 0 & 0 & 1 & 0 \end{vmatrix}, \alpha^2 = \begin{vmatrix} 0 & 0 & 1 & 0 \\ 0 & 0 & 0 & 1 \\ -1 & 0 & 0 & 0 \\ 0 & -1 & 0 & 0 \end{vmatrix}, \alpha^3 = \begin{vmatrix} 0 & 0 & 0 & 1 \\ 0 & 0 & -1 & 0 \\ 0 & 1 & 0 & 0 \\ -1 & 0 & 0 & 0 \end{vmatrix},$$

$$\beta^1 = \begin{vmatrix} 0 & 1 & 0 & 0 \\ -1 & 0 & 0 & 0 \\ 0 & 0 & 0 & 1 \\ 0 & 0 & -1 & 0 \end{vmatrix}, \beta^2 = \begin{vmatrix} 0 & 0 & 1 & 0 \\ 0 & 0 & 0 & -1 \\ -1 & 0 & 0 & 0 \\ 0 & 1 & 0 & 0 \end{vmatrix}, \beta^3 = \begin{vmatrix} 0 & 0 & 0 & 1 \\ 0 & 0 & 1 & 0 \\ 0 & -1 & 0 & 0 \\ -1 & 0 & 0 & 0 \end{vmatrix}. \qquad (114)$$

We will consider eq. (113). The terms with matrices α^j were examined above, the terms with matrices β^j are new. We restrict ourselves to demonstrating the Lorentz symmetry of eq. (113) under two simplest transformations.

First, let us consider the Euclidean rotation in the plane $(1-2)$, and examine only the term with β-matrices:

$$S\beta^1 S^{-1} = \begin{vmatrix} 0 & \cos a & -\sin a & 0 \\ -\cos a & 0 & 0 & \sin a \\ \sin a & 0 & 0 & \cos a \\ 0 & -\sin a & -\cos a & 0 \end{vmatrix} = \cos a \beta^1 - \sin a \beta^2 = \beta^j O_{j1}, \qquad (115)$$

$$S\beta^2 S^{-1} = \begin{vmatrix} 0 & \sin a & \cos a & 0 \\ -\sin a & 0 & 0 & -\cos a \\ -\cos a & 0 & 0 & \sin a \\ 0 & \cos a & -\sin a & 0 \end{vmatrix} = \sin a\beta^1 + \cos a\beta^2 = \beta^j O_{j2}, \qquad (116)$$

$$S\beta^3 S^{-1} = \begin{vmatrix} 0 & 0 & 0 & 1 \\ 0 & 0 & 1 & 0 \\ 0 & -1 & 0 & 0 \\ -1 & 0 & 0 & 0 \end{vmatrix} = \beta^3 = \beta^j O_{j3}. \qquad (117)$$

We conclude that eq. (113) is symmetrical under Euclidean rotations in accordance with the relations

$$(-i\partial_0 + S\alpha^i S^{-1}\partial_i)M' + (-i\partial_0 + S\beta^i S^{-1}\partial_i)N' = +SJ$$

$$\Rightarrow (-i\partial_0 + \alpha^i \partial'_i)M' + (-i\partial_0 + \beta^i \partial'_i)N' = +J'. \qquad (118)$$

For the Lorentz boost in the plane $(0-3)$ we have

$$M' = SM, \quad N' = S^* N = S^{-1}N, \quad S^* = S^{-1};$$

and eq. (113) takes the form (the additional transformation $\Delta = \Delta_{(\alpha)}$ is combined in terms of α^j)

$$\Delta_{(\alpha)} S\Big[(-i\partial_0 + \alpha^i\partial_i)S^{-1}M' + (-i\partial_0 + \beta^i\partial_i)SN'\Big] = \Delta SJ, \qquad (119)$$

or

$$\Delta_{(\alpha)}\Big[(-i\partial_0 + S\alpha^i S^{-1}\partial_i)M' + S^2(-i\partial_0 + S^{-1}\beta^i S\partial_i)N'\Big] = J', \qquad (120)$$

and further

$$(-i\partial_0' + \alpha^i\partial'_i)M' + \Delta_{(\alpha)}S^2(-i\partial_0 + S^{-1}\beta^i S\partial_i)N' = J'. \qquad (121)$$

It remains to prove the relationship

$$\Delta_{(\alpha)}S^2(-i\partial_0 + S^{-1}\beta^i S\partial_i)N' = (-i\partial_0' + \beta^i\partial_i')N'. \qquad (122)$$

By simplicity reason one may expect two identities:

$$\Delta_{(\alpha)}S^2 = \Delta_{(\beta)} \quad \Leftrightarrow \quad \Delta_{(\alpha)}S = \Delta_{(\beta)}S^{-1}, \qquad (123)$$

$$\Delta_{(\beta)}(-i\partial_0 + S^{-1}\beta^i S\partial_i)N' = (-i\partial_0' + \beta^i\partial_i')N'. \qquad (124)$$

Let us prove them for a Lorentzian boost in the plane $(0-3)$:

$$S = \begin{vmatrix} 1 & 0 & 0 & 0 \\ 0 & cosh b & -i\, sinh b & 0 \\ 0 & i\, sinh b & cosh b & 0 \\ 0 & 0 & 0 & 1 \end{vmatrix}, \quad S^{-1} = \begin{vmatrix} 1 & 0 & 0 & 0 \\ 0 & cosh b & -i\, sinh b & 0 \\ 0 & i\, sinh b & cosh b & 0 \\ 0 & 0 & 0 & 1 \end{vmatrix}.$$

Allowing for (115) – (117) we readily get

$$S^{-1}\beta^1 S = cosh b\beta^1 - i\, sinh b\beta^2 = \beta^j O^{-1}_{j1},$$

$$S^{-1}\beta^2 S = i\, sinh b\beta^1 + cosh b\beta^2 = \beta^j O^{-1}_{j2}, \quad S^{-1}\beta^3 S = \beta^3 = \beta^j O^{-1}_{j3}. \qquad (125)$$

To verify the identity $\Delta_{(\alpha)} S = \Delta_{(\beta)} S^{-1}$, or $(\cosh b - i \sinh b \alpha^3) S = (\cosh b - i \sinh b \beta^3) S^{-1}$, let us calculate separately the left-hand part

$$(\cosh b - i \sinh b \alpha^3) S = \begin{vmatrix} \cosh b & 0 & 0 & -i \sinh b \\ 0 & 1 & 0 & 0 \\ 0 & 0 & 1 & 0 \\ i \sinh b & 0 & 0 & \cosh b \end{vmatrix};$$

and the right-hand part

$$(\cosh b - i \sinh b \beta^3) S^{-1} = \begin{vmatrix} \cosh b & 0 & 0 & -i \sinh b \\ 0 & 1 & 0 & 0 \\ 0 & 0 & 1 & 0 \\ i \sinh b & 0 & 0 & \cosh b \end{vmatrix}.$$

They coincide with each other, so eq. (123) holds. It remains to prove the relation (124). Allowing for the properties of β–matrices $(\beta^0)^2 = -I, (\beta^1)^2 = -I, \beta^1\beta^2 = -\beta^3, \beta^2\beta^1 = +\beta^3$, we readily find

$$\Delta_{(\beta)}(-i\partial_0 + S^{-1}\beta^i S \partial_i) N' =$$
$$= [-i(\cosh b \partial_0 - \sinh b \partial_3) + \beta^3(-\sinh b \partial_0 + \cosh b \partial_3) + \beta^1 \partial_1 + \beta^2 \partial_2] N', \qquad (126)$$

that is

$$\Delta_{(\beta)}(-i\partial_0 + S^{-1}\beta^i S \partial_i) N' = (-i\partial_0' + \beta^1\partial_1 + \beta^2\partial_2 + \beta^3\partial_3') N'. \qquad (127)$$

Thus, the symmetry of the matrix Maxwell equation in media under the Lorentz group is proved.

7. Dirac matrices and electromagnetic field

Let us shortly discuss two points relevant to the above matrix formulation of the Maxwell theory. First, let us write down explicit form for Dirac matrices:

$$\gamma^0 = \begin{vmatrix} 0 & 0 & 1 & 0 \\ 0 & 0 & 0 & 1 \\ 1 & 0 & 0 & 0 \\ 0 & 1 & 0 & 0 \end{vmatrix}, \quad \gamma^5 = \begin{vmatrix} -1 & 0 & 0 & 0 \\ 0 & -1 & 0 & 0 \\ 0 & 0 & 1 & 0 \\ 1 & 0 & 0 & 1 \end{vmatrix},$$

$$\gamma^1 = \begin{vmatrix} 0 & 0 & 0 & -1 \\ 0 & 0 & -1 & 0 \\ 0 & 1 & 0 & 0 \\ 1 & 0 & 0 & 0 \end{vmatrix}, \gamma^2 = \begin{vmatrix} 0 & 0 & 0 & i \\ 0 & 0 & -i & 0 \\ 0 & -i & 0 & 0 \\ i & 0 & 0 & 0 \end{vmatrix}, \gamma^3 = \begin{vmatrix} 0 & 0 & -1 & 0 \\ 0 & 0 & 0 & 1 \\ 1 & 0 & 0 & 0 \\ 0 & -1 & 0 & 0 \end{vmatrix}.$$

Bearing in mind the expressions for α^i and β^i, we immediately see the identities

$$\alpha^1 = i\gamma^0\gamma^2, \quad \alpha^2 = \gamma^0\gamma^5, \quad \alpha^3 = i\gamma^5\gamma^2, \quad \beta^1 = -\gamma^3\gamma^1, \quad \beta^2 = -\gamma^3, \quad \beta^3 = -\gamma^1, \qquad (128)$$

so the Maxwell matrix equation in media takes the form

$$(-i\partial_0 + i\gamma^0\gamma^2\partial_1 + \gamma^0\gamma^5\partial_2 + i\gamma^5\gamma^2\partial_3) M + (-i\partial_0 - \gamma^3\gamma^1\partial_1 - \gamma^3\partial_2 - \gamma^1\partial_3) N = J. \qquad (129)$$

This Dirac matrix-based form does not seem to be very useful to apply in Maxwell's theory, it does not prove much similarities with ordinary Dirac equation (though that analogy was often discussed in the literature).

Now, starting from the electromagnetic tensor $F_{\alpha\beta}$ and dual to it $\tilde{F}_{\rho\sigma}$:

$$\tilde{F}_{\rho\sigma} = \frac{1}{2}\varepsilon_{\rho\sigma\alpha\beta}F^{\alpha\beta}, \quad F_{\alpha\beta} = -\frac{1}{2}\varepsilon_{\alpha\beta\rho\sigma}\tilde{F}^{\rho\sigma},$$

Let us introduce two electromagnetic 4-vectors (below u^{α} is any 4-vector, which in general can not coincide with 4-velocity of a reference frame)

$$e^{\alpha} = u_{\beta}F^{\alpha\beta}, \quad b^{\alpha} = u_{\beta}\tilde{F}^{\alpha\beta}, \quad u^{\alpha}u_{\alpha} = 1; \tag{130}$$

the inverse formulas are

$$F^{\alpha\beta} = (e^{\alpha}u^{\beta} - e^{\beta}u^{\alpha}) - \varepsilon^{\alpha\beta\rho\sigma}b_{\rho}u_{\sigma}, \quad \tilde{F}^{\alpha\beta} = (b^{\alpha}u^{\beta} - b^{\beta}u^{\alpha}) + \varepsilon^{\alpha\beta\rho\sigma}e_{\rho}u_{\sigma}. \tag{131}$$

Such electromagnetic 4-vectors are presented in the literature on the electrodynamics of moving bodies, from the very beginning, see Minkowski [14-17], Gordon [18], Tamm and Mandelstam [19-21]; for instance, see Yépez, Brito, and Vargas [108]. The interest in these variables gets renewed after Esposito paper [116] in 1998.

In 3-dimensional notation $E^1 = -E_1 = F^{10}, cB^1 = cB_1 = \tilde{F}^{10} = -F_{23}, \textit{ and so on}$, the formulas (130) take the form

$$e^0 = uE, \quad e = u^0E + cu\times B, \quad b^0 = cuB, \quad b = cu^0B - u\times E, \tag{132}$$

or symbolically $(e,b) = U(u)(E,B)$; the inverse formulas look like

$$E = eu^0 - e^0u + b\times u, \quad cB = bu^0 - b^0u - e\times u, \tag{133}$$

or in a symbolical form

$$(E,B) = U^{-1}(u)(e,b).$$

The above possibility is often used to produce a special form of the Maxwell equations. For simplicity, let us consider the vacuum case:

$$\partial_{\alpha}F_{\beta\gamma} + \partial_{\beta}F_{\gamma\alpha} + \partial_{\gamma}F_{\alpha\beta} = 0, \quad \partial_{\alpha}F^{\alpha\beta} = \varepsilon_0^{-1}j^{\beta},$$

or differently with the help of the dual tensor:

$$\partial_{\beta}\tilde{F}^{\beta\alpha} = 0, \quad \partial_{\alpha}F^{\alpha\beta} = \varepsilon_0^{-1}j^{\beta}. \tag{134}$$

These can be transformed into variables e^{α}, b^{α}:

$$\partial_{\alpha}(b^{\alpha}u^{\beta} - b^{\beta}u^{\alpha} + \varepsilon^{\alpha\beta\rho\sigma}e_{\rho}u_{\sigma}) = 0, \quad \partial_{\alpha}(e^{\alpha}u^{\beta} - e^{\beta}u^{\alpha} - \varepsilon^{\alpha\beta\rho\sigma}b_{\rho}u_{\sigma}) = \varepsilon_0^{-1}j^{\beta}. \tag{135}$$

They can be combined into the equations for complex field function

$$\Phi^{\alpha} = e^{\alpha} + ib^{\alpha}, \quad \partial_{\alpha}[\Phi^{\alpha}u^{\beta} - \Phi^{\beta}u^{\alpha} + i\varepsilon^{\alpha\beta\rho\sigma}\Phi_{\rho}u_{\sigma}] = \varepsilon_0^{-1}j^{\beta},$$

or differently

$$\partial_{\alpha}[\delta^{\alpha}_{\gamma}u^{\beta} - \delta^{\beta}_{\gamma}u^{\alpha} + i\varepsilon^{\alpha\beta\rho\sigma}g_{\rho\gamma}u_{\sigma}]\Phi^{\gamma} = \varepsilon_0^{-1}j^{\beta}. \tag{136}$$

This is Esposito's representation [116] of the Maxwell equations. One may introduce four matrices depending on 4-vector u^{α}:

$$(\Gamma^{\alpha})^{\beta}_{\ \gamma} = \delta^{\alpha}_{\gamma}u^{\beta} - \delta^{\beta}_{\gamma}u^{\alpha} + i\varepsilon^{\alpha\beta\rho\sigma}g_{\rho\gamma}u_{\sigma}, \tag{137}$$

then eq. (136) becomes

$$\partial_{\alpha}(\Gamma^{\alpha})^{\beta}_{\ \gamma}\Phi^{\gamma} = \varepsilon_0^{-1}j^{\beta}, \quad \textit{or} \quad \Gamma^{\alpha}\partial_{\alpha}\Phi = \varepsilon_0^{-1}j. \tag{138}$$

In the rest reference frame, when $u^\alpha = (1,0,0,0)$, the matrices Γ^α become simpler, and $\Phi = \Psi$:

$$\Gamma^0 = \begin{vmatrix} 0 & 0 & 0 & 0 \\ 0 & -1 & 0 & 0 \\ 0 & 0 & -1 & 0 \\ 0 & 0 & 0 & -1 \end{vmatrix}, \Gamma^1 = \begin{vmatrix} 0 & 1 & 0 & 0 \\ 0 & 0 & 0 & 0 \\ 0 & 0 & 0 & i \\ 0 & 0 & -i & 0 \end{vmatrix}, \Gamma^2 = \begin{vmatrix} 0 & 0 & 1 & 0 \\ 0 & 0 & 0 & -i \\ 0 & 0 & 0 & 0 \\ 0 & i & 0 & 0 \end{vmatrix}, \Gamma^3 = \begin{vmatrix} 0 & 0 & 0 & 1 \\ 0 & 0 & i & \\ 0 & -i & 0 & 0 \\ 0 & 0 & 0 & 0 \end{vmatrix}.$$

correspondingly, eq. (138) takes the form

$$\begin{vmatrix} 0 & \partial_1 & \partial_2 & \partial_3 \\ 0 & -\partial_0 & i\partial_3 & -i\partial_2 \\ 0 & -i\partial_3 & -\partial_0 & i\partial_1 \\ 0 & i\partial_2 & -i\partial_1 & -\partial_0 \end{vmatrix} \begin{vmatrix} 0 \\ E^1 + icB^1 \\ E^2 + icB^2 \\ E^3 + icB^3 \end{vmatrix} = \varepsilon_0^{-1} \begin{vmatrix} \rho \\ j^1 \\ j^2 \\ j^3 \end{vmatrix} = \varepsilon_0^{-1} j, \tag{139}$$

or

$$div(E + icB) = \varepsilon_0^{-1} \rho, \quad -\partial_0 (E + icB) - i\, rot(E + icB) = \varepsilon_0^{-1} j.$$

Whence we get equations

$$div\, cB = 0, \quad rot\, E = -\frac{\partial cB}{\partial ct}, \quad div\, E = \frac{\rho}{\varepsilon_0}, \quad rot\, cB = \frac{j}{\varepsilon_0} + \frac{\partial E}{\partial ct},$$

which coincides with the Maxwell equations. Relations (139) correspond to a special choice of α-matrices:

$$\beta(-i\alpha^0) = \Gamma^0, \beta\alpha^j = \Gamma^j, \; where \; \beta = \begin{vmatrix} 1 & 0 & 0 & 0 \\ 0 & -i & 0 & 0 \\ 0 & 0 & -i & 0 \\ 0 & 0 & 0 & -i \end{vmatrix}. \tag{140}$$

Esposito's representation of the Maxwell equation 4-vector u^α can be easily related to the matrix equation of Riemann–Silberstein–Majorana–Oppenheimer:

$$(-i\alpha^0 \partial_0 + \alpha^j \partial_j)\Psi = J, \tag{141}$$

indeed

$$(-i\alpha^0 \partial_0 + \alpha^j \partial_j) U^{-1} (U\Psi) = J, -i\alpha^0 U^{-1} = \beta\Gamma^0, \quad \alpha^j U^{-1} = \beta\Gamma^j, \quad U\Psi = \Phi,$$

$$\beta(\Gamma^0 \partial_0 + \Gamma^j \partial_j)\Phi = J, \quad \beta^{-1} J = \varepsilon_0^{-1}(j^a), \quad (\Gamma^0 \partial_0 + \Gamma^j \partial_j)\Phi = \varepsilon_0^{-1} j. \tag{142}$$

Eq. (142) is a matrix representation of the Maxwell equations in Esposito's form

$$\partial_\alpha [\delta_\gamma^\alpha u^\beta - \delta_\gamma^\beta u^\alpha + i\varepsilon^{\alpha\beta\rho\sigma} g_{\rho\gamma} u_\sigma] \Phi^\gamma = \varepsilon_0^{-1} j^\beta. \tag{143}$$

Evidently, eqs. (141) and (143) are equivalent to each other. There is no ground to consider the form (143) obtained through the trivial use of identity $I = U^{-1}(u) U(u)$ as having a certain especially profound sense. Our point of view contrasts with the claim by Ivezić [121-125] that eq. (143) has a status of a true Maxwell equation in a moving reference frame (at that u^α is identified with 4-velocity).

References

1. Lorentz HA. De l'influence du mouvement de la terre sur les phénom ènes lumineux. *Archives Néerlandaises des Sciences Exactes et Naturelles*. 1886;21: 103-176.

2. Lorentz HA. La théorie électromagnétique de Maxwell et son application aux corps

mouvants. *Archives néerlandaises des sciences exactes et naturelles.* 1892;25: 363-552.
3. Lorentz HA. Electromagnetic phenomena in a system moving with any velocity less than that of light. *Proceedings of the Section of Sciences, Koninklijke Akademie van Wetenschappen te Amsterdam.* 1904;6: 809-831.
4. Poincaré H. *Électricité et optique*. Paris: Georges Carré; 1890.
5. Poincaré H. La mesure du temps. *Revue de métaphysique et de morale.* 1898;6: 371-384.
6. Poincaré H. La théorie de Lorentz et le principe de réaction. *Archives néerlandaises des sciences exactes et naturelles.* 1900;5: 252-278.
7. Poincaré H. *Électricité et optique: la lumière et les théories électrodynamiques.* Paris: Carré et Naud; 1901.
8. Poincaré H. Sur la dynamique de l'électron. *Compt. Rend. Acad. Sci. Paris.* 1905;140: 1504-1508.
9. Poincaré H. Sur la dynamique de l'électron. *Rendiconti del circolo matematico di Palermo*. 1906;21: 129-176;
10. Poincaré H. La dynamique de l'électron. *Revue générale des sciences pures et appliquées*. 1908;19: 386-402.
11. Einstein A. Zur Elektrodynamik der bewegten Körper. *Annalen der Physik.* 1905;17: 891-921.
12. Einstein A, Laub J. Über die elektromagnetischen Grundgleichungen für bewegte Körper. *Annalen der Physik*. 1908;26: 532-540.
13. Einstein A, Laub J. Die im elektromagnetischen Felde auf ruhende Körper ausgeübten ponderomotorischen Kräfte. *Annalen der Physik.* 1908;26: 541-550.
14. Minkowski H. Die Grundlagen für die electromagnetischen Vorgänge in bewegten Körpern. *Nachrichten von der Königlichen Gesellschaft der Wissenschaften zu Göttingen, mathematisch-physikalische Klasse.* 1908: 53–111; reprint in Math. Ann. 1910;68: 472-525.
15. Minkowski H. Raum und Zeit. *Jahresbericht der deutschen Mathematiker-Vereinigung*. 1909;18: 75-88.
16. Minkowski H. Raum und Zeit. *Physikalische Zeitschrift.* 1909;10: 104-111.
17. Minkowski H. Das Relativitätsprinzip. *Annalen der Physik.* 1915;47: 927-938.
18. Gordon W. Zur lichtfortp anzung nach der relativität-stheorie. *Annalen der Physik. (Leipzig).* 1923;72: 421-456.
19. Tamm IE. Electrodynamics of an anisotropic medium and the special theory of relativity. *Zh. R, F, Kh. O, Fiz. dep.* 1924;56(2-3): 248-262;
20. Tamm IE. Crystal optics in the theory of relativity and its relationship to the geometry of a biquadratic form. *Zh. R, F, Kh. O, Fiz. dep.* 1925;57(3-4): 209-240.
21. Mandelstam LI, Tamm IE. Elektrodynamik der anisotropen Medien und der speziallen Relativitatstheorie**.** *Mathematische Annalen*. 1925;95: 154-160.
22. Dirac PAM. The Quantum theory of the electron. *Proceedings of the Royal Society. London. A.* 1928;117: 610-624;
23. Dirac PAM. The Quantum theory of the electron. Part II. *Proceedings of the Royal Society. London. A.* 1928;118: 351-361.
24. Ivanenko D, Landau L. Zur theorie des magnetischen electrons. *Physikalische Zeitschrift.* 1928;48: 340-348.
25. Neumann J. Einige Bemerkungen zur Diracschen Theorie des relativistischen Drehelectrons. *Physikalische Zeitschrift*. 1929;48: 868-881.
26. Van der Waerden B. Spinoranalyse. *Nachrichten der Akademie der Wissenschaften in Göttingen. II. Mathematisch-Physikalische Klasse*. 1929: 100–109 .
27. Juvet G. Opérateurs de Dirac et Équations de Maxwell. *Commentarii Mathematici Helvetici*. 1930;2: 225-235.
28. Laporte O, Uhlenbeck G. Application of spinor analysis to the Maxwell and Dirac

equations. *Physical Review*. 1931;37: 1380-1397.
29. Rumer Yu. *Spinor Analysis*. Moscow; 1936.
30. Majorana E. *Scientific Papers, Unpublished*.
31. Oppenheimer J. Note on light quanta and the electromagnetic field. *Physical Review*. 1931;38: 725-746.
32. Silberstein L. Elektromagnetische Grundgleichungen in bivectorieller Behandlung. *Annalen der Physik.* 1907;22(3): 579-586.
33. Silberstein L. Nachtrag zur Abhandlung Über "elektromagnetische Grundgleichungen in bivektorieller Behandlung". *Annalen der Physik*. 1907;24(14): 783-784.
34. Weber H. *Die partiellen Differential-Gleichungen der mathematischen Physik nach Riemann's Vorlesungen*. Braunschweig: Friedrich Vieweg und Sohn; 1901.
35. Bialynicki-Birula I. On the wave function of the photon. *Acta Physica Polonica*. 1994;86(1-2): 97-116.
36. Bialynicki-Birula I. Photon wave function. *Progress in Optics*. 1996;36: 248-294.
37. de Broglie L. L'équation d'Ondes du Photon. *Compt. Rend. Acad. Sci. Paris*. 1934. 199. 445–448.
38. de Broglie L, Winter M. Sur le Spin du Photon. *Compt. Rend. Acad. Sci. Paris*. 1934;199: 813-816.
39. de Broglie L. Sur un Cas de Réductibilité en Mécanique Ondulatoire des Particules de Spin 1. *Compt. Rend. Acad. Sci. Paris*. 1939;208: 1697-1700.
40. de Broglie L. Champs Réels et Champs Complexes en Théorie Électromagnétique Quantique du Rayonnement. *Compt. Rend. Acad. Sci. Paris*. 1949;211: 41-44.
41. Mercier A. Expression des équations de l'Électromagnétisme au Moyen des Nombres de Clifford. Thèse de l'Université de Genève. No 953. *Archives des sciences physiques et naturelles. Genève*. 1935;17: 1-34.
42. Petiau G. Contribution à l'étude des équations d'ondes corpusculaires. University of Paris. Thesis; *Mémoires de l'Académie royale des sciences, des lettres et des beaux-arts de Belgique*. 1936;16(2): 1-118.
43. Proca A. Sur les Equations Fondamentales des Particules Élémentaires. *Compt. Rend. Acad. Sci. Paris*. 1936;202: 1490-1492.
44. Proca A. Sur les Équations Relativistes des Particules Élémentaires. *Compt. Rend. Acad. Sci. Paris*. 1946;223: 270-272.
45. Kemmer N. The particle aspect of meson theory. *Proceedings of the Royal Society. London. A*. 1939;173: 91-116.
46. Kemmer N. The algebra of meson matrices. *Mathematical Proceedings of the Cambridge Philosophical Society*. 1943;39: 189-196.
47. Kemmer N. On the theory of particles of spin 1. *Helvetica Physica Acta*. 1960;33: 829-838.
48. Bhabha H. Classical theory of meson. *Proceedings of the Royal Society. London. A*. 1939;172: 384-409.
49. Belinfante F. The undor equation of the meson field. *Physica*. 1939;6: 870-886.
50. Belinfante F. Spin of mesons. *Physica*. 1939;6: 887-898.
51. Taub A. Spinor equations for the meson and their solution when no field is present. *Physical Review*. 1939;56: 799-810.
52. Sakata S, Taketani M. On the wave equation of the meson. *Proceeding of the Phys. Math. Society*. 1940;22: 757-770.
53. Erikson HAS. Vektor-pseudovektor meson theory. *Arkiv för matematik, astronomi och fysik*. 1942;29(10): 1-11.
54. Schrödinger E. Maxwell's and Dirac's equations in expanding universe. *Proceedings of the Royal Irish Academy. A*. 1940;46: 25-47.

55. Schrödinger E. Pentads, tetrads, and triads of meson matrices. *Proceedings of the Royal Irish Academy*. 1943;48: 135-146.
56. Schrödinger E. Systematics of meson matrices. *Proceedings of the Royal Irish Academy*. 1943;49: 29-42.
57. Tonnelat MA. *Sur la théorie du photon dans un espace de Riemann*. Masson & Cie; 1940.
58. Stratton JA. *Electromagnetic Theory*. McGraw-Hill book company inc.; 1941.
59. Heitler W, Peng HW. On the particle equation of the meson. *Proceedings of the Royal Irish Academy*. 1943;49: 1-28.
60. Einstein A, Bargmann V. Bivector fields. I, II. *Annals of Mathematics*. 1944;45: 1-14; 15-23.
61. Harish-Chandra. On the algebra of the meson matrices. *Mathematical Proceedings of the Cambridge Philosophical Society*. 1946;43: 414-421.
62. Harish-Chandra. The correspondence between the particle and wave aspects of the meson and the photon. *Proceedings of the Royal Society. London. A*. 1946;186: 502-525.
63. Hoffmann B. The vector meson field and projective relativity. *Physical Review*. 1947;72: 458-465.
64. Utiyama R. On the interaction of mesons with the gravitational field. *Progress of Theoretical Physics*. 1947;2: 38-62.
65. Schouten JA. On meson fields and conformal transformations. *Review of Modern Physics*. 1949;21: 421-424.
66. Mercier A. Sur les Fondements de l’Électrodynamique Classique (Méthode Axiomatique). *Archives des sciences physiques et naturelles. Genève*. 1949;2: 584-588.
67. de Broglie L, Tonnelat MA. Sur la possibilité d’une structure complexe pour les particules de spin 1. *Compt. Rend. Acad. Sci. Paris*. 1950;230: 1329-1332.
68. Gupta SN. Theory of longitudinal photons in quantum electrodynamics. *Proceedings of the Royal Society. London. A*. 1950;63: 681-691.
69. Bleuler K. Eine neue Methode zur Behandlung der longitudinalen und skalaren Photonen. *Helvetica Physica Acta*. 1950;23: 567-586.
70. Brulin O, Hjalmars S. Wave equations for integer spin particles in gravitational fields. *Arkiv for Fysik*. 1952;5: 163-174.
71. Rosen H. Special theories of relativity. *American Journal of Physics*. 1952;20: 161-164.
72. Fujiwara I. On the Duffin-Kemmer algebra. *Progress of Theoretical Physics*. 1953;10: 589-616.
73. Gürsey F. Dual invariance of Maxwell's tensor. *Review of the Faculty of Science, University of Istanbul. A*. 1954;19: 154-160.
74. Gupta S. Gravitation and electromagnetism. *Physical Review*. 1954;96: 1683-1685.
75. Lichnerowicz A. *Théories Relativistes de la Gravitation et de l’Électromagnetisme*. Paris; 1955.
76. Ohmura T. A new formulation on the electromagnetic field. *Progress of Theoretical Physics*. 1956;16: 684-685.
77. Borgardt A. Matrix aspects of the boson theory. *JETP*. 1956;30: 334-341.
78. Borgardt A. Wave equatons for a photon. *JETF*. 1958;34: 1323-1325.
79. Fedorov F. On the reduction of wave equations for spin-0 and spin-1 to the hamiltonian form. *JETP*. 1957;4: 139-141.
80. Kuohsien T. Sur les Theories Matricielles du Photon. *Compt. Rend. Acad. Sci. Paris*. 1957;245: 141-144.
81. Bludman S. Some theoretical consequences of a particle having mass zero. *Physical Review*. 1957;107: 1163-1168.
82. Good JrR. Particle aspect of the electromagnetic field equations. *Physical Review*. 1957;105: 1914-1919.

83. Moses H. A spinor representation of maxwell equations. *Nuovo Cimento Supplement.* 1958;1: 1-18.
84. Moses E. Solutions of Maxwell’s Equations in terms of a spinor notation: the direct and inverse problems. *Physical Review*. 1959;113: 1670-1679.
85. Moses H. photon wave functions and the exact electromagnetic matrix elements for hydrogenic atoms. *Physical Review. A.* 1973;8: 1710-1721.
86. da Silveira A. Kemmer wave equation in Riemann space. *Journal of Mathematical Physics*. 1960;1: 489-491.
87. da Silveira A. Invariance algebras of the Dirac and Maxwell equations. *Nouvo Cimento. A.* 1980;56: 385-395.
88. Lomont J. Dirac-like wave equations for particles of zero rest mass and their quantization. *Phyical. Review*. 1958;11: 1710-1716.
89. Post EJ. *Formal structure of electrodynamics. General covariance and electromagnetics*. Amsterdam: North-Holland; 1962.
90. Bogush A, Fedorov F. On properties of the Duffin-Kemmer matrices. *Doklady AN BSSR.* 1962;6: 81-85.
91. Sachs M, Schwebel S. On covariant formulations of the Maxwell-Lorentz theory of electromagnetism. *Journal of Mathematical Physics*. 1962;3: 843-848.
92. Ellis J. *Maxwell’s equations and theories of Maxwell form. Ph.D. thesis.* University of London; 1964.
93. Beckers J, Pirotte Ch. Vectorial meson equations in relation to photon description. *Physica.* 1968;39: 205-212.
94. Casanova G. Particules Neutre de Spin 1. *Compt. Rend. Acad. Sci. Paris.* 1969;268: 673-676.
95. Carmeli M. Group analysis of Maxwell equations. *Journal of Mathematical Physics.* 1969;10. 1699–1703.
96. Weingarten D. Complex symmetries of electrodynamics. *Annals of Physics*. 1973;76: 510-548.
97. Mignani R, Recami E, Baldo M. About a Dirac-Like equation for the photon, according to E. Majorana. *Letters to Nuovo Cimento*. 1974;11: 568-572.
98. Newman E. Maxwell equations and complex Minkowski space. *Journal of Mathematical Physics.* 1973;14: 102-107.
99. Frankel T. Maxwell’s equations. *The American Mathematical Monthly*. 1974;81: 343-349.
100. Edmonds J. Comment on the Dirac-Like equation for the photon. *Nuovo Cimento. Letters.* 1975;13: 185-186.
101. Jena P, Naik P, Pradhan T. Photon as the zero-mass limit of DKP field. *J. Phys. A.* 1980;13: 2975-2978.
102. Venuri G. A geometrical formulation of electrodynamics. *Nuovo Cimento. A.* 1981;65: 64-76.
103. Chow T. A Dirac-like equation for the photon. *Journal of Physics. A.* 1981;14: 2173-2174.
104. Fushchich VI, Nikitin AG. *Symmetries of Maxwell's Equations*. Kiev, 1983; Kluwer. Dordrecht. 1987.
105. Cook R. Photon dynamics. *Physical Review. A.* 1982;25: 2164-2167.
106. Cook R. Lorentz covariance of photon Dynamics. *Physical Review. A.* 1982;26: 2754-2760.
107. Giannetto E. A Majorana-Oppenheimer formulation of quantum electrodynamics. *Letters to Nuovo Cimento*. 1985;44: 140-144.
108. Nuez Yépez H, Salas Brito A, Vargas C. Electric and magnetic four-vectors in classical electrodynamics. *Revista Mexicana de Fisica.* 1988;34: 636.

109. Kidd R, Ardini J, Anton A. Evolution of the modern photon. *American Journal of Physics*. 1989;57: 27-35.

110. Recami E. Possible physical meaning of the photon wave-function, according to Ettore Majorana. In: *Hadronic Mechanics and Non-Potential Interactions*. New York: Nova Sc. Pub.; 1990. p.231–238.

111. Hillion P. Spinor electromagnetism in isotropic chiral media. *Advances in Applied Clifford Algebras*. 1993;3: 107-120.

112. Inagaki T. Quantum-mechanical approach to a free photon. *Physical Review. A.* 1994;49: 2839-2843.

113. Sipe J. Photon wave functions. *Physical Review. A.* 1995;52: 1875-1883.

114. Ghose P. Relativistic quantum mechanics of spin-0 and spin-1 bosons. *Foundations of Physics*. 1996;26: 1441-1455.

115. Gersten A. Maxwell equations as the one-photon quantum equation. *Foundations of Physics Letters*. 1998;12: 291-298.

116. Esposito S. Covariant Majorana formulation of electrodynamics. *Foundations of Physics*. 1998;28: 231-244.

117. Torres del Castillo GF, Mercado-Pe’rez J. Three-dimensional formulation of the Maxwell equations for stationary space-times. *Journal of Mathematical Physics*. 1999;40: 2882-1891.

118. Dvoeglazov V. Historical note on relativistic theories of electromagnetism. *Apeiron*. 1998;5: 69-88.

119. Dvoeglazov V. Generalized Maxwell and Weyl equations for massless particles. *Revista Mexicana de Física*. 2003;49: 99-103.

120. Gsponer A. On the "equivalence" of the Maxwell and Dirac equations. *International Journal of Theoretical Physics*. 2002;41: 689-694.

121. Ivezić T. True transformations Relativity and electrodynamics. *Foundations of Physics*. 2001;31: 1139-1183.

122. Ivezić T. The invariant formulation of Special Relativity, or the "true transformations Relativity", and electrodynamics. *Annales de la Fondation Louis de Broglie*. 2002;27: 287-302.

123. Ivezić T. An invariant formulation of Special Relativity, or the true transformations Relativity and comparison with experiments. *Foundations of Physics Letters*. 2002;15: 27-69.

124. Ivezić T. The difference between the standard and the Lorentz transformations of the electric and magnetic fields. Application to Motional EMF. *Foundations of Physics Letters*. 2005;18: 301-324.

125. Ivezić T. Lorentz invariant Majorana formulation of the field equations and Dirac-like equation for the free photon**.** *Electronic Journal of Theoretical Physics*. 2006;3: 131-142.

126. Kravchenko V. On the Relation Between the Maxwell System and the Dirac Equation. *WSEAS Transactions on Systems*. 2002;1(2): 115-118.

127. Varlamov V. About algebraic foundations of Majorana-Oppenheimer quantum electrodynamics and de Broglie-Jordan neutrino. *Theory of Light*. 2003;27: 273-286.

128. Khan S. Maxwell Optics: I. An exact matrix representation of the Maxwell equations in a medium. *Physica Scripta*. 2005;71: 440-442.

129. Macfarlane A. On the restricted Lorentz group and groups homomorphically related to it. *Journal of Mathematical Physics*. 1962;3: 1116-1129.

130. Fedorov FI. *The Lorentz group*. Moscow; 1978.

THE AUTHORS

A.V. Ivashkevich
e-mail: ivashkevich.alina@yandex.by
ORCID: 0000-0002-5029-7901

E.M. Ovsiyuk
e-mail: e.ovsiyuk@mail.ru
ORCID: 0000-0002-7921-7960

V.V. Kisel
e-mail: vasiliy_bspu@mail.ru
ORCID: 0000-0003-4693-4370

V.M. Red'kov
e-mail: v.redkov@ifan.bel.bas-net.by
ORCID: 0000-0001-5318-565X

Materials Physics and Mechanics. 2022;49(1): 44-50
Conference materials
http://dx.doi.org/10.18149/MPM.4912022_3

On resonant scattering states in graphene circular quantum dots

H.V. Grushevskaya, G.G. Krylov✉

Belarusian State University, 4 Nezaleznasti Ave., Minsk, Republic of Belarus

✉ krylov@bsu.by

Abstract. Due to the effect of Klein tunneling, two-dimensional graphene quantum dots do not possess genuine bound states but quasi-bound (resonant tunneling) states only. We discuss in detail the attempt to describe these states within the framework of the Dirac pseudo-fermion model for circular dots. We demonstrate explicitly that introduced earlier the so-called "resonance condition" corresponds to the inconsistent system of linear equations obtained from matching conditions on the boundary of the quantum dot when one tries to use it for complex energy values and in the case of total reflection for the energies coincided with the potential well top.

Keywords: graphene, Klein tunneling, massless pseudo-Dirac fermion, quantum dot, quasi-bound states

***Acknowledgements**. The authors acknowledged the partial support within the projects in "Convergence-2025" and "Energetics" State Programs of the Fundamental Researches of the Republic of Belarus.*

Citation: Grushevskaya HV, Krylov GG. On resonant scattering states in graphene circular quantum dots. *Materials Physics and Mechanics*. 2022;49(1): 44-50. DOI: 10.18149/MPM.4912022_3.

1. Introduction

After more than twenty years of experimental observation, graphene still attracts a lot of attention and attempts to use as a base for super-high-speed electronic devices. The masslessness of graphene carriers in the most popular graphene model, the so-called pseudo-Dirac fermion model, from one side seems to be very attractive due to the high value of the Fermi velocity (of about 10^6 m/s) for the material but failed to artificially form a predefined gap in a band structure needed for transistor-like behavior.

Graphene quantum dots are considered as a variant to find a way of the electric current operation. Experimentally, they can be formed with a few different techniques (see, e.g. [1-3] and references therein). The theoretical description is based usually on the simplest analytically treatable case of circular symmetric quantum dot with radial step potential [4,5] (see also other approaches in [3,6] and references therein).

The specific feature of quantum problems for the 2D massless Dirac equation with the circular symmetric finite height potential barrier is the absence of bound eigenstates. This is stipulated by the fact that solutions of the Dirac radial equation, in a region with a flat potential, are a linear combination of the Bessel functions which asymptotically look like sin and cos; therefore the eigenstates are non-normalizable and correspond to unbound particles.

In the cited references [4] it has been stated the existence of the quasi-bound eigenstates of complex energies, the imaginary part of which corresponds to a level's decay time. The eigenstates were chosen from some sort of a "spectral condition" arisen in consideration. In [4] and [7,8] the deduction of this condition was slightly different, in the first one it has been derived for admissible system eigenstates, in the second paper, the condition was deduced for the scattering problem. In subsequent publications, there were made a lot of experimental work with the result interpretation based on these theoretical predictions [7,9]. Besides a further theoretical analysis of more complicated systems such as bilayer graphene [6], as well as of systems in an electromagnetic field was produced [10-12].

Nevertheless, as we prove with all detail and this is the main goal of the paper, in both cases the statement on the existence of such types of quasi-bound states is erroneous. It appears due to neglecting one of two independent solutions of the corresponding radial Dirac equation when using improper physically ground assumptions.

2. Model

We use 2D massless Dirac fermion model of graphene [13], in tight binding approximation and near the Dirac point excitations, its Hamiltonian operator reads $\hat{H}_0 = \gamma\vec{\sigma}\cdot\vec{k}$ where γ is the band parameter linearly related with the Fermi velocity, $\vec{\sigma} = \{\sigma_x, \sigma_y\}$ is the 2D vector of two Pauli matrixes, $\vec{k}$ is the quasi-momentum. Then, a graphene quantum dot (GQD) can be considered as graphene in some confining potential $V(\vec{r})$. The Hamiltonian reads $\hat{H} = \hat{H}_0 + V(r)$ with a scalar potential incorporated as a diagonal matrix. In the matrix form we have [5]

$$\hat{H} = \begin{pmatrix} V(\vec{r}) & \hat{p}_- \\ \hat{p}_+ & V(\vec{r}) \end{pmatrix} \tag{1}$$

with the operators $\hat{p}_\pm$ given by $\hat{p}_- = -i\frac{\gamma}{\hbar}\frac{\partial}{\partial x} - \frac{\partial}{\partial y}$, $\hat{p}_+ = -i\frac{\gamma}{\hbar}\frac{\partial}{\partial x} + \frac{\partial}{\partial y}$.

As a model GQD we consider a circular quantum dot with a radial step potential, region D is the circle of a radius R,

$$V(\vec{r}) = \begin{cases} 0, \vec{r} \notin D \\ V_0, \vec{r} \in D \end{cases} \tag{2}$$

Due to the system's symmetry, for the eigenproblem $\hat{H}\psi = E\psi$, and the spinor function ψ with components $\psi = (A, B)$, the separation of variables can be achieved in the polar coordinates (ρ, ϕ) introduced via the ordinary relations $x = \rho\cos\phi, y = \rho\sin\phi$. Then, with dimensionless variables $\rho \to \rho / R, \epsilon = RE / \gamma$ we have

$$(V(\rho) - \epsilon)A(\rho,\phi) = -ie^{-i\phi}\left(\frac{\partial B(\rho,\phi)}{\partial\rho} - \frac{i}{\rho}\frac{\partial B(\rho,\phi)}{\partial\phi}\right), \tag{3}$$

$$(V(\rho) - \epsilon)B(\rho,\phi) = -ie^{i\phi}\left(\frac{\partial A(\rho,\phi)}{\partial\rho} + \frac{i}{\rho}\frac{\partial A(\rho,\phi)}{\partial\phi}\right). \tag{4}$$

Substitution

$$\begin{pmatrix} A \\ B \end{pmatrix} = \begin{pmatrix} e^{\imath m\phi}a(\rho) \\ \imath e^{\imath(m+1)\phi}b(\rho) \end{pmatrix}, \tag{5}$$

designation $\xi = \epsilon - V(\rho)$ and account of the fact that ξ is different but constant in both two regions $\rho < 1$ (inner region of the quantum dot) and $\rho > 1$ (outer region), leads to the following system of the radial equations

$$\xi a(\rho) = -b'(\rho) - \frac{(m+1)b(\rho)}{\rho}, \tag{6}$$

$$\xi b(\rho) = a'(\rho) - \frac{ma(\rho)}{\rho}. \tag{7}$$

Since the potential V is step-like flat, expressing $b(\rho)$ from the second equation (7) of the radial system and substituting it into the first one, we get the equation for $a(\rho)$ in the form

$$a(\rho)\left(m^2 - \xi^2\rho^2\right) - \rho\left(\rho a''(\rho) + a'(\rho)\right) = 0, \tag{8}$$

with the general solution given by the superposition of two Bessel functions [15]

$$a(\rho) = c_1 J_m(\rho\,|\,\xi\,|) + c_2 Y_m(\rho\,|\,\xi\,|). \tag{9}$$

The latter can be substituted into equation (7) and one gets

$$b(\rho) = c_1(-J_{m+1}(\rho\,|\,\xi\,|)) - c_2 Y_{m+1}(\rho\,|\,\xi\,|). \tag{10}$$

The boundary condition at $\rho = 0$ for the radial system demands the finiteness of the solution so that one has to omit the second term in (10) as the function Y_m is singular at zero. Outside the quantum dot ($\rho > 1$) one has to use both functions in the solution. The only requirement left is the continuity of the eigenfunctions at the boundary $\rho = 1$ of the quantum dot. The important point of the problem is that the eigenfunctions can not belong to the bound state because, independent of the potential values in both regions, all the Bessel functions asymptotically at infinity ($\rho \to \infty$) trend to plane waves and therefore they are non-normalizable.

Let us designate the coefficients c in the solution by additional upper indexes i and o for the inside region and outside one of the quantum dots respectively. Matching solutions for both spinor components at $\rho = 1$ and choosing the normalization constant in the interior region with $c_1^i = 1$ (due to the equation linearity one can choose an arbitrary normalization) we get the following linear system for the determination of the coefficients

$$J_m(|V_0 - \epsilon|) = c_1^o J_m(|\epsilon|) + c_2^o Y_m(|\epsilon|), \tag{11}$$

$$-J_{m+1}(|V_0 - \epsilon|) = c_1^o(-J_{m+1}(|\epsilon|)) - c_2^o Y_{m+1}(|\epsilon|). \tag{12}$$

It can be shown that the determinant of the matrix of this linear system is given by the formula

$$J_{m+1}(|\epsilon|)Y_m(|\epsilon|) - J_m(|\epsilon|)Y_{m+1}(|\epsilon|), \tag{13}$$

it does not depend on V_0 and is non-zero for all real values of m, and ϵ (see e.g., the energy dependence for $m = 0$ in Fig. 1).

It means that we get the real-value solution of the eigenproblem which is continuous in the space. As an example, both spinor components of the solution are shown in Fig. 2 for $V_0 = 3,\ m = 0,\ \epsilon = 0.09$.

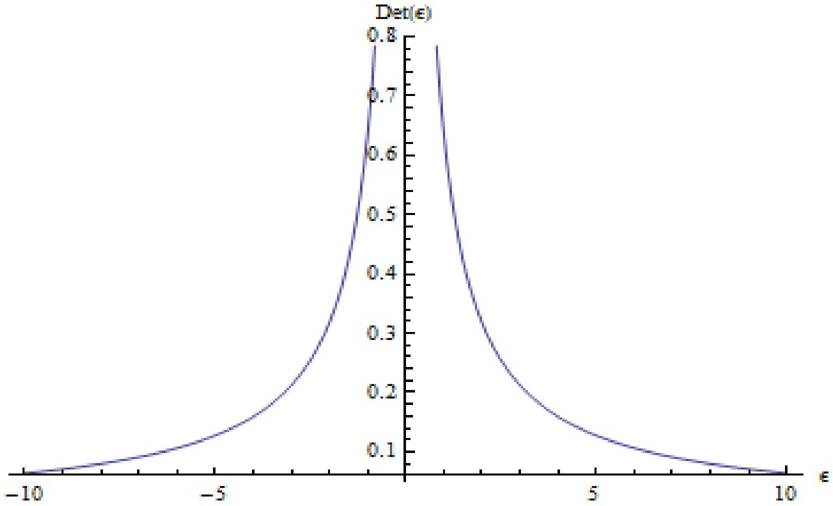

Fig. 1. Dependence of the determinant on energy for $m = 0$

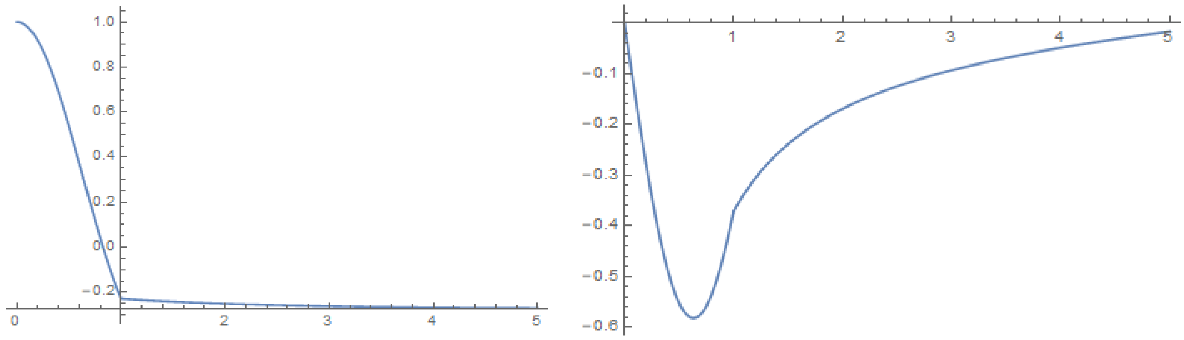

Fig. 2. Upper and lower components of the spinor eigenfunction for $m = 0$, $\epsilon = 0.09$, $V_0 = 3$

Of course, instead of the Bessel functions J_m, Y_m one can use the Hankel functions of the first and second kind $H_m^{(k)}(z) = J_m(z) \pm \imath Y_m(z), k = 1,2$ for the outer region as it has been done in [5] resulting in complex coefficients. However, all eigenfunctions are functions of a real variable and belong to a continuous spectrum. The authors of [5] put the additional requirement that the eigenfunction should asymptotically behave as $\exp\{\imath \,|\, \xi \,|\, r\}$. From the physical point of view, it means that one fixes the phase of the exponential function because a linear combination of the Bessel (or Hankel) functions asymptotically can be represented as $\mathrm{Re}(a \exp\{i(kr + \phi)\})$. This additional restriction leads to the specific condition which was stated in [5] as a "spectral condition"

$$J_{m+1}(|\,\epsilon - V_0\,|) H_m^{(1)}(|\,\epsilon\,|) - J_m(|\,\epsilon - V_0\,|) H_{m+1}^{(1)}(|\,\epsilon\,|) = 0\,. \tag{14}$$

This equation has no real solutions for ϵ, except of those for $m > 1, \epsilon = 0$, but has complex ones which were interpreted in [5] as quasi-bound states with a finite lifetime.

As we intend to demonstrate condition (14) is meaningless because corresponds to an inconsistent system of linear equations followed by the matching conditions at the quantum dot boundary $\rho = 1$. With this in mind, we follow the "scattering scheme" of [7,8] to obtain the matching condition system. For the radial scattering problem inside the GQD, the solution consists of the transient wave and still is described by the Bessel J function with some amplitude $tJ_m(|\,\xi\,|\,r)$ (e.g., for the upper component, letter t is used for transmission coefficient).

The solution outside the GQD is a superposition of two Hankel functions describing the incident and scattered waves, that is $H_m^{(1)}(\epsilon)+rH_m^{(2)}(\epsilon)$ again for the upper component (with "r" letter to designate the reflection coefficient). Then the matching system reads

$$tJ_m(|V0-\epsilon|)-rH_m^{(1)}(|\epsilon|)-H_m^{(2)}(|\epsilon|)=0\,, \tag{15}$$

$$-tJ_{m+1}(|V0-\epsilon|)+rH_{m+1}^{(1)}(|\epsilon|)+H_{m+1}^{(2)}(|\epsilon|)=0\,. \tag{16}$$

Precisely, the determinant of this system is just the left hand side of condition (14). So, our goal is to construct the system in the vicinity of the vanishing determinant. First, we do it for the energy values $\epsilon = V_0$ corresponding to the top of the potential well. The determinant of the matrix, in this case, vanishes due to the properties of Bessel J functions at zero argument. But we apply this energy value directly to the system to get

$$t\times 0-rH_m^{(1)}(|V_0|)-H_m^{(2)}(|V_0|)=0\,, \tag{17}$$

$$-t\times 0+rH_{m+1}^{(1)}(|V_0|)+H_{m+1}^{(2)}(|V_0|)=0\,. \tag{18}$$

The latter means that the reflection coefficient has to be expressed as a ratio ($r = H_m^{(1)}(|V_0|)/H_m^{(2)}(|V_0|)$) of Hankel functions but with the orders differ on "one" for the first and the second equations. Taking into account the fact that the Hankel functions of the first and second kind at a given value of the argument are the conjugated complex numbers, the reflection coefficient as their ratio turns out to be unimodal. But the equality of it for both equations can be only approximately satisfied in an asymptotic regime and for small and intermediate values of the confining potential. For example, we represent in Fig. 3 the value $\mathrm{R}_{\mathrm{arg}}=\arg\left(\dfrac{H_{20}^{(1)}(x)}{H_{20}^{(2)}(x)}\right)/\arg\left(\dfrac{H_{21}^{(1)}(x)}{H_{21}^{(2)}(x)}\right)$ as a function of the potential height V_0 to confirm our statement.

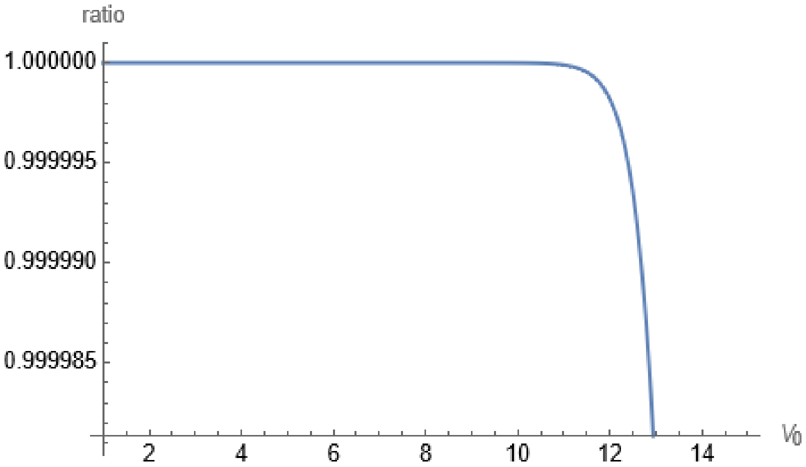

Fig. 3. Dependence of $\mathrm{R}_{\mathrm{arg}}$ on the confining potential height V_0. The region with an approximate unity value of the ratio corresponds to the total reflection case

The last regime corresponds to the same amplitudes for the reflected wave as an incident one with only a phase shift and therefore to zero value for the transmitted wave. The latter means the total wave reflection that hardly is considered as "a bound state" as was stated in [5,6].

Now, we try to understand what happens near the non-trivial complex roots of equation (14) when the energy does not coincide with the well height. We choose the following parameters: $V_0 = 20, m = 0$ and find one of the roots of eqs. (17-18) in the vicinity of point $\epsilon = 3$. This gives $\epsilon = 3.95744 - 1.47721I$. Substitution of this value into the matching condition system and normalization of both equations to make coefficients at variable t equal to unity gives

$$1.t - (1.01973 + 0.160047\,\mathrm{I})r = -0.0390394 + 0.0318167\,\mathrm{I}, \tag{19}$$

$$1.t - (1.01973 + 0.160047\,\mathrm{I})r = 0.0409105 - 0.0408179\,\mathrm{I}. \tag{20}$$

As one can see, indeed the determinant of the system vanishes (since left-hand sides of both equations coincide). This means that we really have a root of the "resonance condition" but the right-hand sides are different for both equations. The latter shows that the system is inconsistent and there are no solutions at all in this case. A similar situation holds for other roots too.

3. Conclusion

We explicitly demonstrated that the "resonance condition", introduced in [5] to construct "quasi-bound" states for GQD with a finite lifetime, leads to the inconsistent system of linear equations describing matching conditions for the solution inside and outside GQD. Therefore it can not be considered valid for any application. We also demonstrated that the "exact localization of electron in the quantum dot" considered in [6] and confirmed in [5] in fact can be approximately the case of the total reflection of an electron on a graphene quantum dot at asymptotically high values of magnetic quantum number m and not the very high value of the confining potential (whispering gallery modes).

References

1. Freitag NM, Chizhova LA, Nemes-Incze P, Woods CR, Gorbachev RV, Cao Y, Geim AK, Novoselov KS, Burgdörfer J, Libisch F, Morgenstern M. Electrostatically confined monolayer graphene quantum dots with orbital and valley splittings. *Nano Letters*. 2016;16(9): 5798.

2. Lee J, Wong D, Velasco jr J, Rodriguez-Nieva JF, Kahn S, Tsai H-Z, Taniguchi T, Watanabe K, Zettl A, Wang F, Levitov LS, Crommie MF. Imaging electrostatically confined Dirac fermions in graphene quantum dots. *Nature Physics*. 2016;12: 1032.

3. Grushevskaya HV, Krylov GG, Kruchinin SP, Vlahovic B, Bellucci Stefano, Electronic properties and quasi-zero-energy states of graphene quantum dots. *Physical Review B*. 2021;103: 235102.

4. Hewageegana P, Apalkov V. Electron localization in graphene quantum dots. *Physical Review B*. 2008;77(24): 245426.

5. Hewageegana P, Apalkov V. Trapping of an electron in coupled quantum dots in graphene. *Physical Review B*. 2009;79(11): 115418.

6. Matulis A, Peeters FM. Quasibound states of quantum dots in single and bilayer graphene. *Physical Review B*. 2008;77:(11) 115423.

7. Gutiérrez Ch, Brown L, Kim Cheol-Joo, Park Jiwoong, Pasupathy AN. Klein tunnelling and electront rapping in nanometre-scale graphene quantum dots. *Nature Physics*. 2016. 12;1069–1075.

8. Gutiérrez C, Brown L, Kim Cheol-Joo, Park Jiwoong, Pasupath AN. Correction notice: Klein tunnelling and electron trapping in nanometre-scale graphene quantum dots. *Nature Physics*. 2016;12: 1069-1075.

9. Fu ZQ, Bai KK, Ren YN, Zhou JJ, He L. Breaking whispering-gallery modes of massless Dirac fermions in graphene quantum dots by Coulomb interaction. *Physical Review B*. 2020;10(23)1: 235310.

10. Recher P, Nilsson J, Burkard G, Trauzettel B. Bound states and magnetic field induced valley splitting in gate-tunable graphene quantum dots. *Physical Review B*. 2009;79(8): 085407.
11. Rossi E, Bardarson JH, Brouwer PW, Das Sarma S. Signatures of Klein tunneling in disordered graphene p-n-p junctions. *Physical Review B*. 2008;81: 121408R.
12. Xiong YJ, Xiong BK. Resonant transport through graphene nanoribbon quantum dots. *Journal of Applied Physics*. 2011;109(10): 103707.
13. Castro Neto AH, Guinea F, Peres NMR, Novoselov KS, Geim AK. The electronic properties of graphene. *Reviews of Modern Physics*. 2009;81(1): 109.
14. Abramowitz M, Stegun IA. (Eds.) *Handbook of Mathematical Functions.* Dover, New York; 1965.

THE AUTHORS

H.V. Grushevskaya
e-mail: grushvskaja@bsu.by
ORCID: 0000-0002-9527-9328

G.G. Krylov
e-mail: krylov@bsu.by
ORCID: 0000-0002-5299-9157

Materials Physics and Mechanics. 2022;49(1): 51-72
Conference materials
http://dx.doi.org/10.18149/MPM.4912022_4

Nucleation and growth of fullerenes and nanotubes having five-fold symmetry

A.I. Melker✉**, M.A. Krupina, A.N. Matvienko**

Peter the Great St. Petersburg Polytechnic University Polytekhnicheskaya 29, 195251, St. Petersburg, Russia

✉ ndtcs@inbox.ru

Abstract. We have studied possible ways of generating and growing the fullerenes having five-fold symmetry. Beginning with cyclopentane C_5H_{10} and clusters C_5C_5, we obtained elementary fullerenes C_{10} and mini-fullerenes C_{20}, and then we produced the fullerenes from C_{20} to C_{70}, perfect (basic) and imperfect, as well as nanotubes. The basic fullerenes C_{20}, C_{30}, C_{40}, C_{50}, C_{60}, and C_{70} have the ordinary five-fold symmetry, the intermediate ones having no such symmetry. Their imperfection is connected with extra 'interstitial' carbon dimers, the dimers playing the role of defects. One can define the imperfect fullerenes with defects as the fullerenes having topological five-fold symmetry. We have calculated the energies of both groups of fullerenes and discussed their dependence on a fullerene size and shape.

Keywords: carbon, embedding, energy, fullerene, fusion reaction, graph representation, growth, nanotube, periodic system, single and double bonds, topological symmetry

***Acknowledgements**. No external funding was received for this study.*

Citation: Melker AI, Krupina MA, Matvienko AN. Nucleation and growth of fullerenes and nanotubes having five-fold symmetry. *Materials Physics and Mechanics*. 2022;49(1): 51-72. DOI: 10.18149/MPM.4912022_4.

1. Introduction

In our early investigations we have tried, as most investigators, to study some popular fullerenes, e.g. C_{20}, C_{24}, $C_{36,}$ C_{60}, and C_{70}, to calculate their energy and to do some conclusions about their stability and other properties. However, with the passage of time, we came to the conclusion that such a style of investigation leads to a dead end. The reason is that these fullerenes have different symmetry and belong to different columns of the periodic table of fullerenes suggested in [1,2]. Moreover, in those cases the main rule of an experiment is violated: the data must be obtained and compared, all other things or factors being equal or the same. It should be emphasized that numerical calculations are not a theory, but a kind of numerical experiment [3]. So such calculations in many cases only increase information entropy [4].

Consequently, there is little sense in doing calculations for the sake of calculations, but at first, one needs to develop a plan and a mathematical model of calculations. It should be pointed out that the mathematical model is meant not a computational method employed, but the interplay between physical processes expressed through mathematics. The first stage of creating any mathematical model is the formulation of the laws that connect the main objects of the model [5]. In our case the main objects are perfect basic fullerenes; we have also the law in the form of the periodic table, but we do not know the structure of all the main objects.

Publisher: Peter the Great St. Petersburg Polytechnic University

Besides, not all the perfect fullerenes, the structure of which is known, are incorporated into the established periodic system. Therefore, it seems reasonable to carry out such studying that allows obtaining the structure of missing fullerenes, with the purpose to incorporate the missing unknown fullerenes in the periodic table, and only afterward to do conclusions, bearing in mind that all the factors being equal or the same.

The periodic table of fullerenes [1,2] consists of horizontal series and vertical columns (groups); they include basic perfect fullerenes from C_{14} to C_{96}. The horizontal series form the Δn periodicities, where the fullerene structure changes from three-fold symmetry to six-fold through four and five ones. The vertical columns include the fullerenes of one and the same symmetry, the mass difference Δm for each column being equal to a double degree of symmetry. We declare that the periodic system must be taken as a base for rigorous fullerene classification. The system leaves room for incorporating into it other fullerene families.

In this contribution, we have studied the nucleation and growth of the fullerenes referring to the column of five-fold symmetry. Similar investigations were done earlier for fullerenes of three-fold [6] and four-fold symmetry [7].

2. Embryos, clusters, folding, fusion, and formation of fullerenes and nanotubes

We assume that the embryo of fullerenes of five-fold symmetry is cyclopentane C_5H_{10} with D_{5h} symmetry [8]. Suppose that we have removed ten hydrogen atoms and added five carbon atoms instead. In doing so we obtain carbon cluster C_5C_5 with several types of carbon atoms. They are shown, together with cyclopentane C_5H_{10}, in Fig. 1. We have calculated the optimized structures and energy of these compounds as well as of the succeeding ones through the use of Avogadro package [9]. The carbon atoms of cyclopentane remain in the initial electronic state; they are considered, as is customary, to be sp^2 hybridized atoms. The newly added ones are reactive carbon atoms; they are connected with the initial carbon atoms by single or double bonds, being ionized to a different degree. The further cluster evolution is folding and forming a penta-angular prism (Fig. 2).

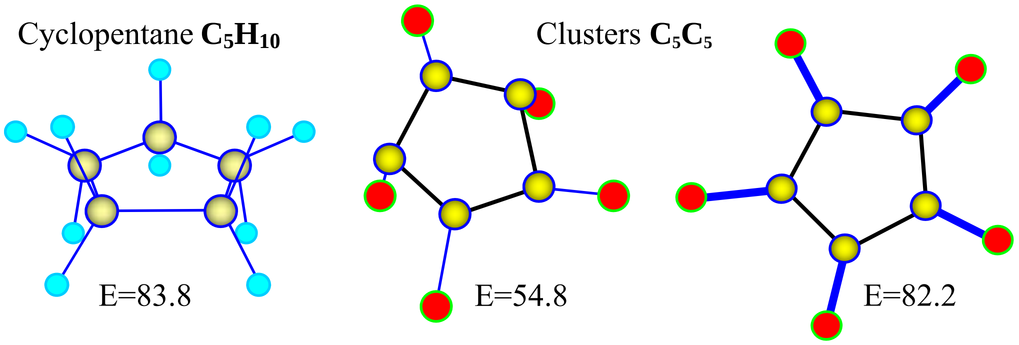

Fig. 1 Cyclopentane and two carbon clusters of five-fold symmetry; energy in kJ/mol

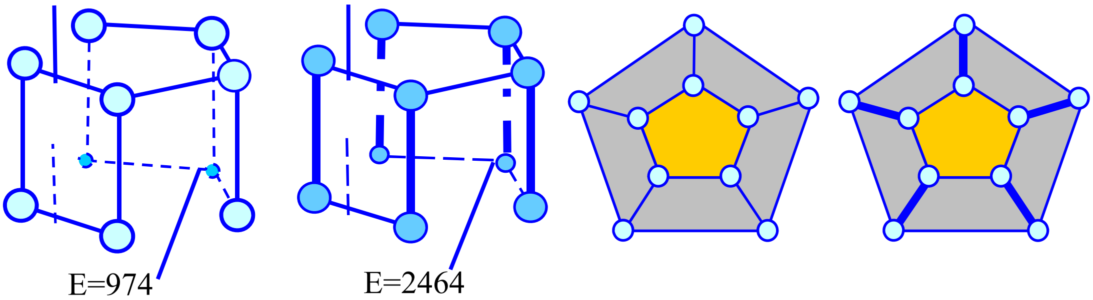

Fig. 2. Folding the clusters into pentagonal prisms: structure and graphs; energy in kJ/mol

Consider cluster folding more closely. The process produces the elementary fullerene of five-fold symmetry which is a pentagonal prism. Two extreme electronic configurations are presented in Fig. 2. In addition to the structures, the graphs of prisms are shown. Here and below we use area-colored graphs because they gain a better understanding of the structures obtained. In our case all the side faces of prisms are tetragons and they are grey painted in graphs; the upper faces are pentagons and they are painted in goldish; the bottom faces are indicated by the external boundaries.

The elementary fullerenes can grow, conserving their symmetry, by the mechanism known as the "fusion of fullerenes having compatible symmetry" [10]. The final structure produced by the fusion of two prisms is shown in Fig. 3. The shape of the fullerene is a dodecahedron. It is one of five regular polyhedrons that Plato (427-347 BC) referred to as ether. It enters into the family of barrel-shaped fullerenes, so-called "mini-fullerenes".

In its turn this fullerene can continue growing and conserve the symmetry, only through the use of the above-mentioned mechanism, i.e. joining another prism (Fig. 4). The reaction is possible since the reacting structures have five-fold symmetry and therefore they are compatible with each other. The subsequent fusion of the fullerenes is presented in Fig. 5. The hexagons in the graphs are painted in yellow.

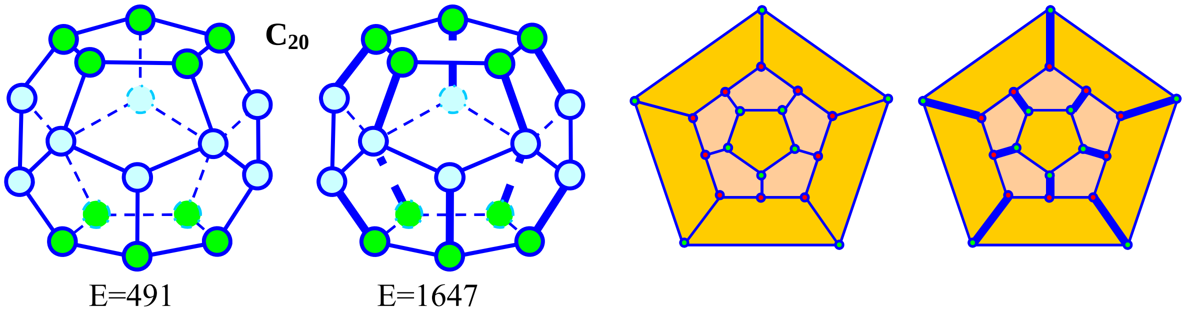

Fig. 3. Dodecahedron C_{20} as a result of prisms fusion; its graphs and energy in kJ/mol

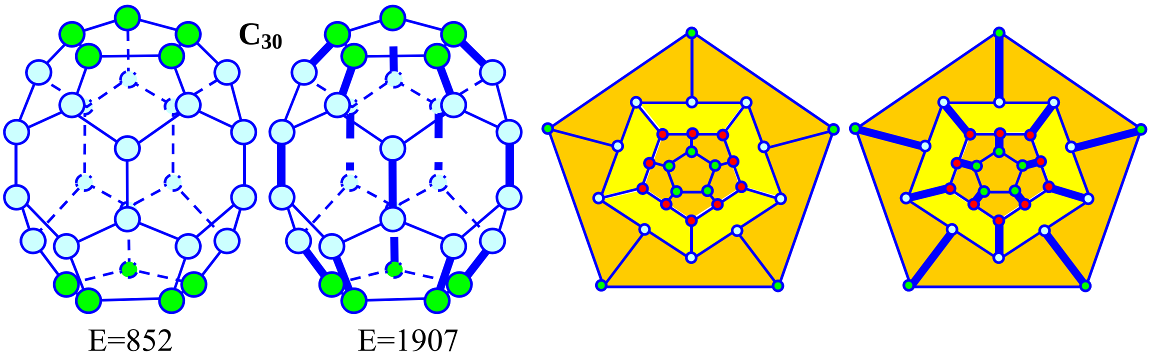

Fig. 4. Joining dodecahedron to a prism; structure, graphs, and energy in kJ/mol

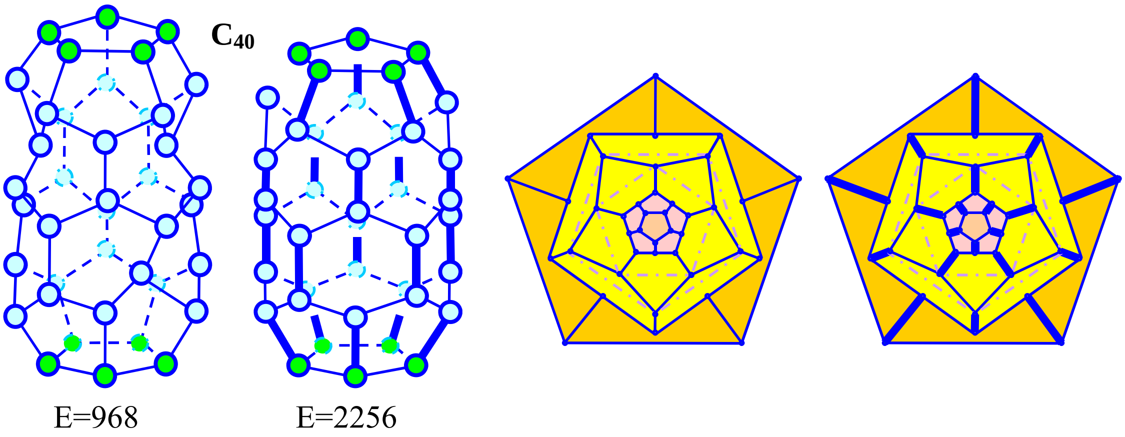

Fig. 5. Joining two dodecahedrons; structure and graphs; energy in kJ/mol

3. Cupolas and their fusion

Another way of looking at the gradual evolution of the clusters shown is the growth of initial clusters which then transform into half-fullerenes (cupolas) conserving the five-fold symmetry (Fig. 6). From the figures it is seen that all the cupolas have one and the same base of ten atoms; therefore they can combine with each other creating new fullerenes as well as nanotubes. Let us investigate this process in detail.

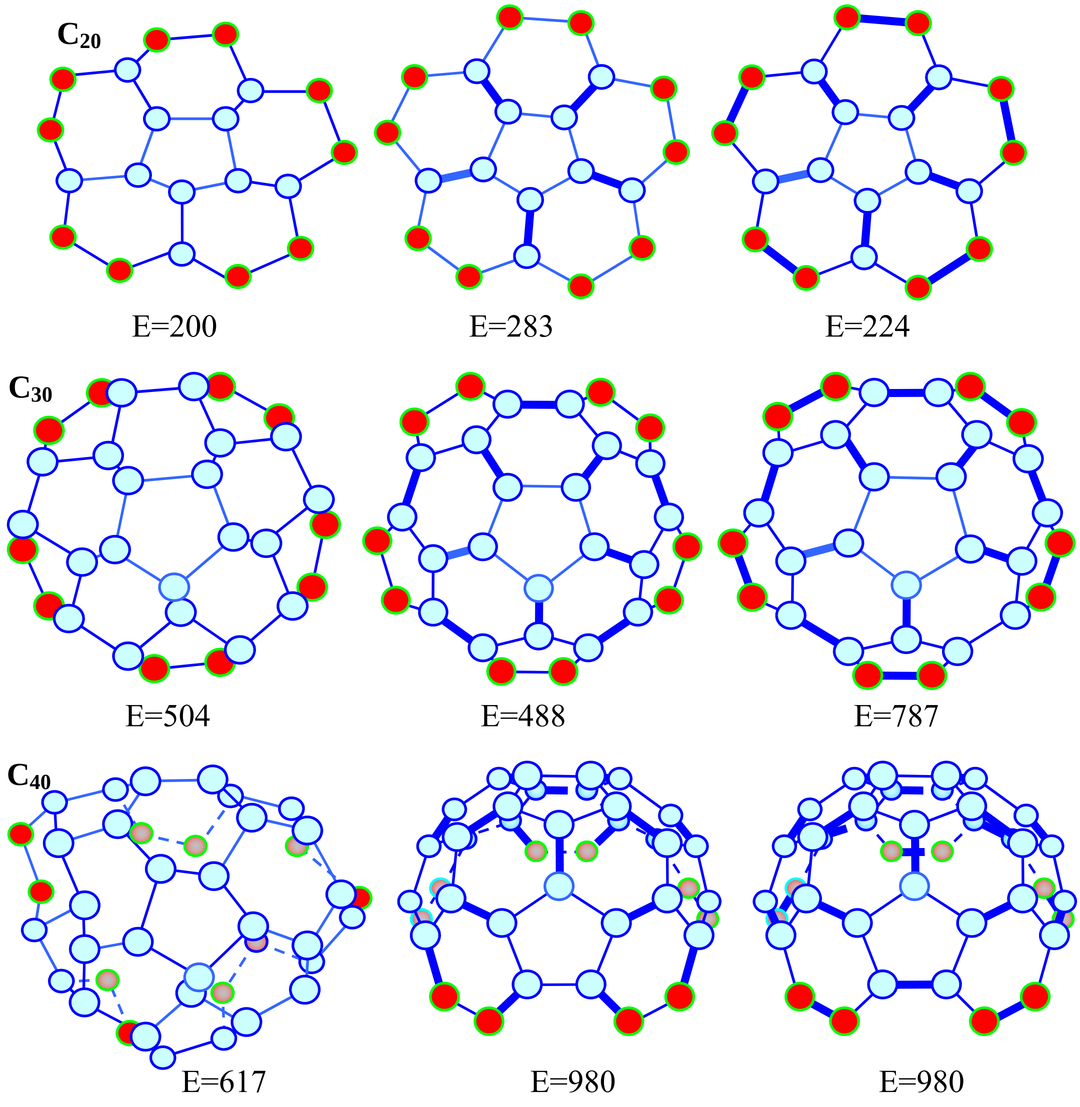

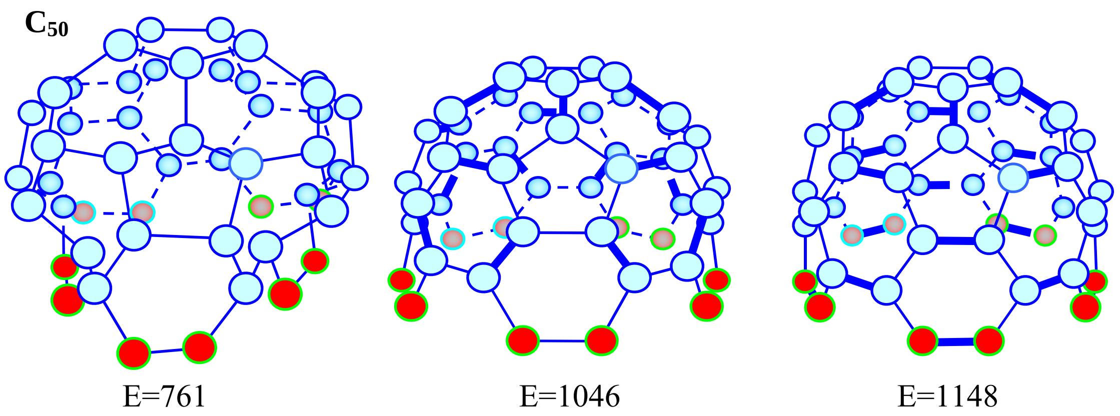

Fig. 6. Growth of cupolas of five-fold symmetry: structure and graphs; energy in kJ/mol

Fusion of cluster C_{10} with cupola C_{20}. Here both initial configurations have five-fold symmetry. The fullerene obtained consists of five tetragons, two pentagons, and ten hexagons; it contains seventeen faces. One may name this perfect isomer, having five-fold symmetry, a truncated five-angular bipyramid (Fig. 7).

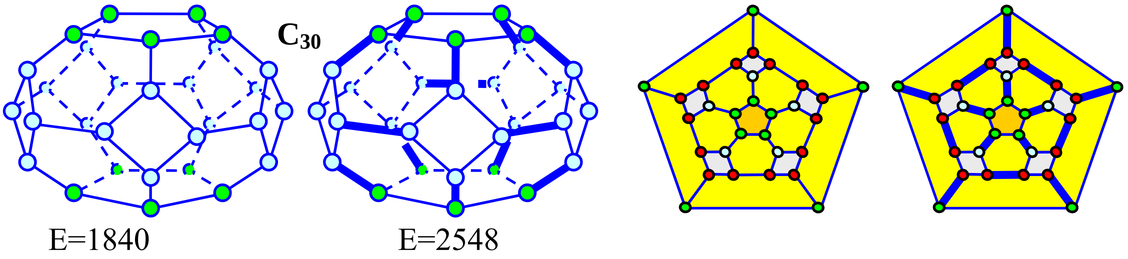

Fig. 7. Truncated five-angular bipyramid C_{30} and its graphs; energy in kJ/mol

Fusion of two cupolas C_{20}. There are two ways of joining: mirror symmetry and rotation-reflection. In the first case (Fig. 8) the lower cupola is a mirror copy of the upper one. The fullerene obtained consists of five tetragons, two pentagons, and fifteen hexagons, and has twenty-two faces. In the second case (Fig. 9) the lower cupola is a rotatory reflection of the upper one. The fullerene obtained contains twelve pentagons and ten hexagons, the number of faces being the same. Its energy is less than that of the first fullerene.

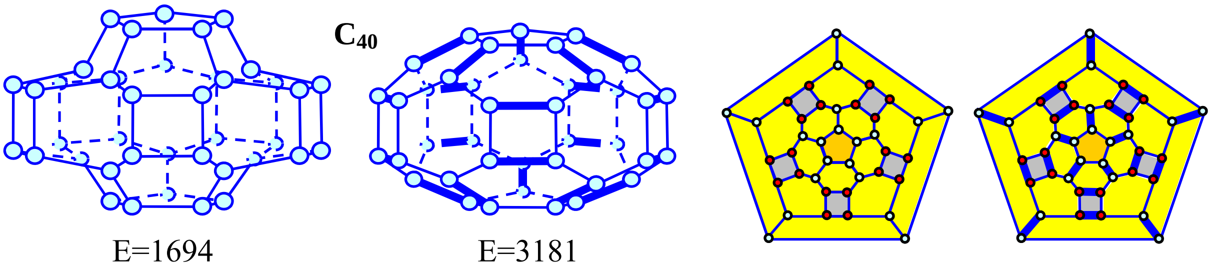

Fig. 8. Joining two cupolas C_{20} of five-fold symmetry: the mirror symmetry fusion, structure and graphs; energy in kJ/mol

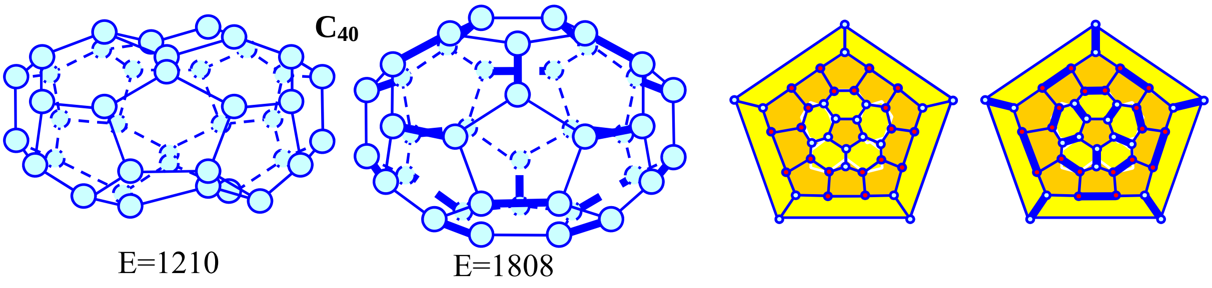

Fig. 9. Joining two cupolas C_{20} of five-fold symmetry: the rotation-reflection symmetry fusion, structure, and graphs; energy in kJ/mol

Fusion of two cupolas: C_{20} and C_{30} (Fig. 10). The atomic structure corresponding to a perfect polyhedron consists of two isolated pentagons, five sets of adjacent pentagons, and fifteen hexagons, so it can be named a penta$_{12}$-hexa$_{15}$ polyhedron.

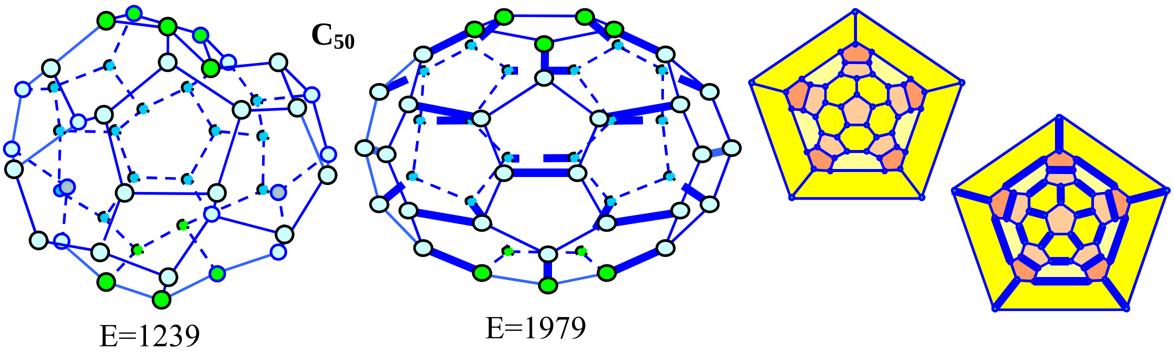

Fig. 10. Mirror symmetry fusion of two cupolas (half-fullerenes) C_{20} and C_{30} of five-fold symmetry; structure and graphs; energy in kJ/mol

Fusion of two cupolas C_{30} (Fig. 11). The atomic structure corresponding to a perfect polyhedron is a truncated icosahedron, which consists of twelve isolated pentagons and twenty adjacent hexagons. It is the most abundant and most celebrated fullerene molecule.

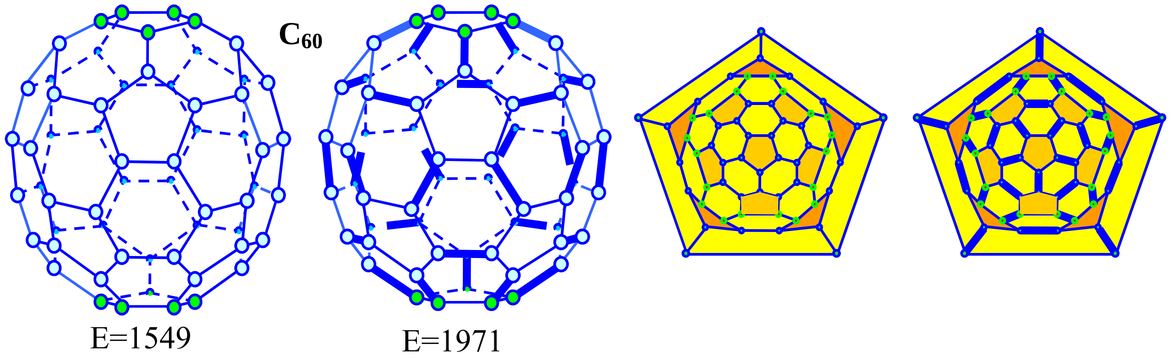

Fig. 11. Joining two cupolas C_{30} of five-fold symmetry: the rotation-reflection symmetry fusion, structure, and graphs; energy in kJ/mol

Fusion of two cupolas: C_{30} and C_{40} (Fig. 12). The atomic structure corresponding to a perfect polyhedron consists of twelve isolated pentagons, as before, and twenty-five adjacent hexagons. Beyond C_{60}, it is the next most abundant fullerene observed in the condensed carbon vapor.

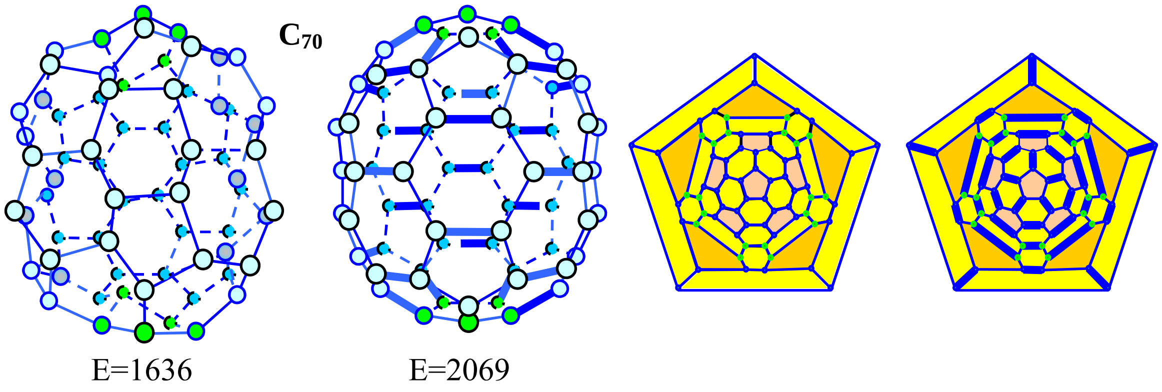

Fig. 12. Mirror symmetry fusion of two cupolas C_{30} and C_{40} of five-fold symmetry; structure and graphs; energy in kJ/mol

Fusion of two cupolas C_{40} (Fig. 13). It is a cigar-shaped molecule giving the beginning of the family of single-wall nanotubes (SWNT).

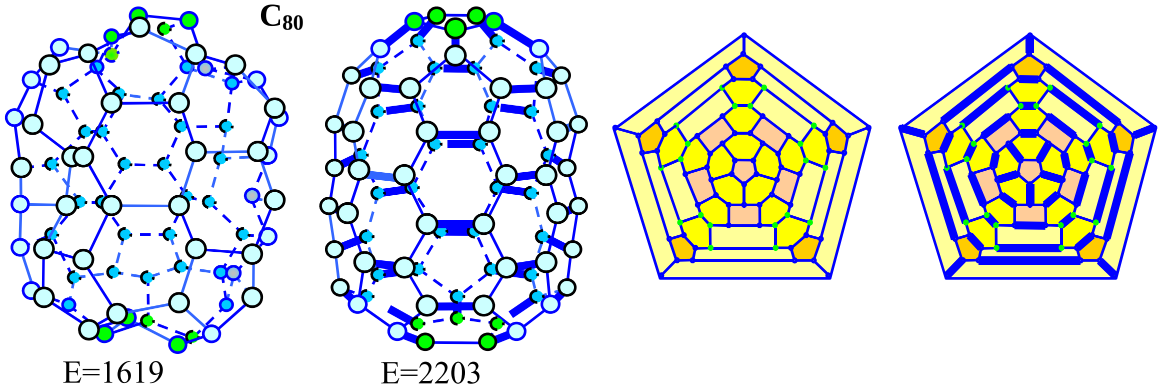

Fig. 13. Rotation-reflection-symmetry joining of two cupolas C_{40} of five-fold symmetry; structure and graphs; energy in kJ/mol

Fusion of two cupolas: C_{40} and C_{50}. The next in the column of five-fold symmetry is C_{90}, which atomic structure is shown in Fig. 14.

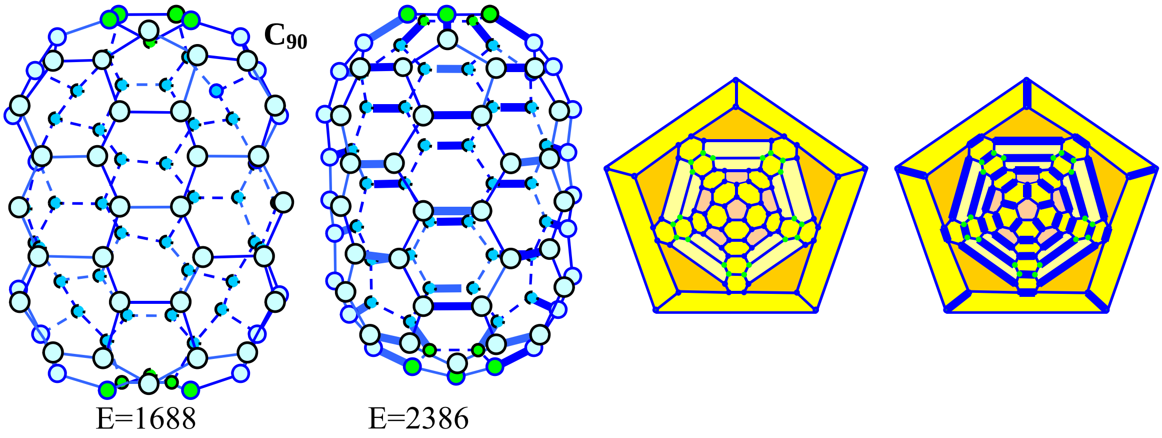

Fig. 14. Mirror symmetry fusion of two cupolas C_{40} and C_{50} of five-fold symmetry; structure and graphs; energy in kJ/mol

Let us analyze Figures 7-14. Hand in hand with different fullerenes of the five-fold symmetry, we have obtained two of the most abundant fullerene molecules C_{60} and C_{70} through the use of the cupola-fusion mechanism. Buckminsterfullerene C_{60}–I_h is a truncated icosahedron [11]. This fullerene is considered an ideal one, having only equal isolated pentagons and forming a perfect sphere; each hexagon has three single and three double bonds. The measured bond lengths are r_{hh} = 1.38 Å and r_{hp} = 1.4654 Å. The larger bonds are singular, the lesser bonds are double ones. However, the formation mechanism, and especially the high yield of C_{60}–I_h and C_{70}–D_{5h}, remains elusive and somewhat controversial.

In 2002 we have suggested and confirmed, through the use of molecular dynamics calculations, the fusion reaction mechanism of joining two hemispheres C_{30} for obtaining fullerene C_{60} [12]. This approach has succeeded in further development, at last leading to designing the periodic system of fullerenes [1,2]. According to the system, fullerene C_{60} belongs to the Δn=12 series, the five-fold symmetry column, and has a lower formation energy than any of its nearest neighbors.

4. Intermediate fullerenes

Growth of fullerene C_{30}. The polyhedron shown in Fig. 4 can be thought of as a primary fullerene having the possibility to use for growing the mechanism known as "embedding carbon dimers" which was suggested by M. Endo and the Nobel Prize winner H.W. Kroto in 1992 [13]. According to it, a carbon dimer embeds into a hexagon of an initial fullerene. This leads to stretching and breaking the covalent bonds which are normal to the dimer and to create new bonds with the dimer. As a result, there arises a new atomic configuration and there is a mass increase of two carbon atoms. The fullerenes designed through the use of the Endo-Kroto mechanism are illustrated in Fig. 15.

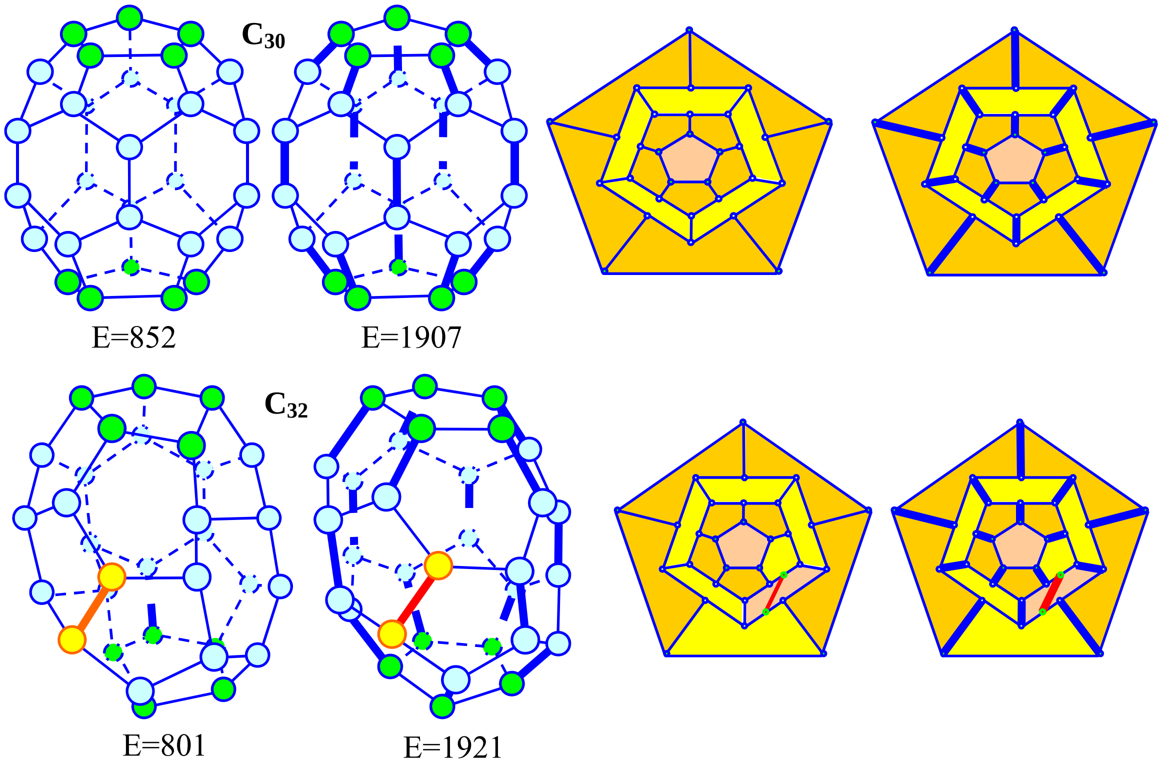

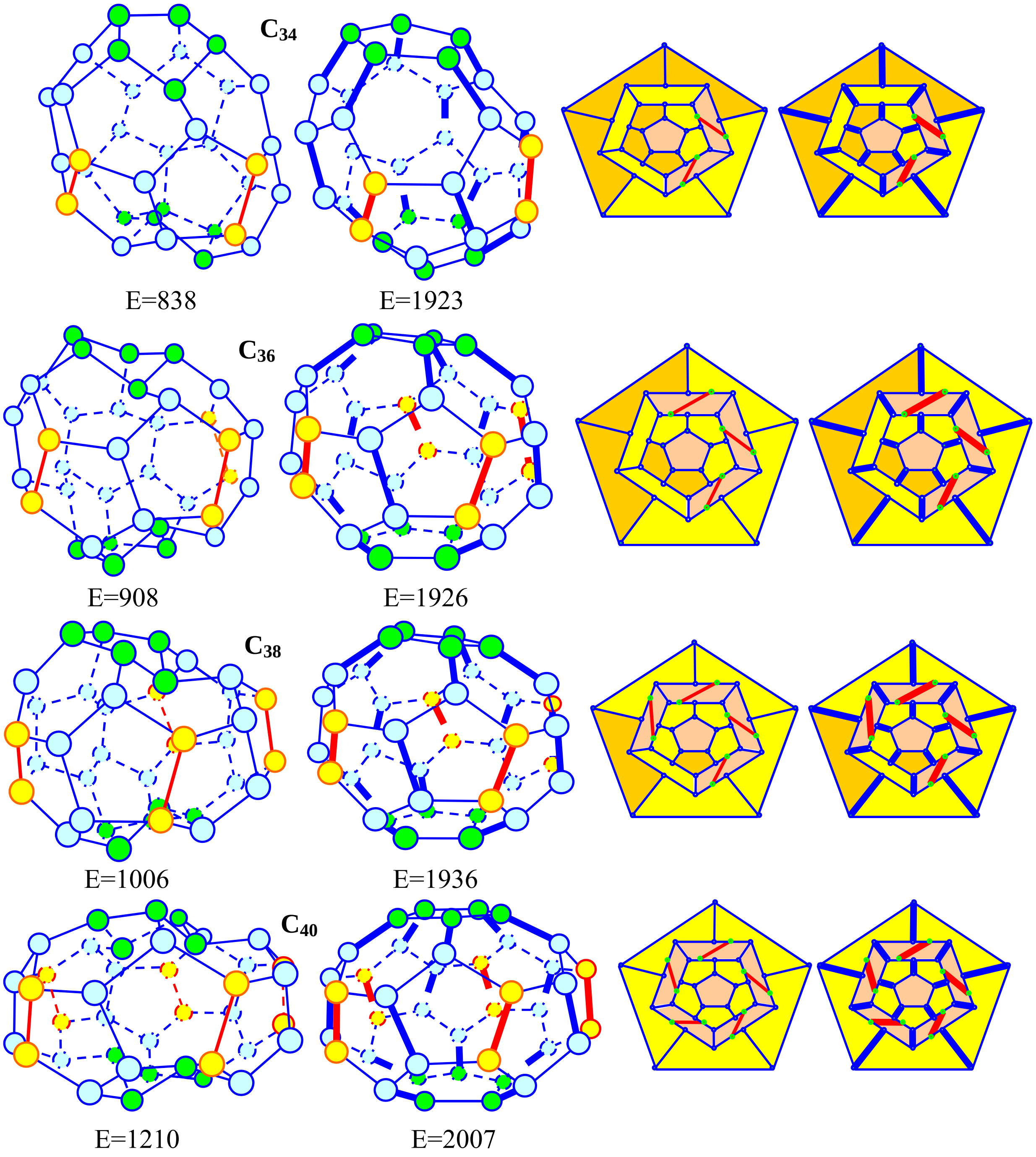

Fig. 15. Fullerenes C_{32}, C_{34}, C_{36}, C_{38}, and C_{40} were obtained one after another by embedding a carbon dimer (yellow atoms) into fullerene C_{30}: structure and graphs; energy in kJ/mol

Growth of fullerene C_{40}.

First cycle. The fullerenes designed through the use of Endo-Kroto's mechanism of dimer embedding into a hexagon are illustrated in Fig. 16. Taking as a base the structure and graph of fullerene C_{40}, we have obtained the fullerenes from C_{42} to C_{50} one after another embedding a carbon dimer (yellow atoms) into fullerene C_{40}.

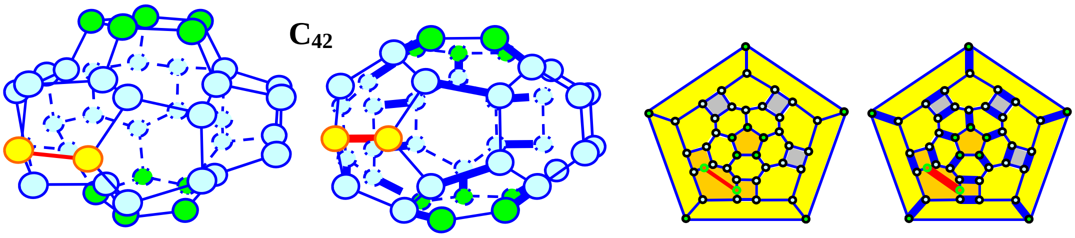

C_{42}

E=1372 E=2755

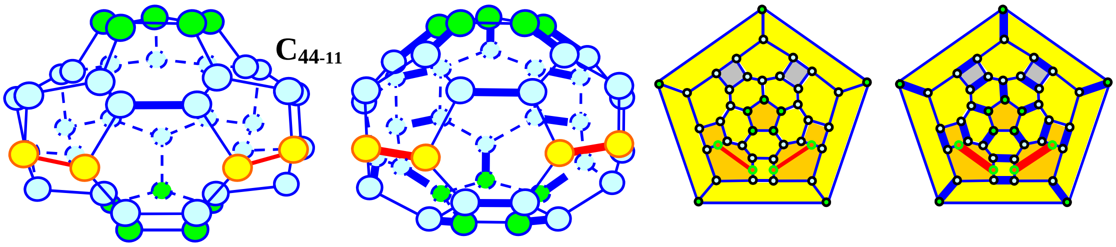

C_{44-11}

E=1243 E=2591

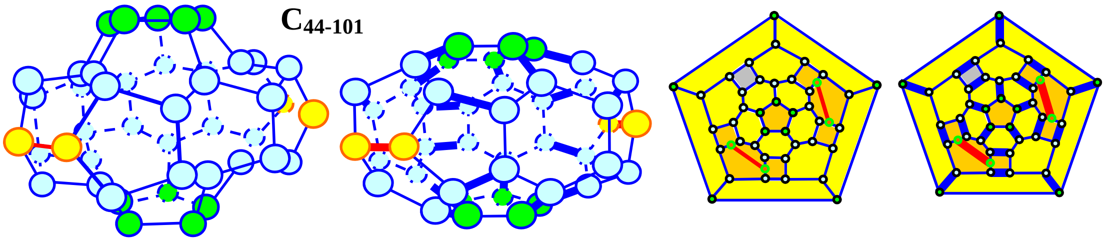

C_{44-101}

E=1070 E=1798

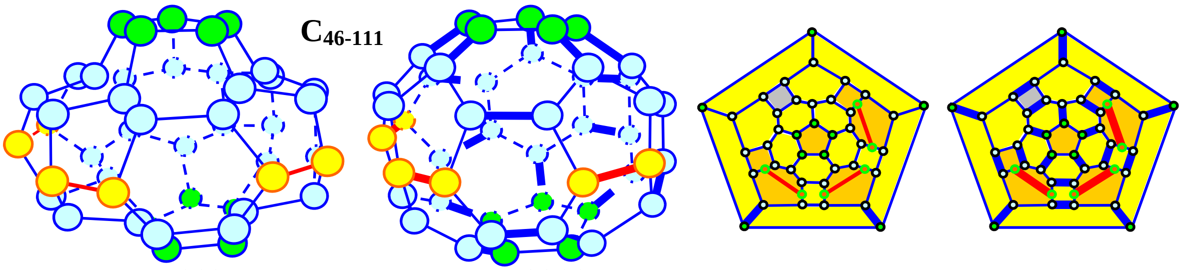

C_{46-111}

E=1137 E=2311

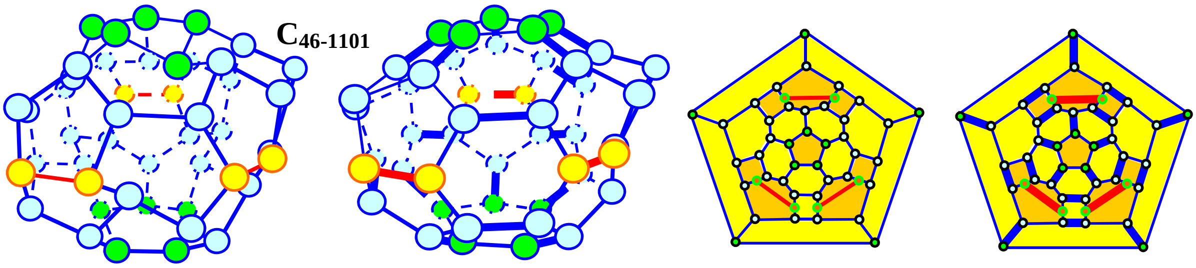

$C_{46-1101}$

E=1029 E=1775

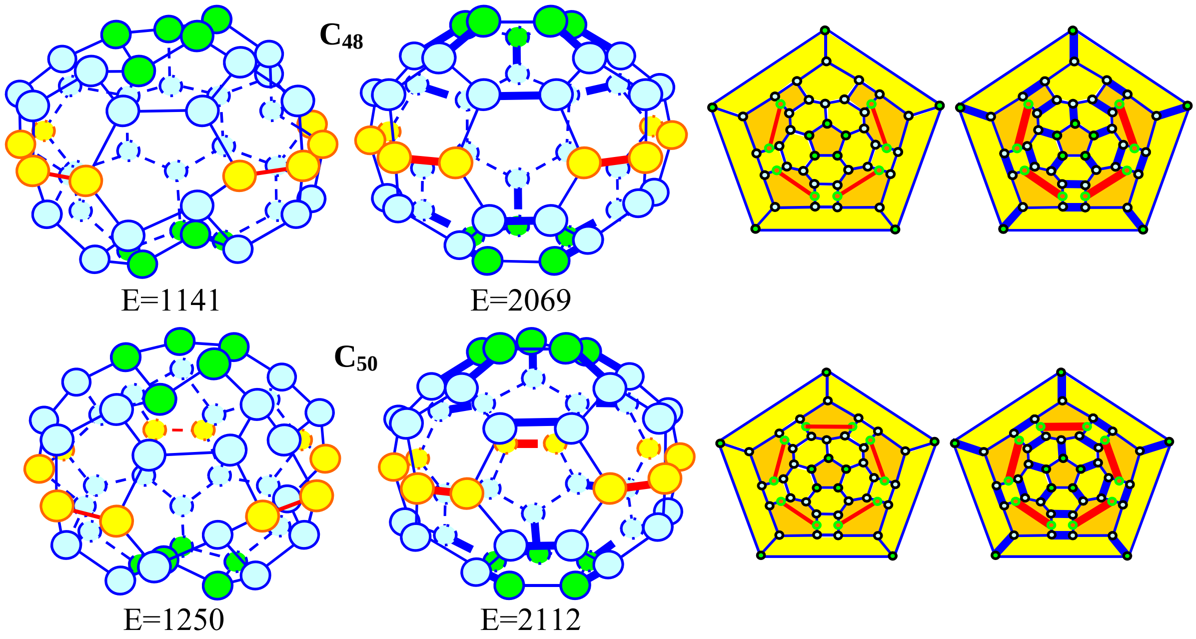

Fig. 16. Fullerenes C_{42}, C_{44}, C_{46}, C_{48}, and C_{50} were obtained one after another by embedding a carbon dimer (yellow atoms) into fullerene C_{40}: structure and graphs; energy in kJ/mol

From the figure, it follows that only the initial and final fullerenes C_{40} and C_{50} have ordinary five-fold symmetry. They are perfect fullerenes. The intermediate fullerenes from C_{42} to C_{48} have topological five-fold symmetry. Among the intermediate fullerenes, there are two isomers of fullerene C_{44} and two isomers of fullerene C_{46} having one and the same topological symmetry but different shapes. The shape difference is connected with the diverse location of embedded dimers at the equator. These fullerenes obtained will be named permutation isomers and be denoted as 11 and 101, and as 111 and 1101. Indices 11 and 111 indicate that the embedded dimers are the nearest (first) neighbors; indices 101 and 1101 point to the fact that two dimers are the second neighbors. It is worth noting that the energy of fullerenes is less in the second case. To gain a better understanding of the mechanism of dimer embedding, its main features are shown schematically in Fig. 17.

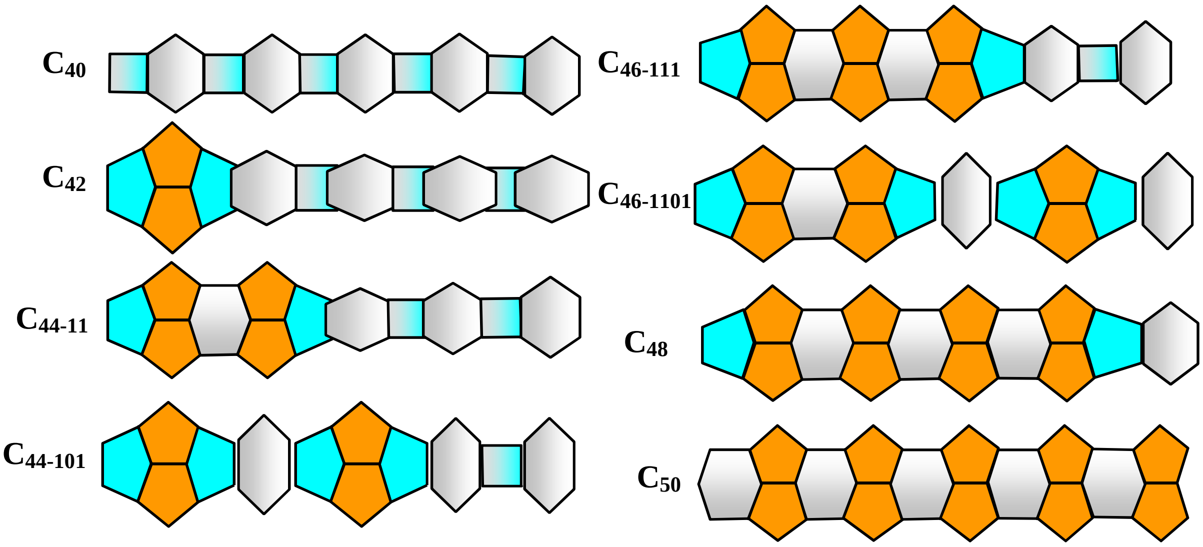

Fig. 17. Scheme of the main structural changes during the first stage growth of fullerene C_{40}

Second cycle. The growth can continue producing imperfect fullerenes from C_{52} to C_{58} and perfect fullerene C_{60} (Fig. 18). To gain a better understanding of the process, its main features are given in the form of schematic representation (Fig. 19).

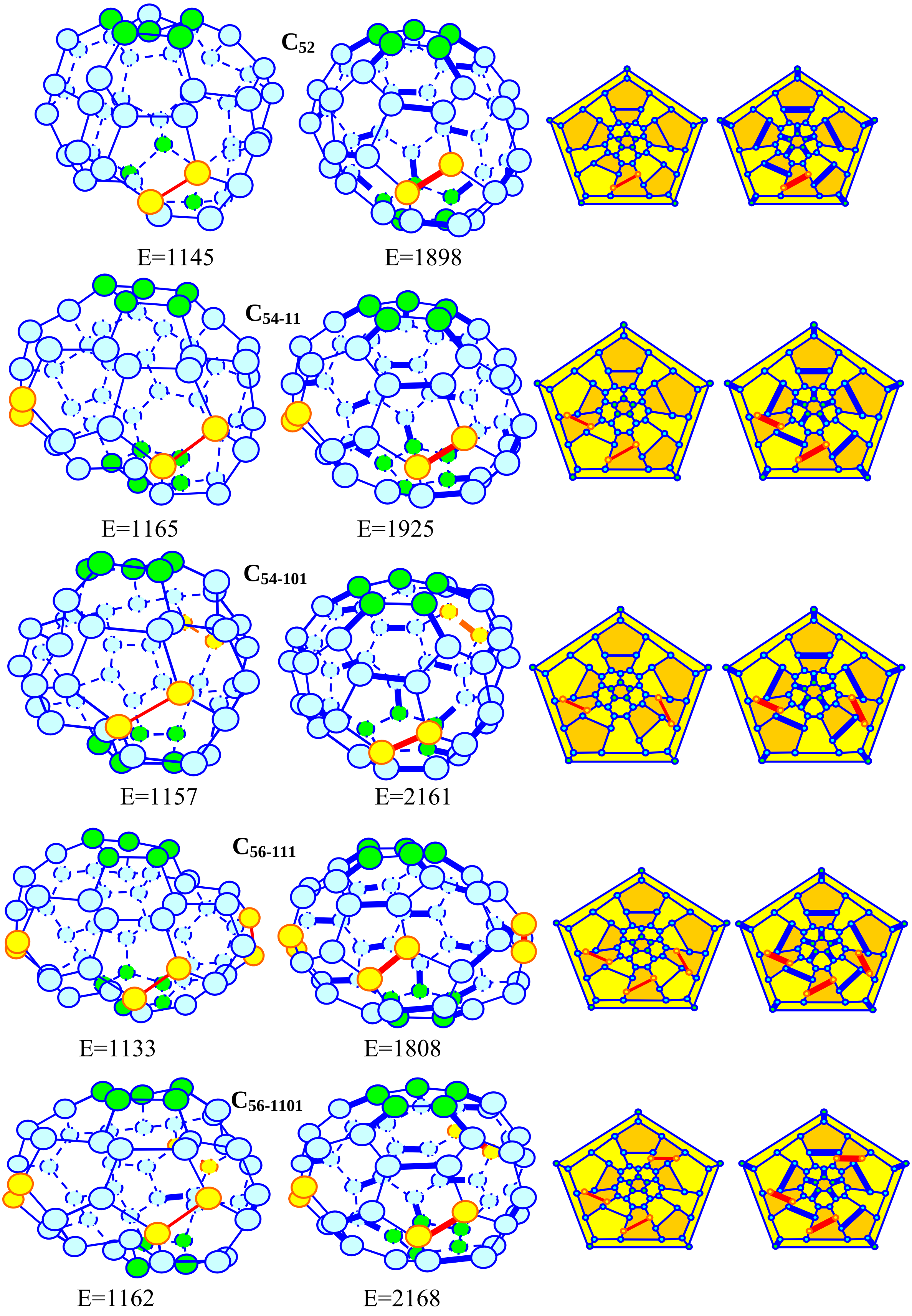

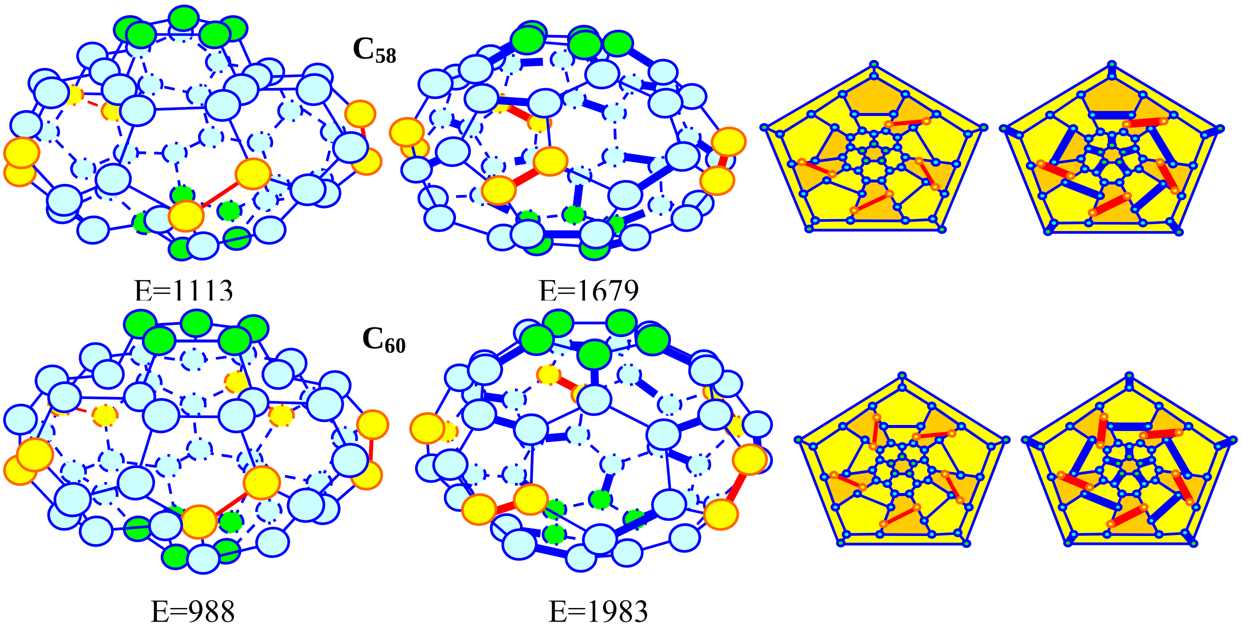

Fig. 18. Fullerenes C_{52}, C_{54}, C_{56}, C_{58}, and C_{60} obtained by one-after-another embedding a carbon dimer (yellow atoms) into fullerene C_{50}: structure and graphs; energy in kJ/mol

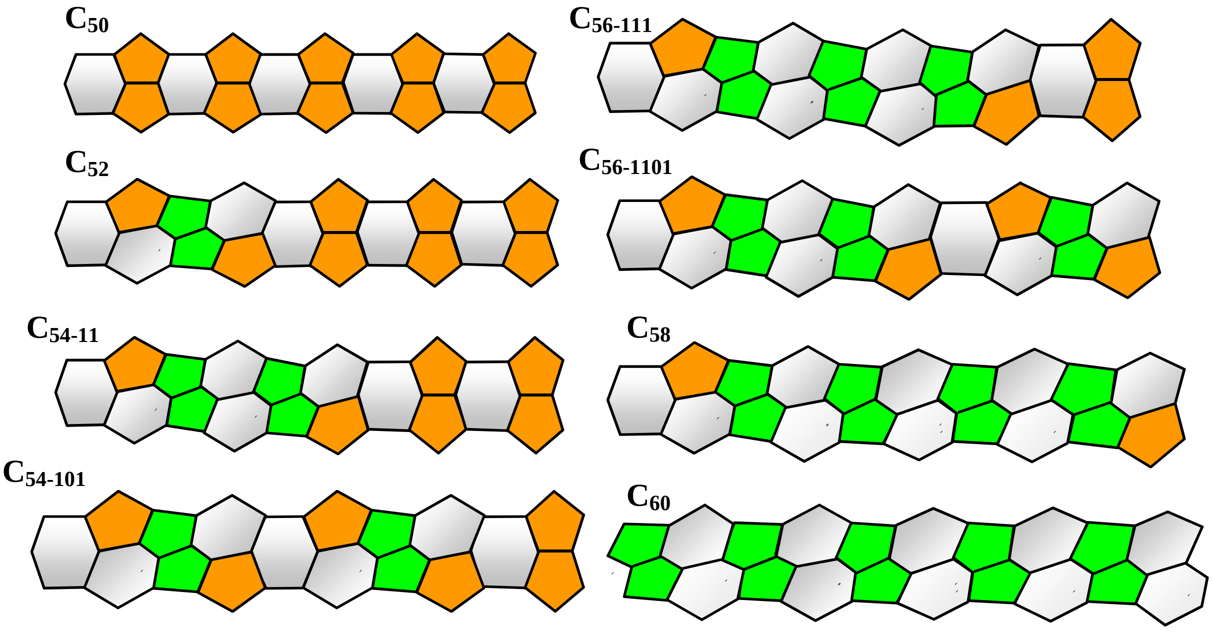

Fig. 19. Scheme of the main structural changes during the first stage growth of fullerene C_{40}

We see that fullerene C_{50} can grow by embedding the dimers only at an angle to its main axis of symmetry; it follows from Figs. 18 and 19. The phenomenon is connected with the fact that embedding can be realized only normally in a direction along which a hexagon has two neighboring mutually antithetic pentagons. During further growth, one obtains fullerenes C_{52}, C_{54}, C_{56}, C_{58}, and C_{60}. Similar to the first cycle, the intermediate fullerenes are imperfect, but fullerene C_{60} having five embedded dimers is perfect. It should be emphasized that in this case, the number of embedded dimers is equal to the degree of symmetry. It should be emphasized that this fullerene differs from that obtained by the fusion of cupolas (Fig. 11).

Growth of fullerene C_{50} (Non-classical fullerenes). The growth of fullerene C_{50} can continue in another way producing also imperfect fullerenes C_{52}, C_{54}, C_{56}, C_{58}, and perfect fullerene C_{60} (Fig. 20). The fullerenes are obtained as a result of embedding one after another carbon dimer into fullerene C_{50} parallel to the five-fold axis. From the figures, we notice again that only the initial and final fullerenes C_{50} and C_{60} have ordinary five-fold symmetry. They are perfect fullerenes. The intermediate fullerenes C_{52}, C_{54}, C_{56}, and C_{58} have topological five-fold symmetry.

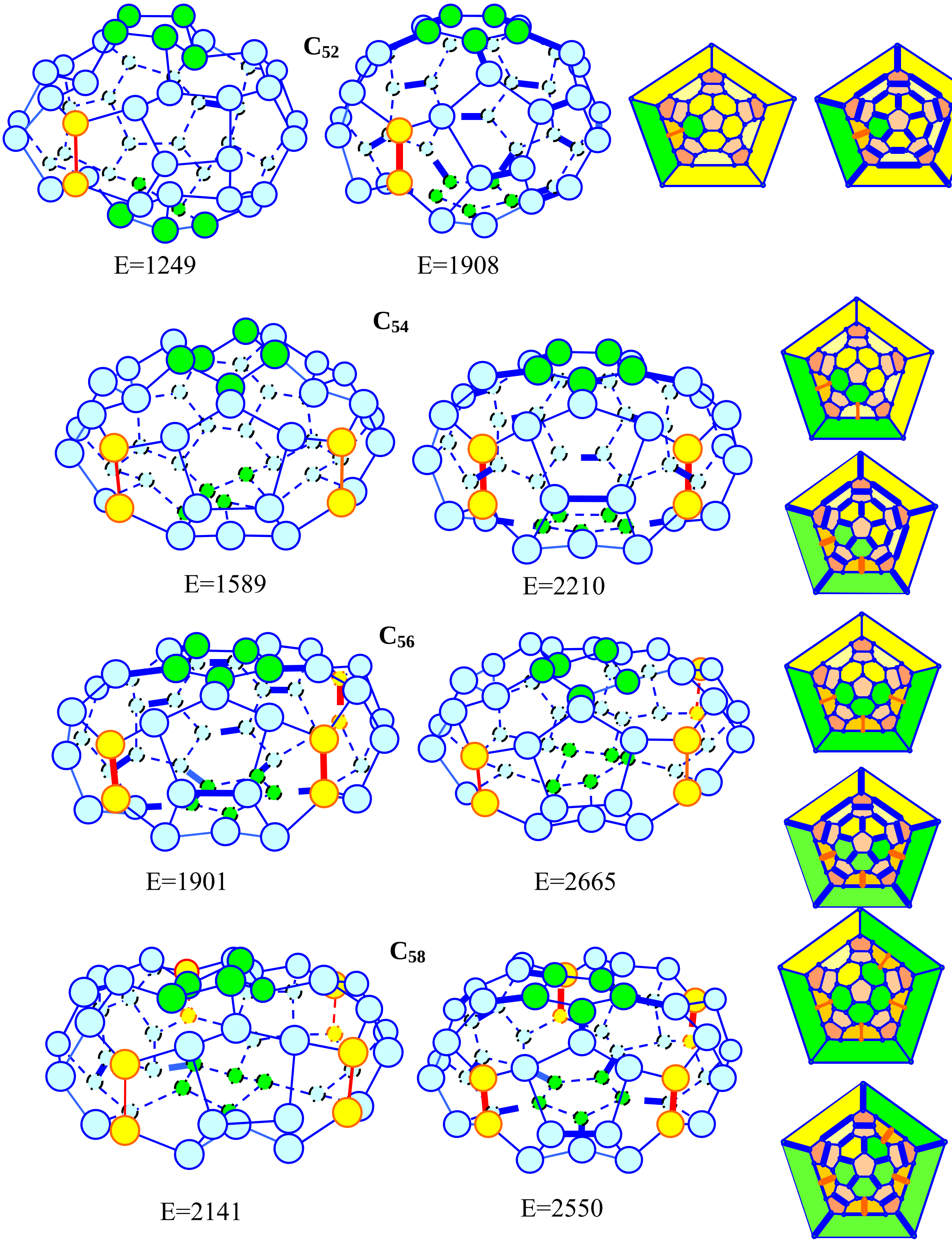

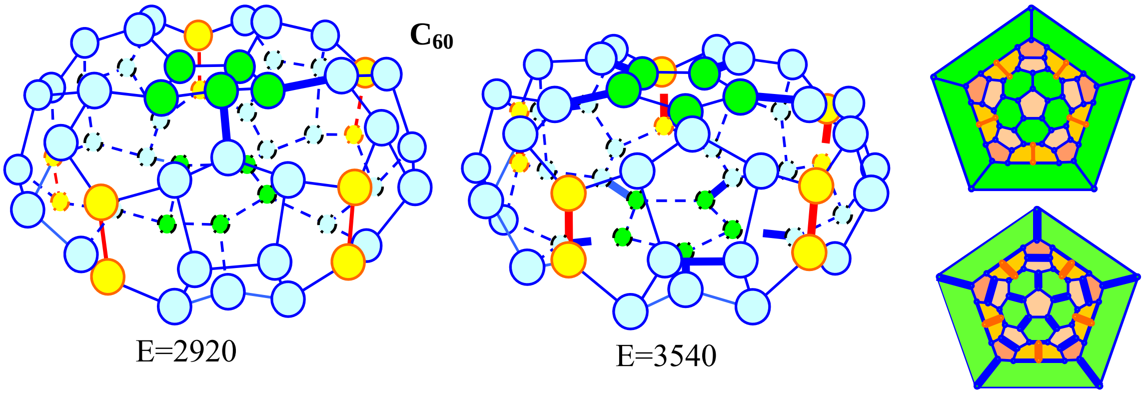

Fig. 20. Fullerenes C_{52}, C_{54}, C_{56}, C_{58}, C_{60} were obtained one-after-another embedding a carbon dimer into fullerene C_{50} parallel to the five-fold axis: structure and graphs; energy in kJ/mol

These results deserve further comment. For a detailed discussion of this subject see [10]. According to the authors, "In general, classical fullerenes are cage-like, hollow molecules of pseudospherical symmetry consisting of pentagons and hexagons *only*, resulting in a trivalent (and in the most ideal case) convex polyhedron with exactly three edges (bonds) joining every vertex occupied by carbon, idealized as sp^2 hybridized atoms. What happens if we relax the rules a little bit, and allow for other types of three-valent (sp^2) carbon framework? There are many generalizations that lead to structures of beautiful shapes that have both elegant mathematical theory and physical realizations: allowing for polygons with faces different from pentagons and hexagons. What kinds of fulleroids, which are fullerene-like structure, are allowed? Can we tile a sphere or a torus with heptagons only, or with only pentagons and heptagons?" Figure 20 answers the questions.

From the configurations shown it follows that the first embedding, which transforms fullerene C_{50} into fullerene C_{52}, influences deeply only one of the hexagons and two of its hexagon neighbours. This hexagon transforms into two adjacent pentagons and its hexagon neighbors become heptagons; the fullerene C_{52} losing ordinary five-fold symmetry. It becomes an imperfect fullerene with the ordinary D_{1h} symmetry, however conserving topological five-fold symmetry. At that in the fullerene, there appears a cell that contains four pentagons. The second embedding transforms fullerene C_{52} into fullerene C_{54}. The third embedding leads to transition from fullerene C_{54} to fullerene C_{56}. It transforms one more hexagon and two of its neighbors into two adjacent pentagons with about heptagons. The fourth embedding acts in a similar manner. At last, the fifth embedding restores D_{5h} symmetry. The perfect fullerene C_{60} obtained contains only pentagons (22) and heptagons (10), and no hexagons. It is a penta_{22}-hepta_{10} polyhedron; its shape resembles more a disk than a spheroid.

Growth of fullerene C_{70}. The fullerene belongs to the column of basic perfect fullerenes having five-fold symmetry. It can produce the natural isomers shown in Fig. 21.

C_{70}

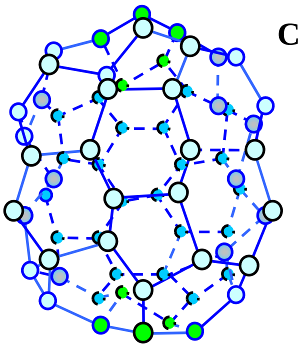

E=1636

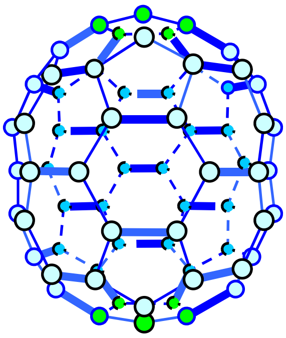

E=2069

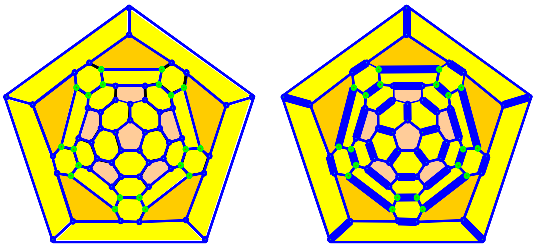

C_{72}

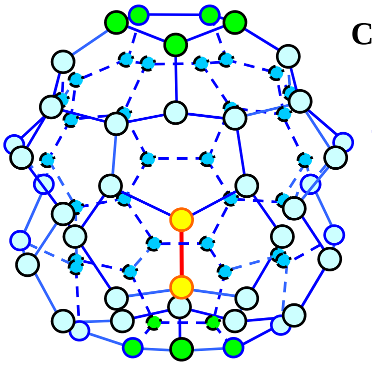

E=1614

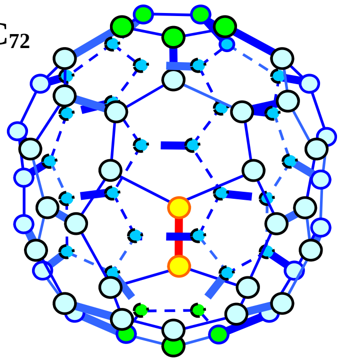

E=1832

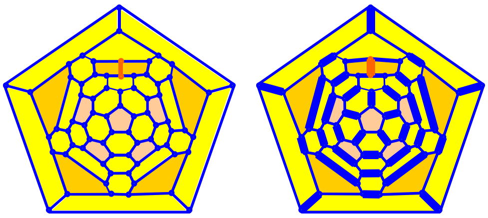

C_{74}

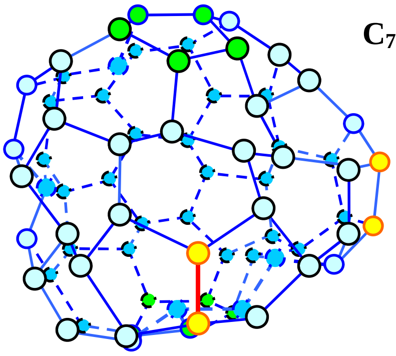

E=1626

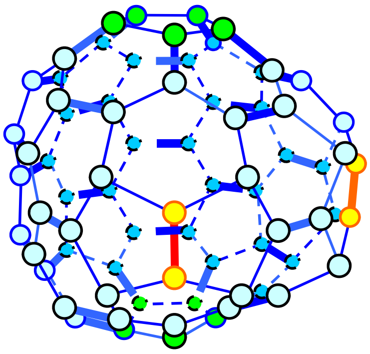

E=1770

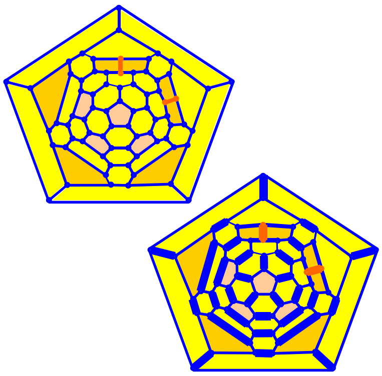

C_{76}

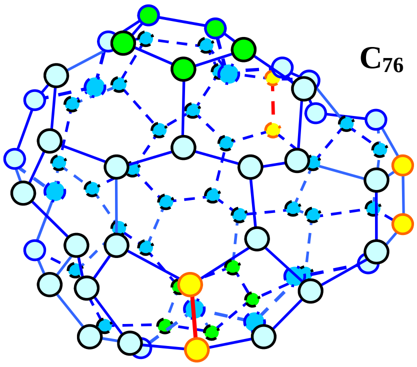

E=1535

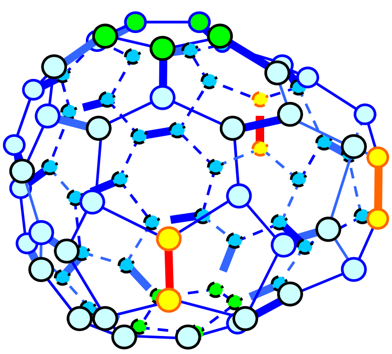

E=1583

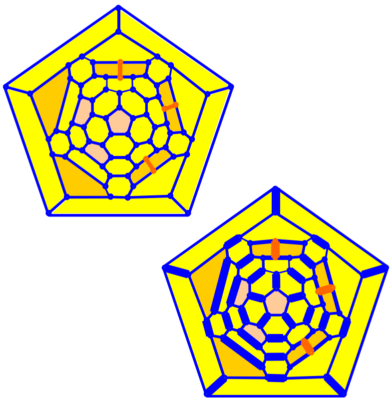

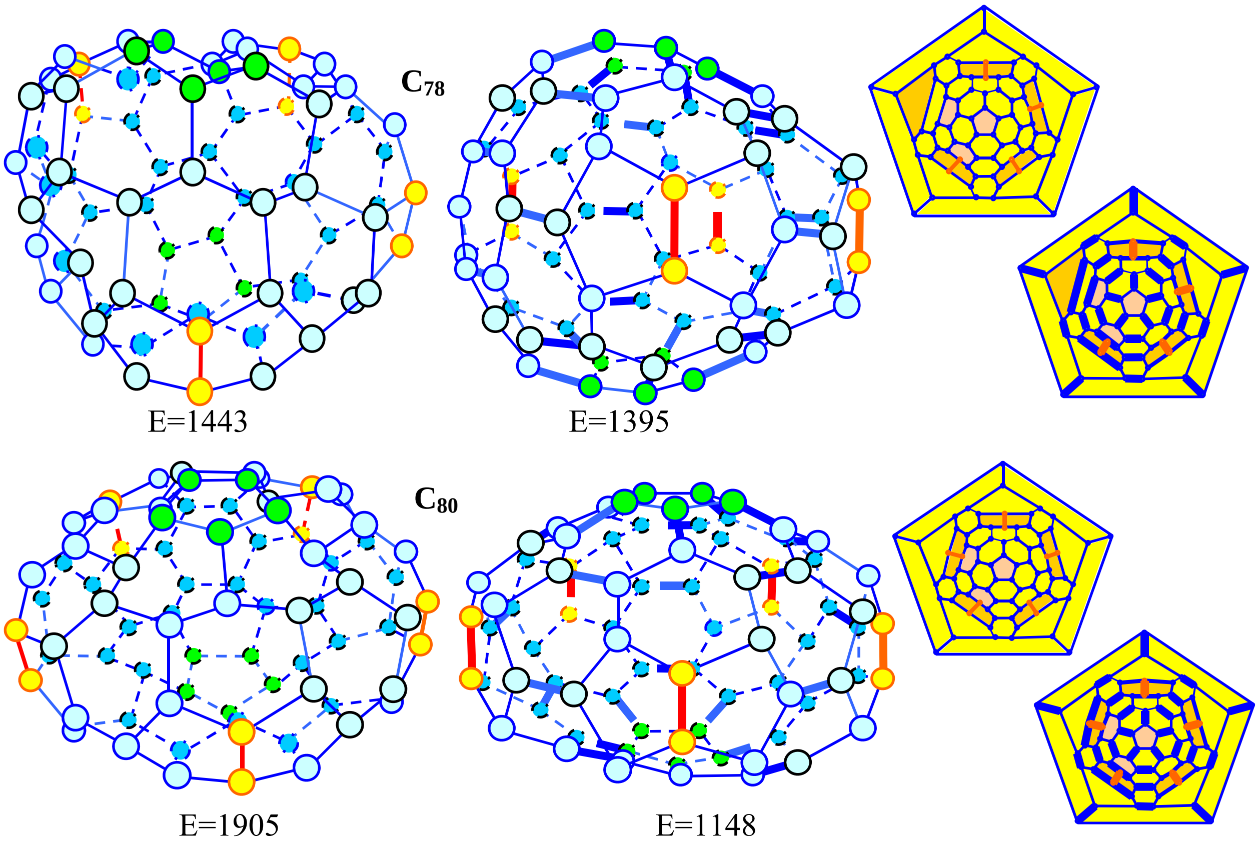

Fig. 21. Fullerenes C_{58}, C_{60}, C_{62}, and C_{64} as a result of one-after-another carbon dimer embedding into fullerene C_{56}: structure and graphs; energy in kJ/mol

5. Corannulene, sumanene and fullerene C_{60}

We have designed the most abundant and most celebrated fullerene molecule C_{60} by fusion of two cupolas C_{30} (Fig. 11). The atomic structure corresponding to a perfect polyhedron is a truncated icosahedron, which consists of twelve isolated pentagons and twenty adjacent hexagons. It should be emphasized that the formation and structure of cupolas were postulated. The question arises: Are there in nature similar molecules, from which it is possible to obtain the cupolas? To our mind corannulene $C_{20}H_{10}$ with C_{5v} symmetry and sumanene $C_{21}H_{12}$, which possesses C_{3v} symmetry, could be such molecules. These molecules are usually considered key fullerene fragments [14,15]. Being π-conjugated compounds, they are bowl-shaped or cupola-shaped species; it depends on a point of view (Fig. 22). The bowl of sumanene (1.15 Å) is anticipated to be deeper than that of corannulene (0.89 Å). According to [13], deeper π-bowls are more interesting because they may have properties more similar to those of fullerenes.

Early we investigated the possible ways of fullerene obtained from sumanene [16]. Now discuss the role of corannulene and compare it with those of sumanene. Suppose that we have removed ten hydrogen atoms from corannulene, then we obtain cupola C_{20}. If afterward add ten carbon atoms to the cupola, one gets cupola C_{30} (Fig. 23). The fusion of two cupolas leads to the appearance of the most famous fullerene molecule C_{60} (Fig. 24). To gain a better understanding of the fusion reactions, their main features are given in the form of a scheme (Fig. 25).

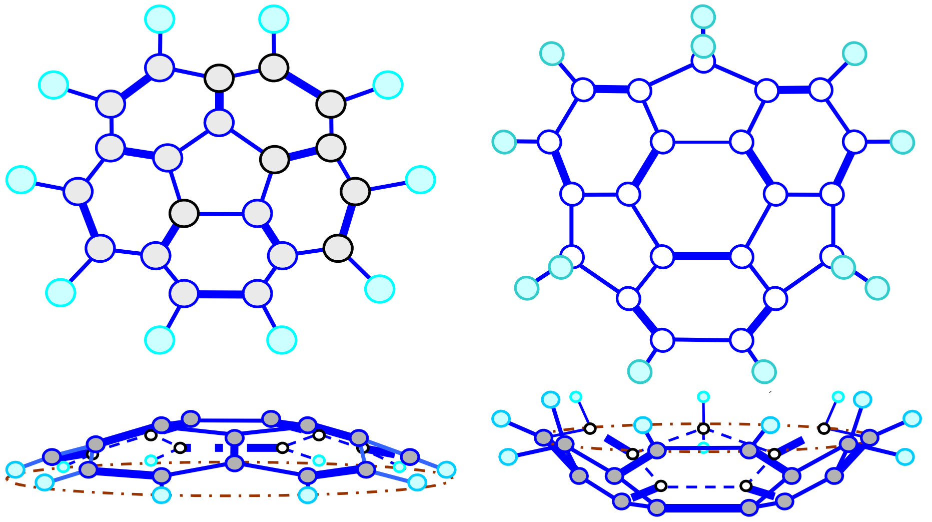

Corannulene $C_{20}H_{10}$ Sumanene $C_{21}H_{12}$

Fig. 22. Corannulene as a cupola and sumanene as a bowl (energy, kJ/mol)

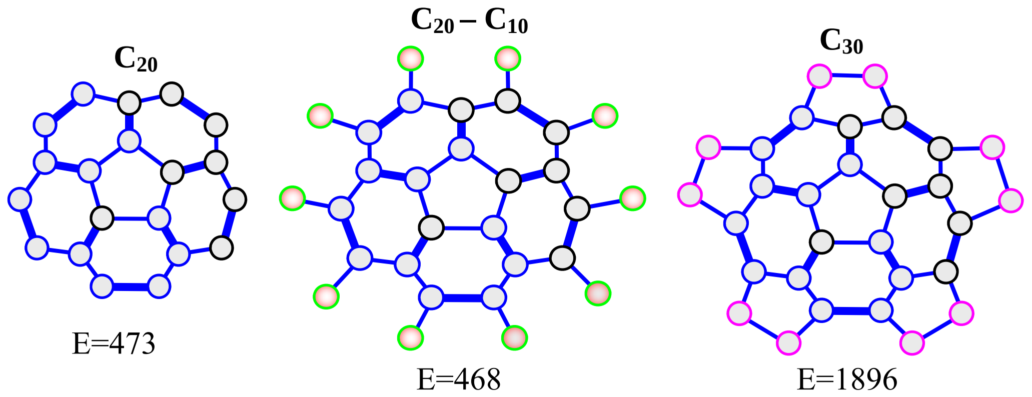

C_{20} E=473

$C_{20}-C_{10}$ E=468

C_{30} E=1896

Fig. 23. Carbon cupolas generated on the basis of corannulene: energy in kJ/mol

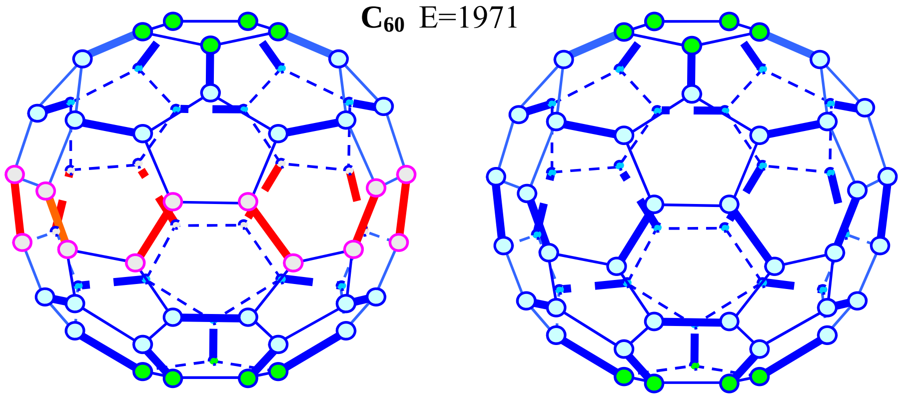

C_{60} E=1971

Fig. 24. Fullerene C_{60} was obtained by the fusion of two corannulene cupolas C_{30}: energy in kJ/mol

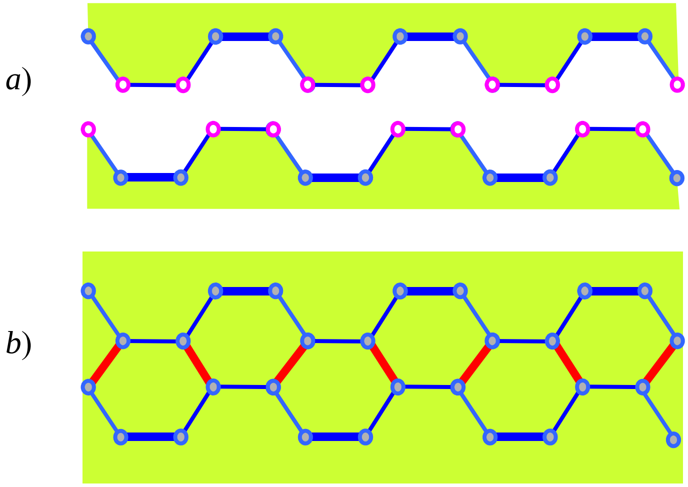

Fig. 25. Scheme reflecting the main structural changes during the fusion of cupolas: a) boundary-atom configuration of separate cupolas; b) fusion zone

In a similar manner it is possible to obtain from sumanene successively cupolas C_{21} and C_{30} and afterward fullerene C_{60} (Figs. 26 and 27). Interestingly enough that the final structures of the fullerenes obtained in different ways are the same. However, in the second case, there are possible fusion faults (Figs. 28 and 29).

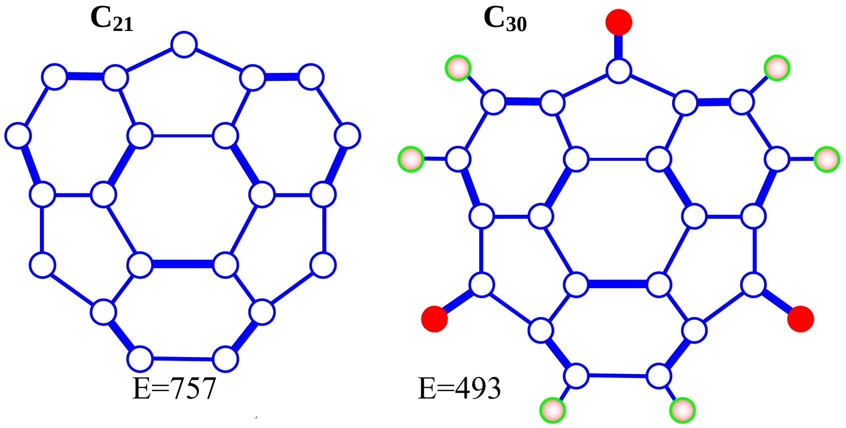

Fig. 26. Carbon cupolas generated on the basis of sumanene: energy in kJ/mol

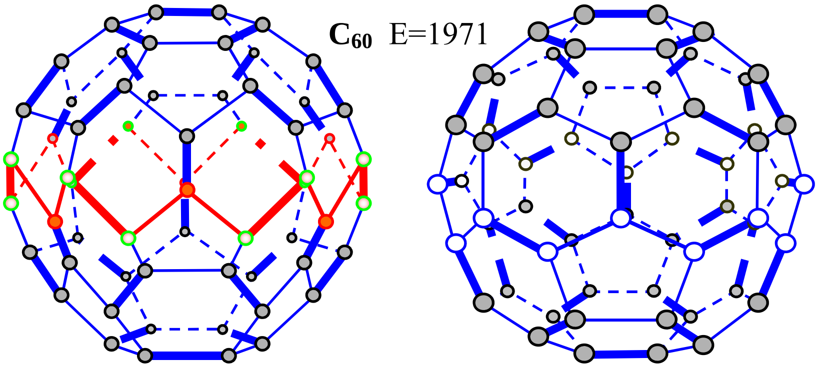

Fig. 27. Fullerene C_{60} was obtained by the fusion of two sumanene cupolas C_{30}: energy in kJ/mol

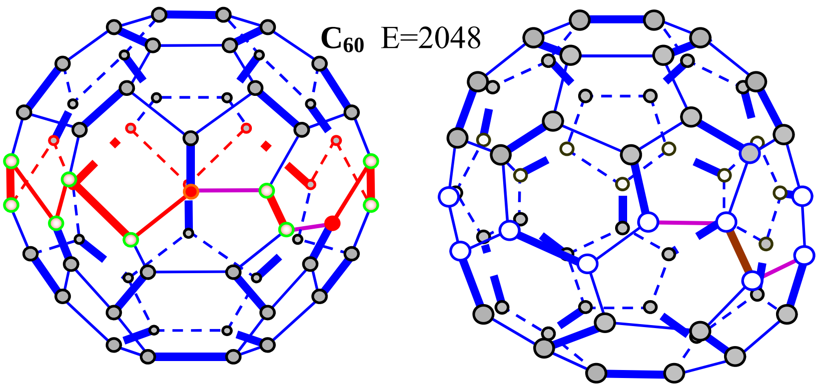

Fig. 28. Fullerene C_{60} was obtained by the fault-fusion of sumanene cupolas C_{30}: energy in kJ/mol

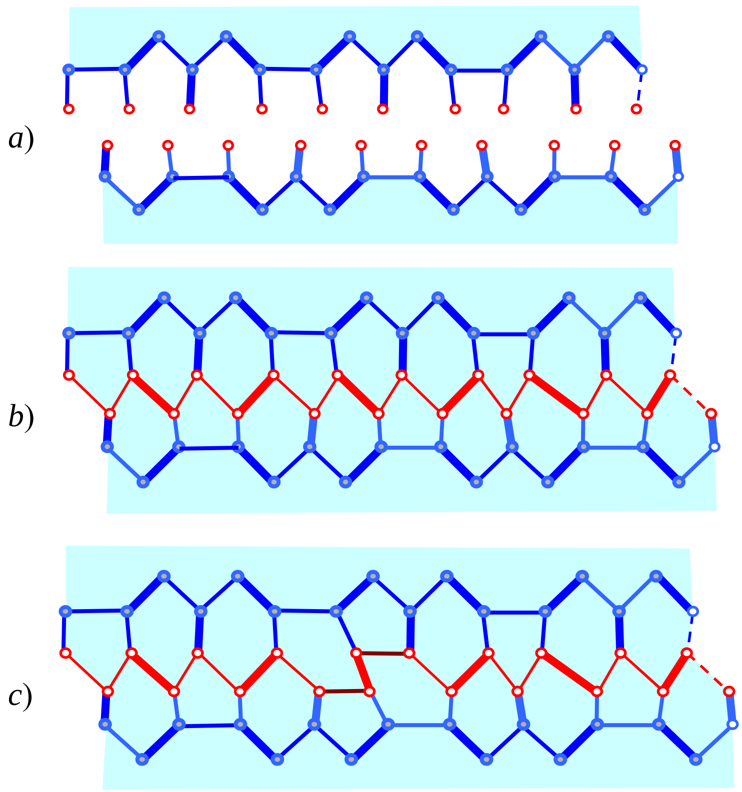

Fig. 29. Scheme reflecting the main structural changes during the fusion of cupolas: a) boundary-atom configuration of separate cupolas; b) fusion zone, perfect reaction; c) fusion zone, fault one

These results deserve further comment. The mechanism of fusion resembles that known in biophysics as lock-key adhesion [17]. The adhesion is due to the formation of specific molecular bonds between complementary pairs of proteins which are denoted by "lock" (L) and "key" (K). In our case, the boundary-atom configurations of cupolas play simultaneously the role of both lock and key. For the corannulene cupolas, the LK atoms are rather rigidly connected with the whole cupolas by two interatomic bonds; it follows from Fig. 25a. On contrary, for the sumanene cupolas thermal fluctuations are more important for the LK atoms since these atoms are connected with the cupolas only by one bond, single or double, (Fig. 29a). As a result, the "sumanene" fullerenes can contain fusion faults (Fig. 29c).

6. Conclusion

We have studied possible ways of generating and growing the fullerenes having five-fold symmetry. Beginning with cyclopentane C_5H_{10} and clusters C_5C_5, we obtained at first elementary fullerenes C_{10} and mini-fullerenes C_{20}, and then the fullerenes from C_{30} to C_{80}, perfect and imperfect, as well as nanotubes. The imperfection is connected either with extra 'interstitial' carbon dimers, the dimers playing the role of defects. Only the basic fullerenes C_{30}, C_{40}, C_{50}, C_{60}, C_{70}, and C_{80} have the ordinary five-fold symmetry in the corresponding column of the periodic system of fullerenes, the intermediate fullerenes having no such symmetry. Considering the latter as imperfect due to defects, one can define them as the fullerenes conserving *topological* five-fold symmetry. We have calculated the energies of the possible fullerenes.

We have designed the most abundant and most celebrated fullerene molecule C_{60} by fusion of two cupolas C_{30}. The atomic structure corresponding to a perfect polyhedron is a truncated icosahedron, which consists of twelve isolated pentagons and twenty adjacent hexagons. It should be emphasized that the formation and structure of cupolas were postulated. The question arises: Are there in nature similar molecules, from which it is possible to obtain the cupolas? To our mind corannulene $C_{20}H_{10}$ with C_{5v} symmetry and sumanene $C_{21}H_{12}$, which possesses C_{3v} symmetry, could be such molecules. These molecules are usually considered key fullerene fragments. Being π-conjugated compounds, they are bowl-shaped or cupola-shaped species. The mechanism of fusion resembles that known in biophysics as lock-key adhesion. The adhesion is due to the formation of specific molecular bonds between complementary pairs of proteins which are denoted by "lock" (L) and "key" (K). In our case, the boundary-atom configurations of cupolas play simultaneously the role of both lock and key. For the corannulene cupolas, the LK atoms are rather rigidly connected with the whole cupolas by two interatomic bonds. On contrary, for the sumanene cupolas, thermal fluctuations are more important for the LK atoms since these atoms are connected with the cupolas only by one bond (single or double). As a result, the "sumanene" fullerenes can contain fusion faults.

References

1. Melker AI, Krupina MA. Modeling growth of midi-fullerenes from C_{48} to C_{72}. *Materials Physics and Mechanics*. 2017;34(1): 29-36.

2. Melker AI, Krupina MA, Zarafutdinov RM. Fullerenes of the Δn=12 series. *Materials Physics and Mechanics*. 2017;34(1): 46-50.

3. Melker AI. *Modeling Experiment*. Moscow: Znanie; 1991.

4. Melker AI, Starovoitov SA, Vorobyeva TV. Information, entropy, temperature. *Materials Physics and Mechanics*. 2010;9(3): 210-227.

5. Prokhorov YV. (Ed.) *Mathematical Encyclopedic Dictionary*. Moscow: Soviet Encyclopedia; 1988.

6. Melker AI, Krupina MA, Zarafutdinov RM. Periodic system of fullerenes: the column of three-fold symmetry. *Nonlinear Phenomena in Complex Systems*. 2019;22(4): 383-394.

7. Melker AI, Krupina MA, Matvienko AN. Nucleation and growth of fullerenes and nanotubes having four-fold symmetry. *Materials Physics and Mechanics*. 2021;47(1): 315-343.

8. Sverdlov LM, Kovner MA, Krainov EP. *Vibration Spectra of Many-Atomic Molecules*. Nauka: Moscow; 1970.

9. Hanwell MD, Curtis DE, Lonie DC, Vandermeersch T, Zurek E, Hutchison GR. Avogadro: an advanced semantic chemical editor, visualization, and analysis platform. *Journal of Cheminformatics*. 2012;4: 17.

10. Melker AI, Matvienko AN. Periodic system of fullerenes: isomers from C_{20} to C_{28}. In: *Proc. 18th Int. Workshop: Nano-Design, Technology, Computer Simulations*. 2019. p.72-78.
11. Schwerdtfeger P, Wirz LN, Avery J. The topology of fullerenes. *WIREs Comput. Mol. Sci.* 2015;5: 96.
12. Melker AI. Fullerenes and nanotubes. Molecular dynamics study. *Proc. SPIE.* 2004;5400: 54-64.
13. Endo M, Kroto HW. Formation of carbon nanofibers. *J. Phys. Chem.* 1992;96(17): 6941-6944.
14. Hirao T, Sakurai H. First and practical synthesis of sumanene, a C_{3v} symmetric partial structure of fullerene. *Annual Report of Osaka University.* 2004;5: 27-29.
15. Amaya T, Natata T, Hirao T. Synthesis of highly strained π-bowls from sumanene. *J. American Chemical Soc.* 2009;131(31): 10810-10811.
16. Melker AI, Krupina MA, Zarafutdinov RM. Sumanene and fullerene C_{60}. *Materials Physics and Mechanics*. 2019;41(1): 45-51.
17. Bruinsma R. Physical aspects of adhesion of leukocytes. In: *Physics of Biomaterials: Fluctuations, Selfassembly and Evolution*. Riste T, Sherrington D. (Eds.) Dordrecht: Kluwer Academic Publishers; 1996. p.61-102.

THE AUTHORS

Alexander I. Melker
e-mail: ndtcs@inbox.ru
ORCID: -

Maria A. Krupina
e-mail: krupina_ma@spbstu.ru
ORCID: 0000-0001-8504-9302

Aleksandra N. Matvienko
e-mail: matvienko_an@spbstu.ru
ORCID: 0000-0002-3012-1407

Materials Physics and Mechanics. 2022;49(1): 73-84
Conference materials
http://dx.doi.org/10.18149/MPM.4912022_5

Magnetic properties of low-dimensional MAX_3 (M=Cr, A=Ge, Si and X=S, Se, Te) systems

M.S. Baranava✉, **V.R. Stempitsky**

Belarusian State University of Informatics and Radioelectronics, P. Brovki Str 6, 119, 220013, Minsk, Belarus

✉ baranova@bsuir.by

Abstract. The article presents the results of a magnetism study in quasi-two-dimensional MAX_3 (M=Cr, A=Ge, Si and X=S, Se, Te) systems. We calculated the microscopic magnetic parameters using quantum mechanical methods and showed that MAX_3 can have a high spin polarization. The easy magnetization axis lies normal to the layer plane. The main magnetic order of the $CrGeSe_3$, $CrGeTe_3$, $CrSiSe_3$, and $CrSiTe_3$ atomic systems is ferromagnetism. $CrGeS_3$ and $CrSiS_3$ exhibit antiferromagnetism. The low energy stability of the magnetic order is confirmed by the calculated values of the exchange interaction integral (J). We showed that the magnetic order realizes only at low temperatures. A study of the dependences of J and the magnetic anisotropy energy on the structural (distance between magnetic ions, distortion of the octahedral complex) and electronic properties (population and hybridization of atomic and molecular orbitals) has been performed. The dependences indicate three possible mechanisms of the exchange interaction. We have given ways of influencing a specific mechanism for managing exchange interaction.

Keywords: ab initio calculation, exchange energy, exchange integral, magnetic anisotropy, nanomagnetic**,** $CrSiS_3$, $CrGeTe_3$, $CrSiTe_3$

***Acknowledgements**. This work was supported by grant 3.02.6 of Belarusian National Scientific Research Program "Convergence – 2025" and grant 2.07 of Belarusian National Scientific Research Program "Materials science, new materials and technologies".*

Citation: Baranava MS, Stempitsky VR. Magnetic properties of low-dimensional MAX_3 (M=Cr, A=Ge, Si and X=S, Se, Te) systems. *Materials Physics and Mechanics*. 2022;49(1): 73-84. DOI: 10.18149/MPM.4912022_5.

1. Introduction

Low-dimensional magnetism is a quantum cooperative phenomenon. It belongs to the promising area of research in condensed matter physics. The objects under study are atomic systems in which the magnetic interaction is limited in one or more spatial directions. The Mermin-Wagner-Hohenberg (1966) theorem [1] states that thermal fluctuations destroy the long-range magnetic order at any finite temperature in low-dimensional isotropic magnetic systems. However, confirmation of the possibility of low-dimensional magnetism in monolayer samples was presented earlier (1944) in the theoretical work [2]. The arising contradictions are explained by different representations of spin magnetic moments in the Ising model [3], which was used in the work by Onsager, and the Heisenberg model [4], which was used for the proof of the Mermin-Wagner-Hohenberg theorem [1].

Limiting the dimensionality of magnetic systems can lead to strong magnetic anisotropy [5]. In this case, the vector of the magnetic moment of an atom has an orientation along only one crystallographic direction. The total spin of atoms has only one spatial coordinate. The Heisenberg model is not suitable for describing such materials. Therefore, the Mermin-Wagner-Hohenberg theorem, which is valid only for the isotropic Heisenberg model, cannot be applied to low-dimensional magnets. Such atomic structures are usually represented within the framework of the Ising model, which provides for only one degree of freedom of the magnetic moment of an atom [6]. These materials belong to the class of Ising magnets [7].

In 2016, a new stage began in the physics of low-dimensional magnetism due to the development of mechanical and chemical exfoliation of thin films from van der Waals structures [8]. These structures have strong chemical bonds in the layer plane and weak interplanar bonds. Such structure leads to a strong magnetic uniaxial anisotropy in the monolayer which is necessary for observing low-dimensional Ising-type magnetism.

Low-dimensional ferromagnetic order (FM) was implemented in unstable structures [8-13]. Also, the magnetic order was obtained in van der Waals systems for bulk modifications [14-29] which structures consist of several layers [30-34]. A stable low-dimensional magnetic order at a high Curie temperature (room temperature) has not yet been realized. Ternary MAX_3 (M=Cr, A=Ge, Si and X=S, Se, Te) compounds are van der Waals structures. The bulk phase consists of three monolayers located through the van der Waals gap with ABC stacking (Fig. 1).

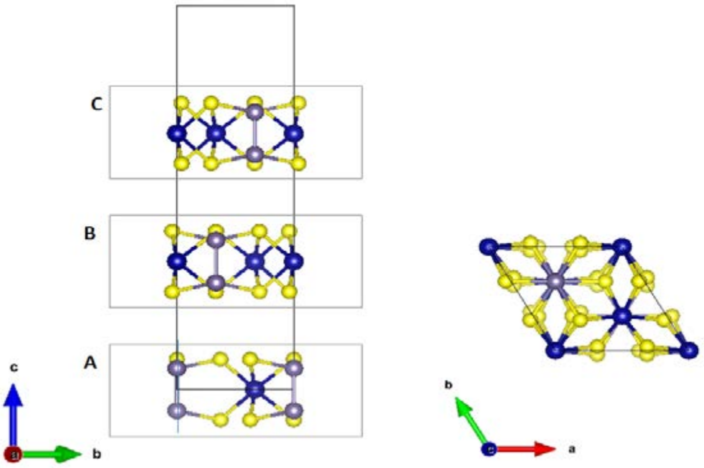

Fig. 1. Structure of transition metal chalcogenide MAX_3

The energy of magnetocrystalline anisotropy and the energy of exchange interaction make the dominant contributions to the magnetic energy of an atomic system for low-dimensional magnets as was shown by using quantum mechanical calculations. Spin-orbit interaction and exchange interaction are the sources of these contributions. These phenomena have a strict dependence on the composition, structure, and electronic properties of materials.

For practical applications of low-dimensional magnetic materials, research efforts should be directed to such important issues as increasing T_c for the operation of spintronic devices at room temperatures and above, searching for two-dimensional materials with magnetic anisotropy in the sample plane to reduce the switching current and increasing the residual magnetic induction. Such materials with magnetic anisotropy energy more than the thermal activation energy k_BT, having reduced thermal noise, expand the element base.

The article presents the study of the relationship between the composition, structure, magnetic and electronic properties in the framework of quantum mechanical calculation of microscopic magnetic parameters. Theoretical substantiation of the MAX_3 properties allows finding ways to enhance the magnetic energy and furnish insight into the nature of low-dimensional magnetism.

2. Methods

The study of MAX_3 magnetic parameters was carried out in several stages. In the first stage, the quantum mechanical calculation was carried out with spin polarization preliminary ionic relaxation in the VASP software package [35]. Static self-consistent calculations were performed for the ground state structural parameters. Calculations of the ground quantum state band structures were carried out for the Γ-K-M-Γ contour in the Brillouin zone. In the second stage, the microscopic magnetic parameters were calculated. The exchange interaction integral was calculated using the Heisenberg model [4].

Computational cells consisting of 2×2×1 elementary cells were created to take into account the exchange interaction between the central Cr ion and the first (J_1), second (J_2), and third nearest magnetic ion. Four magnetic configurations were set for each cell, three corresponding to the antiferromagnetic state and one to the ferromagnetic state (Fig. 2).

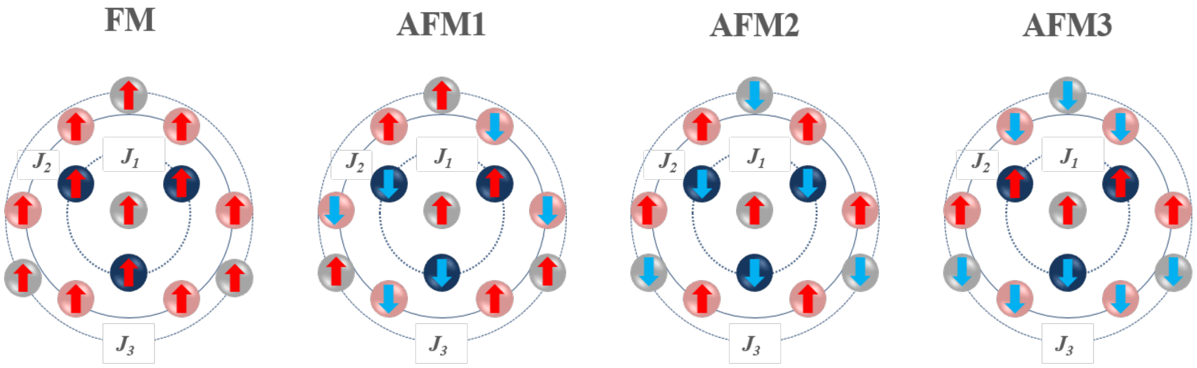

Fig. 2. Magnetic configurations of the chromium sublattice

The equations of the total energy of the system for four magnetic configurations are:

$$E_{AFM1} = E_0 + \frac{1}{2}S^2(-J_1 - J_2 + J_3), \quad (1)$$

$$E_{AFM3} = E_0 + \frac{1}{2}S^2(J_1 - J_2 - J_3), \quad (2)$$

$$E_{AFM2} = E_0 + \frac{1}{2}S^2(-3J_1 + 3J_2 - J_3), \quad (3)$$

$$E_{FM} = E_0 + \frac{1}{2}S^2(3J_1 + 3J_2 + J_3). \quad (4)$$

The computational cells of quasi-two-dimensional atomic structures were optimized for all considered magnetic configurations, which are presented in Fig. 2. The final structural parameters correspond to the ground magnetic state.

The Curie temperature (T_c) was calculated using the equation:

$$T_C = 2zJS(S+1)/3k_B, \quad (5)$$

where z is the number of the nearest neighbors, S is the spin of the magnetic ion, k is Boltzmann constant.

Spin polarization was calculated by the equation:

$$P = (n_\uparrow - n_\downarrow)/(n_\uparrow + n_\downarrow), \quad (6)$$

where $n_\uparrow$ is the density of states of electrons with spin up, $n_\downarrow$ is the density of states of electrons with spin down.

The deviation of the angles of the octahedral complex from the ideal value was calculated by the equation [36]:

$$\varsigma^2 = \sum_{i=1}^{n}[(\theta_i - 90)^2/6], \quad (7)$$

where θ_i is the bond angle in the octahedral complex.

In the third stage, the dependence of microscopic magnetic parameters on structural and electronic properties was analyzed.

3. Results and Discussion

Quantum mechanical simulation. An analysis of the magnetization distribution showed a local magnetic moment on Cr atoms, which ranges from 2.94 to 3.44 μ_B. This indicates the presence of three electrons with uncompensated spins. Therefore, the chromium atom in MAX_3 compounds is an ion with a charge of +3e (Cr^{3+}). According to the calculations, 90-95% of the total magnetic moment is localized on the d-orbitals of Cr^{3+}. It makes it possible to use magnetic models based on the principles of localized electronic states, such as the Ising and Heisenberg models [3,4], as well as to interpret the results in terms of the crystal field theory.

The main magnetic order of the studied compounds is FM, except for those compounds where S acts as a chalcogen. In this case, the main magnetic order is AFM. Deviation of the local magnetic moment from an integer value upwards is observed in compounds with FM, and downwards in compounds with AFM. It indicates the possible hybridization of Cr^{3+} *d*-electrons with surrounding ions. A study of this issue is given below.

Electronic properties calculations of the MAX_3 two-dimensional configurations for the main magnetic states show that all compounds are indirect-gap semiconductors. Figure 3 presents the band structure of $CrSiSe_3$ as an example. The top of the valence band is at the Γ-point. The bottom of the conduction band is located between points M and Γ.

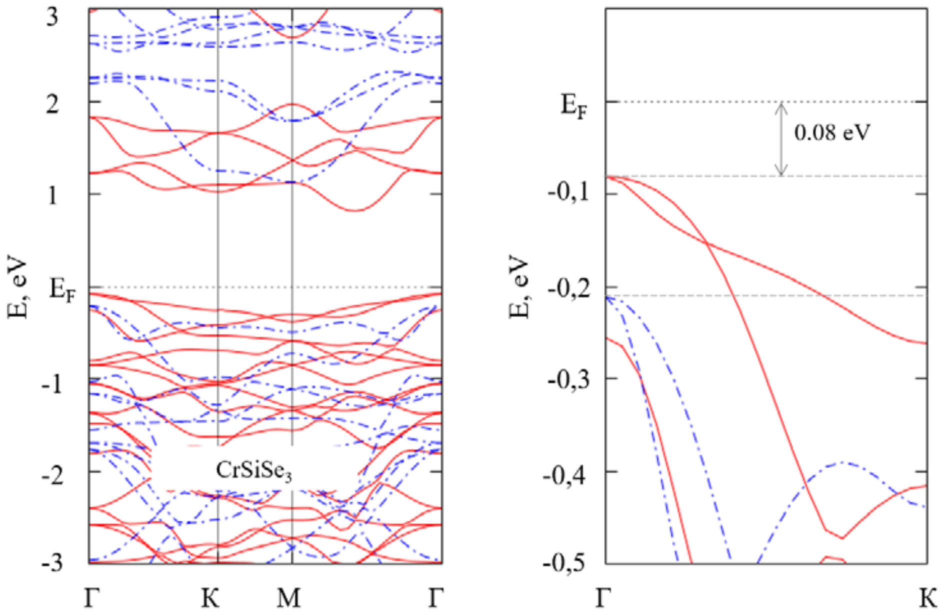

Fig. 3. $CrSiSe_3$ band structure
(Red solid bands correspond to the energy states of electrons with spin up, and blue dash bands correspond to the energy states of electrons with spin down)

The bottom of the conduction band is formed due to the *d*-orbitals of Cr. The *p* -orbitals of chalcogens make the main contribution to the formation of the top of the valence band in all cases, except for AFM atomic systems with X=S. In this case, the top of the valence band is formed by the *d*-orbitals of Cr, the *p*-orbitals of chalcogens, and the *p*-orbitals of Ge and Si ions. In the $CrGeS_3$ compound, *p*-orbitals of Ge prevail in the formation of the top of the valence band. The band gaps for the two spin subsystems differ by factors of 1.51 and 1.60 (E_g^{up}/E_g^{dw}) in $CrSiSe_3$ and $CrSiTe_3$, respectively. This makes it possible to generate the motion of spin-polarized charge carriers with a large polarization coefficient. The energy gap between the top of the valence band and E_f ranges from 0.08 eV to 0.18 eV. These values are 0.08 eV and 0.11 eV for $CrSiSe_3$ and $CrSiTe_3$, respectively.

With an increase in temperature or the application of an external electric field, it is possible to change the band structure from a semiconductor type of conductivity to a metal one. The conductivity, similar to a semimetallic, can be obtained for $CrSiSe_3$ and $CrSiTe_3$ using an external action.

Calculation of microscopic magnetic parameters in MAX_3. The exchange interaction integral was calculated based on the results of the local magnetic moments simulation and using the Heisenberg Hamiltonian. Spin in equations (1-4) is taken as 3/2 because the magnetic moment has a strong localization on Cr^{3+}. The equations for calculating the exchange interaction integral are determined through the difference in energies of various magnetic configurations:

$$J_1 = (-E_{AFM2} + E_{AFM3} + E_{FM} - E_{AFM1}), \tag{8}$$

$$J_2 = \frac{(E_{AFM2} - E_{AFM3})}{288} + J_1, \tag{9}$$

$$J_3 = \frac{(E_{AFM3} - E_{AFM1})}{216} + J_1. \tag{10}$$

The exchange interaction integrals calculated are given in Table 1.

Table 1. Microscopic magnetic parameters

MAX_3	J_1, meV	J_2, meV	J_3, meV	E_{MAE}, meV	T_c, K	P	d_{M-M}, Å	$\alpha_{Cr\text{-}X\text{-}Cr}$, deg	ς^2, deg^2
$CrGeS_3$	-0.06	0.04	0.09	–	–	–	3.47	91.31	51.52
$CrGeSe_3$	0.68	-0.18	0.0005	-0.55	59.22	0.69	3.64	90.87	72.61
$CrGeTe_3$	2.07	0.04	0.50	-0.27	180.50	0.38	3.98	92.14	47.98
$CrSiS_3$	-1.53	0.17	0.01	–	–	–	3.40	88.68	39.18
$CrSiSe_3$	1.74	-0.13	0.07	-0.92	151.68	0.98	3.99	91.82	37.00
$CrSiTe_3$	1.48	-0.03	-0.16	-0.28	129.01	0.73	3.98	89.71	32.19

Dependence of microscopic magnetic parameters on electronic properties. In the MAX_3 atomic structures, the Cr^{3+} ion is surrounded by six chalcogen ligands (Fig. 4a). This allows analyzing the electronic properties within the framework of the theory developed for octahedral complexes. The crystal field of the ligands causes the *d*-orbitals to split into three-fold degenerate states (t_{2g}), which consist of d_{xy}, d_{zx} and d_{yz}, and two-fold degenerate states (e_g), which consist of d_{z2} and $d_{x2\text{-}y2}$.

Before calculating the partial density of electronic states (DOS), the vectors of the computational cells were rotated. Accordingly, the bonds between the vertices of the octahedron (chalcogen ions) and the Cr^{3+} located in the center were parallel to the axes of the Cartesian coordinate system (Fig. 4a). Otherwise, the calculation results will show a non-standard linear combination of atomic orbitals and "mixing" of partial DOS. This impedes analyzing the results. The partial DOS for Cr^{3+} *d*-electrons with rotated computational cells shows the classical splitting of energy levels into t_{2g} and e_g states (Fig. 4b).

Figure 5 shows the obtained partial DOS for octahedral complexes consisting of Cr^{3+} and ligands in the corresponding MAX_3 compounds.

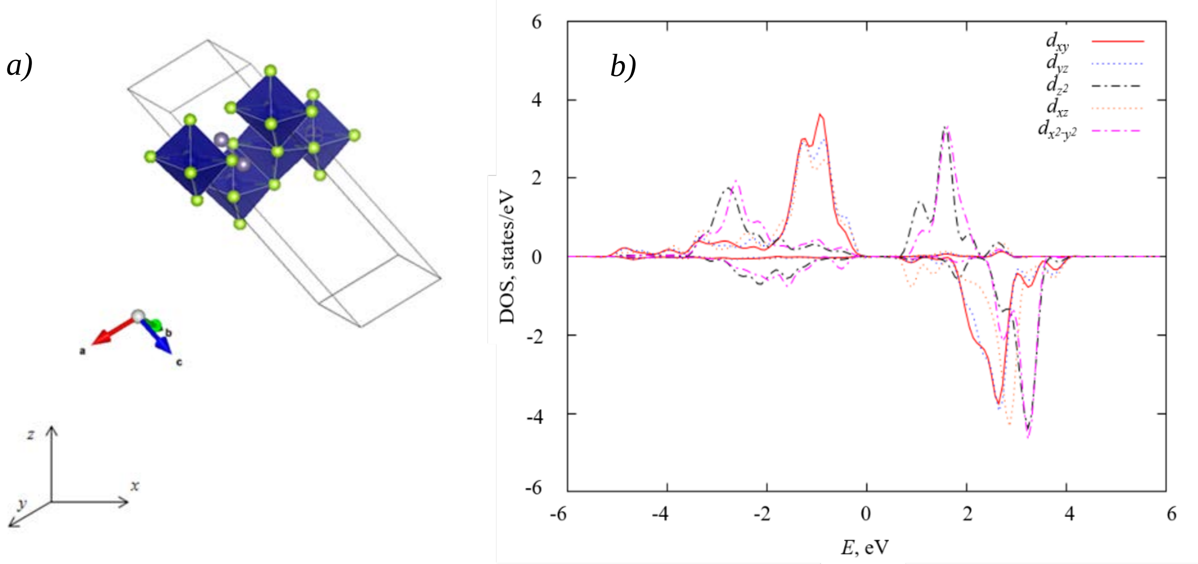

Fig. 4. Rotated computational cell (*a*); partial DOS of d-electrons (*b*)

A common feature of the obtained partial DOS is the existence of localized t_{2g} states that are located below the Fermi level for electrons with spins up, i.e., correspond to filled states, and also above the Fermi level, i.e., correspond to unoccupied states. Unoccupied e_g orbitals have energy higher than t_{2g}. The energy difference between these orbitals is determined by electrostatic splitting and is responsible for the formation of the high-spin state. In all atomic systems, this parameter does not change. The presence of filled e_g levels is explained by the hybridization of the corresponding atomic states of Cr^{3+} and surrounding ions, which leads to the formation of a common molecular orbital σ with decreasing energy. The energy split between t_{2g} and σ characterizes the degree of hybridization. In compounds with X=Se, the energy difference between filled molecular orbitals and t_{2g} orbitals is higher than in atomic systems with Te, which indicates greater hybridization, since more overlap leads to an energetically favorable state.

Bader analysis [37] presents that 5.8 electrons are located on the t_{2g} orbitals of Cr^{3+} ions. This value is unchangeable for all atomic systems. The molecular orbital σ contains 8.40 and 8.50 spin-up electrons, as well as 8.10 and 8.15 spin-down electrons in the $CrSiSe_3$ and $CrGeSe_3$ atomic systems, respectively. For $CrSiTe_3$ and $CrGeTe_3$, the corresponding values are 7.70 and 7.65 spin-up electrons and 7.10 and 7.15 spin-down electrons. Changes in the population of molecular orbitals are observed only when the chalcogen changes, and do not depend on other components of the atomic system. The increase in this value occurs due to the electronegativity of the chalcogen *p*-orbital (2.10 for Te, 2.55 for Se). Therefore, the degree of hybridization is affected by the *p*-orbitals of the chalcogen.

We can conclude that Si and Ge do not have a direct effect on the corresponding dependencies between electronic properties and magnetic parameters, because the σ population depends only on the chalcogen, and t_{2g} in the structures under study is determined by the crystal symmetry. Thus, it suffices to analyze the influence of ligands on J to formulate the dependencies of the magnetic parameters on the electronic properties.

The electronic configurations of ligand atoms have the form: Te [Kr] $3d^{10}5s^25p^4$, Se [Ar] $3d^{10}4s^24p^4$, S [Ne] $3s^23p^4$. The difference between the electronic configurations is the main quantum number (n) of the outer valence shell, while the filling of the sublevels is similar. The value of J_3 increases with increasing n (Table 1), which characterizes the exchange interaction with the third neighboring magnetic ion. Therefore, the diffuseness of the valence shell affects the longest-range exchange interaction, i.e. J_3. For example, the outer electron shell Te has a higher n and is more diffuse. Thereby $CrGeTe_3$ and $CrSiTe_3$ have the highest modulus J_3. Also, the diffuseness of the Te valence shell suggests the weakest hybridization in atomic systems with this element, and consequently the smaller exchange interaction J_1. The energy difference between the occupied e_g and t_{2g} states is larger for $CrGeSe_3$ than for $CrGeTe_3$ according to the partial DOS (Fig. 3). The formation of a molecular orbital in $CrGeSe_3$ is energetically more favorable, and hybridization should be stronger. However, the calculation results for J_1 confirmed the above conclusion for compounds with A=Si but did not demonstrate this dependence for compounds with A=Ge. This is explained by the strong influence of structural parameters on magnetic properties.

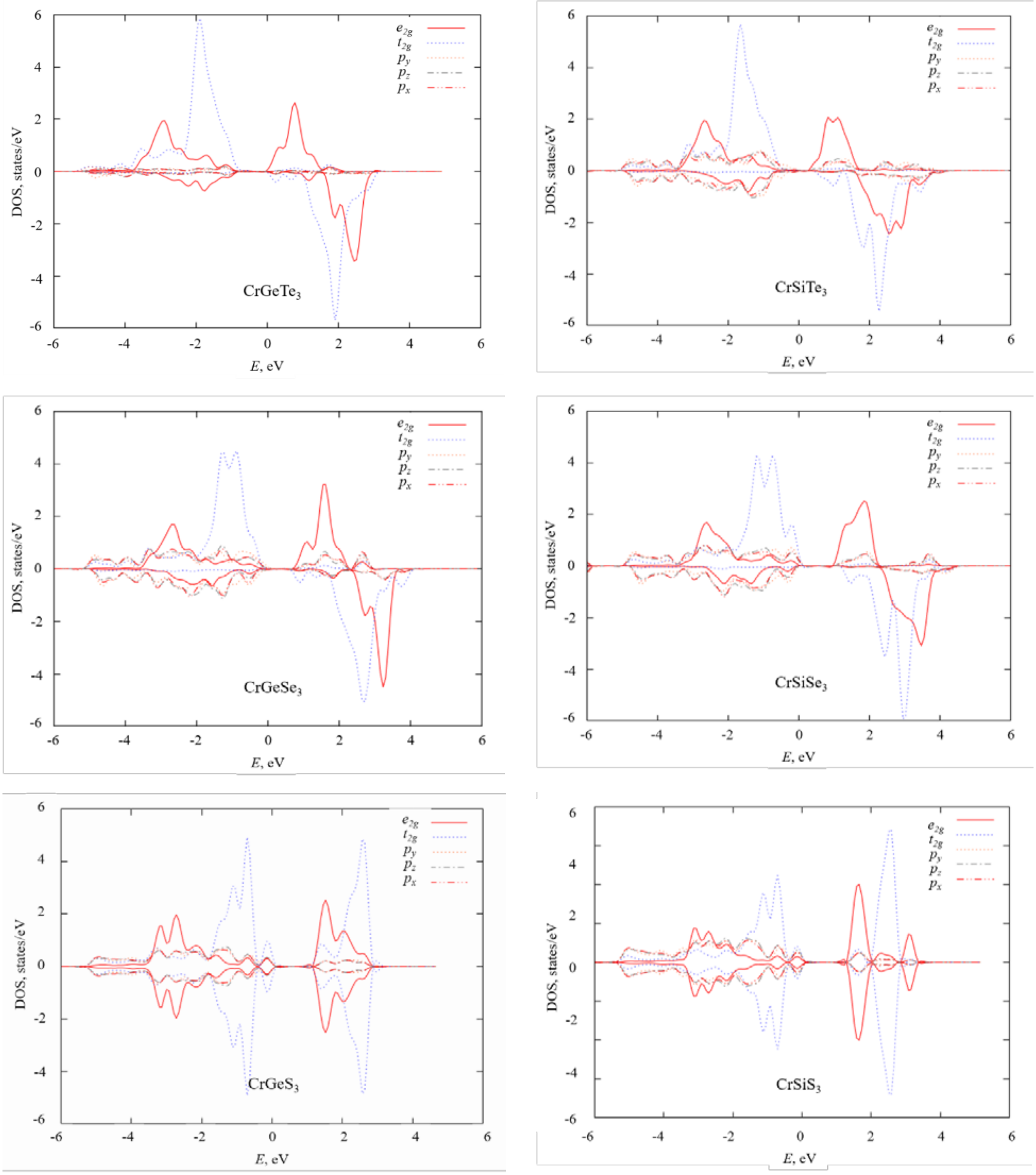

Fig. 5. Partial DOS of MAX_3 two-dimensional atomic systems

Dependence of microscopic magnetic parameters on the structural properties. Atomic systems with Ge have a larger value of ς^2 (Table 1) compared to atomic systems containing Si. Since E_{MAE} (Table 1) depends on the crystal field [38], the symmetry lowering should cause modulation of this microscopic parameter. In $CrSiSe_3$ and $CrGeSe_3$, the ς^2 values are 37.00 and 72.61 deg^2, respectively, which leads to a decrease in E_{MAE} from 0.92 meV to 0.55 meV. In $CrSiTe_3$ and $CrGeTe_3$, the difference in ς^2 values is not so significant and equals 32.19 and 47.98 deg^2, respectively. It leads to insignificant changes in the E_{MAE} values (0.28 and 0.27 meV, respectively). This behavior is explained by the different diffuseness and the degree of deformation of *p*-orbitals of chalcogens. Therefore, lattice distortion affects the E_{MAE} to a lesser extent in compounds where the chalcogens have a larger *n* value. Thus, E_{MAE} has a significant dependence on Si and Ge, as well as on chalcogen.

$CrGeTe_3$, $CrSiSe_3$, $CrSiTe_3$ have a distance between the two nearest Cr^{3+} ($d_{M\text{-}M}$) in the range from 3.98 to 3.99 Å. Moreover, these compounds possess FM. In $CrGeSe_3$, this parameter is 3.64 Å, while the exchange interaction between the two nearest Cr^{3+} indicates FM several times weaker than in $CrGeTe_3$, $CrSiSe_3$, and $CrSiTe_3$. In $CrGeS_3$ and $CrSiS_3$ the $d_{M\text{-}M}$ are 3.47 and 3.40 Å, and the exchange interaction is AFM. A decrease in the distance between the nearest Cr^{3+} leads to a weakening of the FM and an increase in the AFM. This dependence indicates the direct exchange interaction responsible for the AFM. The difference in J_1 for $CrSiS_3$ and $CrGeS_3$ is then explained by the strong dependence of the direct exchange interaction on the symmetry breaking of the crystal. Direct exchange interaction enhances AFM, but FM dominates in the compounds where $d_{M\text{-}M}$ has a large value. Thus, the dominant mechanism of the exchange interaction between Cr^{3+} in $CrGeSe_3$, $CrGeTe_3$, $CrSiSe_3$, and $CrSiTe_3$ is superexchange through chalcogen atoms. The above conclusion confirms the Goodenough-Kanamori-Anderson rule [39], which states that superexchange interaction is possible between half-filled Cr^{3+} *d*-orbitals and filled ligand orbitals at a value of $\alpha_{Cr\text{-}X\text{-}Cr}$ close to 90 deg.

Exchange interaction mechanism. Figure 4 shows two octahedral complexes with central Cr atoms connected through common vertices. Chalcogens are located in the vertices. The spatial arrangement of Cr in the environment of chalcogens leads to the emergence of six hybrid atomic orbitals of the sp^3d^2 type in Cr, which consist of d_{z2}, $d_{x2\text{-}y2}$, s, p_x, p_y, p_z according to Pauling's hybridization theory. These orbitals correspond to bonding states. The other three orbitals d_{xz}, d_{yz} and d_{xy} keep atomic-like (t_{2g} according to the crystal field theory). They are filled with electrons, which form the intrinsic magnetic moment of the transition metal. The hybrid atomic orbitals are directed from the central atom towards the vertices of the octahedral complex, where they bond with the *p*-orbitals of the chalcogen and form the bonding molecular orbital σ.

Exchange interaction is possible to implement by three mechanisms. The first mechanism occurs between *d*-orbitals of the same symmetry (t_{2g}) of two Cr^{3+}. This is a direct kinetic exchange (J_{kin}, Fig. 6). The interaction angle is 180° or close to it, and the exchange occurs between partially filled orbitals. In this case, according to the Goodenough-Kanamori-Anderson rules, AFM can be formed. The evidence for the implementation of this mechanism into MAX_3 is based on the following: the distance decrease between two nearest Cr^{3+} weakens FM and increases AFM. Besides the larger ς^2 is in compounds with AFM ($CrSiS_3$ and $CrGeS_3$), the smaller J_1.

The second mechanism is carried out due to electron hopping (tunneling) between the molecular orbital σ of the first Cr^{3+} and t_{2g} atomic orbitals of the second Cr^{3+} (J_{te} , Fig. 6). The proof for the implementation of this mechanism rests on the results listed below. Firstly, the hybridization of sp^3d^2 orbitals with p-orbitals of the chalcogen was observed in all studied atomic systems (i.e., σ orbital) in accordance with the partial DOS presented in Fig. 3. Secondly, the exchange occurs between an empty electron shell and a partially filled one, the valence angle of exchange interaction path having a value close to 90° (from 88.68° to 92.14°). According to the Goodenough-Kanamori-Anderson rules, such an exchange interaction is a superexchange interaction that forms FM. Thirdly, the FM increases with increasing $d_{M\text{-}M}$, which indicates a weakening possible direct exchange interaction, which is the AFM.

The third mechanism is AFM. It occurs between t_{2g} orbitals of different symmetry on two Cr^{3+} through hybridization with p-orbitals of the chalcogen (J_{tt}, Fig. 6). This exchange is insignificant and is determined by a small deviation of the local magnetic moment on the t_{2g} orbitals. The total exchange interaction integral consists of contributions given by each exchange interaction mechanism:

$$J = J_{tt} + J_{kin} + J_{te}. \qquad (11)$$

The first and second terms of the equation are responsible for the AFM. The third term has a negative sign and reflects the contribution of the FM. Thus, to form a stable high-temperature FM, it is necessary to increase J_{te} using strategies aimed at enhancing hybridization and/or decreasing J_{tt} and J_{kin} using strategies that affect structural properties.

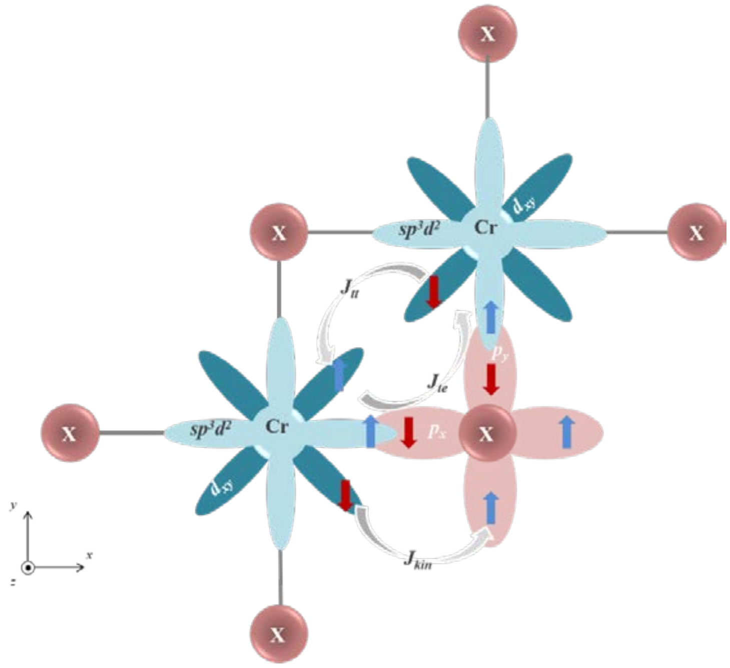

Fig. 6. Mechanisms of exchange interaction

Influence of the Hubbard coefficient on the simulated magnetic order. The hybridization of electron orbitals is highly dependent on the Hubbard coefficient (U) in quantum mechanical calculations. Since hybridization is the key phenomenon that determines the dominant exchange interaction mechanism in MAX_3, then U can have a strong influence on the main magnetic order and the quantitative value of J. We performed quantum mechanical calculations of J_1 for various U (Table 2).

AFM weakens as U increases from 0 to 3 eV, in $CrSiS_3$. The weak AFM in $CrGeS_3$ transforms into an unstable FM. FM is enhanced in other atomic systems. The choice of U remains an important criterion for characterizing the exchange interaction. The differences between the results of similar theoretical works mainly lie in different choices of this parameter.

Table 2. Exchange interaction integral for different values of *U*, meV

MAX_3	J_1 (*U*=0 eV)	J_1 (*U*=1 eV)	J_1 (*U*=3 eV)
$CrGeS_3$	0.72	0.06	-0.39
$CrGeSe_3$	-0.18	-0.68	-1.04
$CrGeTe_3$	-1.73	-2.07	-2.35
$CrSiS_3$	2.47	1.53	0.85
$CrSiSe_3$	-1.59	-1.74	-1.88
$CrSiTe_3$	-1.26	-1.48	-1.61

4. Conclusions

The main magnetic order of $CrGeSe_3$, $CrGeTe_3$, $CrSiSe_3$, and $CrSiTe_3$ atomic systems is FM. $CrGeS_3$ and $CrSiS_3$ exhibit AFM. 90-95% of the total magnetic moment is localized on the *d*-orbitals of Cr^{3+} and ranges from 2.94 to 3.44 μ_B. A slight deviation from the integer value indicates the hybridization of the Cr^{3+} *d*-electrons with the surrounding ions.

Increasing the principal quantum number of the outer electron shell of the chalcogen leads to weakening the hybridization of the atomic orbitals of Cr^{3+} and surrounding ions, with the formation of a common molecular orbital σ, as well as increasing J_3. Si and Ge do not have a direct influence on the relationships between electronic properties and magnetic parameters. An increase in $d_{M\text{-}M}$ leads to FM, as well as an increase in ς^2 in AFM compounds ($CrSiS_3$ and $CrGeS_3$) leads to a decrease in the value of J_1.

The found dependencies indicate three competing mechanisms of exchange interaction. FM is formed due to the mechanism of superexchange interaction. AFM exchange interaction is carried out by kinetic direct exchange and superexchange interaction.

It has been established that the axis of easy magnetization lies normal to the plane of quasi-two-dimensional layers, i.e., along the [001] crystallographic direction. This provides an increase in the energy efficiency of spintronic devices. T_c for the studied compounds lying in the range from 59.22 to 129.01 K. To form a stable high-temperature FM, the exchange interaction by the superexchange FM mechanism should be increased using strategies aimed at enhancing hybridization (external electric field, deformation), and/or reducing AFM direct exchange interaction through the use strategies that affect structural properties (deformation). Another way is to increase the E_{MAE} by varying the composition.

References

1. Mermin ND, Wagner H. Absence of ferromagnetism or antiferromagnetism in one-or two-dimensional isotropic Heisenberg models. *Physical Review Letters*. 1966;17(22): 1133.
2. Onsager L. Crystal statistics. I. A two-dimensional model with an order-disorder transition. *Physical Review*. 1944;65(3-4): 117.
3. Singh SP. The Ising model: Brief introduction and its application. In: *Solid State Physics-Metastable, Spintronics Materials and Mechanics of Deformable Bodies-Recent Progress.* IntechOpen; 2020.
4. Nowak U. Classical spin models. In: *Fundamentals of micromagnetism and discrete computational models.* Wiley; 2007. p.858-876.
5. Cortie DL, Causer GL, Rule KC, Fritzsche H, Kreuzpaintner W, Klose F. Two-dimensional magnets: forgotten history and recent progress towards spintronic applications. *Advanced Functional Materials*. 2020;30(18): 1901414.
6. Niss M. History of the Lenz–Ising Model 1950–1965: from irrelevance to relevance. *Archive for History of Exact Sciences*. 2009;63(3): 243-287.
7. Wolf WP. The Ising model and real magnetic materials. *Brazilian Journal of Physics*. 2000;30(4): 794-810.

8. Lee JU, Lee S, Ryoo JH, Kang S, Kim TY, Kim P, Cheong H. Ising-type magnetic ordering in atomically thin FePS3. *Nano Letters*. 2016;16(12): 7433-7438.

9. Du KZ, Wang XZ, Liu Y, Hu P, Utama MIB, Gan CK, Kloc C. Weak van der Waals stacking, wide-range band gap, and Raman study on ultrathin layers of metal phosphorus trichalcogenides. *ACS Nano*. 2016;10(2): 1738-1743.

10. Wang X, Du K, Liu YYF, Hu P, Zhang J, Zhang Q, Xiong Q. Raman spectroscopy of atomically thin two-dimensional magnetic iron phosphorus trisulfide (FePS3) crystals. *2D Materials*. 2016;3(3): 031009.

11. Lee S, Choi KY, Lee S, Park BH, Park JG. Tunneling transport of mono-and few-layers magnetic van der Waals MnPS3. *APL Materials*. 2016;4(8): 086108.

12. Lin MW, Zhuang HL, Yan J, Ward TZ, Puretzky AA, Rouleau CM, Xiao K. Ultrathin nanosheets of CrSiTe 3: a semiconducting two-dimensional ferromagnetic material. *Journal of Materials Chemistry C*. 2016;4(2): 315-322.

13. Huang B, Clark G, Navarro-Moratalla E, Klein DR, Cheng R, Seyler KL, Xu X. Layer-dependent ferromagnetism in a van der Waals crystal down to the monolayer limit. *Nature*. 2017;546(7657): 270-273.

14. Casto LD, Clune AJ, Yokosuk MO, Musfeldt JL, Williams TJ, Zhuang HL, Mandrus D. Strong spin-lattice coupling in CrSiTe3. *APL Materials*. 2015;3(4): 041515.

15. Williams TJ, Aczel AA, Lumsden MD, Nagler SE, Stone MB, Yan JQ, Mandrus D. Magnetic correlations in the quasi-two-dimensional semiconducting ferromagnet CrSiTe 3. *Physical Review B*. 2015;92(14): 144404.

16. Carteaux V, Brunet D, Ouvrard G, Andre G. Crystallographic, magnetic and electronic structures of a new layered ferromagnetic compound Cr2Ge2Te6. *Journal of Physics: Condensed Matter*. 1995;7(1): 69.

17. Ji H, Stokes RA, Alegria LD, Blomberg EC, Tanatar MA, Reijnders A, Cava RJ. A ferromagnetic insulating substrate for the epitaxial growth of topological insulators. *Journal of Applied Physics*. 2013;114(11): 114907.

18. Alegria LD, Ji H, Yao N, Clarke JJ, Cava RJ, Petta JR. Large anomalous Hall effect in ferromagnetic insulator-topological insulator heterostructures. *Applied Physics Letters*. 2014;105(5): 053512.

19. Zhang X, Zhao Y, Song Q, Jia S, Shi J, Han W. Magnetic anisotropy of the single-crystalline ferromagnetic insulator Cr2Ge2Te6. *Japanese Journal of Applied Physics*. 2016;55(3): 033001.

20. Yang D, Yao W, Chen Q, Peng K, Jiang P, Lu X, Zhou X. Cr2Ge2Te6: high thermoelectric performance from layered structure with high symmetry. *Chemistry of Materials*. 2016;28(6): 1611-1615.

21. Liu S, Yuan X, Zou Y, Sheng Y, Huang C, Zhang E, Xiu F. Wafer-scale two-dimensional ferromagnetic Fe3GeTe2 thin films grown by molecular beam epitaxy. *2D Materials and Applications*. 2017;(1): 1-7.

22. Pei QL, Luo X, Lin GT, Song JY, Hu L, Zou YM, Sun YP. Spin dynamics, electronic, and thermal transport properties of two-dimensional CrPS4 single crystal. *Journal of Applied Physic*. 2016;119(4): 043902.

23. Mayorga-Martinez CC, Sofer Z, Sedmidubsky D, Huber S, Eng AYS, Pumera M. Layered metal thiophosphite materials: magnetic, electrochemical, and electronic properties. *ACS Applied Materials & Interfaces*. 2017;9(14): 12563-12573.

24. McGuire MA, Garlea VO, Santosh KC, Cooper VR, Yan J, Cao H, Sales BC. Antiferromagnetism in the van der Waals layered spin-lozenge semiconductor CrTe3. *Physical Review B*. 2017;95(14): 144421.

25. McGuire MA, Clark G, Santosh KC, Chance WM, Jellison Jr GE, Cooper VR, Sales BC. Magnetic behavior and spin-lattice coupling in cleavable van der Waals layered CrCl 3 crystals. *Physical Review Materials*. 2017;1(1): 014001.
26. Sun X, Yao T, Hu Z, Guo Y, Liu Q, Wei S, Wu C. In situ unravelling structural modulation across the charge-density-wave transition in vanadium disulfide. *Physical Chemistry Chemical Physics.* 2015;17(20): 13333-13339.
27. Zhong D, Seyler KL, Linpeng X, Cheng R, Sivadas N, Huang B, Xu X. Van der Waals engineering of ferromagnetic semiconductor heterostructures for spin and valleytronics. *Science Advances*. 2017;3(5): e1603113.
28. Yang J, Wang W, Liu Y, Du H, Ning W, Zheng G, Zhang Y. Thickness dependence of the charge-density-wave transition temperature in VSe2. *Applied Physics Letters*. 2014;105(6): 063109.
29. Shao Y, Song S, Wu X, Qi J, Lu H, Liu C, Gao HJ. Epitaxial fabrication of two-dimensional NiSe2 on Ni (111) substrate. *Applied Physics Letters*. 2017;111(11): 113107.
30. Huang B, Clark G, Navarro-Moratalla E, Klein DR, Cheng R, Seyler KL, Xu X. Layer-dependent ferromagnetism in a van der Waals crystal down to the monolayer limit. *Nature*. 2017;546(7657): 270-273.
31. Kuo CT, Neumann M, Balamurugan K, Park HJ, Kang S, Shiu HW, Park JG. Exfoliation and Raman spectroscopic fingerprint of few-layer NiPS3 van der Waals crystals. *Scientific Reports*. 2016;6(1): 1-10.
32. Kuo CT, Balamurugan K, Shiu HW, Park HJ, Sinn S, Neumann M, Noh TW. The energy band alignment at the interface between mechanically exfoliated few-layer NiPS3 nanosheets and ZnO. *Current Applied Physics*. 2016;16(3): 404-408.
33. Xing W, Chen Y, Odenthal PM, Zhang X, Yuan W, Su T, Han W. Electric field effect in multilayer Cr2Ge2Te6: a ferromagnetic 2D material. *2D Materials*. 2017;4(2): 024009.
34. Chu J, Wang F, Yin L, Lei L, Yan C, Wang F, He J. High-performance ultraviolet photodetector based on a few-layered 2D NiPS3 nanosheet. *Advanced Functional Materials*. 2017;27(32): 1701342.
35. Kresse Georg. VASP the Guide. Available from: http://cms. mpi. univie. ac. at/vasp.
36. Hazen RM, Downs RT, Prewitt CT. Principles of comparative crystal chemistry. *Reviews in Mineralogy and Geochemistry*. 2000;41(1): 1-33.
37. Tang W, Sanville E, Henkelman G. A grid-based Bader analysis algorithm without lattice bias. *Journal of Physics: Condensed Matter*. 2009;21(8): 08420
38. Wood DL, Ferguson J, Knox K, Dillon Jr JF. Crystal-field spectra of d 3, 7 ions. III. Spectrum of Cr3+ in various octahedral crystal fields. *Journal of Chemical Physics*. 1963;39(4): 890-898.
39. Naruse Y, Takamori A. Orbital Phase Perspective of Goodenough-Kanamori-Anderson Rules (GKA Rules) in Superexchange Interaction. 2020. ChemRxiv [Preprint]. Available from: 10.26434/chemrxiv.10251563.v2.

THE AUTHORS

Maria S. Baranava
e-mail: baranova@bsuir.by
ORCID: 0000-0002-2618-4464

Viktor R. Stempitsky
e-mail: vstem@bsuir.by
ORCID: 0000-0001-9362-7539

Materials Physics and Mechanics. 2022;49(1): 85-96
Conference materials
http://dx.doi.org/10.18149/MPM.4912022_6

Silicon carbide membranes for micro-electro-mechanical-systems based CMUT with influence factors

Moumita Pal[1,2], **Niladri Pratap Maity**[1]✉, **Reshmi Maity**[1]

[1]Department of Electronics and Communication Engineering, Mizoram University (A Central University),
Aizawl-796004, India

[2]Department of Electronics and Communication Engineering, JIS College of Engineering, Kolkata, India

✉ maity_niladri@rediffmail.com

Abstract. An analytical model is developed for evaluating the characteristic parameters of silicon carbide (SiC) based capacitive micromachined ultrasonic transducer (CMUT) under the effect of a high-k dielectric insulation layer. The performance of parallel plate structured CMUT is investigated by considering various widths of the insulation layer, membrane thickness, diameter, and bias followed by validation of results using finite element method (FEM) simulation. Consideration of the fringing effect results in noticeable improvements in device capacitance. This enhancement leads to improvement in displacement due to static bias, signal, and coupling coefficient. The comparative analysis is carried out between hafnium oxide (HfO_2) and silicon nitride (Si_3N_4) insulation layers. CMUT having HfO_2 insulation of 500 nm thickness exhibits resonance at 1.62 MHz and displacement of 405 nm. Approximately 20% enhancement occurs in displacement as compared with Si_3N_4 as insulation.

Keywords: CMUT, HfO_2 insulation, High-k dielectric material, SiC actuation layer

Acknowledgements*. No external funding was received for this study.*

Citation: Pal M, Maity NP, Maity R. Silicon carbide membranes for micro-electro-mechanical-systems based CMUT with influence factors. *Materials Physics and Mechanics*. 2022;49(1): 85-96. DOI: 10.18149/MPM.4912022_6.

1. Introduction

Ultrasonic transducers are involved in medical imaging, which involves the usage of ceramics, different crystals of polymer, piezoelectric, and piezo composite materials. To overcome the shortcomings of piezoelectric transducers, micromachined ultrasonic transducers (MUTs) are introduced. Based on the variation of device capacitance CMUT works and thus modulation of electrostatic force takes place. This capacitive device is mostly involved in the emission and detection of ultrasonic waves [1-4]. The MEMS fabrication technique allows for the creation of CMUTs with high flexibility, low-temperature fabrication, downsizing, and, most importantly, good reproducibility. Significant advancements in material science have made it possible to use a wide choice of MEMS materials for fabrication, based on the prime needs in the various application domains. Metals like Ni (nickel), Al (aluminium), non-metals like Si (silicon), Ge (germanium), polymers like SU8, polyimide like diamond, SiC (silicon carbide), Si_3N_4 (silicon nitride), and SiO_2 (silicon dioxide) are utilised in membrane fabrication [5-8]. Many research have shown that the

Publisher: Peter the Great St. Petersburg Polytechnic University

structure and composition of the membrane have a significant impact on resonance frequency. Employing surface micromachining technology Si_3N_4 is used for fabricating both the membrane and the insulating layer material. Si is used as the membrane in another Si_3N_4-based CMUT, and SiO_2 is used to form insulation layer in transducers fabricated by wafer-bonding technique. [9-11].

Modeling a CMUT cell with a circular Si_3N_4 membrane and varied electrode configurations is used to investigate the effects of collapse and snapback voltage. The CMUT's static finite element calculations were validated using a licenced FEM application (PZFlex) [12-13]. Applying bias to the structure, an equivalent swing will take place due to the membrane's displacement while operating in transmission mode. Electrostatic force holds a non-linear relationship for the bias to the transduction gap [14], hence, to operate at a low voltage effectively, transduction gap between top and bottom electrodes is to be reduced. Considering all the limitations caused by fabrication, transmission of desired pressure at operating frequency is only possible by maintaining a minimum transduction gap. During a complete swing in transmission mode and a collapsed condition in receiving mode, the distance between the top and bottom electrodes can be spanned, which results in an electrical shock. As a precaution against being affected by electric shock, a dielectric layer must now be presented. Due to electrostatic attraction force, the insulating layer must withstand the generated electric field in the device.

In addition to this during collapsed mode also electrodes get separated due to this insulation layer [14-15]. Inclusion of the insulation layer reduces both the electric field and device capacitance as separation between two electrodes increases, so to retain the same membrane displacement the choice of a dielectric layer is an essential factor for determining the performance. The parameters can be rescued from having detrimental value by laying the actuation layer patterning above the top electrode. In case of less separation gap, the generated electrostatic pressure is a much smaller value compared to Van der Waals pressure. When the top electrode approached the bottom electrode and made contact, it remained stuck due to the low energy level, as the total removal energy reached a minimum level. This total energy is made up of energy that has been restored due to the surface's deformation and attraction.

Analytical modeling [16] is well demonstrated about a SiC-based CMUT having an insulation layer of Si_3N_4 having a 110 µm diameter membrane. A resonance of 1.65 MHz is exhibited by this CMUT array which consists of higher device capacitance, enhanced displacement in the membrane, larger coupling factor, and lower collapse voltage as compared to a non-insulated counterpart with the same device dimension. As a transducer, the features of the insulated construction are desirable. All of the results are compared to FEM, and there is a lot of consistency. The use of a high-k dielectric material improves the effectiveness of creating a high electric field while keeping the transduction gap the same. Moreover further increase of bias is not required for both in transmitting and receiving mode.

In this paper, a comparative analysis is done based on different high- k dielectric materials [17-19] strongly supported by FEM simulation outcomes.

2. Structure of insulated CMUT with silicon carbide-based membrane

CMUT is a capacitive device having metalized membrane upon a top electrode and another bottom electrode [20-27]. The insulating layer is developed by patterning the top electrode just below the thin metalized membrane of 2 µm and electrode diameter of 110 µm forming one of the electrodes over a tiny gap of 450 nm over the entirely doped Si in an insulated element as shown in Fig. 1.

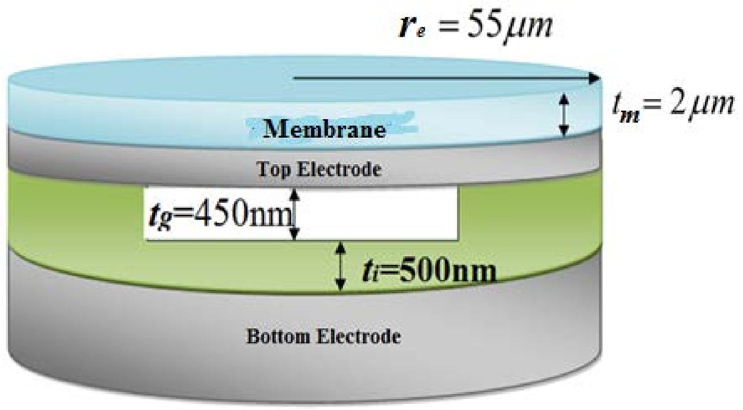

Fig. 1. 3D model of insulated CMUT

3. Proposed analytical model

Considering the fringing effect by Landau and Lifschitz's approach [16], the gap capacitance is C_{gf} and C_{if} is the same for the insulation layer. This gives, the following equations respectively

$$C_{gf} = \varepsilon_g \left[\left(\frac{\pi r_e^2}{t_g} \right) + r_e \ln \left\{ \left(\frac{16\pi r_e}{t_g} \right) - 1 \right\} \right], \tag{1}$$

$$C_{if} = \varepsilon_a \left[\left(\frac{\pi r_e^2}{t_i} \right) + r_e \ln \left\{ \left(\frac{16\pi r_e}{t_i} \right) - 1 \right\} \right]. \tag{2}$$

Now C_{eqf} is considered as the equivalent series capacitance due to fringing for both the insulation layer and the air gap. As a result, an insulated structure's equivalent device capacitance can be represented as

$$C_{eqf} = \frac{\left\{ \frac{\pi r_e}{t_g} + \ln\left(\frac{16\pi r_e}{t_g} - 1 \right) \right\} \left\{ \frac{K_i \pi r_e}{t_i} + K_i \ln\left(\frac{16\pi r_e}{t_i} - 1 \right) \right\}}{\left\{ \frac{\pi r_e}{t_g} + \ln\left(\frac{16\pi r_e}{t_g} - 1 \right) \right\} + \left\{ \frac{K_i \pi r_e}{t_i} + K_i \ln\left(\frac{16\pi r_e}{t_i} - 1 \right) \right\}}. \tag{3}$$

Here, t_g is denoted for the air gap, t_i is the width of the insulation layer and the area of the electrodes is represented by $A = \pi r_e^2$, where r_e is the electrode radius. Permittivity of the insulating layer is expressed as $K_i \varepsilon_g = \varepsilon_i$, the dielectric constant of the insulation layer is K_i. the gap permittivity value ε_g is 8.85 × 10^{-12} $C^2/(N\text{-}m^2)$. Generally, the electrostatic force due to fringing can be expressed as

$$F_f = \frac{1}{2} \left\{ \frac{v(t)^2 C_{if}^2}{C_{gf}^2 \left(\frac{C_{if}}{C_{gf}} + 1 \right)^2} \right\} \left[\varepsilon_g \left(\frac{\pi r_e^2}{t_g^2} \right) + \frac{\varepsilon_g r_e}{\left(\frac{16\pi r_e}{t_g} - 1 \right)} \times \left(\frac{16\pi r_e}{t_g^2} \right) \right]. \tag{4}$$

A large bias is rendered along the signal to produce an observable amount of electrostatic force at resonance. Mason's analysis can be used to determine the mechanical behaviour of the CMUT membrane. The motion of a membrane under strain will be expressed as

$$\left\{\frac{\left(Y_m+T_m\right)t_m^{\ 3}}{12\left(1-\sigma_m^{\ 2}\right)}\right\}\nabla^4 w_m-\left(T_m\right)\nabla^2 w_m-P+t_m\rho_m\left(\frac{\partial^2 w_m}{\partial t^2}\right)=0\,. \tag{5}$$

Here t_m is the membrane thickness, Y_m is Young's modulus of the membrane, σ_m is the Poisson ratio and w_m is the membrane displacement involving Mason's model, T_m is the membrane tension and ρ_m is the material density of actuating material. For an insulated element with a fringing effect, the peak displacement at the centre under static bias becomes

$$w_{m_{bias}}=\left(\frac{1}{8AT_m}\right)\left\{\frac{V_{dc}^{\ 2}C_{if}^{\ 2}r_m^{\ 2}}{\left(\dfrac{C_{if}}{C_{gf}}+1\right)^2 C_{gf}^{\ 2}}\right\}\times\left[\left(\frac{\varepsilon_g\pi r_e^{\ 2}}{t_g^{\ 2}}\right)+\left(\frac{\varepsilon_g r_e}{\left(\dfrac{16\pi r_e}{t_g}\right)-1}\right)\times\left(\frac{16\pi r_e}{t_g^{\ 2}}\right)\right]. \tag{6}$$

The dynamic response is carried out due to the application of signal in the device and is given by

$$w_{signal}(r)=\frac{P_{signal}}{\omega^2\rho_m t_m}\left\{\left(J_0\left(\frac{\omega}{\upsilon}r\right)\Big/J_0\left(\frac{\omega}{\upsilon}r_m\right)\right)-1\right\}. \tag{7}$$

The description of the membrane's Z_m acoustic impedance is now essential for the model's correct calculation. The measurement of effective mechanical impedance of the membrane is carried out by the ratio of the applied pressure to the surface's average velocity. Estimation of the volume velocity through the device is attained by integrating the velocity given by $w_m(r_m,t)$ over the surface, considering the entire circular membrane.

$$V_{total}=\int_0^{r_m}\left(\dot{w}\left(r_m,t\right)\right)\left(2\pi r_m\right)dr_m=2\pi\int_0^{r_m}\left(\dot{w}\left(r_m,t\right)\right)r_m dr_m=j2\pi\omega\int_0^{r_m}w\left(r_m\right)r_m dr_m\,. \tag{8}$$

The applied pressure to the surface's average velocity will be given by

$$V_{average}=\frac{j2\pi\omega}{\pi r_m^{\ 2}}\int_0^{r_m}w\left(r_m\right)r_m dr_m=\frac{j2}{r_m^{\ 2}}\frac{P_{signal}}{\omega\rho_a t_a}\left[\frac{1}{J_0\left(kr_m\right)}\int_0^{r_m}r_m J_0\left(kr_m\right)dr_m-\int_0^{r_m}r_m dr_m\right]. \tag{9}$$

Employing the well-known integral, $\int rJ_0\left(kr\right)dr=\frac{J_1(kr)}{k}$, The membrane's effective mechanical impedance is defined as

$$Z_m=\left[\frac{-j\omega\rho_a t_m kr_m J_0\left(kr_m\right)}{2J_1\left(kr_m\right)-kr_m J_0\left(kr_m\right)}\right]. \tag{10}$$

For a capacitive element, measurement of collapse voltage is quite an impacted factor while operated at its best working point. The operating bias applied to the MUT determines its performance. Different operating modes exist based on the membrane's behaviour under static conditions, such as collapsed mode and conventional mode. The electrostatic force generated by the applied DC voltage pulls the membrane towards the substrate, which is countered by the membrane's mechanical restoring force. An increase in bias also enhances membrane displacement. A voltage imbalance between these restorative and electrostatic forces occurs over a specific voltage, causing the membrane to collapse down onto the substrate. The mathematical analysis is initiated with the assumption that the sum of the capacitor and spring forces actuates mass, hence the equation is expressed as

$$F_{CAPACITOR}+F_{SPRING}=F_{MASS}\,. \tag{11}$$

Hence, the collapse voltage can be expressed as

$$V_{collapse} = \sqrt{\frac{8K_m\left(t_g+\left(\frac{\varepsilon_g}{\varepsilon_i}\right)t_i\right)^3}{27\varepsilon_g A}}, \tag{12}$$

where K_m is the spring constant. The dimensionless factor coupling coefficient is a characterization parameter that measures the energy transformation capability of the transducer from one type to another. Most influencing parameters that have a great impact on coupling coefficients are stress distribution, presence of the electric field, and cell geometry, as well as the type of material, all of which influence coupling coefficients [16]. The dynamic coupling factor is expressed as

$$k_w = \sqrt{\frac{\varepsilon_g A V_{dc}^2}{\varepsilon_g A V_{dc}^2 + 26.28\times(P_r t_m d_{eff}^3)}}, \tag{13}$$

where,

$$d_{eff} = \left(t_g + \frac{\varepsilon_g}{\varepsilon_i} t_i\right). \tag{14}$$

4. Results and Discussion

A mathematical model is used to investigate the capacitance behaviour, collapse voltage, and coupling factor of the CMUT. For optimizing the device's energy conversion, sensitivity, operating point, and efficiency, all the factors should be considered. A smaller gap and thinner insulator suggest a closer distance between the pair of electrodes, resulting in a higher voltage across the plates (field force) and charge composed on the plates (flux) for any voltage applied across the two electrodes, resulting in larger capacitance. Materials with a high dielectric constant have a higher permittivity than materials with a lower permittivity, allowing them to suggest less field flux disagreement for a given field force. All of these results may be deduced from a simple observation of ordinary capacitor plates, and the analytical model can be used to calculate capacitance for any pair of unconnected conductors. FEM simulation is used to verify all of the results. At a 55 µm membrane radius, the device capacitance calculated for the CMUT is 0.163 pF, providing a force of 1.263 µN.

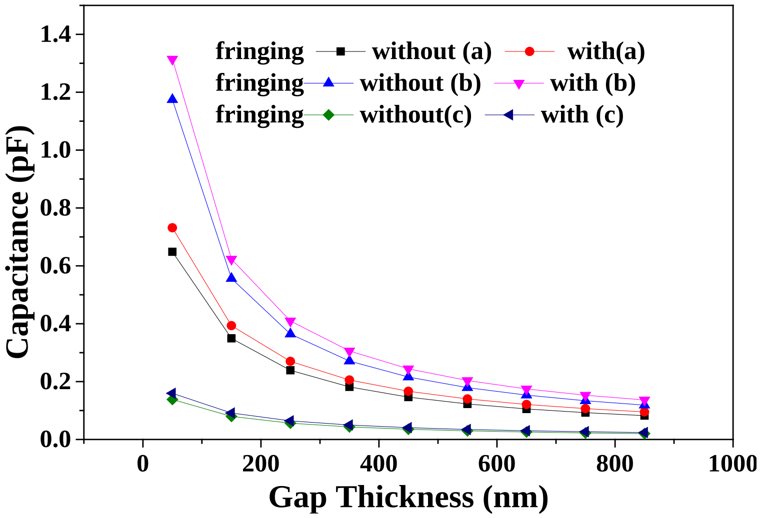

Fig. 2. Capacitance of the device with varying width of air gap for a) r_e = 55 µm, t_i = 500 nm, b) r_e = 65 µm, t_i = 300 nm, c) r_e = 27.5 µm, t_i = 650 nm

Figure 2 depicts the variance in device capacitance as a function of gap thickness. With regard to gap thickness, the capacitance drops in a parabolic way. The device capacitance is higher when the electrode radius is larger and the insulation thickness is thinner. As seen in Fig. 3, the gap thickness increases the fringe capacitance.

The fringing effect is amplified by greater gap thickness, smaller electrode radius, and larger valued insulation thickness. An average E'_C of 13.27% enrichment takes place for $t_g = 650$ nm, $t_i = 300$ nm, and 16.79% for $t_g = 300$ nm, $t_i = 650$ nm.

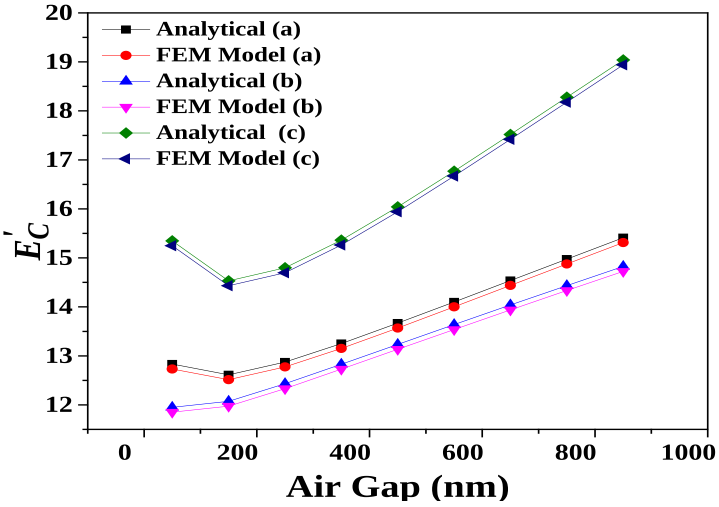

Fig. 3. E'_C with respect to air gap for a) $r_e = 55$ µm, $t_i = 500$ nm, b) $r_e = 65$ µm, $t_i = 300$ nm, c) $r_e = 27.5$ µm, $t_i = 650$ nm

Figure 4 illustrates the electrostatic force as a function of insulation thickness, with the electrostatic force decreasing as the insulation thickness of the dielectric layer increases. It is critical to select the proper dielectric insulation thickness because it is one of the determining factors in producing excellent accuracy and electrostatic force. Figure 5 further indicates that the fringing approach improves electrostatic force significantly with respect to insulation thickness. The fringing effect has a bigger impact above 300 nm of insulation thickness and lesser in lower values. An average value E'_F of 11.24% is observed by changing the insulation thickness while designing is done.

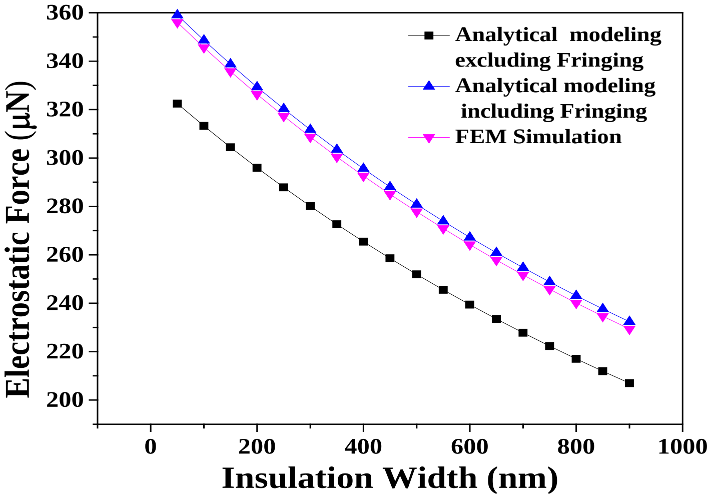

Fig. 4. For variable insulation layer thicknesses, electrostatic force is used

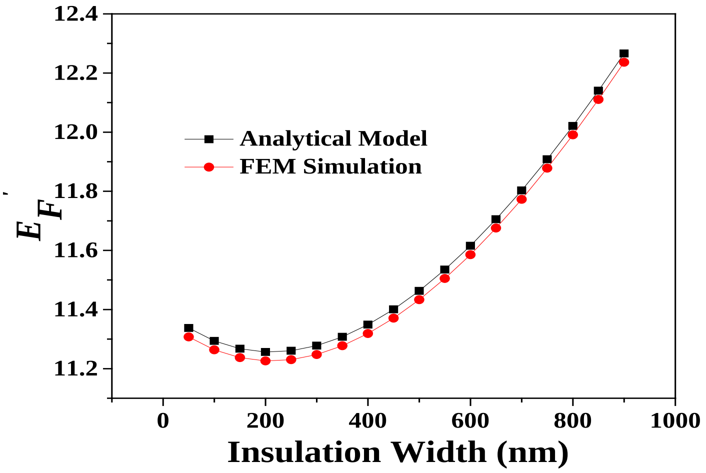

Fig. 5. E'_F for varying thickness of insulation layer

Figure 6 illustrates that when the membrane radius is at its largest, the material permittivity displacement is at its highest. The figure depicts the changing type of membrane displacement as both parameters are increased. Displacement decreases as insulation thickness increases, resulting in maximum displacement at the minimum insulation width and maximum membrane radius, as shown in Figure 7.

The coupling capacitance reduces as the coupling distance (effective gap distance) grows, diminishing the intensity of the output energy. The membrane in CMUT transports in the presence of an applied electric field, with no transverse membrane vibration. In a CMUT, the coupling distance is also influenced by the gap distance and insulator thickness. At a bias voltage of 40 V DC, the coupling factor of the proposed structure is 0.384, indicating that the CMUT's coupling efficiency is 38.3 percent. When the surface tension of the membrane increases, the surface area of the membrane reduces, diminishing the coupling capacitance and the coupling factor. CMUTs have been shown in numerous investigations to work in both the conventional and collapse modes. The predicted collapse voltage is 78.16 V, with a coupling factor of 0.7, indicating that increasing the coupling factor has a substantial impact on transducer efficiency. The collapse voltage characteristics indicate that the collapse voltage decreases with increasing membrane radius and increases with increasing membrane thickness. This is connected with the fact that when the membrane's spring constant decreases, it becomes less stiff, and when it increases, it becomes stiffer, resulting in greater elasticity. FEM simulation is also used to validate all of the data.

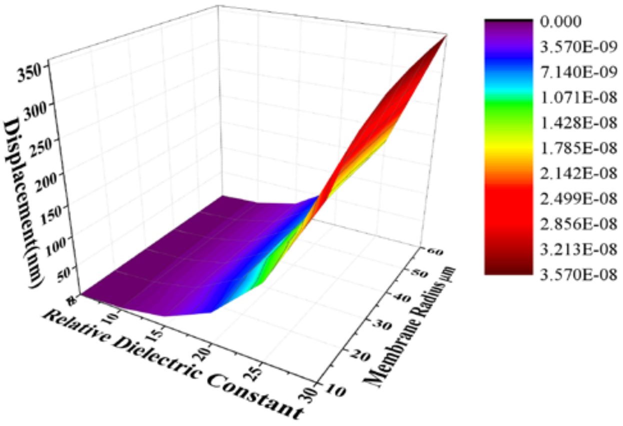

Fig. 6. Deviation of static displacement with simultaneous change in r_m and K

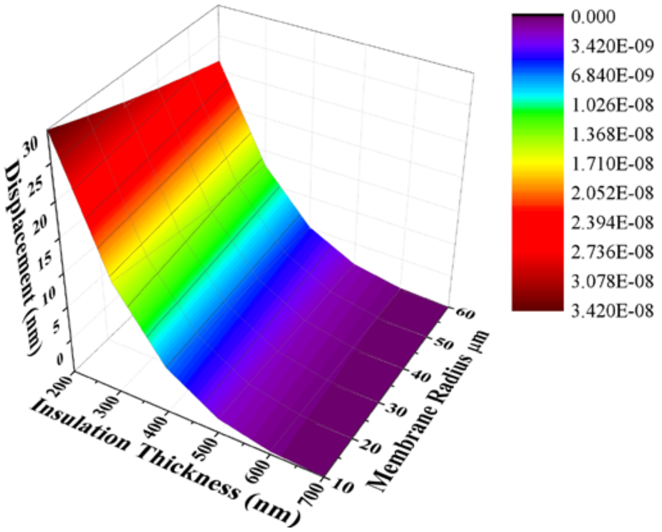

Fig. 7. Deviation of static displacement with simultaneous variation in r_m and t_i

Figure 8 depicts the variation of the membrane's spring constant and collapse voltage with changing membrane radius. Because the collapse voltage has a linear connection with the spring constant, an increase in radius reduces the spring constant. Furthermore, as demonstrated in Fig. 9, a decrease in membrane thickness lowers the collapse voltage value.

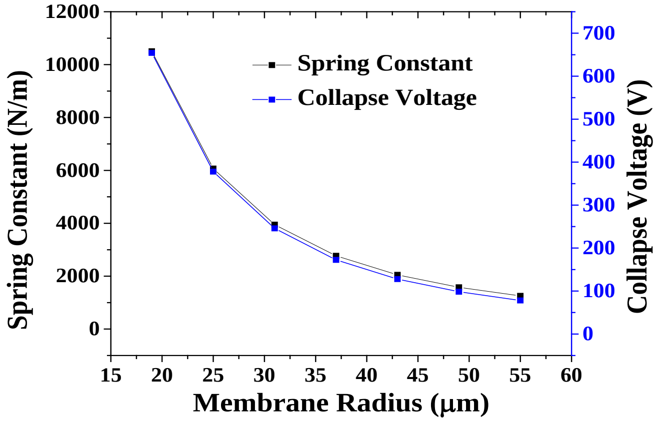

Fig. 8. Collapse voltage and spring constant as functions of a membrane radius

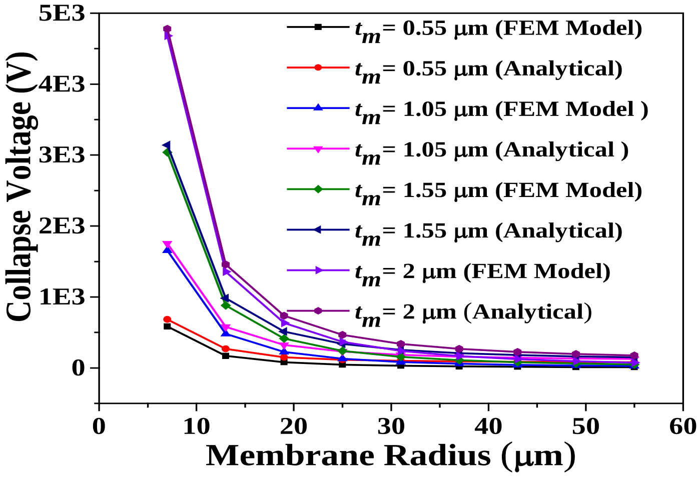

Fig. 9. Changes in collapse voltage when the membrane radius changes due to varied membrane thickness values

Figure 10 represents the variation of 3D displacement as a feature of frequency and membrane radius. The displacement of the membrane has maximum at the device's centre point. The resemblance of the designed structure's resonance during AC actuation, where resonance can be seen at 1.62 MHz [18], can be used for further validation. The resonance displacement is a maximum of 50 Å which matches the displacement shown in the constructed structure and is validated by simulation results. The presence of several resonances in CMUT is observed, as shown in the image. At first resonance, the maximum amplitude is observed, with sole dependency upon material usage and geometrical features of the device. The mechanical impedance is determined by the pressure-to-velocity ratio at the membrane's centre. As shown in Fig. 11, by obtaining the displacement with a particular pressure load, the variation of mechanical impedance can be measured. At the device resonance frequency, overall impedance is reduced to a minimum.

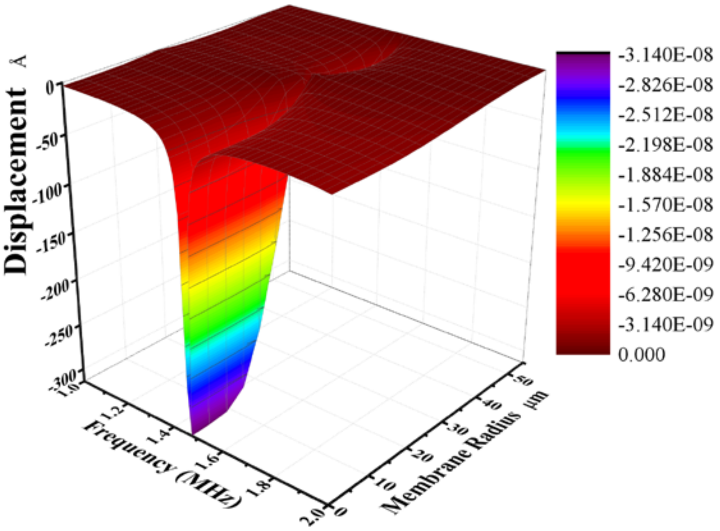

Fig. 10. 3D Frequency response of 110 µm actuated membrane

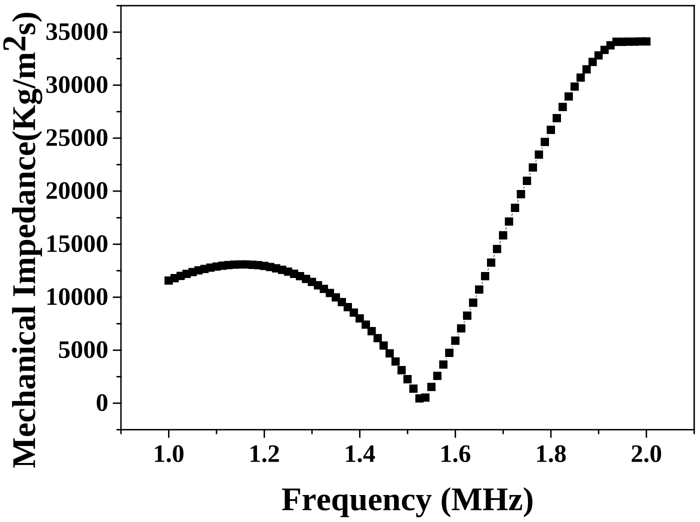

Fig. 11. Impedance profile as a function of frequency

5. Conclusion

The general functionality of SiC membranes CMUT is demonstrated in this study, along with its influencing factors. Higher sensitivity is achieved when the device capacitance is greater than the force exerted by the membrane. To achieve a high-sensitivity CMUT, the transduction gap and insulator layer thickness must be extremely thin, with a wide membrane radius, and the insulating layer material must have a high relative permittivity. A novel approach to fringing field capacitance is also included in the characteristic study of SiC-based CMUT. When compared to PECVD Si_3N_4, the performance of CMUT is superior in all respects. This increase in CMUT parameters will surely improve its sensitivity for high-frequency applications and in the acoustic medium. The AC response and impedance profile of the CMUT element were simulated using Mason's model for circular-shaped devices. Theoretical findings are supported by simulation findings, leading to even greater agreement. The imitative analytical model for the vented capacitive element contains multiple resonances. Because main resonance has a greater peak value displacement than secondary resonance, it will take precedence over secondary resonance. Because of its matched impedance to air and water, the device is suitable for both acoustic and air mediums. In this case, the coupling coefficient is around 0.67, and it is higher for thinner but larger-diameter membranes. In terms of membrane material, SiC outperforms Si_3N_4 as a structural layer in larger deformation and high-frequency implementations.

References

1. Hasan A, Nurunnabi M, Morshed M, Paul A, Polini A, Kuila T, Hariri M, Lee Y, Jaffa A. Recent advances in application of biosensors in tissue engineering. *BioMed Research International.* 2014;2014: 1-18.
2. Ramadoss R, Dean R, Xiong X. MEMS testing. In: *System-on-Chip Test Architectures.* 2008. p.591-651.
3. Mills DM. Medical imaging with capacitive micromachined ultrasound transducer (cMUT) arrays. *IEEE Ultrasonics Symposium Proceedings.* 2004;1: 384-390.
4. Ladabaum I, Jin X, Soh HT, Atalar A. Khuri-Yakub BT. Surface micromachined capacitive ultrasonic transducers. *IEEE Transactions on Ultrasonics, Ferroelectrics, and Frequency Control*. 1998;45(3): 678-690.
5. Logan A, Yeow JT. Fabricating capacitive micromachined ultrasonic transducers with a novel silicon-nitride-Based wafer bonding process. *IEEE Transaction on Ultrasonics, Ferroelectrics and Frequency Control*. 2009;56(5): 1074-1084.
6. Cetin M, Bayram, B. Diamond-Based Capacitive Micromachined Ultrasonic Transducers in Immersion. *IEEE Transaction on Ultrasonics, Ferroelectrics and Frequency Control*. 2013;60(2): 414-420.
7. Gerardo D, Cretu E, Rohling R. Fabrication and testing of polymer-based capacitive micromachined ultrasound transducers for medical imaging. *Microsystems & Nanoengineering*. 2018;4(19): 568-579.
8. Maity R, Maity NP, Rao KS, Guha K, Baishya S. A new compact analytical model of nanoelectromechanical systems-based capacitive micromachined ultrasonic transducers for pulse echo imaging. *Journal of Computational Electronics.* 2018;17(3): 1334-1342.
9. Huang Y, Zhuang X, Haeggstrom EO, Ergun AS, Cheng CH, Khuri-Yakub BT. Capacitive micromachined ultrasonic transducers with piston-shaped membranes: Fabrication and experimental characterization. *IEEE Transactions on Ultrasonics, Ferroelectrics, and Frequency Control.* 2009;56(1): 136-145.
10. Caronti A, Caliano G, Iula A, Pappalardo M. An accurate model for capacitive micro machined ultrasonic transducers. *IEEE Transactions on Ultrasonics, Ferroelectrics, and Frequency Control.* 2002;49(2): 159-168.
11. Lohfink A, Eccardt P. Linear and nonlinear equivalent circuit modeling of CMUTs. *IEEE Transactions of Ultrasonics, Ferroelectrics, and Frequency Control.* 2005;52(12): 2163-2172.

12. Nikoozadeh A, Bayram B, Yaralioglu G, Khuri-Yakub BT. Analytical calculation of collapse voltage of CMUT membrane. *IEEE Ultrasonics Symposium Proceedings*. 2004;1: 256-259.
13. Koymen H, Atalar A, Aydogdu E, Kocabas C, Oguz HK, Olcum S, Ozgurluk A, Unlugedik A. An improved lumped element nonlinear circuit model for a circular CMUT cell. *IEEE Transactions on Ultrasonics, Ferroelectrics, and Frequency Control*. 2012;59(8): 1791-1799.
14. Wygant IO, Kupnik M, Khuri-Yakub BT. Analytically calculating membrane displacement and the equivalent circuit model of a circular CMUT cell. *IEEE Ultrasonics Symposium*, 2008: 2111-2114.
15. Maity R, Maity NP, Thapa RK, Baishya S. Investigation of Si_3N_4 as an Excellent Membrane Material for MEMS Ultrasonic Transducers. *Applied Mechanics and Materials*. 2017;45: 567-571.
16. Pal M, Lalengkima C, Maity R, Baishya S, Maity NP. Effects of fringing capacitances and electrode's finiteness in improved SiC membrane based micromachined ultrasonic transducers. *Microsystem Technologies*. 2021;27: 3679-3691.
17. Panchanan S, Maity R, Baishya S, Maity NP. Modeling, simulation and analysis of surface potential and threshold voltage: application to high-K material HfO_2 based FinFET. *Silicon*. 2021;13(1): 3271-3289.
18. Maity NP, Maity R, Maity S, Baishya S. A new surface potential and drain current model of dual material gate short channel metal oxide semiconductor field effect transistor in sub-threshold regime: application to high-k material HfO_2. *Journal of Nanoelectronics and Optoelectronics.* 2019;14(6): 868-876.
19. Chakrabarti H, Maity R, Baishya S, Maity NP. An accurate model of threshold voltage and effect of high-k material for fully depleted graded channel DMDG MOSFET. *Silicon*. 2022. DOI: 10.1007/s12633-021-01412-w.
20. Maity R, Suvra S, Maity S, Maity NP. Collapse voltage analysis of central annular ring metallized membrane based MEMS micromachined ultrasonic transducer. *Microsystem Technologies.* 2020;26: 1001-1009.
21. Pal M, Maity NP, Maity R. An improved displacement model for micro-electro-mechanical-system based ultrasonic transducer. *Microsystem Technologies*. 2019;25: 4685-4692.
22. Maity R, Gogoi K, Maity NP. Micro-electro-mechanical-system based capacitive ultrasonic transducer as an efficient immersion sensor. *Microsystem Technologies*. 2019;25: 4663-4670.
23. Maity R, Maity NP, Baishya S. An efficient model of nanoelectromechanical systems based ultrasonic sensor with fringing field effects. *IEEE Sensors Journal*. 2020;20(4): 1746-1753.
24. Maity R, Maity NP, Guha K, Baishya S. Analysis of fringing capacitance effect on the performance of micro-electromechanical-system-based micromachined ultrasonic air transducer. *IET Micro and Nano Letters*. 2018;13(6): 872-876.
25. Maity R, Maity NP, Thapa RK, Baishya S. Analysis of frequency response behaviour of capacitive micromachined ultrasonic transducers. *Journal of Computational and Theoretical Nanoscience.* 2015;12(10): 3492-3494.
26. Maity R, Maity NP, Thapa RK, Baishya S. Analytical characterization and simulation of a 2-D capacitive micromachined ultrasonic transducer array element. *Journal of Computational and Theoretical Nanoscience.* 2015;12(10): 3692-3696.
27. Maity R, Singh A, Islam A, Maity NP, Thapa RK, Baishya S. Lumped electromechanical modeling of capacitive micromachined ultrasonic transducers. *Journal Materials Today: Proceedings.* 2016;3(6): 2289-2294.

THE AUTHORS

Moumita Pal
e-mail: moumitajisceece@gmail.com
ORCID: 0000-0002-8665-478X

Niladri Pratap Maity
e-mail: maity_niladri@rediffmail.com
ORCID: 0000-0002-1256-5856

Reshmi Maity
e-mail: reshmidas_2009@rediffmail.com
ORCID: 0000-0002-1254-3075

Materials Physics and Mechanics. 2022;49(1): 97-107
Conference materials
http://dx.doi.org/10.18149/MPM.4912022_7

First-principles study of anisotropic thermal conductivity of GaN, AlN, and $Al_{0.5}Ga_{0.5}N$

D.C. Hvazdouski✉**, M.S. Baranava, V.R. Stempitsky**

R&D Department, Belarusian State University of Informatics and Radioelectronics,
Minsk, P. Brovki Str 6, 119, 220013, Republic of Belarus
✉ gvozdovsky@bsuir.by

Abstract. The thermal stability of devices based on GaN, AlN, and $Al_{0.5}Ga_{0.5}N$ semiconductors is a critical property for efficient and reliable operation. The thermal conductivity of these materials has anisotropic nature. We proposed an approach for calculating the anisotropic thermal conductivity based on harmonic and anharmonic interatomic force constants of a lattice. The thermal-conductivity coefficient of GaN, AlN, and $Al_{0.5}Ga_{0.5}N$ in the [100], [001], and [111] directions were calculated using *ab initio* methods by solving the linearized Boltzmann transport equation. It equals $\lambda_{[100]} = 259.28$, $\lambda_{[001]} = 335.96$ and $\lambda_{[111]} = 309.56$ W/(m·K) for GaN; $\lambda_{[100]} = 396.06$, $\lambda_{[001]} = 461.65$ and $\lambda_{[111]} = 435.05$ W/(m·K) for AlN; and $\lambda_{[100]} = 186.74$, $\lambda_{[001]} = 165.24$ and $\lambda_{[111]} = 177.62$ W/(m·K) for $Al_{0.5}Ga_{0.5}N$ at 300 K. The dependence of the coefficient $\lambda(T)$ on temperature in the range from 250 to 750 K is presented. A comparative analysis of the GaN thermal conductivity investigations has been carried out for experimental studies and theoretical calculations.

Keywords: aluminum nitride, first-principle calculation, gallium nitride, thermal conductivity

***Acknowledgements**. This work was supported by grant 3.02.3 of Belarusian National Scientific Research Program "Convergence – 2025" and the grant of The Belarusian Republican Foundation for Fundamental Research for young scientists "Science M – 2021" (contract № F21M-122). Computing cluster of BSUIR was used for computer modeling.*

Citation: Hvazdouski DC, Baranava MS, Stempitsky VR. First-principles study of anisotropic thermal conductivity of GaN, AlN, and $Al_{0.5}Ga_{0.5}N$. *Materials Physics and Mechanics*. 2022;49(1): 97-107. DOI: 10.18149/MPM.4912022_7.

1. Introduction

The structures based on GaN, AlN, and AlGaN semiconductor nitrides are considered promising materials for electronic and optoelectronic technology. For many applications, GaAs is gradually changed by GaN because of its high polarization, chemical, and physical stability, and wide band gap. Gallium nitride appears as a perspective material for the development of the high-frequency, heat-resisting, and power semiconductor devices [1]. GaN transistors, unlike GaAs transistors, are suitable as high-frequency power amplifiers via high operating voltage and working temperatures [2]. Strong self-heating is typical for similar devices that give rise to thermal properties investigation of this material since the temperature stability is critical for effective and reliable work in many electronic devices and systems.

Publisher: Peter the Great St. Petersburg Polytechnic University

Thermal simulation can help to manage temperature mode, define the main reason for heating and estimate the wide spectrum of alternative variants for construction optimization. Heat transfer simulation in the device structure consists in solving the heat flow equation. The main parameter of this equation is thermal conductivity [3].

Discrepancies both in experimental and theoretical values given in the literature motivated our investigation. The empiric values of GaN and AlN thermal conductivities differ from each other significantly which is mostly associated with the difference in purity and microstructure of samples [4-9]. Theoretical models of thermal conductivity consist of a combination of the first-principle calculations and the solution of the linearized Boltzmann transport equation for phonons. They also have distinction, although less significant [10-15].

Furthermore, AlN, GaN, and $Al_{0.5}Ga_{0.5}N$ have C_{6v}^{4}-$P6_3mc$ symmetry space group that corresponds to hexagonal syngony [16]. Thus, anisotropy manifestation of the thermodynamic properties (including thermal conductivity) is typical for these materials. In this case, λ is introduced as a second rank tensor. However, in many papers, the thermal conductivity coefficient is considered a constant value [4-7,9,11,12]. Therefore the thermal conductivity models which take into consideration both temperature dependence and anisotropy are necessary for applied aims.

The main task of the presented work is the temperature dependence calculation of thermal conductivity of AlN, GaN, and $Al_{0.5}Ga_{0.5}N$ for different crystallographic directions via first-principal methods. Moreover, a comparative analysis of our results and those of other authors, where the results were obtained by both theoretical and experimental methods, is given.

2. Methodology of thermal conductivity calculation

For the thermal conductivity calculation, we take into account interactions at some physical levels. The first level is the atomic one (~ 10^{-9} m or some nanometers). The main objects on this level are recognized to be electrons. The calculations of structural and electronic properties of the systems studied are performed through the use of quantum-mechanics methods [17]. For the result verification, the obtained physical properties were compared with the experimental data of other authors. On the basis of the crystal structure got, the phonon spectra were determined by the methods [18,19]. We ignore electron contribution to the thermal conductivity since in the case of wide band gap gallium nitride GaN, aluminum nitride AlN, and gallium nitride – aluminum nitride alloy $Al_xGa_{1-x}N$, the contribution of electrons to the heat transfer is negligibly small compared to phonons. Really, according to [20], electron contribution to the thermal conductivity is about 1000 times less than phonon contribution for bulk crystal GaN sample (dopant concentration ~10^{16}-10^{18} cm^{-3}).

The next physical level is microscopic (~ 10^{-6} m or some micrometers), at which the interaction of objects of study (ions and valence electrons) can be described via classic interatomic potentials. On this level calculation of the lattice thermal conductivity of the material is performed using the software *Phono3py* [21,22]. In this case, the lattice thermal conductivity of a material is defined by solving the linearized Boltzmann equation (LBTE) for the phonons with the one-mode approximation of relaxation time [23] on the basis of calculated second rank harmonic interatomic force constants (IFC) and third rank anharmonic IFC.

The last physical level is macroscopic (~ 10^{-2} m or some centimeters), which is of interest for technology applications. Interactions in the system are usually described by the phenomenological theories on the macroscopic scale [24]. On this level, the crystal anisotropy and geometric dimensions are taken into account.

3. Results of the thermal conductivity calculations

First-principle calculation. Choice of the parameter set (computational grid for k-points, cutoff energy, etc.), exchange-correlation energy calculation methods, and pseudopotential set was performed based on convergence criteria of test calculation. During calculations of the structure properties, the energy difference between two iterations must not exceed 10^{-6} eV; during calculations of the phonon properties; the analogous value must not exceed 10^{-8} eV. The obtained numerical values of structural properties (crystal elementary cell characteristics) with setting calculation parameters must be close to experimental values (difference less than 5%). The supercells for further phonon dispersion calculation and for evaluating thermal conductivity were created by the elementary cell in the ground state.

To perform a series of first-principle calculations we used VASP software. PBE functional was used as exchanged-correlation functional. For all investigated structures, the cutoff energy of the plane waves was equal to 520 eV. The valence electron configurations for nitrogen N, aluminum Al, and gallium Ga were taken as $[He]2s^2 2p^3$, $[Ne]3s^2 3p^1$, and $[Ar]4s^2 3d^{10} 4p^1$, respectively. Non-self-consistent calculations were performed along the contour "M-K-Γ-A" between high symmetry points of the first Brillouin zone.

In Table 1 calculated crystal structure characteristics of GaN, AlN, and $Al_{0.5}Ga_{0.5}N$ are compared with the experimental data [25,26].

Table 1. Structure properties of the investigated crystals

Crystal	Symmetry group	Lattice constants, Å		Dispersion, %
		Calculated	Experimental	
GaN	C_{6v}^4-$P6_3mc$	$a = 3.164$ $c = 5.114$ $a/c = 0.618$	$a = 3.189$ $c = 5.186$ $a/c = 0.615$ [25]	1.388
AlN	C_{6v}^4-$P6_3mc$	$a = 2.983$ $c = 4.933$ $a/c = 0.605$	$a = 3.112$ $c = 4.982$ $a/c = 0.624$ [25]	4.145
$Al_{0.5}Ga_{0.5}N$	C_{6v}^4-$P6_3mc$	$a = 3.135$ $c = 4.917$ $a/c = 0.637$	$a = 3.149$ $c = 5.079$ $a/c =0.621$ [26]	3.189

For calculating the harmonic-second-rank-interatomic-force constants, 2×2×2 supercells were created. The 3×3×3 supercells with atom displacement of 0.01 Å were used for anharmonic IFC calculations. We considered the phonon-phonon interaction with the three closest atoms inside the supercell. The necessary information for supercell building was taken from the calculations of the structure properties.

Based on the harmonic and anharmonic interatomic force constants calculated with quantum-mechanics methods, the thermal conductivity coefficients were determined in the main crystallographic directions [100], [010], and [001] for GaN, AlN, and $Al_{0.5}Ga_{0.5}N$ in the temperature range from 0 to 1000 K with the help of software *Phono3py*. The hexagonal syngony of the crystals under investigation points on thermal conductivity characteristic features in crystallographic directions: $\lambda_{[100]} = \lambda_{[010]} = \lambda_{[110]}$, and also $\lambda_{[101]} = \lambda_{[011]} = \lambda_{[111]}$.

The obtained values of calculated thermal conductivity coefficients at 300 K are $\lambda_{[100]} = 259.28$ and $\lambda_{[001]} = 335.96$ W/(m·K) for GaN crystal; $\lambda_{[100]} =396.06$ and $\lambda_{[001]} = 461.65$ W/(m·K) for AlN crystal; $\lambda_{[100]} = 186.74$ and $\lambda_{[001]} = 165.24$ W/(m·K) for $Al_{0.5}Ga_{0.5}N$ crystal.

Anisotropy of the thermal conductivity. Using calculated values of the thermal conductivity coefficients in the crystallographic directions [100], [010], and [001], it is possible to define numerical values of thermal conductivity coefficients for crystallographic direction [u v w].

For some physical properties described by the second rank symmetric tensor (electrical conductivity, electrical dielectric permittivity, dielectric susceptibility, diffusion, thermal conductivity, thermal expansion, deformation), there is the simple geometric method of their presentation in quadric view. The thermal conductivity quadric for hexagonal syngony represents the spheroid generated by the rotation of an ellipse about the Z-axis with semi-axes λ_{xx}, λ_{xx}, and λ_{zz} (Fig. 1a). Form of the thermal conductivity tensor for crystals with hexagonal syngony is presented in Fig. 1b. Conversion from Cartesian coordinate system to spherical was performed for quadric presentation of thermal conductivity.

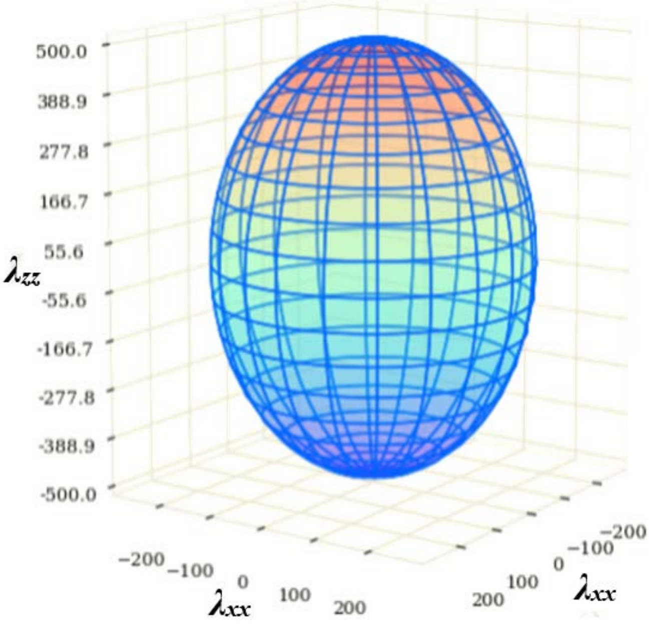

a

$$\lambda = \begin{bmatrix} \lambda_{xx} & 0 & 0 \\ 0 & \lambda_{xx} & 0 \\ 0 & 0 & \lambda_{zz} \end{bmatrix}$$

b

Fig. 1. Crystals with hexagonal syngony:
a) thermal conductivity quadric; b) form of thermal conductivity tensor

According to the Fourier law, heat flow q is associates with the temperature gradient and material thermal conductivity λ in the following way:

$$q = -\lambda \cdot \nabla T, \qquad (1)$$

where q is the local heat flow density, W/m^2, λ is the thermal conductivity of the material, W/(m·K), ∇T is the temperature gradient, K/m.

Since the thermal conductivity in the anisotropic materials appears to be a second-rank tensor, then the thermal-conductivity Fourier law (1) can be presented in a tensor form when transiting to a spherical coordinate system through the use of the following ratio:

$$q(\theta, \varphi) = -[\sin\theta \cdot \cos\varphi \quad \sin\theta \cdot \sin\varphi \quad \cos\theta] \begin{bmatrix} \lambda_{xx} & \lambda_{xy} & \lambda_{xz} \\ \lambda_{yx} & \lambda_{yy} & \lambda_{yz} \\ \lambda_{zx} & \lambda_{zy} & \lambda_{zz} \end{bmatrix} \frac{\partial T}{\partial r} \begin{bmatrix} \sin\theta \cdot \cos\varphi \\ \sin\theta \cdot \sin\varphi \\ \cos\theta \end{bmatrix} = \qquad (2)$$

$$= -\lambda(\theta, \varphi) \frac{\partial T}{\partial r},$$

where θ is a polar angle, φ is an azimuth angle.

Eq. (2) allows determining the material thermal conductivity in any crystallographic direction, taking into account that for this direction relevant θ and φ angles are defined.

For the definition of the thermal conductivity coefficient in crystal directions of interest with hexagonal syngony ($\lambda_{xx} = \lambda_{yy} \neq \lambda_{zz}$), inserting numeric values of thermal conductivity tensor in the main directions [100] and [001] reduces equation (2) to the simpler form:

$$\lambda(\theta, \varphi) = \lambda_{xx} \cdot \sin^2\theta + \lambda_{zz} \cdot \cos^2\theta. \tag{3}$$

The polar angle θ for crystallographic direction [111] can be defined using the ratio:

$$\theta = arctg\left(\frac{\lambda_{[100]}}{\lambda_{[001]}}\right). \tag{4}$$

For visualizing the thermal conductivity coefficients of the material having hexagonal syngony, it is convenient to use an isotherm instead of a bulk quadric. This connected with the fact that according to eq. (3) the value of the thermal conductivity coefficients does not change at any value of azimuth angle φ. To set the isotherm, we need to know the numerical values of the thermal conductivity coefficients in the [100] and [001] directions.

Figure 2 presents the calculated isotherms of the thermal conductivities for AlN, GaN, and $Al_{0.5}Ga_{0.5}N$ crystals at a temperature of 300 K and the values of the polar angle θ in the range from 0 to 360 degrees.

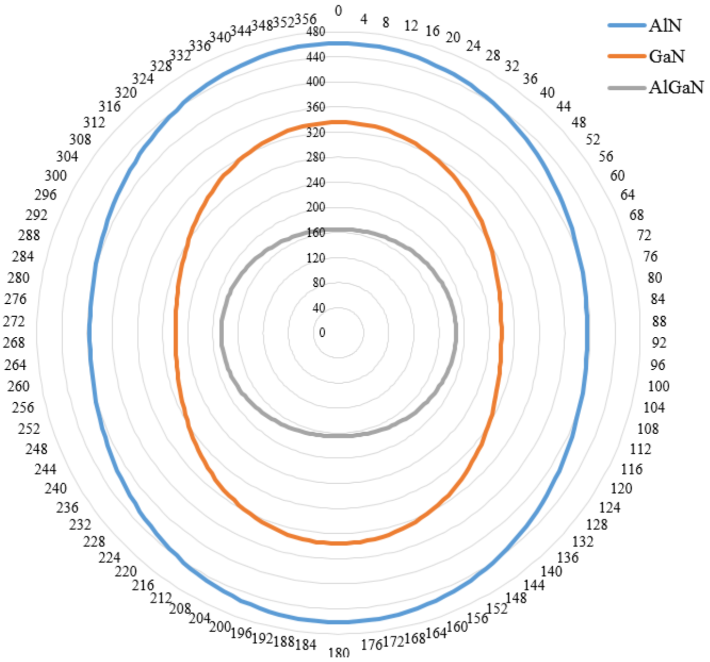

Fig. 2. Isotherms of the thermal conductivity dependencies of AlN, GaN, and $Al_{0.5}Ga_{0.5}N$ crystals on the polar angle θ (at 300 K)

As one can see in Fig. 2, the maximum of the thermal conductivity coefficient for AlN and GaN refers to the [001] direction and equals 461.65 and 335.96 W/(m·K), respectively. The minimum is directed along the [100] direction and equals 396.06 and 259.28 W/(m·K), respectively. For $Al_{0.5}Ga_{0.5}N$ crystal maximum λ = 186.74 W/(m·K) lies in the [100] direction, and minimum λ = 165.24 W/(m·K) is in the [001] direction.

Temperature dependence of the thermal conductivity. For traditional silicon technology, the electronic devices usually are limited by work temperatures less than 380 K. In GaAs and GaN technologies work temperatures can reach 770 K. Thereby the range from 250 to 750 K was chosen for investigating the temperature dependence of the thermal conductivity of AlN, GaN, and $Al_{0.5}Ga_{0.5}N$. Figure 3 shows for AlN, GaN, and $Al_{0.5}Ga_{0.5}N$ compounds the dependence of the thermal conductivity on temperature along the crystallographic directions. The temperature dependence of the lattice thermal conductivity of the material can be expressed as follows:

$$\lambda(T) = \lambda_{300} \cdot \left(\frac{T}{300}\right)^{\delta}, \tag{5}$$

where λ_{300} is the thermal conductivity of material at 300 K, δ is a temperature changing coefficient.

The dot lines represent the smoothing power functions derived from eq. (5). Calculated constants of the thermal conductivity equations for materials under investigation are presented in Table 2.

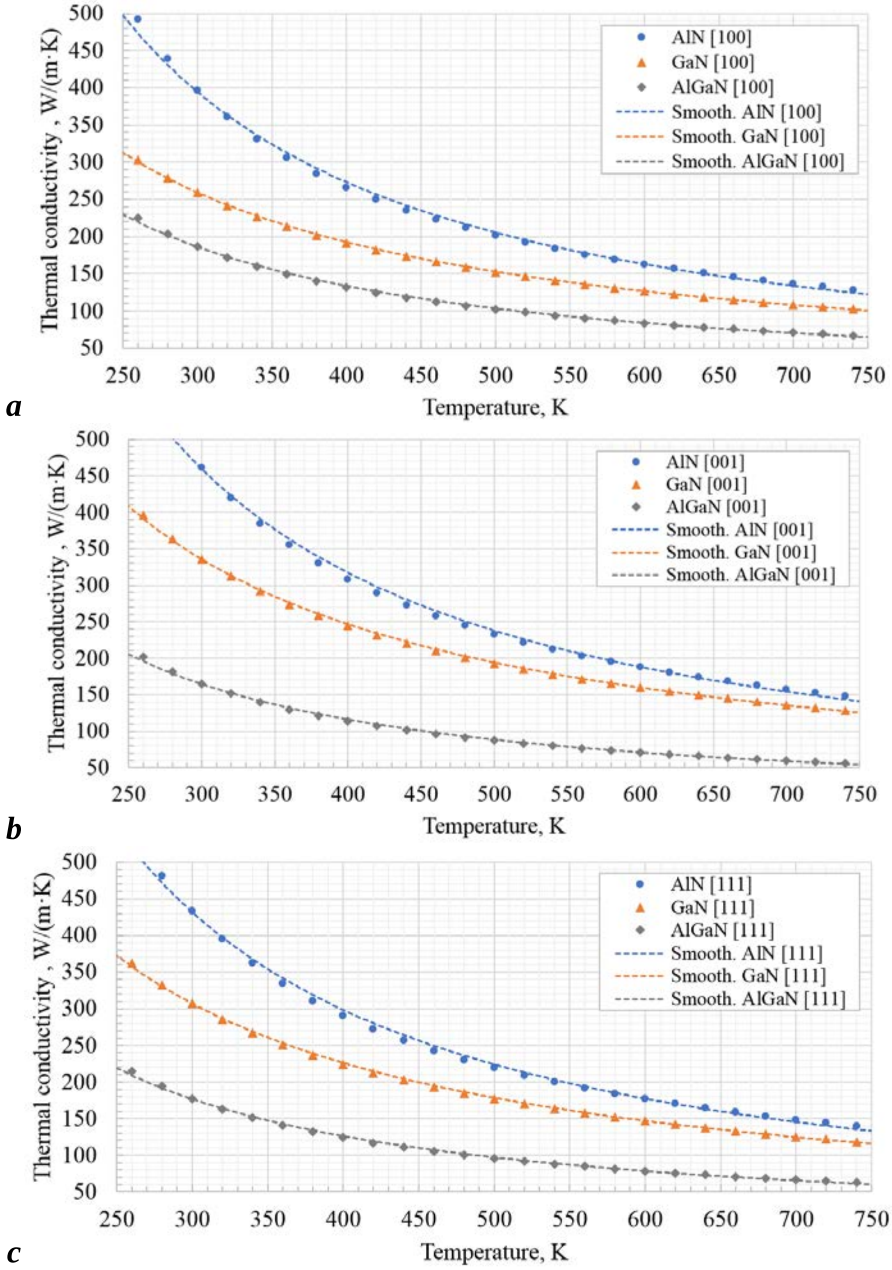

Fig. 3. Dependencies of the thermal conductivity for AlN, GaN, and $Al_{0.5}Ga_{0.5}N$ on temperature along the directions: *a* – [100], *b* – [001], and *c* – [111]

Reliability values of approximations R^2 are calculated. The closer R^2 value to 1, the more reliable the power function is. Since numeric values R^2 are in the range from 0.997 (for AlN in the [001] direction) to 1.000 (for GaN in the [111] direction), it can be concluded that the reliability level of the power equations obtained for the thermal conductivity is very high.

Table 2. Constants for the thermal conductivity power equations

Structure	Direction	λ_{300}, W/(m·K)	δ	R^2
AlN	[100]	394.4	-1.28	0.997
	[001]	459.5	-1.29	0.997
	[111]	431.9	-1.28	0.997
GaN	[100]	259.2	-1.03	1.000
	[001]	335.7	-1.07	0.999
	[111]	307.2	-1.06	1.000
$Al_{0.5}Ga_{0.5}N$	[100]	186.3	-1.15	0.999
	[001]	164.6	-1.21	0.998
	[111]	176.8	-1.17	0.998

4. Analysis of results

We have compared the calculated thermal conductivity of GaN with the data of other authors who used both first-principle calculation methods and experimental ones. The values from the first data published by Sitchel and Pankov in 1977 to the results obtained by us in 2021 are presented in Fig. 4. The quantum-mechanical results differ from the experimental values.

For comparison, we accepted the following assumptions. If the thermal conductivity of material was presented with one numerical value without pointing the crystallographic direction, we assumed that this value refers to the [001] direction. In the case when the thermal conductivity was given as a range of values (without designation of the crystallographic direction), it was recognized that the smallest value refers to the [100] direction, and the largest to the [001] direction. The temperature of measurements was not specified, it is assumed to be equal to 300 K.

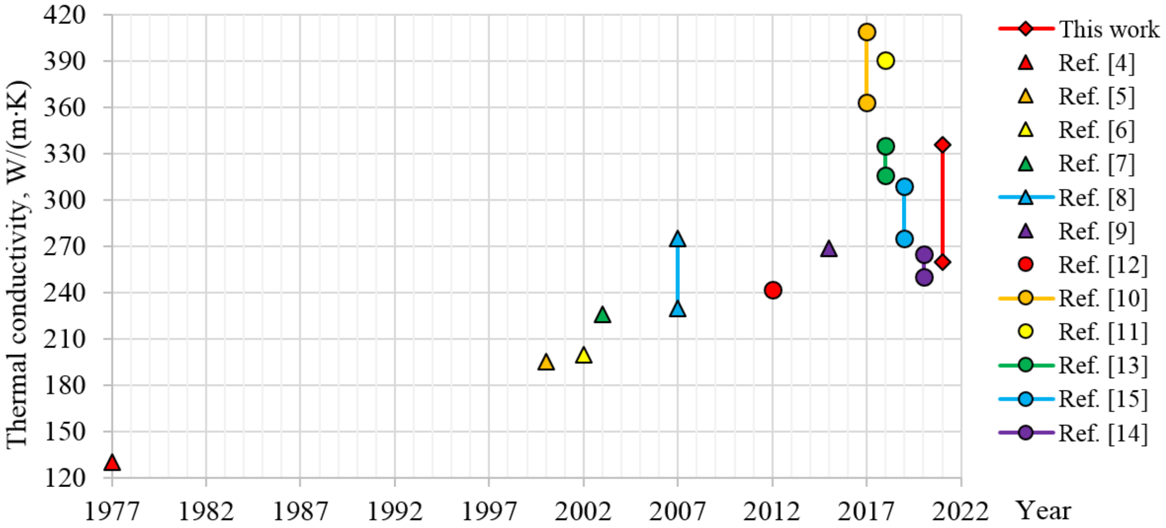

Fig. 4. GaN thermal conductivity investigations over the years (theoretical data are displayed as circles, experimental ones as triangles, and our data as rhombuses)

Comparison to theoretical works. In [10] the highest thermal conductivity values were obtained. The distinction from other works can be explained by the fact that crystal structure parameters had been taken right from experiments, i.e. structural relaxation had not been performed. Unlike other works the authors [11] calculated using different software. In [12] GaN lattice thermal conductivity and its dependence on isotopic composition were investigated. The thermal conductivity value corresponding to a natural isotope concentration was in good agreement with experimental values in a wide range of temperatures. The authors have shown that rising of the gallium isotope concentration leads to a large frequency gap between acoustic and optic phonon branches. The gap produces unusually weak anharmonic phonon-phonon scattering that enters into the heat transfer mechanism of the material.

The remaining works gave values which are close to ours. Some different model parameters used by other authors, e.g. supercell size, cutoff energy, etc. lead to minor inconsistencies in the numerical values of lattice thermal conductivity [13-15].

Comparison to experimental works. The tendency of increasing the numeric value of thermal conductivity obtained experimentally from the earliest to the last works was noticed. This fact can be explained by the improvement of methods of crystal growing and sample preparation, betterment of measuring equipment, and mathematical treatment of the results obtained. Experimental results depend on the crystal orientation of a sample, its thickness, point defects presence (impurities or vacancies), and the substrate on which the sample is placed.

In all experimental works, GaN samples were grown by chloride-hydride gas-phase epitaxy (HVPE). Unlike the liquid phase, epitaxy HVPE allows controlling of crystal growth. Thermal conductivity values in the experimental works correspond to room temperature. One of the first studies on GaN thermal conductivity is [4]. The authors investigated a bulk GaN sample of thickness of 400 μm on the sapphire substrate, roughly rectangular shape with sizes 5×2.65×0.31 mm. The thermal conductivity was equal to 130 W/(m·K) along the [001] direction. As it will be shown further, the thermal conductivity of a monocrystal exceeds this value significantly. Up to 2000, Sichel-Pankov's work was the only one on GaN thermal conductivity when progress in the synthesis of this material allowed create high-quality crystals. That led to comprehensive research of its properties with application perspectives in electronics.

In [5] GaN films were grown on sapphire (0001) substrate in a vertical type reactor. Film thermal conductivity was about 195 W/(m·K) at a gallium concentration of $N = 6.9\times10^{16}$ cm^{-3} in the sample. The authors [6] have got GaN monocrystal samples on the sapphire substrate. The thermal conductivity value of 200 W/(m·K) was obtained for GaN sample with the impurities of oxygen ($N = 2.1\times10^{16}$ cm^{-3}) and silicon ($N = 0.37\times10^{16}$ cm^{-3}). According to [7] GaN thermal conductivity is equal to 226 W/(m·K). The samples under investigation had the following impurities: oxygen ($N = 1\times10^{20}$ cm^{-3}), silicon ($N = 1\times10^{17}$ cm^{-3}), hydrogen ($N = 7\times10^{17}$ cm^{-3}), carbon ($N = 1\times10^{19}$ cm^{-3}) and magnesium ($N = 1\times10^{18}$ cm^{-3}). Concentration of Ga vacancies was equal to $N = 1\times10^{18}$ cm^{-3}.

It is known that the heat properties of a gallium monocrystal are very sensitive to structure defects, but the authors [8] managed to get an almost perfect GaN crystal with the minimum number of point defects. GaN monocrystal thermal conductivity had been measured by the vertical type laser flash method at room temperature and was equal to 253 ± 8.8 % W/(m·K). There is the experiment [9] where the measured value of thermal conductivity is equal to 269 W/(m·K) at room temperature with high oxygen impurity concentration. The authors explained it by the fact that at this oxygen impurity concentration phonon scattering on free charge carriers is negligible, which leads to thermal conductivity increases.

The distinction between the results of theoretical investigation and experimental data can be explained as follows. *Phono3py* determines all possible variants of atomic displacements in the supercell under study. Depending on atom number in the supercell and crystal symmetry, the number of atomic-pair configurations can be large enough and exceed computation resources. To reduce computation time and the number of supercells with displacements, the "cutoff-pair" parameter is used which limits the distance between cutoff pairs in the supercell. Thereby, some amount of the supercells with displacements could be not taken into account.

The large variety of defects arises during material layer formation. For example, the presence of impurities and dislocations significantly reduces the thermal conductivity of GaN films [27,28]. The measured thermal conductivity for GaN thin films [29] is significantly less than the thermal conductivity for bulk GaN crystal at room temperature [6].

The type of defects and their number depends on the synthesis method, subsequent thermal processing, substrate materials, etc. Receiving the result that will represent the real picture by using quantum-mechanical calculations is impossible because of the huge number of possible defect variants.

The supercell method lets us evaluate point defects' impact on properties of a material under investigation, in particular, structural and electron properties. However, in the case of thermal conductivity calculations huge computing resources are needed. For this reason for a wide range of materials, heat properties calculations are performed for idealized structures. It is worth noting that the influence of crystal grain boundaries and surface is not taken into account in quantum-mechanical calculations. So the periodic boundary conditions, which assume that the crystal under study has quasi-infinite size, are used.

Methodology of thermal conductivity experimental measurements gives values without many factors accounting: 1) contribution of heat exchange to the substrate, on which the film of the material under investigation is applied; 2) significant contribution of the heat exchange with the environment; 3) technical difficulties of measurements associated with small sample size. Thereby the thermal conductivity data taken from the literature and obtained experimentally are not ideal. In its turn, computer simulation at the atomic level does not allow taking into account all the factors described above.

5. Conclusions

The thermal conductivity along the [100], [010], and [001] main crystallographic directions for GaN, AlN, and $Al_{0.5}Ga_{0.5}N$ materials have been calculated in the temperature range from 250 to 750 K. An equation is presented for determining the thermal conductivity of a material in the required crystallographic direction.

The maximum values of the thermal conductivity coefficients of AlN and GaN are in the [001] direction and equal to 461.65 and 335.96 W/(m·K), respectively, while the minimum values are along the [100] direction and equal to 396.06 and 259.28 W/(m·K), respectively. For the $Al_{0.5}Ga_{0.5}N$ crystal, the maximum λ = 186.74 W/(m·K) is in the [100] direction, and the minimum λ = 165.24 W/(m·K) is in the [001] direction.

Models are presented that describe changes in the lattice thermal conductivity of materials with temperature. The calculated constants (the temperature change coefficient and the thermal conductivity of material at 300 K) are given for the power-law heat conduction equations along the [100], [001], and [111] crystallographic directions for the studied AlN, GaN, and $Al_{0.5}Ga_{0.5}N$ materials. The values of the reliability approximations R^2 are in the range from 0.996 (for AlN in the [001] direction) to 0.9996 (for GaN in the [111] direction). It means that the level of reliability of the obtained power-law equations of heat conduction is quite high.

A comparative analysis of the GaN thermal conductivity studies has been carried out. The peculiarities of determining the thermal conductivity of GaN were established for experimental studies and theoretical calculations.

The technical complexity of measurements in the experiment is associated with a small size of sample. Besides, the measuring technique for thermal conductivity of materials neglects the contribution of substrate and environment. Thus, the experimental data of the numerical values of thermal conductivity taken from the literature are not ideal, since they include a number of shortcomings in the measurement methods. At this moment it is impossible to obtain a result that reflects the real picture due to limitations on the power of computing equipment and time resources for quantum mechanical simulation. The atomic level of computer simulation does not allow taking into account the influence of most structural defects (impurities, dislocations, crystal grain boundaries, surface effects). Therefore, calculations of the thermal properties of materials are carried out for an idealized structure.

References

1. Okumura H. Present status and future prospect of widegap semiconductor high-power devices. *Japanese Journal of Applied Physics.* 2006;45(10R): 7565.
2. Ahi K. Review of GaN-based devices for terahertz operation. *Optical Engineering.* 2017;56(9): 090901.
3. Wachutka GK. Rigorous thermodynamic treatment of heat generation and conduction in semiconductor device modeling. *IEEE Transactions on Computer-Aided Design of Integrated Circuits and Systems.* 1990;9(11): 1141-1149.
4. Sichel EK. Thermal conductivity of GaN, 25-360 K. *J. Phys. Chem. Solids.* 1977;38(3): 330-330.
5. Florescu DI, Asnin VM, Pollak FH, Molnar RJ, Wood CE. High spatial resolution thermal conductivity and Raman spectroscopy investigation of hydride vapor phase epitaxy grown n-GaN/sapphire (0001): Doping dependence. *Journal of Applied Physics.* 2000;88(6): 3295-3300.
6. Slack GA, Schowalter LJ, Morelli D, Freitas JrJA. Some effects of oxygen impurities on AlN and GaN. *Journal of Crystal Growth.* 2002;246(3-4): 287-298.
7. Jeżowski A, Danilchenko BA, Boćkowski M, Grzegory I, Krukowski S, Suski T, Paszkiewicz T. Thermal conductivity of GaN crystals in 4.2-300 K range. *Solid State Communications.* 2003;128(2-3): 69-73.
8. Shibata H, Waseda Y, Ohta H, Kiyomi K, Shimoyama K, Fujito K, Nagaoka H, Kagamitani Y, Simura R, Fukuda T. High thermal conductivity of gallium nitride (GaN) crystals grown by HVPE process. *Materials Transactions.* 2007;48(10): 2782-2786.
9. Jeżowski A, Churiukova O, Mucha J, Suski T, Obukhov IA, Danilchenko BA. Thermal conductivity of heavily doped bulk crystals GaN: O. Free carriers contribution. *Materials Research Express.* 2015;2(8): 085902.
10. Jiang Y, Cai S, Tao Y, Wei Z, Bi K, Chen Y. Phonon transport properties of bulk and monolayer GaN from first-principles calculations. *Computational Materials Science.* 2017;138: 419-425.
11. Garg J, Tengfei L, Gang C. Spectral concentration of thermal conductivity in GaN – A first-principles study. *Applied Physics Letters.* 2018;112(25): 252101.
12. Lindsay L, Broido DA, Reinecke TL. Thermal conductivity and large isotope effect in GaN from first principles. *Physical Review Letters.* 2012;109(9): 095901.
13. Yuan K, Zhang X, Tang D, Hu M. Anomalous pressure effect on the thermal conductivity of ZnO, GaN, and AlN from first-principles calculations. *Physical Review B.* 2018;98(14): 144303.
14. Tang DS, Qin GZ, Hu M, Cao BY. Thermal transport properties of GaN with biaxial strain and electron-phonon coupling. *Journal of Applied Physics.* 2020;127(3): 035102.
15. Minamitani E, Masayoshi O, Satoshi W. Simulating lattice thermal conductivity in semiconducting materials using high-dimensional neural network potential. *Applied Physics Express.* 2019;12(9): 095001.
16. Jungnickel C, McCormmach R. Methods of Theoretical Physics. *The Second Physicist: on the History of Theoretical Physics in Germany.* Springer, Cham, 2017. 289-314.

17. Hiller JR. Quantum Mechanics Simulations. *Computers in Physics.* 1996;10(3): 260-260.
18. Katre A, Togo A, Tanaka I, Madsen GK. First principles study of thermal conductivity cross-over in nanostructured zinc-chalcogenides. *Journal of Applied Physics.* 2015;117(4): 045102.
19. Ikeda Y, Seko A, Togo A, Tanaka I. Phonon softening in paramagnetic bcc Fe and its relationship to the pressure-induced phase transition. *Physical Review B.* 2014;90(13): 134106.
20. Florescu DI, Asnin VM, Pollak FH, Molnar RJ, Wood CE. C. High spatial resolution thermal conductivity and Raman spectroscopy investigation of hydride vapor phase epitaxy grown n-GaN/sapphire (0001): Doping dependence. *Journal of Applied Physics.* 2000;88(6): 3295-3300.
21. Togo A, Laurent C, Isao T. Distributions of phonon lifetimes in Brillouin zones. *Physical Review B.* 2015;91(9): 094306.
22. Mizokami K, Atsushi T, Isao T. Lattice thermal conductivities of two SiO_2 polymorphs by first-principles calculations and the phonon Boltzmann transport equation. *Physical Review B.* 2018;97(22): 224306.
23. Chaput L. Direct solution to the linearized phonon Boltzmann equation. *Physical Review Letters.* 2013;110(26): 265506.
24. Lu G, Ellad B, Efthimios K. From electrons to finite elements: A concurrent multiscale approach for metals. *Physical Review B.* 2006;73(2): 024108.
25. Levinshtein ME, Rumyantsev SL, Shur MS. (Eds.) *Properties of Advanced Semiconductor Materials: GaN, AIN, InN, BN, SiC, SiGe.* John Wiley & Sons; 2001.
26. Ponce FA, Major JrJS, Plano WE, Welch DF. Crystalline structure of AlGaN epitaxy on sapphire using AlN buffer layers. *Applied Physics Letters.* 1994;65(18): 2302-2304.
27. Kotchetkov D, Zou J, Balandin AA, Florescu DI, Pollak FH. Effect of dislocations on thermal conductivity of GaN layers. *Applied Physics Letters.* 2001;79(26): 4316-4318.
28. Zou J, Kotchetkov D, Balandin AA, Florescu DI, Pollak FH. Thermal conductivity of GaN films: Effects of impurities and dislocations. *Journal of Applied Physics.* 2002;92(5): 2534-2539.
29. Belousov A, Katrych S, Hametner K, Günther D, Karpinski J, Batlogg B. $Al_xGa_{1-x}N$ bulk crystal growth: Crystallographic properties and p-T phase diagram. *Journal of Crystal Growth.* 2010;312(18): 2585-2592.

THE AUTHORS

D.C. Hvazdouski
e-mail: gvozdovsky@bsuir.by
ORCID: 0000-0001-8702-7748

M.S. Baranava
e-mail: baranova@bsuir.by
ORCID: 0000-0002-2618-4464

V.R. Stempitsky
e-mail: vstem@bsuir.by
ORCID: 0000-0001-9362-7539

Materials Physics and Mechanics. 2022;49(1): 108-135
Conference materials
http://dx.doi.org/10.18149/MPM.4912022_8

Nuclear geometry: from potassium to titanium

A.I. Melker✉

St. Petersburg Academy of Sciences on Strength Problems, Polytekhnicheskaya 29, 195251, St. Petersburg, Russia

✉ ndtcs@inbox.ru

Abstract. Nuclear geometry has been developed by analogy with the fullerene geometry. On the basis of this geometric approach, it was possible to design the structure of potassium, calcium, scandium, and titanium isomers as well as their isotopes, which can be obtained by means of nuclear synthesis. The nuclei can be classed into two groups: basic nuclei having equal numbers of protons and neutrons and isotopes having one, two, and more neutrons. The latter ensure their mechanical stability with respect to shear stresses, sending their electron to the coat of mail created by the basic nuclei.

Keywords: calcium, graph representation, isomer, isotope, nuclear electron, nuclear geometry, nuclear reaction, potassium, scandium, titanium

***Acknowledgements**. No external funding was received for this study.*

Citation: Melker AI. Nuclear geometry: from potassium to titanium. *Materials Physics and Mechanics*. 2022;49(1): 108-135. DOI: 10.18149/MPM.4912022_8.

1. Introduction

There are various models of nuclear structure, but [1] "all the nuclear models play the role of more or less probable working hypotheses. The nuclear models are approximate representations used for the description of some properties of nuclei. It is assumed that a nucleus is identical to a physical system, which properties are well studied". Although these models often contradict each other, usually they describe different features of a nucleus and therefore supplement each other. Any model is based on experimental facts and allows explaining some properties which are of interest. At the same time "the consistent explanation of the most important properties of atomic nuclei on the *firm basis of general physical principles* is one of the unsolved fundamental problems of nuclear physics" [1].

The modern existing nuclear models were developed in the framework of the proton-neutron conception. Their general feature is that they are shapeless, i.e. they describe quantum states but not the geometry of nuclei. How to find the firm basis for constructing a consistent nuclear theory? Let us return to Aristotle (384-322 BC). He assumed that all essential originates and consists of two principia: matter and form; the form being the leading principle. The matter in itself is the passive principle of nature; it is the possibility for the appearance of a real thing. In order for the thing to become reality; it must receive the form, which transforms the possibility into reality [2, p. 27].

Up to now in nuclear physics, we have only the matter (protons, neutrons, electrons, etc.), but no space form. In other words, the leading principle is absent in nuclear physics elsewhere. To my mind, the firm ground for constructing a new consistent theory of nuclear physics is nuclear geometry, i.e. 'Aristotle's form' of nuclei. The nuclear geometry has been created and developed by analogy with fullerene geometry in [3-7]. It should be emphasized that such a geometric approach explained not only the generation of elements from hydrogen to argon but also that of *their isotopes and isomers* in the framework of one and the same unified approach. Moreover, the geometric models of nuclei have given us an insight into the problem, of why the nuclei have a definite number of stable isotopes and isotopes having a large half-decay period.

2. Parallels between tetrahedral fullerene C_4 and helium $_2He^4$

Tetrahedral fullerene C_4 can be inscribed into a sphere (Fig. 1a). The atoms and shared electron pairs, forming covalent bonds, are located on one and the same sphere [3]. It should be emphasized that the covalent bond can be represented not only as a straight line but as a small arc on a geodesic line (great circle). Being less than a semicircle, it is the least path between the ends of the arc [8].

The covalent bonds are created by shared electron pairs [9]. According to the theory by Sidgwick and Powell [9,10], each shared electron pair can be considered as a point charge; all the charges repel each other and arrange themselves into such a configuration, which ensures their maximal removal from each other. Tetrahedral fullerene C_4 has four atoms and six point charges. All the charges are located on the great circles, which pass through any two atoms connected by a respective electron pair. It is interesting to note that six point charges form a regular octahedron inscribed into the same sphere (Figs. 1b and 1c).

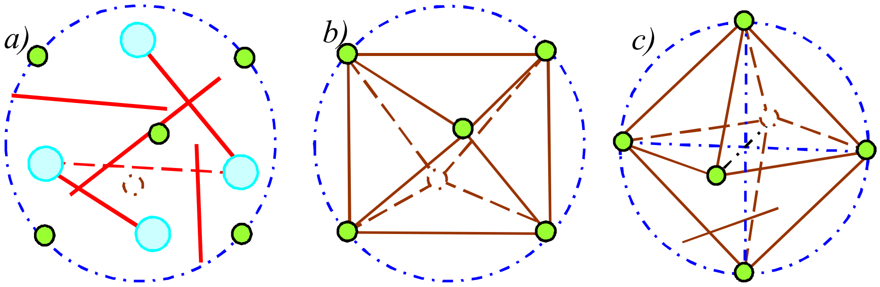

Fig. 1. Tetrahedral fullerene C_4; large turquoise spheres are atoms and small green spheres are shared electron pairs. Here: (a) position of the shared electron pairs on geodesic lines; (b) point charge octahedron corresponding to (a); (c) usual form of a regular octahedron

Consider a nucleus of helium $_2He^4$. The name derives from the Greek ηλιος for "sun". The element was discovered by spectroscopy during a solar eclipse in the sun's chromosphere by the French astronomer Pierre-Jules-Cesar Janssen in 1868. It was independently discovered and named helium by the English astronomer Joseph Norman Lockyer. It was thought to be only a solar constituent until it was later found to be identical to the helium in the uranium ore cleveite by the Scottish chemist William Ramsay in 1895. Ramsay originally called his gas krypton, until it was identified as helium. The Swedish chemists Per Theodore Cleve and Nils Abraham Langet independently found helium in cleveite at about the same time [11].

According to the proton-neutron conception [1], helium 4 has 2 protons and 2 neutrons. Similar to tetrahedral fullerene C_4, they can form a tetrahedron; however such tetrahedron is asymmetric from the physical and geometric standpoint. The structure does not look beautiful, so it cannot be a veritable from an aesthetic point of view. In order to conserve the symmetry of proton-neutron tetrahedron, one is compelled to accept for a fact that

- Each neutron in a nucleus decomposes into a proton and negatively charged particles.
- All the apices of the tetrahedron are equivalent and therefore they must be protons.

- For helium 4, the number of negatively charged particles is equal to the number of the tetrahedron edges, so they must have a charge ⅓ that of an electron.
- The negatively charged particle will be named a tertion (Latin *tertia* − one third).
- Interaction of the tertions creates hidden symmetry of the electronic pattern (tertion net).
- The electronic symmetry does not coincide with that of the protonic cell but determines it.

It should be emphasized that the last postulate is advanced by analogy with the experimental result for fullerenes [12]. The example is shown in Fig. 1.

The question arises as to whether postulate 1 is formulated on legal grounds. It is known that a free neutron is unstable and decays according to the scheme $n \rightarrow p + e^- + \tilde{\nu}_e$ into proton, electron, and antineutrino (β−decay), the average lifetime being equal approximately to 15.3 min [13]. It seems very illogical that the neutron becomes stable inside a nucleus in the strong electric field created by surrounding protons. Apparently "the absolutely new assumption according to which each nuclear electron is connected with one of the nuclear protons forming a neutron" (George Gamov, 1932) needs to be reformulated. To my mind, neutron electrons are similar to valence electrons in molecules and solids, having a possibility to be removed from their parent neutrons in order to create "covalent" bonds. At that, the neutron electron can form various orbitals. Moreover, both subsystems, nuclear protons, and nuclear electrons produce their own patterns of different symmetry.

On the basis of these postulates, it is possible to design the structure of other nuclei [3-7]; for helium, which are shown in Fig. 2.

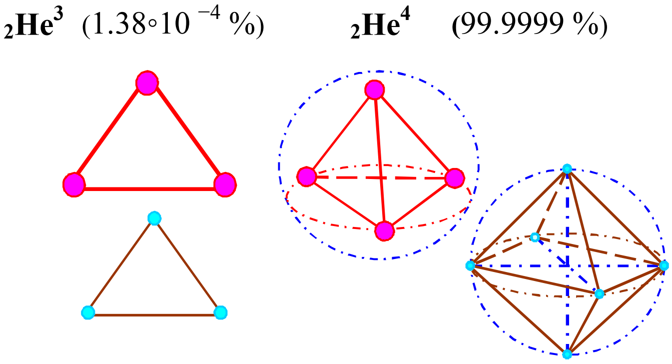

Fig. 2. Proton cells (red) and tertion nets (brown) of helium and its isotope

3. Parallels between lithium, beryllium, and body-centered crystals

The name lithium derives from the Latin *lithos* for "stone" because lithium was thought to exist only in minerals at that time. It was discovered by the Swedish mineralogist Johan August Arfwedson in 1818 in the mineral petalite $LiAl(Si_2O_5)_2$. Lithium was isolated in 1855 by the German chemists Robert Wilhelm Bunsen and Augustus Matthiessen [11]. There are two stable isotopes of lithium: $_3Li^6$ (7.5 %) and $_3Li^7$ (92.5 %) [14].

The name beryllium derives from the Greek word βηρυλλος for a gemstone "beryl" ($3BeO\_Al_2O_3\_6SiO_2$), in which it is found. It was discovered by the French chemist and pharmacist Nicholas-Louis Vauquelin in beryl and emerald in 1797. The element was first separated in 1828 by the French chemist Antoine-Alexandre-Brutus Bussy and independently by the German chemist Friedrich Wöhler. Because the salts of beryllium have a sweet taste, the element was also known as glucinium from the Greek γλυκυς for "sweet", until IUPAC selected the name beryllium in 1949 [11]. There is only one stable isotope of beryllium: $_4Be^9$ (100 %) [14].

On the basis of the postulates considered above, it is possible to design the structure of these nuclei and explain also their stability (Fig. 3).

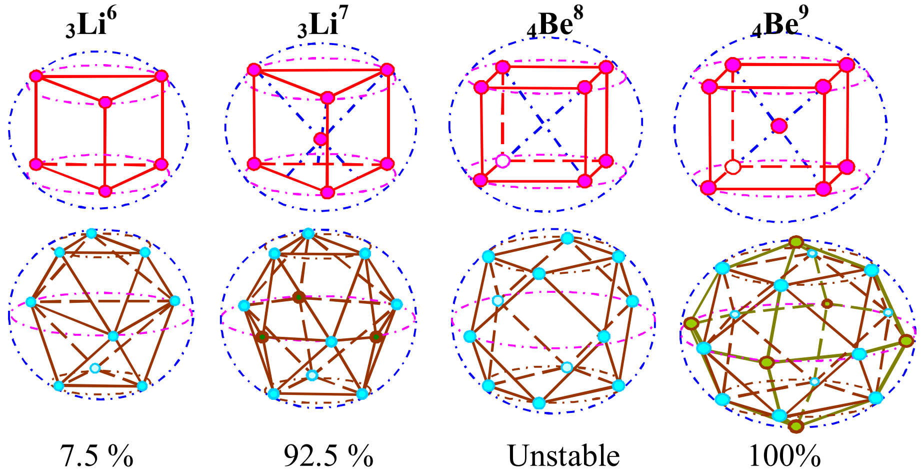

Fig. 3. Proton cells (red) and tertion nets (brown) of lithium, beryllium, and their isotopes

These results deserve further comment. The radioactive isotope ${}_1H^3$ is also known as tritium with the symbol T; its nucleus is named triton. Combining triton with helium 3 through the use of reaction ${}_1H^3 + {}_2He^3 \rightarrow {}_3Li^6$, one can obtain lithium ${}_3Li^6$. The further reaction $n + {}_3Li^6 \rightarrow {}_3Li^7$ gives lithium 7. Here a neutron penetrates into lithium ${}_3Li^6$, where it decays producing a proton and an electron. It is reasonable to accept that a neutron inside lithium 6 is similar to a hydrogen atom. It is known that spectral-line splitting in an electric field (Stark effect) depends on the principal quantum number n. For hydrogen, if n=1, there is no splitting at all; if n=2, there appear three states of equal energy [15]. By analogy with the hydrogen atom, it is valid to say that formally the core-neutron electron gives rise to 2s, $2p_x$, $2p_y$ orbitals, producing a 'valent state' of the core neutron. This state corresponds to the excited sp^2 state, where each of three valent tertions is not in s- or p-state, but in a hybridized state, which can be obtained by mixing a single 2s-state with two 2p-states. The latter is described by a wave function being a linear combination of s- and p-functions. At that, three sp^2 orbitals are located on a plane normal to the three-fold axis of symmetry of lithium. The negatively charged particles (tertions) of the core neutron correspond to three sp^2 orbitals; they are incorporated in the existing tertion net lithium 6 and are painted brown-green in Fig. 3. As a result, there forms a denser tertion net. The proton cell, having a shape of a regular triangle prism, becomes a body-centered one. Such structure is more abundant.

Similar to the algorithm developed for lithium, consider reaction $n + {}_4Be^8 \rightarrow {}_4Be^9$. Here a neutron penetrates into beryllium ${}_4Be^8$, where it decays. As a result, there forms a denser tertion net, and the proton cell, having a shape of a cube, becomes a body-centered cube (Fig. 3). While beryllium 8 is unstable, the abundance of ${}_4Be^9$ is 100%. Therefore its structure has super stability. To my mind, stability is ensured by two factors. The first is the packing density of the proton cell; the second is the density of the coat of mail (tertion net). Both factors take place in the case of beryllium 9, giving its structure super stability and abundance of 100%.

One further comment should be made. Hitherto it was assumed that the negative particle charge is ⅓. From the results obtained for beryllium 9, it follows that the core neutron decays into a proton and six negatively charged particles, having a charge $^1/_6$. The difference may be attributed to the Stark effect, where spectral-line splitting depends on the principal quantum number n. If n=2, there are three states of equal energy, for n=3, the number of states becomes six [15]. Formally the neutronic electron gives rise to $2p_x$, $2p_y$, and $2p_z$ orbitals, producing a 'valent state' of the core neutron.

Now consider potassium. I hope that after the rather detailed introduction a reader can easily catch the author's meaning. Designing the structures, it is necessary to bear in mind that the structures obtained must satisfy "the principle of least complexity", i.e. they are the simplest among all possible.

4. Isomers of potassium and their isotopes

The name derives from the English "potash" or "pot ashes" because it is found in caustic potash (KOH). The chemical symbol K derives from the Latin kalium via the Arabic qali for alkali. It was first isolated by the British chemist Humphry Davy in 1807 from the electrolysis of potash [11]. What do we know about potassium? There are two stable isotopes of potassium: $_{19}\mathrm{K}^{39}$ (93.2581%) and $_{19}\mathrm{K}^{41}$ (6.7302%), and one isotope $_{19}\mathrm{K}^{40}$, has a very large half-decay period being equal to $1.277 \cdot 10^{6}$ [14].

The problem is how to explain these data in the framework of a unified model. Previously [3-7] the nuclei were separated into two main types: basic nuclei having equal numbers of protons and neutrons, and isotopes having one or more additional core neutrons. A better understanding can be gained if we begin with basic nuclei having equal numbers of protons and neutrons. Consider again the parallels between fullerenes and nuclei.

Isomers of fullerene C_{38}. From the periodic table of fullerenes [16,17], it follows that there is only one perfect fullerene of the mass 38, having 3-fold S-symmetry. To it, one needs to add the semi-perfect fullerene having rotation-reflection 4-fold symmetry. The reason is connected with the fact that this semi-perfect fullerene has almost the same energy as the perfect one. The fullerenes, which were considered, were designed previously [17,18]. With knowledge of the fullerene structure, it is possible to design nuclear structures. They can be obtained in various ways through the use of the most probable geometrically compatible reactions. Consider some possible reactions.

Joining deuteron to argon. One of the possible reactions is illustrated in Fig. 4. It can be written as d+$_{18}$ Ar ^{36}(1) → $_{19}$ K ^{38}(1). The structure of argon was obtained in [7]. Here a deuteron is incorporated into the surface of the basic nucleus of argon. From Figure 4 it follows that for argon only four protons from thirty-six take part in the reaction. They are pink. The nucleus obtained contains one square, ten pentagons, and ten hexagons. The graph representation of this reaction is shown in Fig. 5.

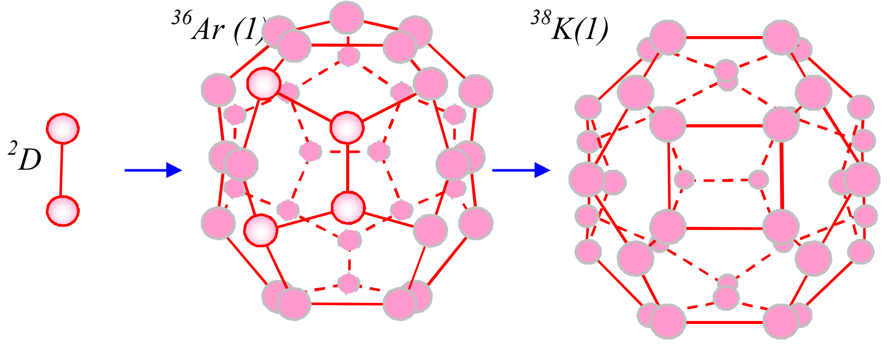

Fig. 4. Attachment of deuteron to argon (1) and formation of potassium (1)

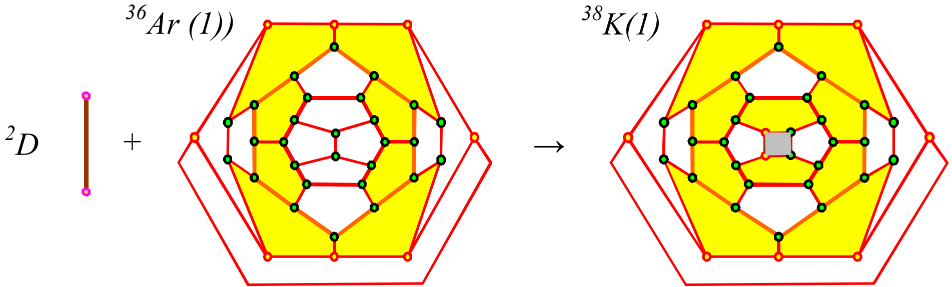

Fig. 5. Graph of nuclear reaction d + $_{18}$ Ar ^{36}(1) → $_{19}$ K ^{38}(1)

Joining three-fold symmetry-cupola oxygen to two-fold-symmetry sodium. Consider the reaction $^{16}O + {}^{22}Na \rightarrow {}^{38}K$ (2). It consists in joining a cupola of three-fold symmetry to a spheroid having two-fold symmetry (Fig. 6). Their structures were obtained previously [5,6,19].

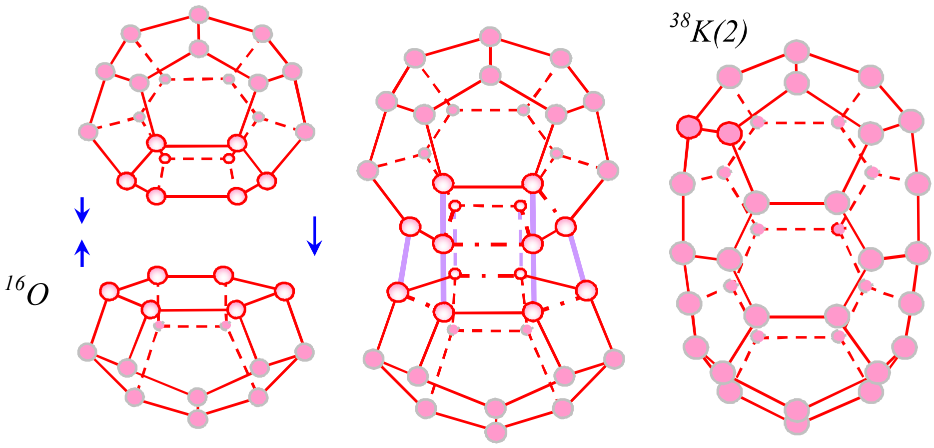

Fig. 6. Fusion of oxygen with sodium and formation of potassium (2): neutral protons (dark pink spheres), reacting protons (light pink spheres), proton bonds (red lines), intermediate-compound bonds to be broken (red dot lines), new bonds to be formed (lilac firm lines)

The graph representation of this reaction is shown in Fig. 7. To fully appreciate the nuclear reactions discussed above, the electronic structure (tertion net) of the potassium isomers is presented in Fig. 8. Similar to beryllium 8, these basic nuclei are unstable.

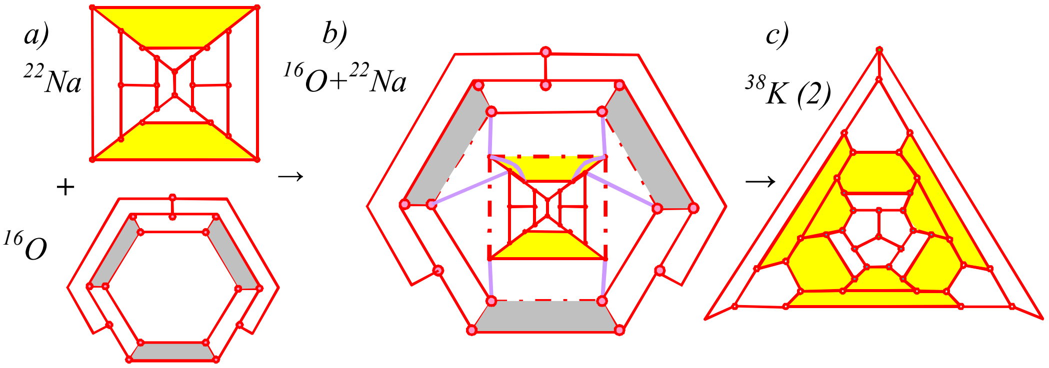

Fig. 7. Graph of nuclear reaction $_8O^{16} + {}_{11}Na^{22} \rightarrow {}_{19}K^{38}(2)$. Embedding the sodium graph into the oxygen graph: a) separate graphs, b) embedding, c) graph of potassium (2)

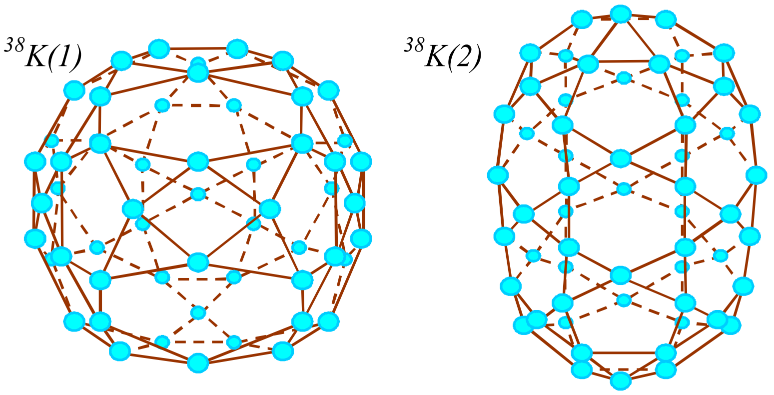

Fig. 8. Electronic structure of potassium isomers

One-neutron-core isotopes. From the results obtained for the basic nuclei, it follows that the isotope ${}_{19}\mathrm{K}^{39}$ having different symmetry is able to form two isomers. They can be got by incorporating a neutron, $\mathrm{n} + {}_{19}\mathrm{K}^{38} \rightarrow {}_{19}\mathrm{K}^{39}$. The protons cells and tertion nets of the isomers are shown in Fig. 9.

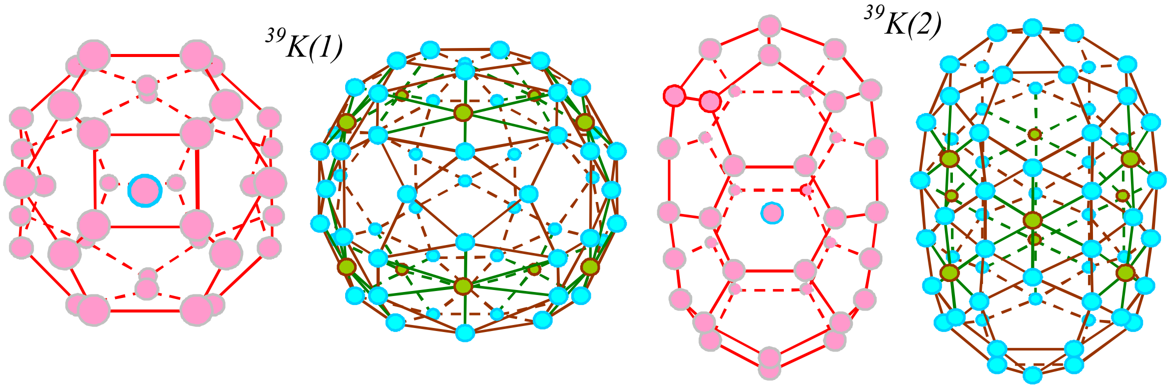

Fig. 9. Protonic cells and tertion nets of the isomers of potassium isotope ${}_{19}\mathrm{K}^{39}$

It should be emphasized the following. Extra core neutrons of isotope isomers are inside the corresponding nuclei. Here they are subjected to the electric field of their surroundings. It turned out that, due to the Stark effect [15], the decomposition of an internal core neutron into a proton and tertions differs from that of an external neutron; namely, the number of components of electron splitting depends on the symmetry of the surroundings. It is reasonable to leave the name "tertian" for an electron component, but change its charge. In our case, the internal core neutron's tertions have the charge $^{1}/_{10}\ e$ for $^{39}\mathrm{K}$ (1) and $^{1}/_{9}\ e$ for $^{39}\mathrm{K}$ (2). The regular thing is that the number of such tertions is equal to the number of hexagons in the tertion net of a basic nucleus.

Two-neutron-core isotopes. It is possible to obtain two isomers of the isotope ${}_{19}\mathrm{K}^{40}$ through the use of the reaction $\mathrm{n} + {}_{19}\mathrm{K}^{39} \rightarrow {}_{19}\mathrm{K}^{40}$ (Fig. 10).

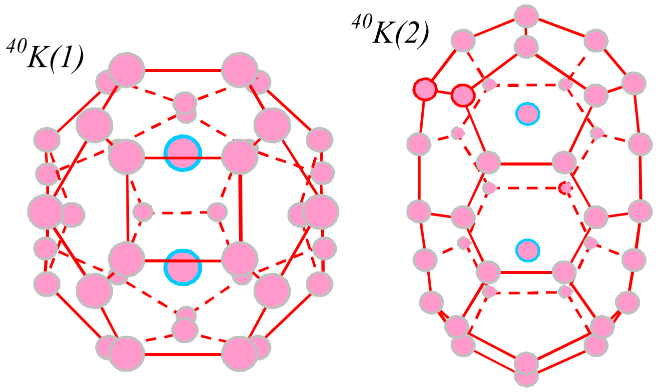

Fig. 10. Protonic cells of the isomers of potassium isotope ${}_{19}\mathrm{K}^{40}$

Consider isotopes $^{40}\mathrm{K}$. From Figure 10 it follows that two core neutrons are removed from one another at the distance larger than the parameter of the proton cell. When the neutrons decompose into protons and tertions under the action of the external surroundings, the protons fell in the minima of the double-well potential directed along the main symmetry axis. However, now the protons are only slightly connected with one another. It means that they behave themselves almost independently sending their tertions into the existing coat of mail. As a result, the shape of tertion net does not change. It looks like in Fig. 9, but the tertions produced by the core neutrons now have double charge, $^1/_5$ *e* for ^{40}K (1) and $^2/_9$ *e* for ^{40}K (2), respectively.

Three-neutron-core isotope. From the results obtained for silicon, sulfur, and argon [7], it follows that, if the isotopes contain more than two internal neutrons, they can form clusters inside the nucleus. However, the cluster symmetry must be compatible with that of the external surroundings. In our case, only the isotope ^{40}K(2) of three-fold S-symmetry is able to incorporate one more neutron and generate a core of compatible symmetry. There are two possible isomers of the core: a linear chain and an equilateral triangle (Fig. 11). The approximate position of the "neutron" triangle can be found in a purely geometric way as it is shown in Fig. 11, at the right. In the first case, the tertions of the third neutron have the charge ½ *e*, and in the second one ⅓ *e*. The structure of the coat of mail (the external tertion net) remains unchanged.

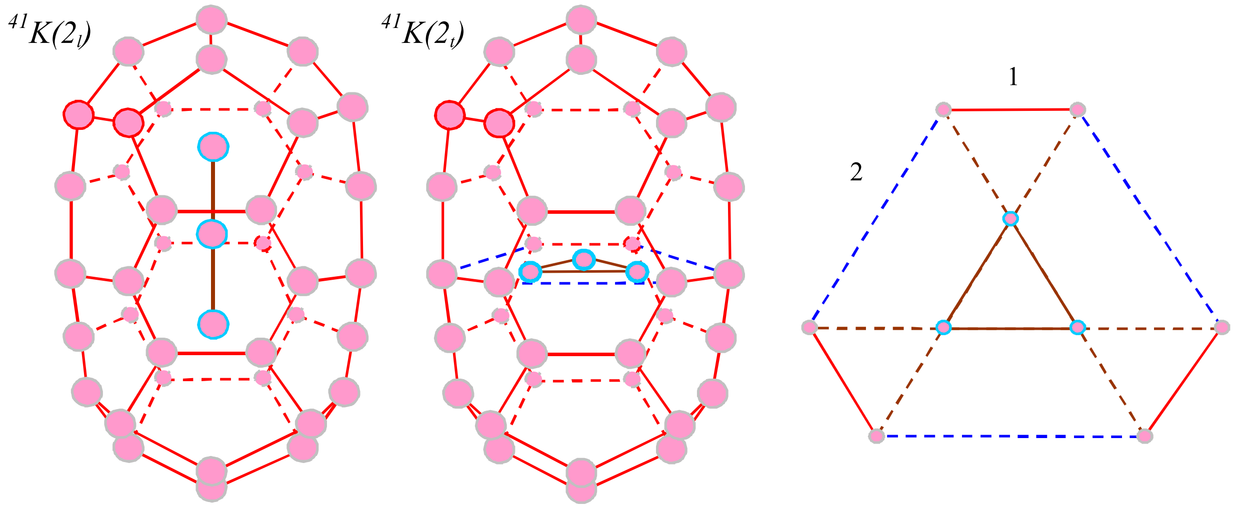

Fig. 11. Protonic cell of isotope ^{41}K(2) and the equatorial section (at the right)

These results deserve more consideration. Up to now, when there were two internal core neutrons, they were decomposed into protons and tertions by the external surroundings, the protons being tightly connected with the electronic coat of mail and maybe only slightly connected to one another. Now it is seen that the internal protons form the linear or triangle core, they being tightly connected to one another. In the second case, the triangle-core structure resembles that of helium-3 proposed previously [3]. The fact that there are two stable core structures sets one thinking that helium-3 may also be realized as an isomer having the liner shape. Moreover, one is inclined to think that the existence of the two isomers provokes the appearance of two superfluid phases of helium-3.

5. Isomers of calcium and their isotopes

The name derives from the Latin *calx* for "lime (CaO)" or "limestone ($CaCO_3$)" in which it was found. It was first isolated by the British chemist Humphry Davy in 1808 with help from the Swedish chemist Jöns Jacob Berzelius and the Swedish court physician M.M. af Pontin [11].

There are five stable isotopes of calcium: $_{20}Ca^{40}$ (96.947%), $_{20}Ca^{42}$ (0.647%), $_{20}Ca^{43}$ (0.135%), $_{20}Ca^{44}$ (2.086%), $_{20}Ca^{46}$ (0.004%) and $_{20}Ca^{48}$ ($>2\cdot10^{18}$ y, 0.187%). Besides, there is isotope $_{20}Ca^{41}$, having a very large half-decay period equal to $1.4\cdot10^5$ y, and isotope $_{20}Ca^{45}$ with an average half-decay period of 164 diurnals [14]. The problem is the same as before, how to explain these data in the framework of a unified model. Consider again the parallels between fullerenes and nuclei. A better understanding can be gained if we begin with basic nuclei having equal numbers of protons and neutrons.

Isomers of fullerene C_{40}. From the periodic table of fullerenes [16,17], it follows that there are three perfect fullerenes of the mass 40. They belong to 4-fold-symmetry, 5-fold, and tetrahedral. To them, one needs to add the two perfect fullerenes having rotation-reflection 4-fold symmetry and tetrahedral one, and moreover, the imperfect fullerene having 3-fold S-symmetry (simultaneously the perfect fullerene of 2-fold symmetry). The reason is connected with the fact that the latter fullerene has an energy which is close to that of the perfect ones and even less. The fullerenes, which are considered, have been designed previously [20,21]. They can be obtained through the use of the most probable geometrically compatible reactions in different ways.

With knowledge of the fullerene structure, it is possible to obtain nuclear structures. They can be designed in various ways through the use of the most probable geometrically and physically compatible reactions. By analogy with the fullerenes, consider some possible nuclear reactions.

Joining deuteron to potassium of three-fold symmetry. The possible reaction is presented in Fig. 12. It can be written as $d + {}_{19}K^{38}(2) \rightarrow {}_{20}Ca^{40}(1)$, the structure of potassium being obtained above. Here a deuteron is incorporated into a basic nucleus of potassium. From Figure 12 it follows that for potassium only four protons from thirty-eight take part in the reaction. They are pink. The nucleus obtained contains six pentagons and ten hexagons. The graph representation of this reaction is shown in Fig. 13.

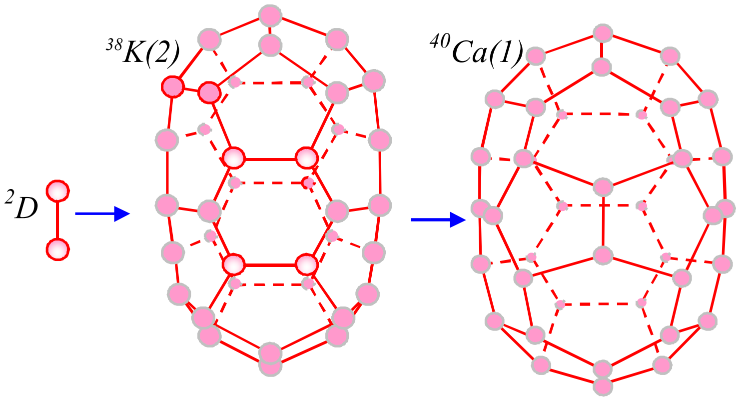

Fig. 12. Attachment of deuteron to potassium (2) and formation of calcium (1)

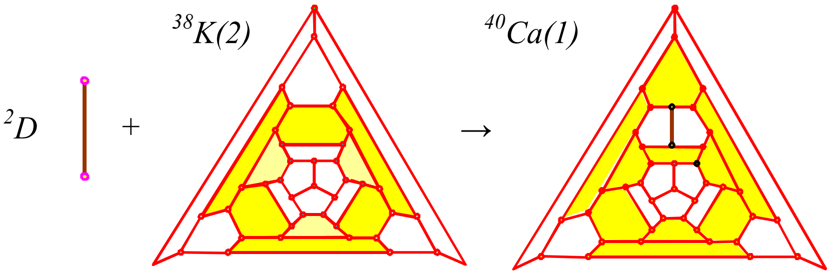

Fig. 13. Graph representation of the nuclear reaction $d + {}_{19}K^{38}(2) \rightarrow {}_{20}Ca^{40}(1)$

Joining two deuterons to argon of four-fold symmetry. The reaction is illustrated in Fig. 14 and can be written as $d + \rightarrow {}_{18}Ar^{36}(4\text{-fold}) + d \rightarrow {}_{20}Ca^{40}(2)$. Here two deuterons are incorporated in series into one of the basic nucleus of sulfur having four-fold symmetry. From Figure 14 it follows that for argon eight protons from thirty-six take part in the reaction. They are pink. The nucleus obtained contains twelve pentagons and five hexagons. The graph representation of the two-stage reaction is shown in Fig. 15.

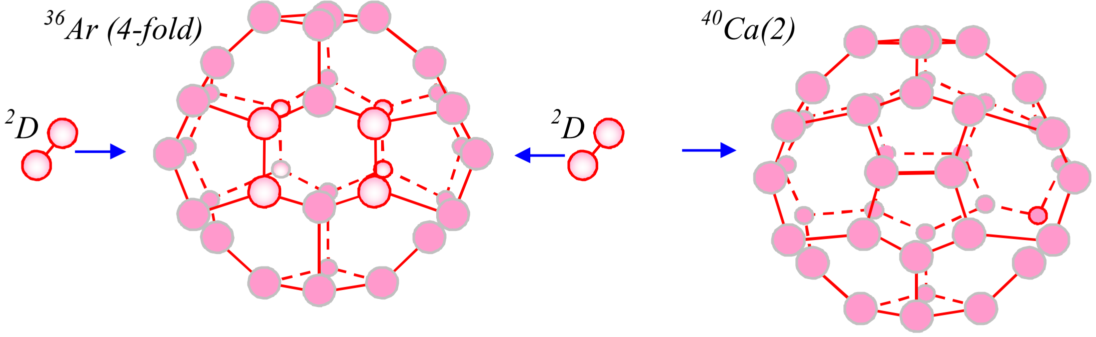

Fig. 14. Attachment of two deuterons to argon (4-fold) and formation of calcium (2)

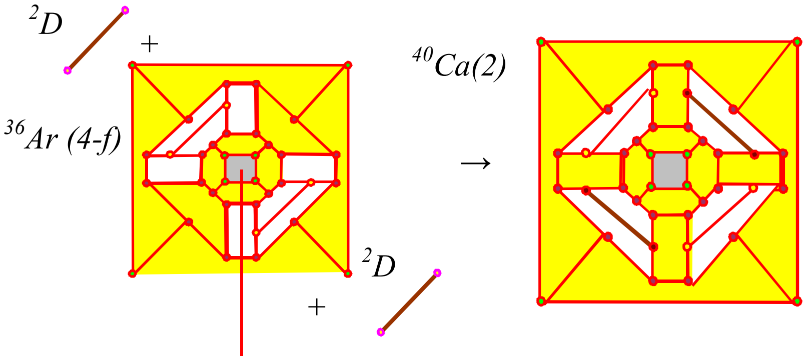

Fig. 15. Graph representation of the nuclear reaction $d + {}_{18}Ar^{36}$(4-fold)→ ${}_{20}Ca^{40}(2)$

Joining deuteron to potassium having rotation-reflection 4-fold symmetry. One of the possible reactions is illustrated in Fig. 16. It can be written as $d + {}_{19}K^{38}(1) \rightarrow {}_{20}Ca^{40}(3)$, the structure of potassium 38 (1) being obtained above. Here a deuteron is incorporated into a basic nucleus of potassium. From the figure, it follows that for potassium only four protons from thirty-eight take part in the reaction. They are pink. The nucleus obtained contains two squares, eight pentagons, and twelve hexagons. The graph of this reaction is shown in Fig. 17.

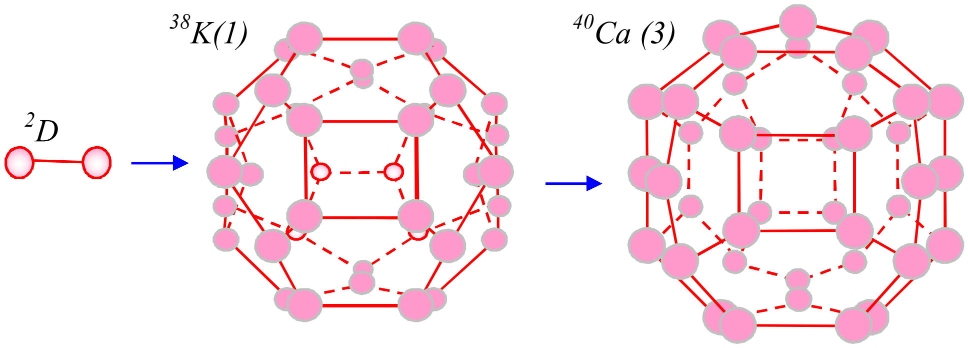

Fig. 16. Attachment of deuteron to potassium (1) and formation of calcium (3)

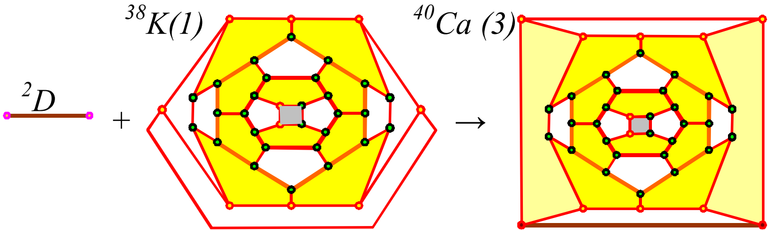

Fig. 17. Graph representation of the nuclear reaction $d + {}_{18}K^{38}(1) \rightarrow {}_{20}Ca^{40}(3)$

To fully appreciate the nuclear reactions discussed above, the electronic structure (tertion net) of the calcium isomers is presented in Fig. 18.

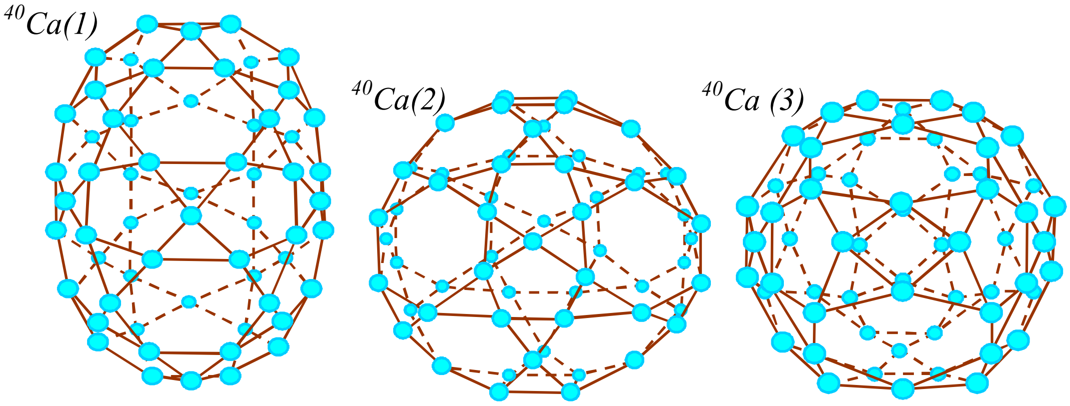

Fig. 18. Electronic structure of calcium isomers

Nuclear polymerization, folding, and fusion. Consider the parallels between polymers and nuclei. By analogy with biosynthesis [22], one inclines to think that there is the following chain of nuclear reactions creating α-process (Fig. 19). At first, two single alpha-particles (a) combine forming a dimer (b). Then the dimer adds another alpha-particle producing a linear trimer. The trimer has one proton, which is slightly connected with the trimer through the use of only one bond (c). Then the trimer attaches one more alpha-particle creating a four-link chain with two slightly connected protons (d). The process is continuing producing a five-link chain (e). Similar to the interactions of electronic and atomic degrees of freedom in molecules [23], the interaction of tertions (they are not shown in the figure) and protons leads to internal rotation [24] of the slightly connected protons (f). This structure is able to fold up creating the neon nucleus of five-fold symmetry (g) in the shape of a cupola Therefore calcium isomers of five-fold symmetry can be also obtained by means of the following reactions

$$^{4}\mathrm{He}+{}^{4}\mathrm{He}\rightarrow({}^{4}\mathrm{He}{}^{4}\mathrm{He})+{}^{4}\mathrm{He}\rightarrow({}^{4}\mathrm{He}{}^{4}\mathrm{He}{}^{4}\mathrm{He})+{}^{4}\mathrm{He}\rightarrow({}^{4}\mathrm{He}{}^{4}\mathrm{He}{}^{4}\mathrm{He}{}^{4}\mathrm{He})+{}^{4}\mathrm{He}\rightarrow{}^{20}\mathrm{Ne}$$
$$\rightarrow{}^{20}\mathrm{Ne}+{}^{20}\mathrm{Ne}\rightarrow{}^{40}\mathrm{Ca}.$$

It should be emphasized that there are two ways of neon cupola fusion: mirror symmetry and rotation-reflection. As a result, there appear two isomers of calcium. The protons cells and tertion nets of the isomers are shown in Fig. 20. The graphs of the nuclear cells are presented in Fig. 21.

Fusion of two neon-dodecahedron nuclei. There are three isomers of neon 20: classical dodecahedron of pentagons, (tetra-hexa)$_3$-penta$_6$-dodecahedron, and (tetra-hexa)$_6$ dodecahedron [5]. Among the fullerenes having similar shapes, the classical dodecahedron has the highest probability of formation [19]. For this reason, it is worthwhile to investigate the reaction $_{10}\mathrm{Ne}^{20} + {}_{10}\mathrm{Ne}^{20} \rightarrow {}_{20}\mathrm{Ca}^{40}$, where both constituents are classical dodecahedra. The reaction is illustrated in Fig. 22.

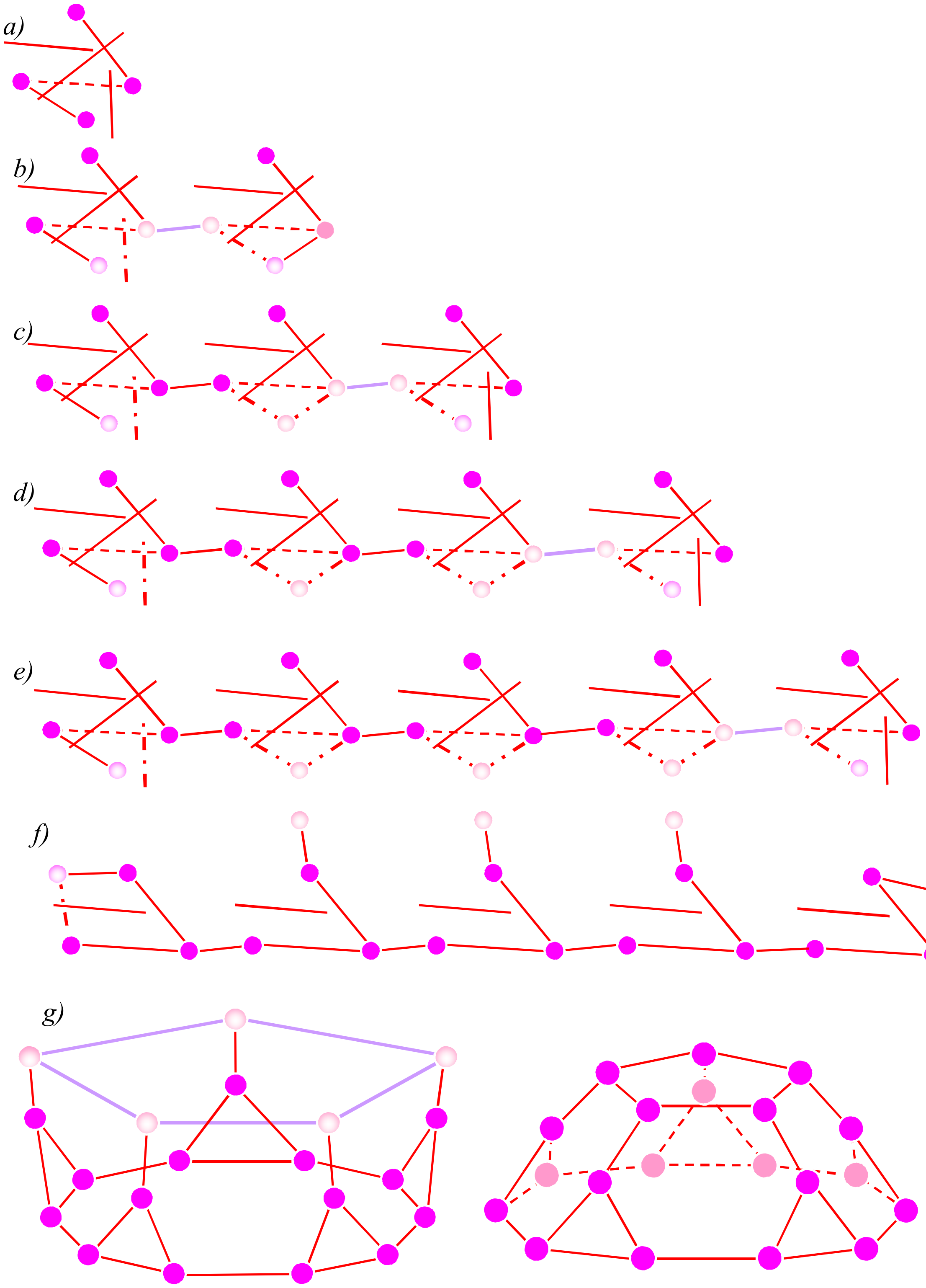

Fig. 19. Generation of cupola-neon-20 isomer: a) single α-particle; b) dimer formation; c) trimer formation with one slightly connected proton; d) four-link chain with two slightly connected protons; e) five-link chain with three slightly connected protons; f) internal rotation of five protons, g) folding of the five-link chain and formation of a five-fold symmetry cupola

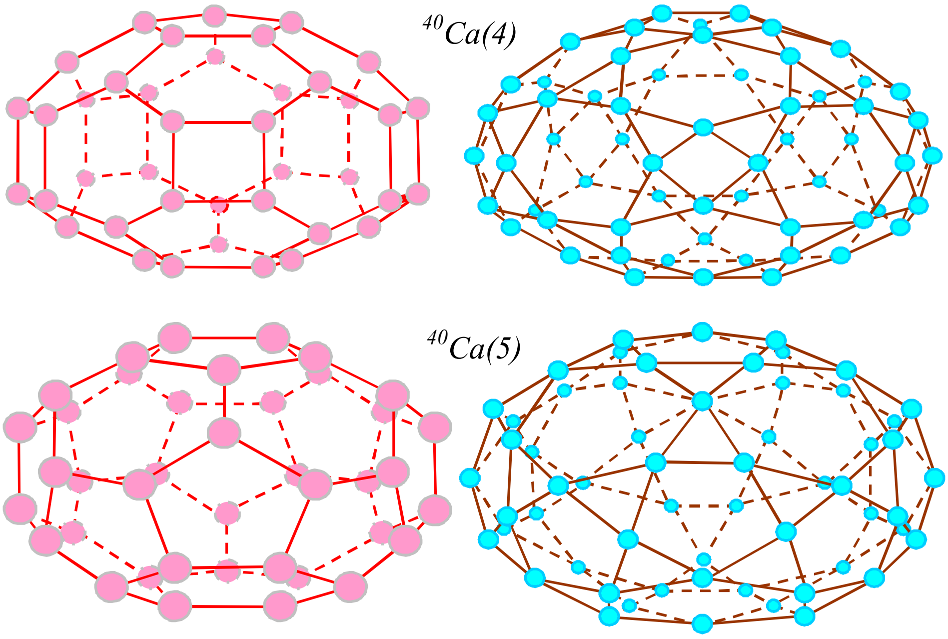

Fig. 20. Protonic and electronic structure of the isomers of calcium $_{20}$Ca^{40} (4 & 5)

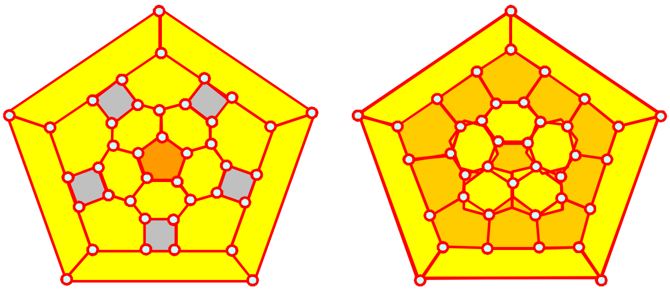

Fig. 21. Graph of the tetra$_5$–penta$_2$−hexa$_{15}$ polyhedron at the left and that of the penta$_{12}$−hexa$_{10}$ polyhedron at the right

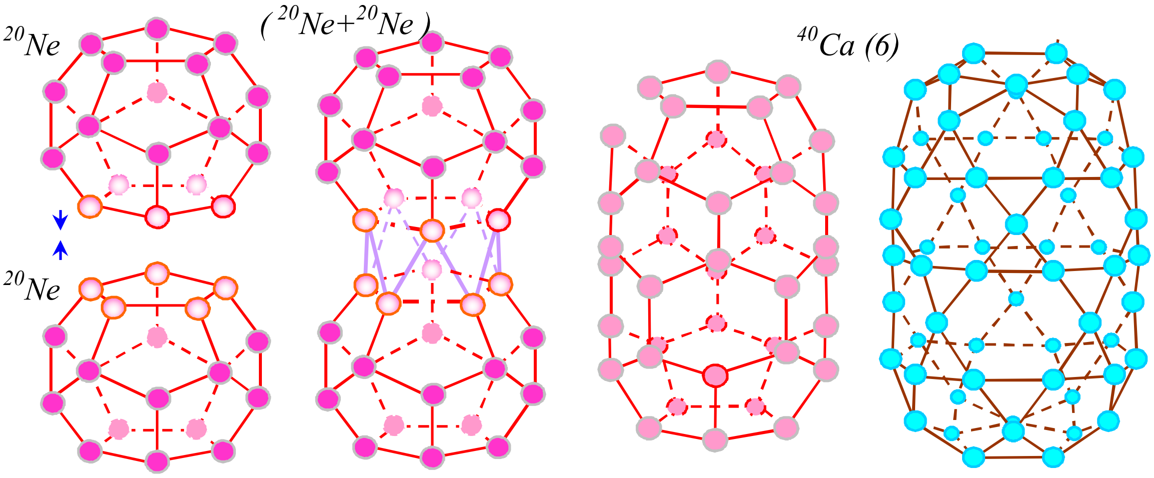

Fig. 22. Fusion of two neon nuclei and formation of calcium (5)

From the figure, it follows that for each neon nucleus only five protons from twenty take part in the reaction. They are pink. The nucleus obtained contains twelve pentagons and ten hexagons; it has five-fold symmetry. The graph of the reaction is shown in Fig. 23.

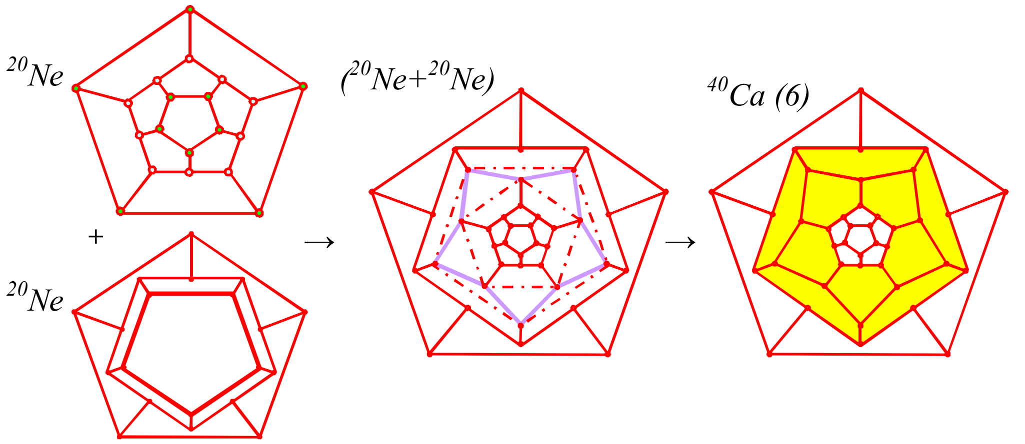

Fig. 23. Graph representation of the nuclear reaction ${}_{10}\mathrm{Ne}^{20} + {}_{10}\mathrm{Ne}^{20} \rightarrow {}_{20}\mathrm{Ca}^{40}$(5)

Joining carbon of six-fold symmetry with tetrahedral silicon. The reaction is illustrated in Fig. 24 and can be written as ${}_{6}\mathrm{C}^{12} + {}_{12}\mathrm{Si}^{28} \rightarrow {}_{20}\mathrm{Ca}^{40}$(7). The nucleus obtained consists of pentagons and hexagons only. The graph representation of this reaction is shown in Fig. 25. It should be emphasized that the first reacting component has six-fold symmetry whereas the second one refers to tetrahedral symmetry. By analogy with designing the fullerenes of tetrahedral symmetry [25], it was assumed that this reaction would give a nucleus of tetrahedral symmetry. However, contrary to the expectation, the nucleus obtained had no tetrahedral symmetry. Under such circumstances, I should look again at the fullerene science.

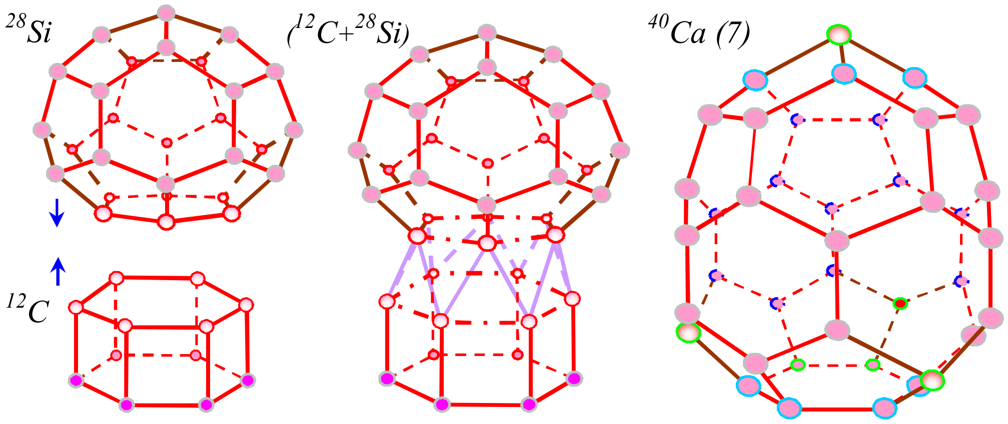

Fig. 24. Fusion of carbon with silicon and formation of calcium (7)

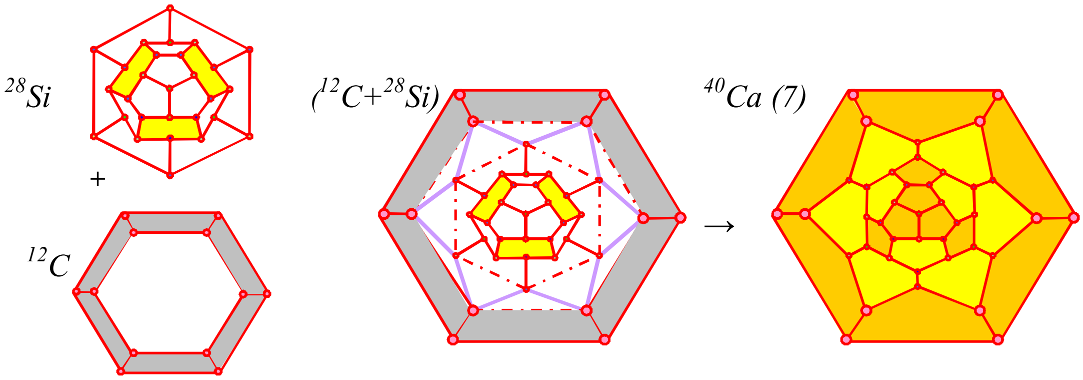

Fig. 25. Graph representation of the nuclear reaction ${}_{6}\mathrm{C}^{12} + {}_{12}\mathrm{Si}^{28} \rightarrow {}_{20}\mathrm{Ca}^{40}$(7)

Stone-Wales transformation of fullerenes. Sometimes an asymmetric fullerene is undergone to Stone-Wales transformation [26] for obtaining a more stable and symmetric isomer [27-30]. The transformation [26] was designed for "spheroidal molecules of sp^2 hybridized carbon atoms with different arrangements of the hexagonal and pentagonal rings. The rearrangement formally requires two sigma bonds to be broken and new bonds to be formed."

Stone-Wales transformation of nuclei. However, the scheme [26] shows only an isolated event. When one has to deal with a whole molecule or with a whole nucleus, where many such events take place, for clarity's sake, it will be more illustrative and informative to use graph language. The Stone-Wales' graph transformation for calcium (4) is shown in Fig. 26. Here the broken edges (bonds) are given using red dot lines; new edges are specially marked, they being painted lilac; the other color designations are the same as before. Really, using three Stone-Wales' transformations we obtained the tetrahedral nucleus of calcium (5). The space shape of protonic cells and tertion nets is shown in Fig. 27.

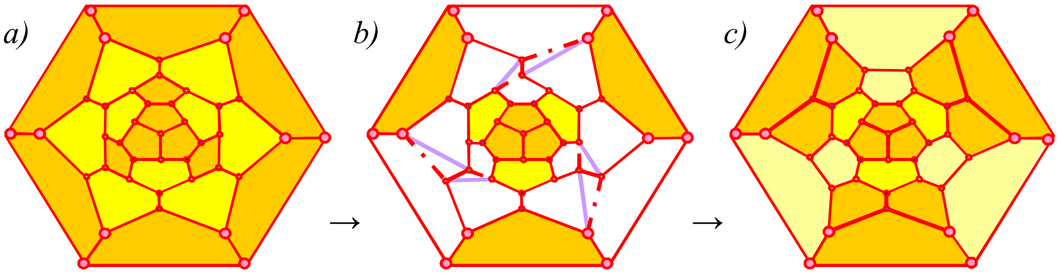

Fig. 26. Graph representation of three Stone-Wales' transformations

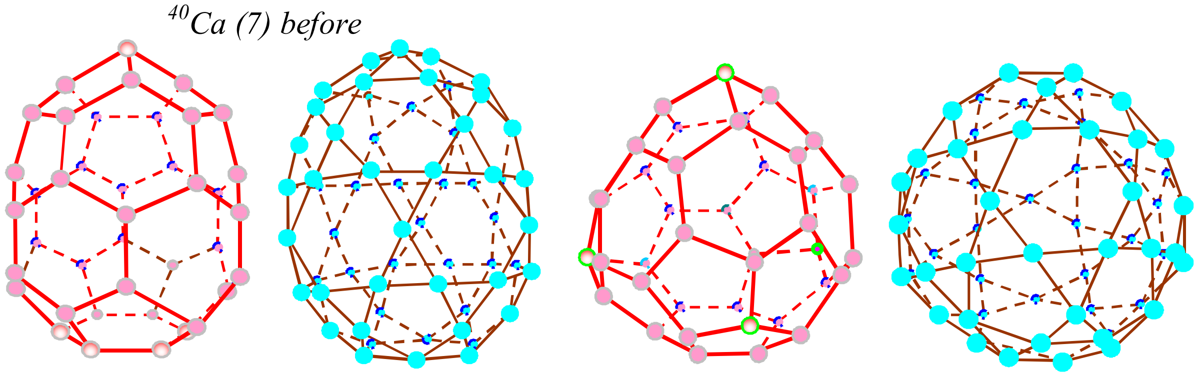

Fig. 27. Protonic cell and tertion net of the calcium isomers 7 and 8

One-neutron-core isotopes. The results obtained for the basic nuclei ${}_{20}Ca^{40}$ show that it is able to form seven isomers. Therefore for the isotope ${}_{20}Ca^{41}$ there is also such possibility. The corresponding isomers can be got by incorporating a neutron into the basic nucleus according to reaction $n + {}_{20}Ca^{40} \rightarrow {}_{20}Ca^{41}$. The protons cells and tertion nets of the isomers obtained are shown in Fig. 28.

^{41}*Ca(1)*

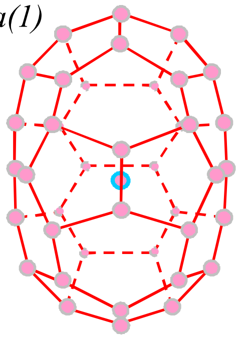

^{41}*Ca(2)*

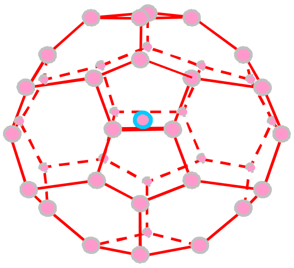

^{41}*Ca (3)*

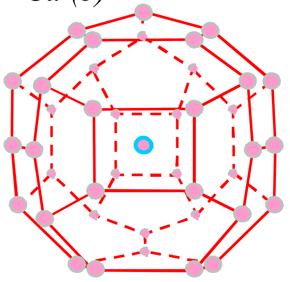

^{41}*Ca(1)*

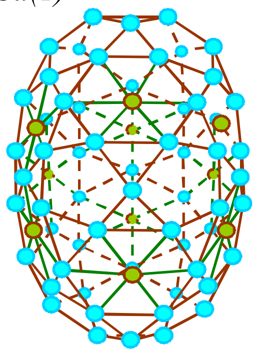

^{41}*Ca(2)*

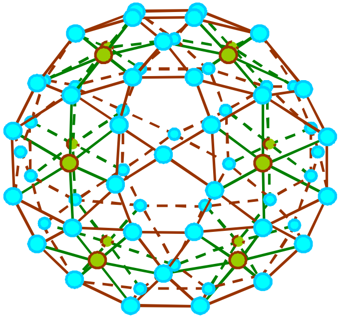

^{41}*Ca(3)*

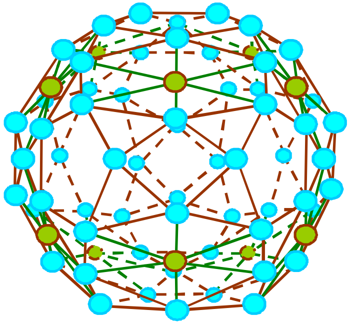

^{41}*Ca(4)*

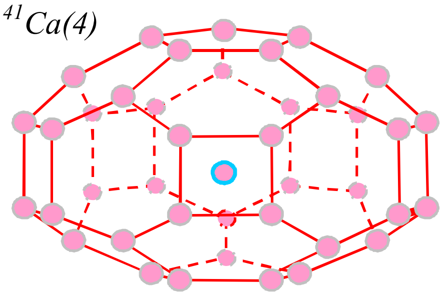

^{41}*Ca(5)*

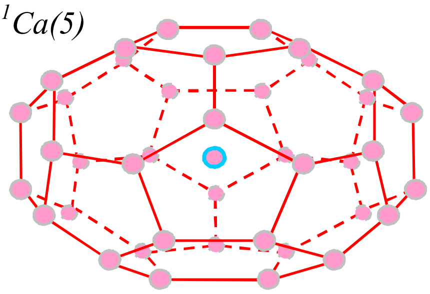

^{41}*Ca(4)*

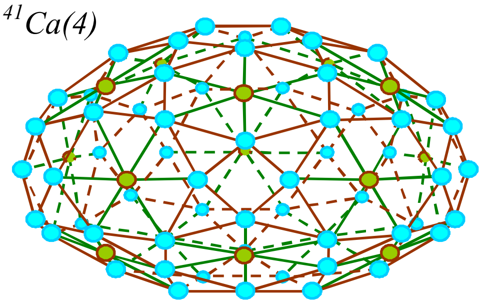

^{41}*Ca(5)*

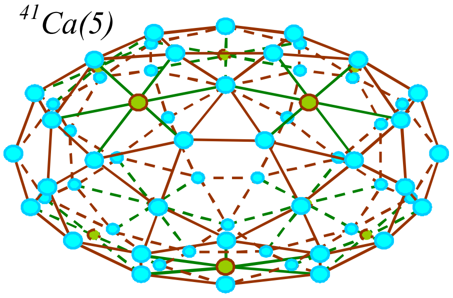

^{41}*Ca (6)*

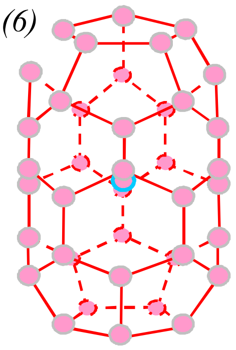

^{41}*Ca (7)*

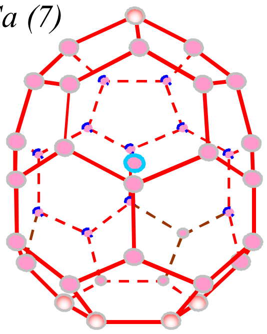

^{41}*Ca (8)*

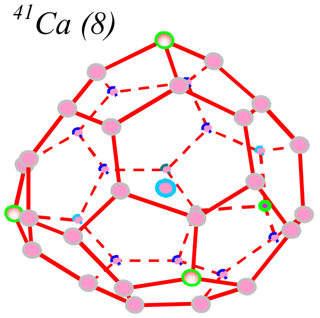

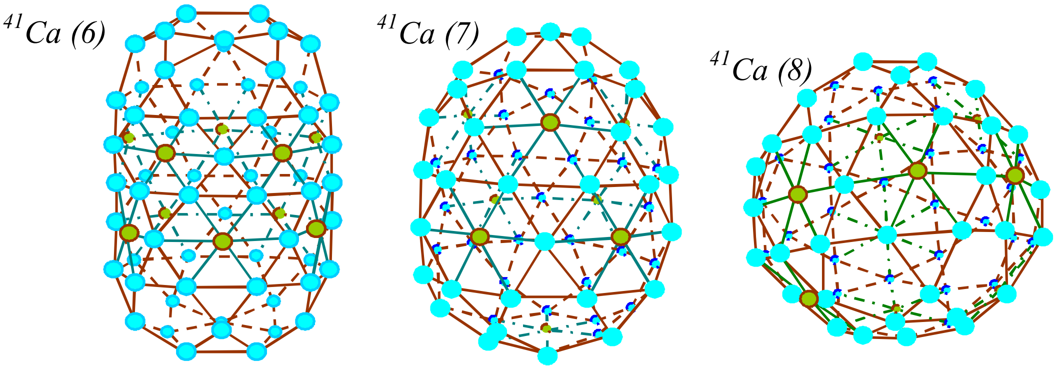

Fig. 28. Protonic cells and tertion nets of the isomers of calcium isotope $_{20}\mathrm{Ca}^{41}$.

It should be emphasized the following. Core extra neutrons of isotope isomers are inside the corresponding nuclei. Here they are subjected to the electric field of their surroundings. It turned out that, due to the Stark effect [15], the decomposition of an internal core neutron into a proton and tertions differs from that of an external neutron; namely, the number of electronic-splitting components depends on the symmetry of the surroundings. It is reasonable to leave the name "tertian" for an electron component, but change its charge. In our case the tertions of the core neutrons have the charge $^{1}/_{10}\,e$ for ^{41}Ca (1), $^{1}/_{12}\,e$ for ^{41}Ca (2) and ^{41}Ca (3), $^{1}/_{15}\,e$ for ^{41}Ca (4), $^{1}/_{10}\,e$ for ^{41}Ca (5), ^{41}Ca (6), ^{41}Ca (7) and ^{41}Ca (8). The regular thing is that the number of such tertions is equal to the number of hexagons in the tertion net of a basic nucleus.

Two-neutron-core isotopes. It is possible to obtain seven isomers of the isotope $_{20}\mathrm{Ca}^{42}$ through the use of the reaction $\mathrm{n} + {}_{20}\mathrm{Ca}^{41} \rightarrow {}_{20}\mathrm{Ca}^{42}$ (Fig. 29).

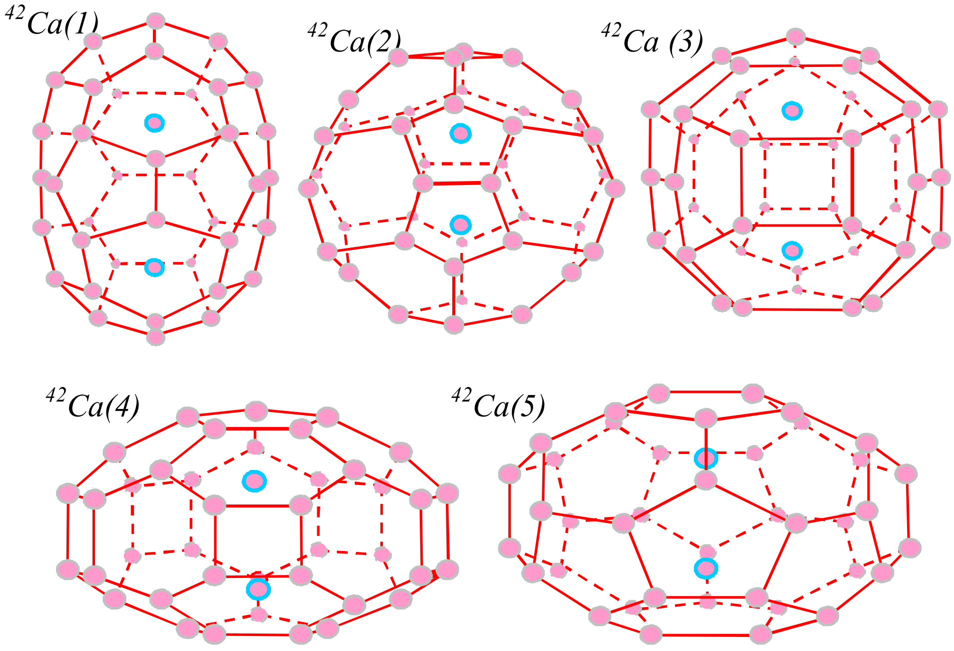

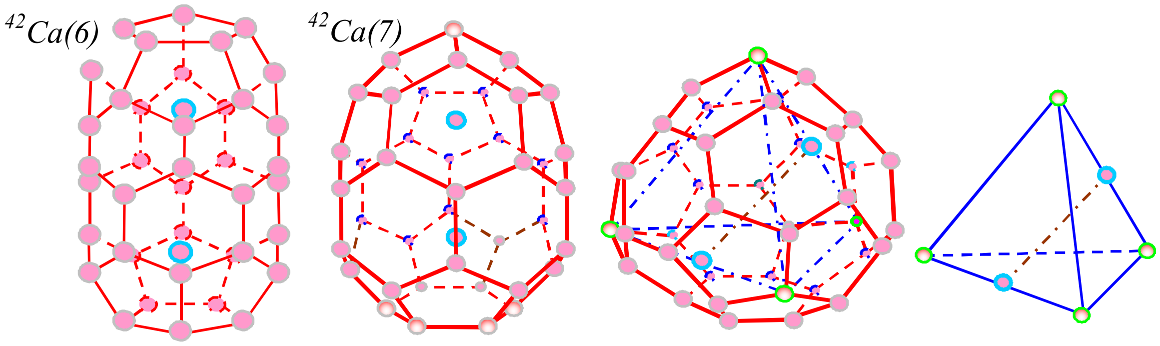

Fig. 29. Protonic cells of the isomers of calcium isotope $_{20}$Ca^{4}

Consider isotopes ^{42}Ca. From Figure 29 it follows that two internal neutrons are removed from one another at the distance larger than the parameter of the proton cell. When there are two internal neutrons, the latter decomposes into protons and tertions by the external surroundings. The protons are localized in the minima of the double-well potential directed along the main symmetry axis. However, now the protons are only slightly connected with one another. It means that they behave themselves almost independently sending their tertions into the coat of mail. As a result, the shape of tertion net does not change. It looks like in Fig. 28, but the neutron's tertions now have double charge, $^1/_5$ e for ^{42}Ca (1), $^1/_6$ e for ^{42}Ca (2) and ^{42}Ca (3), $^2/_{15}$ e for ^{42}Ca (4), $^1/_5$ e for ^{42}Ca (5), ^{42}Ca (6), ^{42}Ca (7) and ^{42}Ca (8), respectively.

Three-neutron-core isotopes. From the results obtained for silicon, sulfur, argon [7], and potassium, it follows that, if the isotopes contain more than two internal neutrons, they can form clusters inside the nucleus. However, the cluster symmetry must be compatible with that of the external surroundings. The simplest structure of the core is a linear chain of three protons lying along the main axis of symmetry. Therefore the seven isotopes having such a core can be generated. Besides the isotope ^{42}Ca(7$_t$) with a triangle core can be created (Fig. 30).

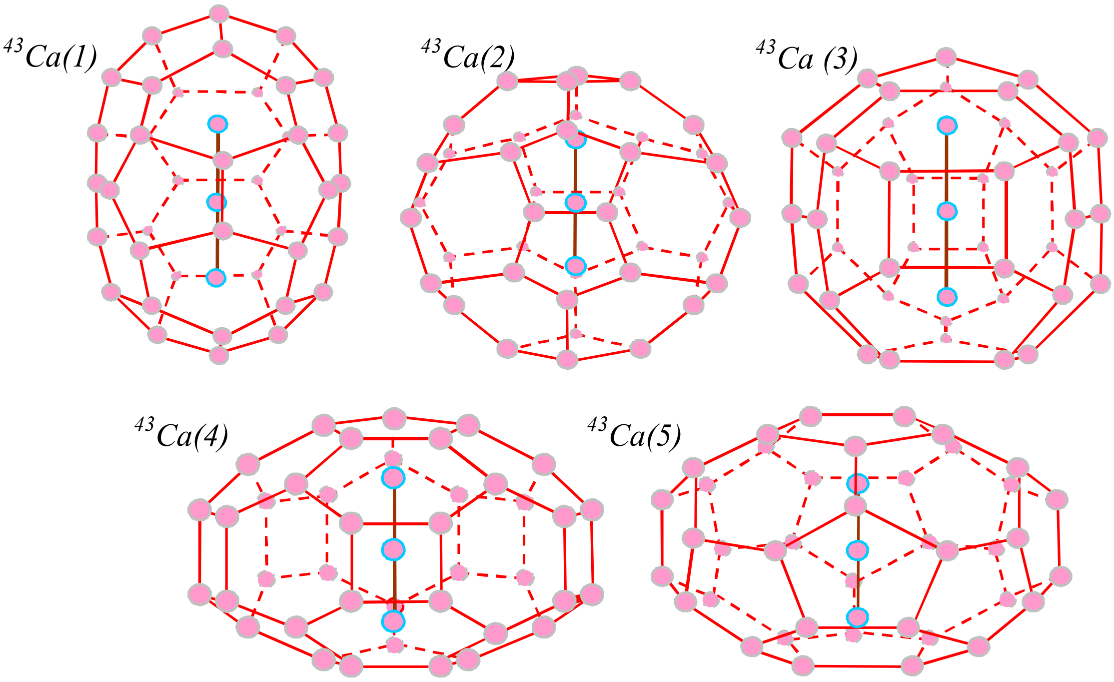

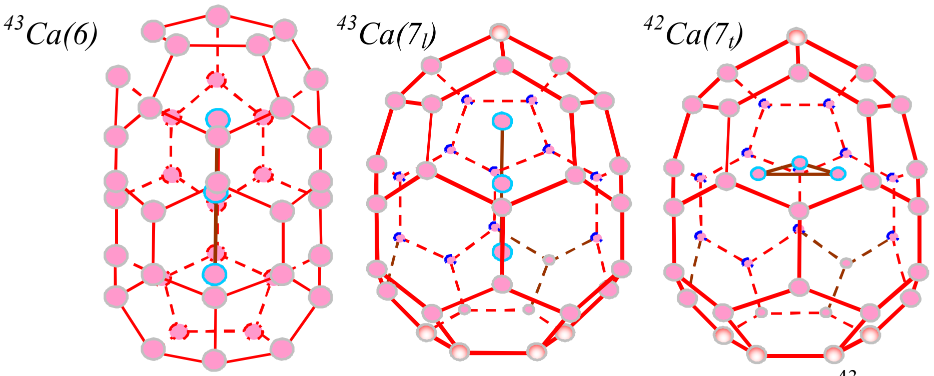

Fig. 30. Protonic cells of the isomers of calcium isotope $_{20}$Ca^{43}

Four-neutron-core isotopes. In view of the symmetry restrictions considered above, only two isomers from eight, ^{44}Ca(2) of four-fold symmetry and ^{44}Ca(8) of tetrahedral one can be formed (Fig. 31). The cores of these isotopes have symmetry compatible with the surroundings.

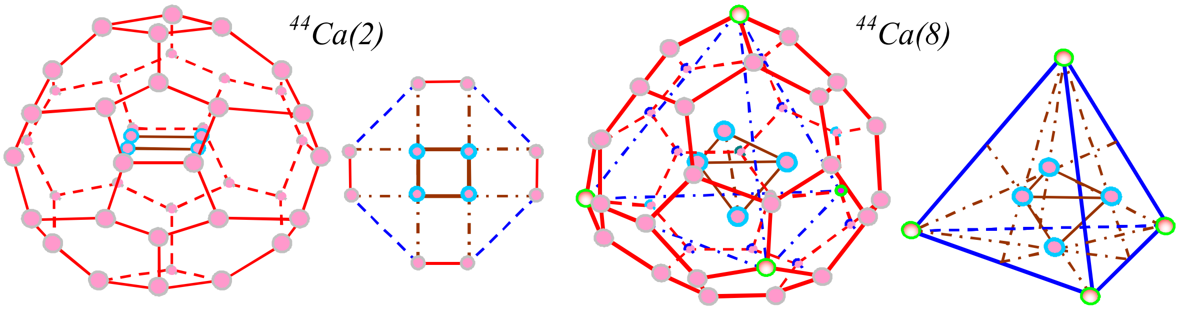

Fig. 31. Protonic cells of the isomers of calcium isotope $_{20}$Ca^{44}

Five-neutron-core isotopes. Similar to the four-neutron-core isotopes, in view of the symmetry restrictions, only two isomers from eight, ^{45}Ca(4) and ^{45}Ca(5) of five-fold symmetry can be formed (Fig. 32). The cores of these isotopes have symmetry compatible with the surroundings.

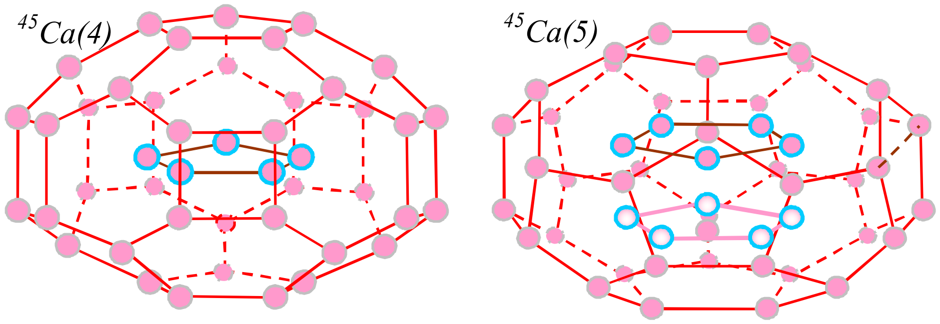

Fig. 32. Protonic cells of the isomers of calcium isotope $_{20}$Ca^{45}

Internal rotation. The isotope ^{45}Ca(5) has a rotation-reflection axis of five-fold symmetry. The core of isotope ^{45}Ca(5) can occupy two different positions inside the nucleus; one in the upper part of the nucleus, and another identical position in the lower part can be achieved through a spiral motion of the core. The core's protons in the lower part of nucleus are specially marked in the figure; they and their bonds are pale pink. Similar to the molecules [1], one can consider such different space core forms of one and the same nucleus as *nuclear* *conformers*. In our case, there are two conformers. One can continue the analogy and come to the conclusion that there exists internal rotation of some cores inside some nuclei.

Six-neutron-core isotope. Only one isomer from eight, ^{46}Ca(7), can be formed. However, it has two different space cores which have symmetry compatible with the surroundings (Fig. 33).

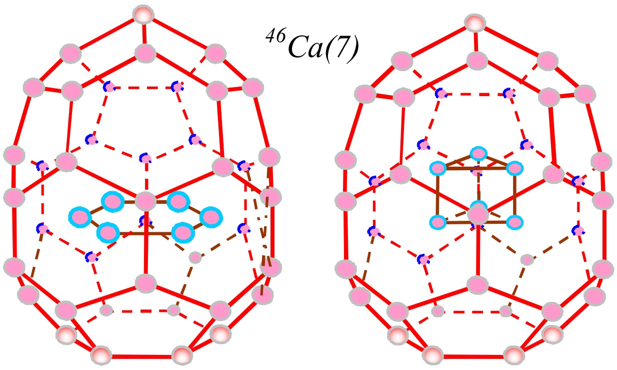

Fig. 33. Protonic cells of the calcium isotopes $_{20}$Ca^{46}

Eight-neutron-core isotope. As before, only one isomer from eight, ^{48}Ca(2), can be formed. However, it has two different space cores which have symmetry compatible with the surroundings (Fig. 34).

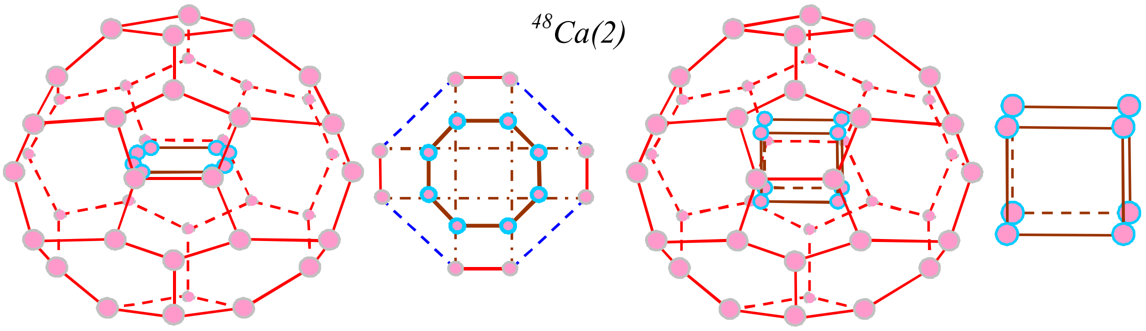

Fig. 34. Protonic cells of the calcium isotopes $_{20}$Ca^{48}

Summary. The results obtained deserve further comment. From the figures above it follows that the nucleus cores are compact. What is more interesting, is the fact that in some cases the cores have the shape of the first elements of the periodic system; namely, helium-3, helium-4, lithium-6, and beryllium-8. As for the electronic structure, it is the same one as for the isotopes with a lesser number of internal core neutrons. Really, although each next neutron above two ones gives an additional electron or some tertions, they are going for constructing the core; the external coat of mail remains without changing.

6. Isomers of scandium

The name derives from the Latin *scandia* for Scandinavia, where the mineral was found. It was first isolated by the Swedish chemist Lars-Fredrik Nilson in 1879 in an ytterbium sample. In the same year, the Swedish chemist Per Theodore Cleve proved that scandium was Mendeleev's hypothetical element "eka-boron" [11].

What do we know about scandium? There are 21 elements that are considered to be monoisotopic. Among them: Be, F, Na, Al, P, and Sc; the first five ones were investigated before now. With the exception of beryllium, all monoisotopic elements have odd numbers of protons, even numbers of neutrons, and, therefore, odd atomic numbers. Scandium has one stable isotope ${}_{21}Sc^{45}$ (100%) [14].

The problem is how to explain these data in the framework of a unified model. Previously [3-7] the nuclei were separated into two main types: basic nuclei having equal numbers of protons and neutrons, and isotopes having one or more additional neutrons. A better understanding can be gained if we begin with basic nuclei having equal numbers of protons and neutrons. Consider again the parallels between fullerenes and nuclei.

Isomer of fullerene C_{42}. From the periodic table of fullerenes [16,17], it follows that there is only one perfect fullerene of the mass 42, having 3-fold T-symmetry. The fullerene was designed previously [17,18]. With knowledge of the fullerene structure, it is possible to obtain a nuclear structure. It can be designed in various ways through the use of the most probable geometrically compatible reactions. Consider one of the possible reactions.

Joining two deuterons to potassium of three-fold S-symmetry. The reaction is presented in Fig. 35. It can be written as ${}_{19}K^{38}(2)+d+d \rightarrow {}_{20}Ca^{40}(1)$, the structure of potassium being obtained above. Here two deuterons are incorporated into a basic nucleus of potassium. From the figure, it follows that for potassium only six protons from thirty-eight take part in the reaction. They are pink. The nucleus obtained contains two trigons, six pentagons, and ten hexagons. The graph representation of this reaction is shown in Fig. 36.

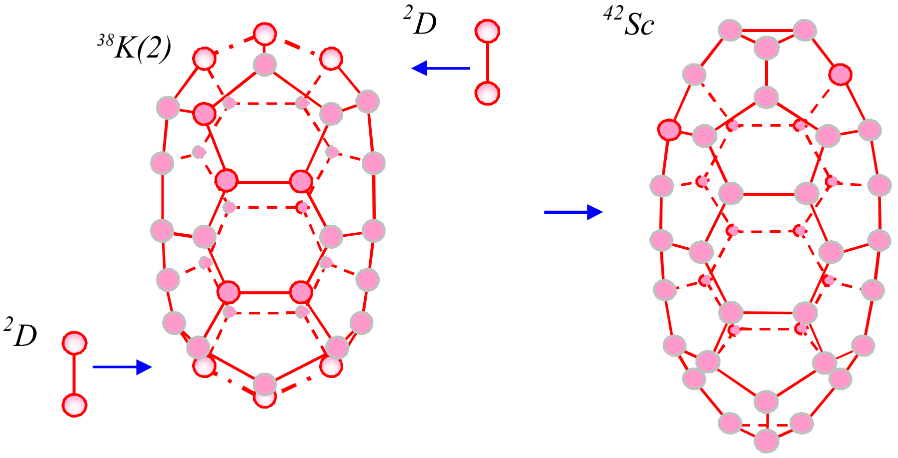

Fig. 35. Attachment of two deuterons to potassium (2) and formation of scandium

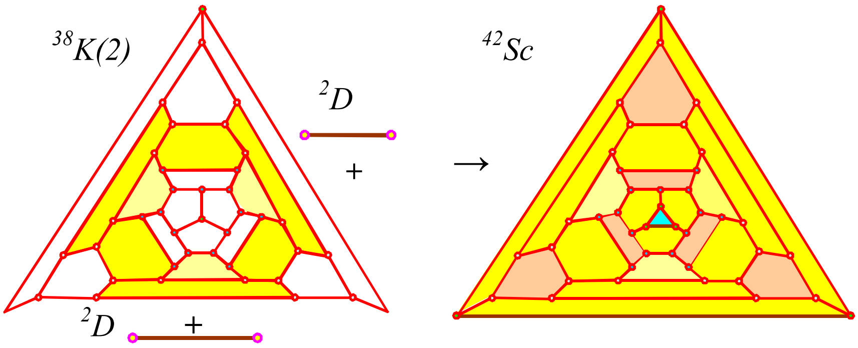

Fig. 36. Graph representation of the nuclear reaction ${}_{19}K^{38}(2)+d+d \rightarrow {}_{21}Sc^{42}(1)$

Three-neutron-core isotope. The only stable isotope ^{45}Sc can be designed from the basic nucleus ^{42}Sc of three-fold T-symmetry by incorporating three neutrons into the center of the basic nucleus. From the results obtained for silicon, sulfur, and argon [7], it follows that the isotopes, containing more than two internal neutrons, form clusters inside the nucleus. With all this going on, the cluster symmetry must be compatible with that of the external surroundings. In our case, it means that the core must have the shape either of a linear chain of three protons, lying along the main axis of symmetry or of an equilateral triangle (Fig. 37). The approximate position of the neutron triangle can be found in a purely geometric way as it is shown in Fig. 37, at the right. The tertion nets of the isotopes ^{42}Sc and ^{45}Sc are shown in Fig. 38.

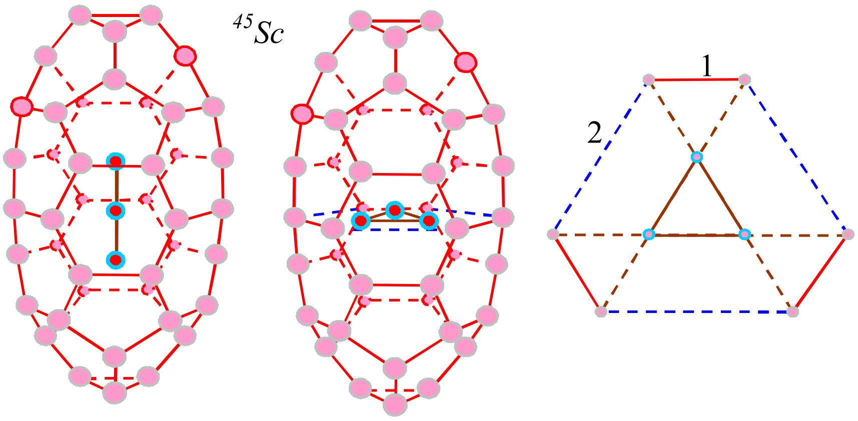

Fig. 37. Protonic cells of isotope ^{45}Sc and the equatorial section at the right (100%)

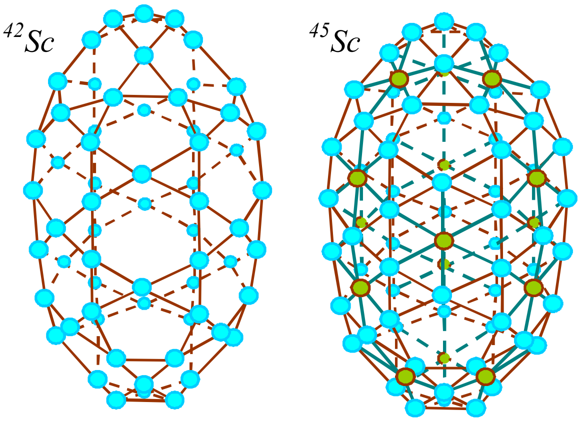

Fig. 38. Electronic structure of scandium isotopes

These results deserve more consideration. One can see that the internal protons of ^{45}Sc form the linear or triangle core, they being tightly connected to one another. Three internal neutrons give three electrons. It is reasonable to assume that one of them remains in the internal core forming two tertions of the charge ½ *e* or three tertions of the charge ⅓ *e*. The other two electrons can be sent to the external electronic coat of mail (tertion net) where they decompose into tertions. The number of tertions must be equal to that of the hexagons of the tertion net of the basic nucleus. In our case, there are fifteen hexagonal faces of the coat of mail. Therefore the tertions sent have the charge $^2/_{15}$ *e*. At that, the tertion-net hexagons became face-centered.

7. Isomers of titanium and their isotopes

The name derives from the Latin *titans*, who were the mythological "first sons of the earth". It was originally discovered by the English clergyman William Gregor in the mineral ilmenite ($FeTiO_3$) in 1791. He called this iron titanite menachanite and the element menachin, for the Menachan parish where it was found. It was rediscovered in 1795 by the German chemist Martin Heinrich Klaproth, who called it titanium because it had no characteristic properties to use as a name. Titanium metal was first isolated by the Swedish chemists Sven Otto Pettersson and Lars Fredrik Nilson [11].

There are five stable isotopes of titanium: $_{22}\mathrm{Ti}^{46}$ (8.0%), $_{22}\mathrm{Ti}^{47}$ (7.30%), $_{22}\mathrm{Ti}^{48}$ (73.8%), $_{22}\mathrm{Ti}^{49}$ (5.5%), $_{22}\mathrm{Ti}^{50}$ (5.4%). Besides, there is isotope $_{22}\mathrm{Ti}^{44}$, having the rather large half-decay period being equal to 47.3 y [14].

From the periodic table of fullerenes [16,17], it follows that there is only one perfect fullerene of mass 44, having 3-fold S-symmetry. The fullerene was designed previously [17,18]. With knowledge of the fullerene structure, one is able to design a nuclear structure. The problem is the same as before, how to design the nuclear structure of titanium's isotopes and isomers. A better understanding can be gained again if we begin with the basic nucleus having equal numbers of protons and neutrons. Consider some possible reactions.

Joining three deuterons to potassium of three-fold S-symmetry. The possible reaction is presented in Fig. 39. It can be written as $_{19}K^{38}(2)+d+d+d \rightarrow {}_{22}Ti^{44}(2)$. Here three deuterons are incorporated into a basic nucleus of potassium having three-fold S-symmetry. From Figure 39 it follows that for potassium only four protons from thirty-eight take part in the reaction. They are pink. The structure of the titanium design is shown in Fig. 39 on the right. The nucleus obtained contains twelve pentagons and twelve hexagons and has three-fold S-symmetry. The reaction graph is presented in Fig. 40.

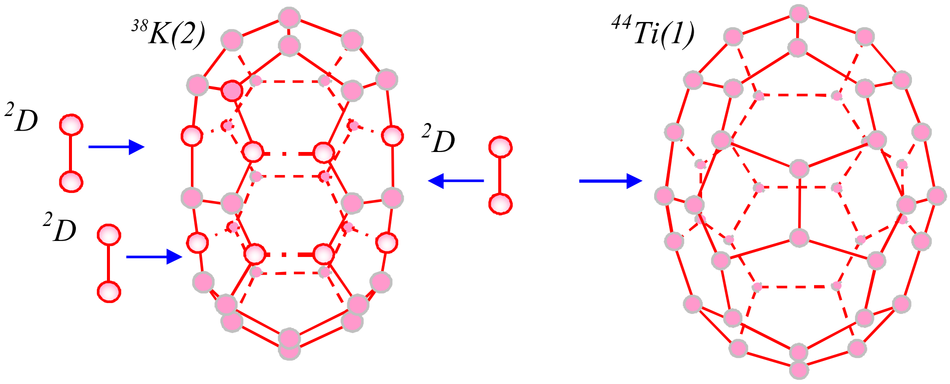

Fig. 39. Attachment of three deuterons to potassium (2) and formation of titanium (1)

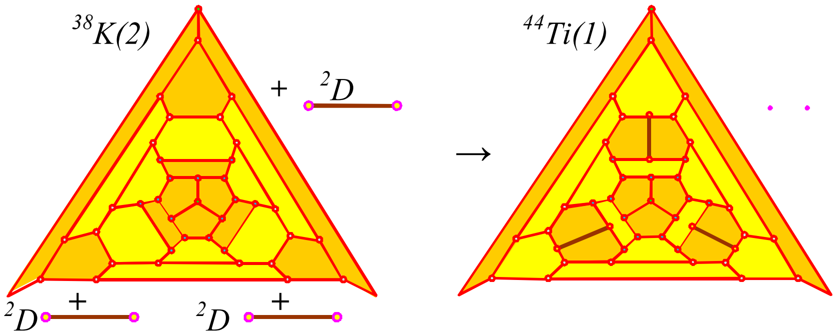

Fig. 40. Graph representation of the nuclear reaction $_{19}K^{38}(2)+d+d+d \rightarrow {}_{22}Ti^{44}(1)$

Joining two α-particles to argon of six-fold symmetry. The reaction is presented in Fig. 41. It can be written as $_{18}Ar^{36}(2)+\alpha+\alpha \rightarrow {}_{22}Ti^{44}(1)$. Here two alpha-particles are incorporated into a basic nucleus of argon having six-fold symmetry. From Figure 39 it follows that for argon twelve protons from thirty-six take part in the reaction. They are pink. The structure of the titanium design is shown in Fig. 41 on the right. The nucleus obtained contains twelve pentagons and twelve hexagons and has also three-fold S-symmetry. The graph of this reaction is presented in Fig. 40.

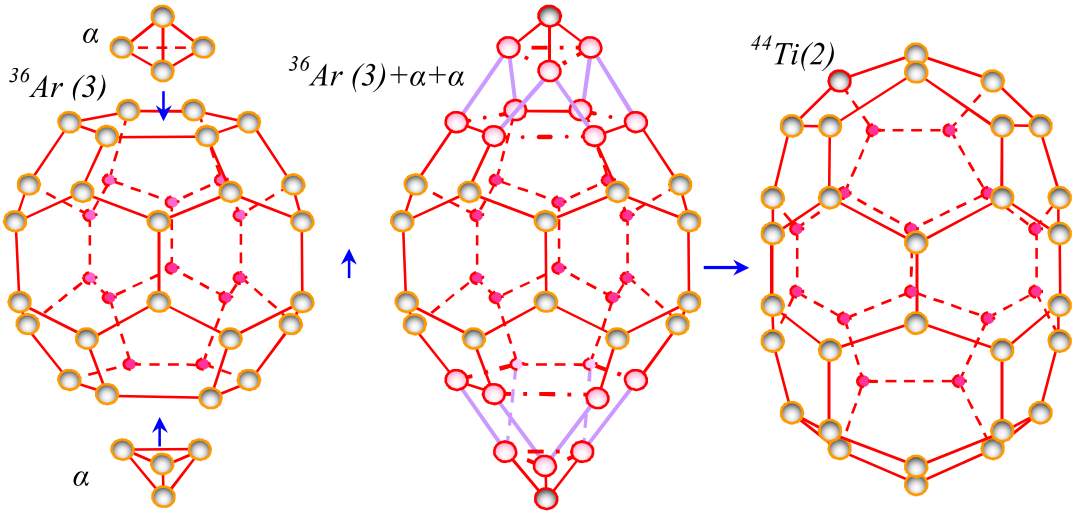

Fig. 41. Attachment of two alpha-particles to argon (3) and formation of titanium (2)

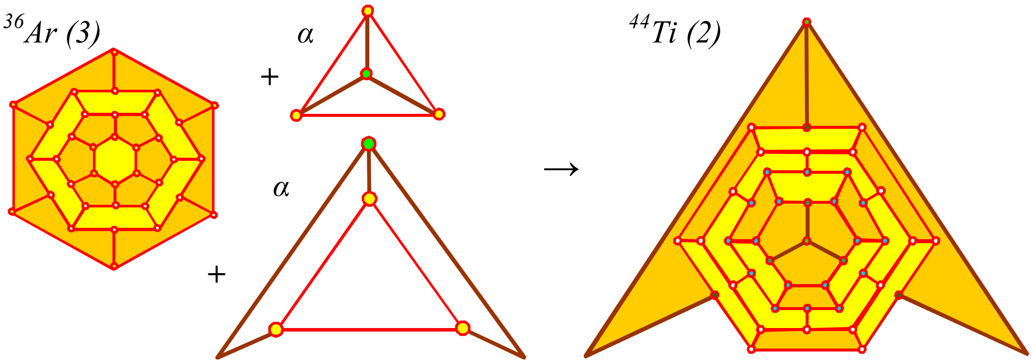

Fig. 42. Graph representation of the nuclear reaction $_{18}Ar^{36}(3)$+α+α→ $_{22}Ti^{44}(2)$

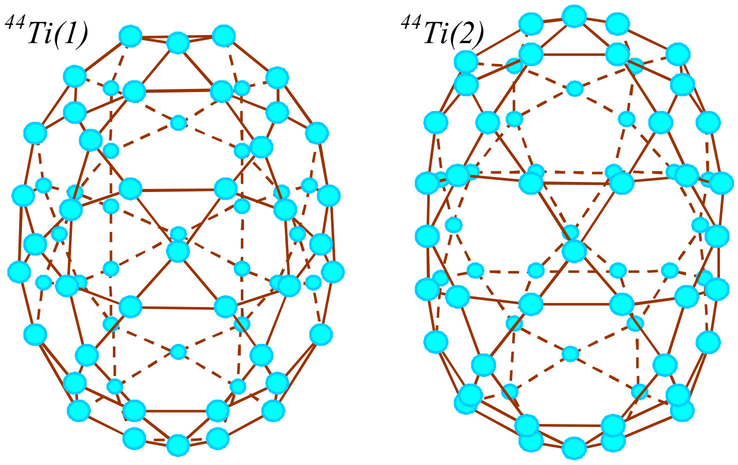

Fig. 43. Electronic structure of two basic titanium isomers

Neutron-core isotopes of titanium isomers. As pointed out above, there are five stable isotopes of titanium: $_{22}Ti^{46}$, $_{22}Ti^{47}$, $_{22}Ti^{48}$, $_{22}Ti^{49}$, and $_{22}Ti^{50}$. They can be got by successive incorporating neutrons: $_{22}Ti^{44}+n\rightarrow{}_{22}Ti^{45}+n\rightarrow{}_{22}Ti^{46}+n\rightarrow{}_{22}Ti^{47}+n\rightarrow{}_{22}Ti^{48}+n\rightarrow{}_{22}Ti^{49}+n\rightarrow{}_{22}Ti^{50}$. The protons cells of the isotopes are shown in Figs. 44 and 45.

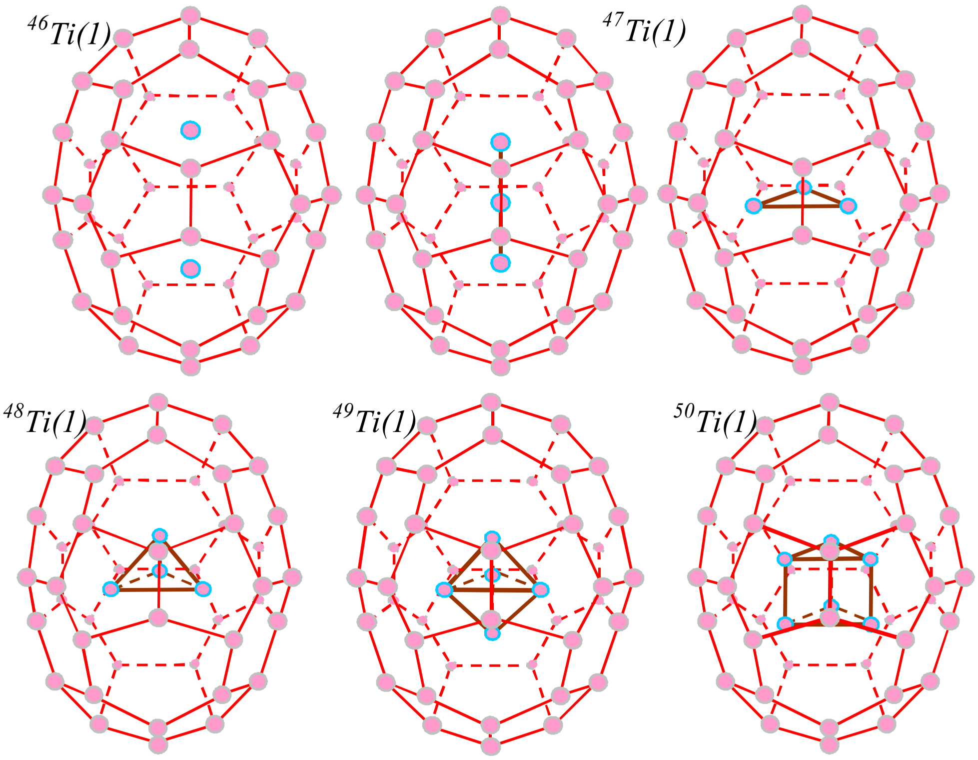

Fig. 44. Isotopes of titanium-1 isomer

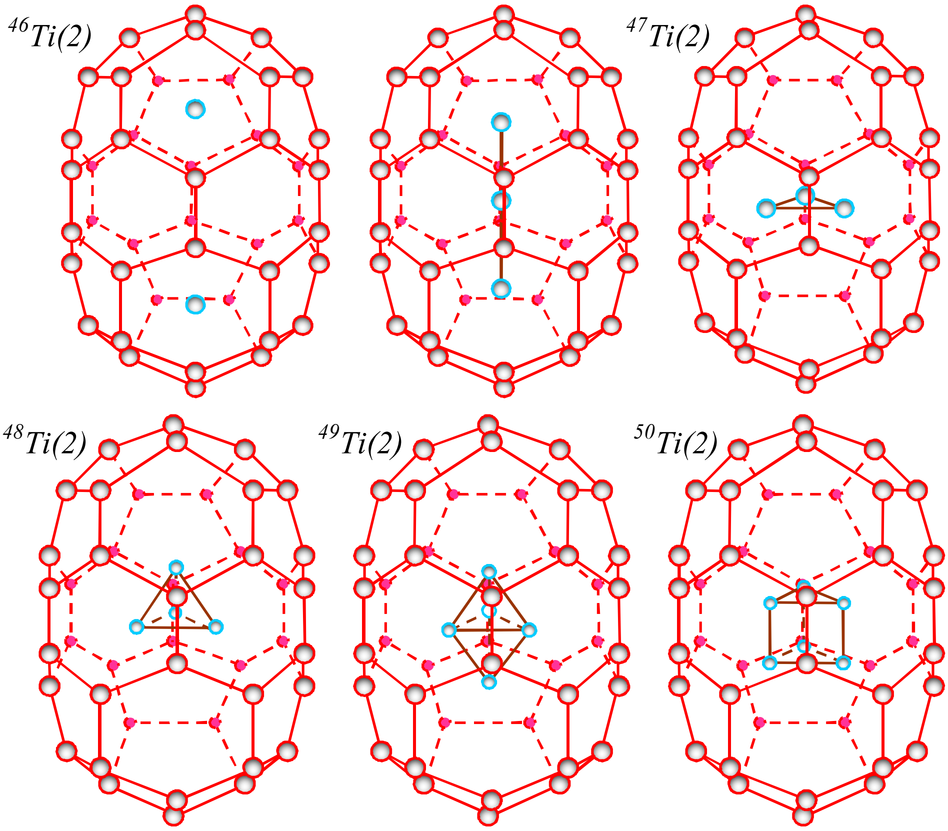

Fig. 45. Isotopes of titanium-2 isomer

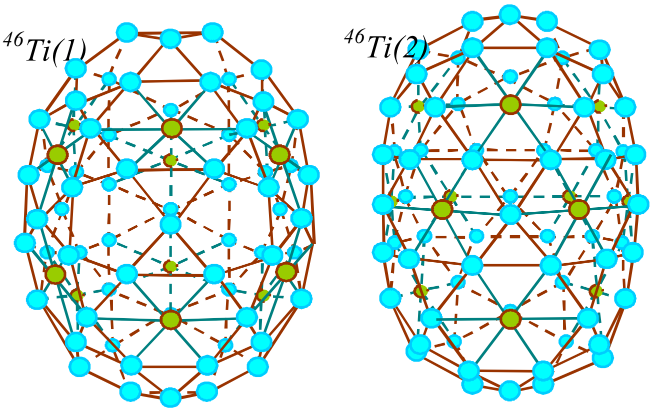

Fig. 46. Tertion nets of the isomers of titanium isotope ${}_{22}\mathrm{Ti}^{46}$

From the results obtained previously, it follows that the isotopes, containing two internal core neutrons, decompose into two protons and two electrons. The latter decomposes into the tertion, the number of which and hence the charge being depended on the structure of the external coat of arms (tertion net). Being removed from one another at the distance larger than the parameter of the proton cell, the core protons do not interact with each other and send their tertions to the external coat of mail. Since there are twelve hexagons, each face-centered hexagon has a tertion of charge $^1/_6$ *e*.

If the isotopes contain more than two internal neutrons, the latter form clusters (core) inside the nucleus. However, the core symmetry must be compatible with that of the external surroundings. From the figures above it follows that the nucleus cores are compact. What is more interesting, is the fact that the cores have the shape of the first elements of the periodic system; namely, helium-3, helium-4, and lithium-6. At the same time, the electronic structure is unchangeable; it is the same one as for the isotopes with two internal core neutrons. This is no surprise. Although each next neutron above two ones gives an additional electron (or three tertions), its tertions are going for fastening the formed proton to the already existing core, so the external coat of mail remains without changing.

8. Summary

By analogy with fullerenes, nuclear geometry has been designed. The nuclei can be classed into two groups: basic nuclei having equal numbers of protons and neutrons and isotopes having one, two, or more additional neutrons. The latter ensures the mechanical stability of the structure with respect to thermal vibrations and shear stresses. If the number of additional neutrons exceeds two, the latter can form a core whose symmetry is compatible with that of the basic nuclei.

On the basis of the geometric approach, it is possible to design the structure of potassium, calcium, scandium, and titanium isomers together with their isotopes, within the framework of one and the same assumptions.

References

1. Prokhorov AM. (Ed.) *Physical Encyclopedic Dictionary*. Moscow: Great Russian Encyclopedia; 1995.

2. Melker AI. *Dynamics of Condensed Matter*, *Vol. 3*, *Noophysics (Science and Scientists)*. St. Petersburg Academy of Sciences on Strength Problems; 2006.

3. Melker AI. Nuclear geometry: from hydrogen to boron. *Materials Physics and Mechanics*. 2020;45(1): 132-149.

4. Melker AI. Isomers and isotopes of carbon. *Materials Physics and Mechanics*. 2020;45(1): 150-166.

5. Melker AI. Nuclear geometry: from nitrogen to neon. *Materials Physics and Mechanics*. 2020;46(1): 149-167.
6. Melker AI. Nuclear geometry: sodium, magnesium, aluminum. *Materials Physics and Mechanics*. 2020;46(1): 168-181.
7. Melker AI. Nuclear geometry: from silicon to argon. *Reviews on Advanced Materials and Technology*. 2021;3(2): 53-78.
8. Prokhorov YV. *Mathematical Encyclopedic Dictionary*. Moscow: Soviet Encyclopedia; 1988.
9. Gillespie RJ. *Molecular Geometry*. London: Van Nostrand Reinhold; 1972.
10. Sidgwick NV, Powell HM. Bakerian lecture: Stereochemical types and valency groups. *Proc. Roy. Soc. Series A*. 1940;176(965): 153-180.
11. de Laeter JR, Böhlke JK, de Bièvre P, Hidaka H, Peiser HS, Rosman KJR, Taylor PDP. Atomic weights of the elements: Review 2000 (IUPAC technical report). *Pure Appl. Chem.* 2003;75(6): 683-800.
12. Melker AI, Krupina MA. Hidden symmetry or why cyclic molecules have so strange forms. *Materials Physics and Mechanics*. 2010;9(1): 11-19.
13. Vlasov NA. *Neutrons*. Moscow: Nauka; 1971.
14. Grigoriev IS, Meilikhov ES. *Physical Values, Handbook*. Moscow: Energoatomizdat; 1991.
15. Kondratiev VN. *Structure of Atoms and Molecules*. Moscow: Fizmatgiz; 1959.
16. Melker AI, Krupina MA. Modeling growth of midi-fullerenes from C_{48} to C_{72}. *Materials Physics and Mechanics*. 2017;34(1): 29-36.
17. Melker AI, Krupina MA, Zarafutdinov RM. Fullerenes of the $\Delta n=12$ series. *Materials Physics and Mechanics*. 2017;34(1): 46-50.
18. Melker AI, Krupina MA, Zarafutdinov RM, Periodic system of fullerenes: the column of three-fold symmetry, *Nonlinear Phenomena in Complex Systems.* 2019;22(4): 383-394
19. Melker AI, Matvienko AN, Natural isomers of fullerenes from C_{20} to C_{28}. *Materials Physics and Mechanics*. 2020;45(1): 49-59.
20. Melker AI, Matvienko AN, Krupina MA. Natural isomers of fullerenes from C_{30} to C_{40}. *Materials Physics and Mechanics*. 2020;45(1): 60-78.
21. Melker AI, Matvienko AN, Krupina MA. Classification of fullerene isomers from C_{40} to C_{48}. To be published in *Reviews on Advanced Materials and Technology*. 2022.
22. MacGregor EA. Polymers, Natural. In: *Encyclopedia of Physical Science and Technology.* Orlando: Academic Press; 1987. p.85-119.
23. Melker AI. Fiftieth anniversary of molecular dynamics. *Proceedings of SPIE.* 2007;6597: 659702.
24. Krupina MA, MelkerAI. Unified approach to vibrations and rotations of molecules and macromolecules. *St. Petersburg State Polytechnical University Journal: Physics and Mathematics.* 2009;2(77): 112-116.
25. Melker AI, Starovoitov SA, Zarafutdinov RM. Tetrahedral mini- and midi-fullerenes. *Materials Physics and Mechanics*. 2019;41(1): 52-61.
26. Stone AJ, Wales DJ. Theoretical studies of icosahedral C_{60} and some fuzlated species. *Chemical Physics Letters.* 1986;128(5,6): 501-503.
27. Podlivaev AI, Openov LA. Stone–Wales transformation paths in fullerene C_{60}. *Journal of Experimental and Theoretical Physics Letters*, 2005; 81(10): 533-537.
28. Ma J, Alfè D, Michaelides A, Wang E. Stone-Wales defects in graphene and other planar sp^2-bonded materials. *Physical Review.* 2009;B80(3): 033407(4).
29. Irle S, Page AJ, Saha B, Wang Y, Chandrakumar KRS, Nishimoto Y, Qian H-J, Morokuma K. Atomistic mechanisms of carbon nanostructure self-assembly as predicted by nonequilibrium QM/MD simulations. In: Leszczynski J, Shukla MK. (Eds.) *Practical*

Aspects of Computational Chemistry II: An Overview of the Last Two Decades and Current Trends. Springer; 2012.
30. Heggie MI, Haffenden GL, Lathem CD, Trevetan T. The Stone-Wales transformation: from fullerenes to graphite, from radiation damage to heat capacity. *Philos Trans A Math Phys Eng Sci*. 2016;374(2076): 20150317.

THE AUTHORS

Alexander I. Melker
e-mail: ndtcs@inbox.ru
ORCID:

Materials Physics and Mechanics. 2022;49(1): 136-144
Conference materials
http://dx.doi.org/10.18149/MPM.4912022_9

Modeling of PKA energy spectra and the concentration of vacancy clusters in materials irradiated with light ions

N.A. Voronova[1], A.A. Kupchishin[1], A.I. Kupchishin[1,2]✉, T.A. Shmygaleva[2]

[1]Abai Kazakh National Pedagogical University, Dostyk, 13, Almaty, Kazakhstan

[2]Al-Farabi Kazakh National University, 71 Al-Farabi Ave., Almaty, Kazakhstan

✉ ankupchishin@mail.ru

Abstract. The work was carried out within the framework of the cascade-probabilistic method, the essence of which is to obtain and further apply cascade-probabilistic functions. The obtained models make it possible to trace the entire process in development and in the future can be used in industry to obtain materials with predetermined characteristics. The results of the obtained studies can also be used by specialists in the field of solid-state radiation physics, in cosmophysics. The cascade-probability functions, the energy spectra of primary knocked-on atoms (PKA), and the concentration of vacancy clusters in molybdenum irradiated with alpha particles were simulated. Some of their properties and patterns were established. Methods of mathematical analysis, probability theory, and numerical methods were used in the research process.

Keywords: cascade-probability function, energy spectrum, modeling, primary knocked-on atom

***Acknowledgments** This research has been funded by the Science Committee of the Ministry of Education and Science of the Republic of Kazakhstan (Grant No. AP08855701).*

Citation: Voronova NA, Kupchishin AA, Kupchishin AI, Shmygaleva TA. Modeling of PKA energy spectra and the concentration of vacancy clusters in materials irradiated with light ions. *Materials Physics and Mechanics*. 2022;49(1): 136-144. DOI: 10.18149/MPM.4912022_9.

1. Introduction

As is known, the main cause of changes in the structure and physicochemical properties of materials during radiation exposure is the formation of defects [1-4]. In contrast to light particles (electrons, photons, etc.), the interaction of ions with matter creates not only isolated Frenkel pairs, as is considered in many papers, but mostly the clusters of vacancies and interstitial atoms [5].

The process of interaction of ions with matter and their passage through matter is a rather difficult task when creating both physical and mathematical models [5-8]. First of all, this is due to a catastrophic increase in the cross-section for their interaction with electrons and atoms of the medium. At the same time, the depth of penetration of particles into materials with an increase in the mass of incident particles decreases sharply. In calculating the cascade-probability functions in this case it is necessary to apply special methods and techniques. A set of types of incident particles and targets is a huge number of variants. In this

Publisher: Peter the Great St. Petersburg Polytechnic University

case, we can consider different situations where the mass number of incident ions A_1 is less than the mass number of the target A_2, i.e. $A_1 < A_2$, the case when A_1 becomes commensurate with A_2, and finally, very unique processes, with $A_1 > A_2$. As a preliminary analysis shows, all these cases must be taken into account – each of them has its own patterns [9-12].

In addition, using a certain sort of incident particles in a particular material, it is possible to form a predetermined structure and chemical compounds that are rather stable in a wide temperature range [12-16]. Naturally, in this case, the physicochemical properties of such substances will differ from those of the initial materials.

Thus, when considering the passage of ions (including light ions: protons, and alpha particles) through the matter, it is necessary to solve a large variety of physical and mathematical problems [12,17-20]. Most of our work in this direction will be carried out in the framework of the cascade-probability method [12].

2. Calculation method

In this paper, we simulated cascade-probability functions (CPFs), the energy spectra of primary knocked-on atoms (PKA), and the concentration of vacancy clusters in substances irradiated with light ions (protons and alpha particles) taking into account the energy loss. It is assumed that a primary particle formed at a depth of h' interacts with the substance as follows (Fig. 1):

1. A charged particle loses energy for ionization and excitation (the main type of energy loss). These losses are considered continuous during the implantation of the particle into the material.

2. The primary particle forms PKA, at those several interactions creating PKA occur simultaneously with hundreds of interactions with the electrons of the medium (ionization losses).

3. PKA does not form Frenkel pairs (vacancy and interstitial atom) but produces vacancy clusters.

4. For protons, alpha particles, and ions, the nonrelativistic case is considered, the interaction cross-section is selected as the Rutherford cross-section, ionization losses for protons and alpha particles are calculated using the Bethe-Bloch formula, for ions are taken from the tables of parameters of the spatial distribution of ion-implanted impurities (Kumakhov-Komarov).

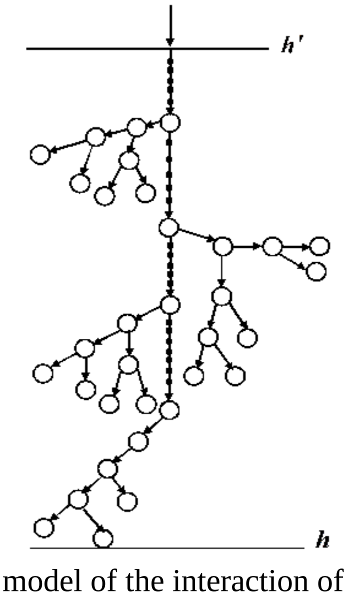

Fig. 1. Physical model of the interaction of ions with target

For protons and alpha particles forming primary knocked-on atoms, the dependence of the cross-section on energy, which, in its turn, depends on the penetration depth, is represented as follows:

$$\sigma(h)=\sigma_0\left(1+\frac{1}{a\left(E_0-kh\right)}\right), \tag{1}$$

where a and E_0 are the approximation parameters obtained by comparing (1) with the calculations of true sections, for example, by electrodynamics methods, by conventional methods, etc.

We have calculated the cascade-probability function (CPF) for ions taking into account the energy loss depending on the interaction parameters. The cascade-probability function, in this case, has the following form (for protons and alpha particles it is the same):

$$\psi_n\left(h',h,E_0\right)=\frac{1}{n!\lambda_0^n}\left(\frac{E_0-kh'}{E_0-kh}\right)^{-l}\exp\left(-\frac{h-h'}{\lambda_0}\right)\left(h-h'+\frac{\ln\left(\frac{E_0-kh'}{E_0-kh}\right)}{ak}\right)^n, \tag{2}$$

where n is the number of interactions, $\lambda_0=1/\sigma_0$, $l=1/\left(\lambda_0 ak\right)$; h', h are the depths of generation and registration, respectively.

PKA spectrum for ions is determined by the following expression:

$$W\left(E_0,E_2,h\right)=\sum_{n=0}^{n_1}\int_{h-k\lambda_2}^{h}\psi_n\left(h'\right)\exp\left(-\frac{h-h'}{\lambda_2}\right)\frac{w\left(E_1,E_2,h'\right)dh'}{\lambda_1\left(h'\right)\lambda_2}. \tag{3}$$

The concentration of vacancy clusters that formed during irradiation of solid with ions is calculated by the formula: max

$$C_k(E_0,h)=\int_{E_c}^{E_{2\max}}W(E_0,E_2,h)dE_2, \tag{4}$$

where E_C is the minimum energy for cluster formation.

3. Results and discussions

As the calculations show, approximation (1) describes the modified cross-sections quite well with a correlation coefficient above 0.99, in particular for molybdenum (Table 1).

Table 1. Approximation values and theoretical correlations for protons in Mo

E_0, [MeV]	σ_0	a	E_0	k	η
1	17176	0.22	4.39	5600	0.999
5	2919	0.0249	31.35	3719	0.9999
10	2123	1.45	1.06	42.1	0.999
15	1694	2.68	0.84	16.92	0.999
20	1413	2.33	1.23	15.19	0.997
25	1227	1.89	1.85	15.64	0.99
30	1067	1.60	2.43	15.01	0.996
40	912.2	0.13	37.98	142.36	0.996
50	790.3	0.11	53.77	136.92	0.99

Let us consider some properties of CPF taking into account the energy loss for protons and alpha particles.

1) $\lim\limits_{h'\to 0}\psi_n\left(h,E_0\right)=\frac{1}{n!\lambda_0^n}\left(\frac{E_0}{E_0-kh}\right)^{-l}\exp\left(-\frac{h}{\lambda_0}\right)\left(h+\frac{\ln\left(\frac{E_0}{E_0-kh}\right)}{ak}\right)^n$,

2) $\lim\limits_{k\to 0}\psi_0\left(h',h,E_0\right)=\exp\left(-\frac{h-h'}{\lambda}\right)$, $\lim\limits_{k\to 0}\psi_n\left(h',h,E_0\right)=\frac{\left(h-h'\right)^n}{n!\lambda^n}\exp\left(-\frac{h-h'}{\lambda}\right)$,

where $\frac{1}{\lambda}=\frac{1}{\lambda_0}\left(1+\frac{1}{aE_0}\right)$.

3) Extremes, areas of decrease and increase.

Find the derivative of $\psi_0^{'}\left(h',h,E_0\right)$ with respect to h:

$$\psi_0^{'}\left(h',h,E_0\right)=\left[\left(\frac{E_0-kh'}{E_0-kh}\right)^{-l}\exp\left(-\frac{h-h'}{\lambda_0}\right)\right]_h^{'}=\frac{1}{\lambda_0}\left(\frac{E_0-kh'}{E_0-kh}\right)\exp\left(-\frac{h-h'}{\lambda_0}\right)*$$

$$*\left[\frac{-1}{a\left(E_0-kh\right)}-1\right];$$

at $-\frac{1}{a\left(E_0-kh\right)}+1=0 \quad \psi_0^{'}\left(h',h,E_0\right)=0$,

therefore $h = E_0/k + 1/ak$ is the point of the extremum.

If $h < E_0/k + 1/ak$, the function $\psi_0(h', h, E_0)$ decreases monotonously, and at $h > E_0/k + 1/ak$ increases monotonously, in this case $h_e = E_0/k + 1/ak$ is the point of minimum.

At $h = E_0/k + 1/ak$

$$\psi_0\left(h_{э},h',E_0\right)=\left[a\left(E_0-kh'\right)\right]^{-\frac{1}{\lambda_0 ak}}\exp\left(\frac{-aE_0-1+h'ak}{\lambda_0 ak}\right).$$

At $n \geq 1$ the equation $d\psi_n/dh = 0$ can be solved only numerically. The point of minimum $h_e = E_0/k + 1/ak$ does not belong to the definition area of $\psi_n(h', h, E_0)$, since $h_e>h_{\max}$ and therefore was not taken into account.

4) Inflection points, the intervals of convexity and concavity. Let us find ψ_0'' and equate it to zero. The equation $d^2\psi_0/dh^2 = 0$ takes place when

$$\left(\frac{E_0}{E_0-kh}\right)^2+\frac{2}{\lambda_0 a}\left(E_0-kh\right)+\left[\frac{1}{\lambda_0 a^2}-\frac{k}{a}\right]=0.$$

Solving this equation, we find:

$$h_1=\frac{E_0}{k}+\frac{\frac{2}{\lambda_0 a}+2\sqrt{\frac{k}{\lambda_0 a}}}{\lambda_0 {k}/{a}};\ h_2=\frac{E_0}{k}+\frac{\frac{2}{\lambda_0 a}+2\sqrt{\frac{k}{\lambda_0 a}}}{\lambda_0 {k}/{a}}.$$

Since the derivative ψ_0'' does not change the sign near points h_1 and h_2 ($\psi_0'' > 0$), the found points are not inflection ones.

5) Asymptotes. To find the vertical asymptotes, we calculate:

$$\lim_{h\to E_0/k}\frac{1}{n!\lambda_0^n}\left(\frac{E_0-kh'}{E_0-kh}\right)^{-l}\exp\left(-\frac{h-h'}{\lambda_0}\right)\left(h-h'+\frac{\ln\left(\frac{E_0-kh'}{E_0-kh}\right)}{ak}\right)^n=0.$$

$$\lim_{h\to E_0/k}\psi_n\left(h',h,E_0\right)=0.$$

Consequently, $h=E_0/k$ is not a vertical asymptote for protons and alpha particles. Obviously, there are no inclined and horizontal asymptotes too, since $h'\le h\le h_{\max}$. The remaining properties of CPF for protons and alpha particles are the same as the properties of the cascade-probability function, which takes into account the energy loss for electrons.

For large values of *n*, CPF calculations were performed using the following modified formula:

$$\psi_n\left(h',h,E_0\right)=\exp\left(-n\lambda_0-\ln n!-\frac{1}{\lambda_0 ak}\ln\left(\frac{E_0-kh'}{E_0-kh}\right)-\frac{h-h'}{\lambda_0}\right)+ \\ +n\ln\left(h-h'+\frac{1}{ak}\ln\left(\frac{E_0-kh'}{E_0-kh}\right)\right). \qquad (5)$$

The software package for calculating CP-functions and selecting the type of theoretical curves is implemented in a Python environment using the Django framework. The calculations are made for protons and α-particles in various targets. As an example, Figures 2 and 3 show the dependence of CPF on the number of interactions and the penetration depth for alpha particles in Mo at E_0 = 10 MeV.

The calculations show that with values of n = 0,1 CPF decrease, depending on *h*, with increasing *n*, they increase, reaching a maximum and begin to decrease. As E_0 grows, the curves shift to the right.

Further to that, the energy spectra of PKA were calculated with formula (3), in particular, for α-particles in Mo. It can be seen that they are decreasing functions (Figs. 4,5). In a good approximation, W (E_2) ~ 1/E_2.

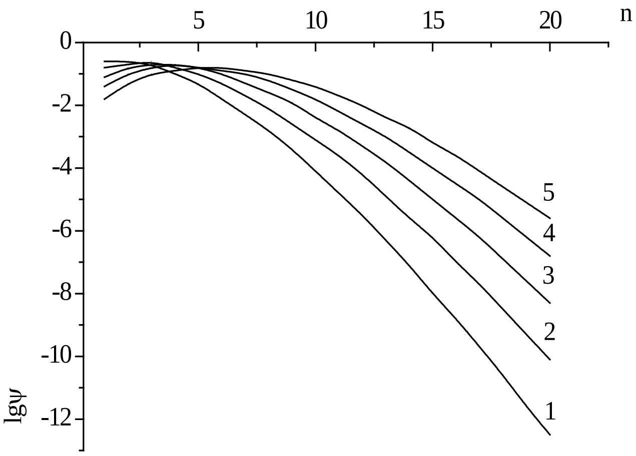

Fig. 2. Dependence of CPF on the number of interactions for alpha particles in molybdenum at E_0 = 10 MeV, *h* = 0.006; 0.008; 0.01; 0.012; 0.014 cm (1-5)

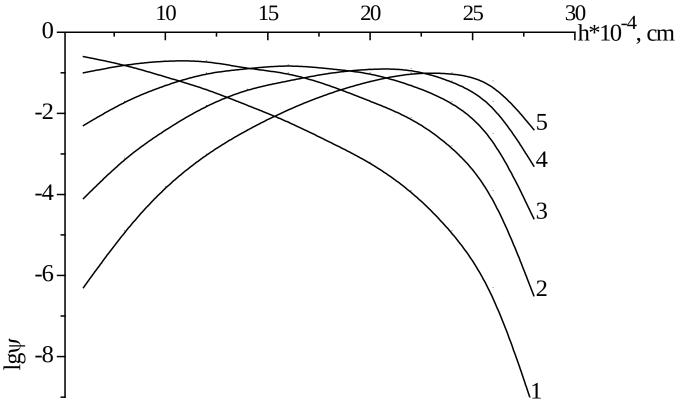

Fig. 3. Dependence of CPF on the penetration depth for alpha particles in molybdenum at E_0 = 10 MeV; n = 1, 4, 7, 10, 13 (1-5)

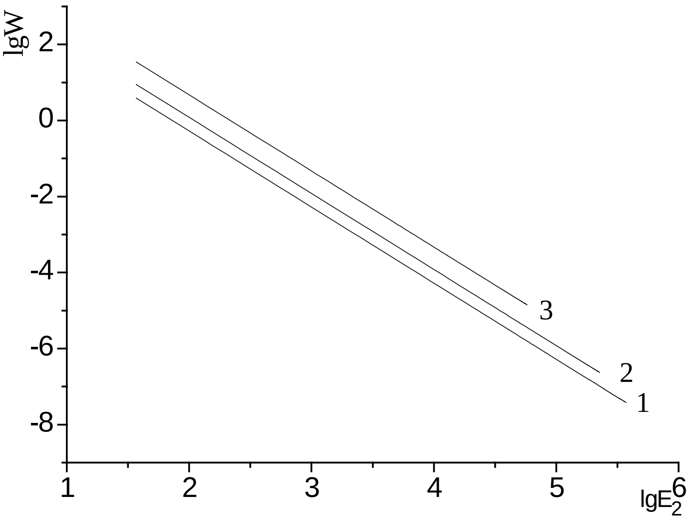

Fig. 4. Dependence $W(E_0, E_2, h)$ for protons in Mo at E_0 = 10 MeV on E_2 at the depths: h = 40 μm (1), h = 156 μm (2), h = 238 μm (3)

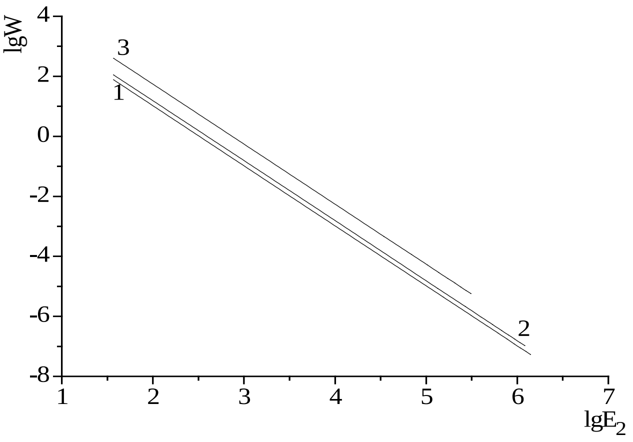

Fig. 5. Dependence $\omega(E_0, E_2, h)$ for α-particles in Mo at E_0 = 10 MeV on E_2 at the depths: h = 4 μm (1), h = 10 μm (2), h = 25 μm (3)

Using formula (4), the concentrations of vacancy clusters were calculated at E_0 = 10, 50 MeV. With increasing depth h, C_k increases, and at the end of the run, it drops sharply to zero. With increasing E_c, the concentration of clusters decreases (Figs. 6 and 7).

Earlier, we calculated the dependence of C_k on h under proton irradiation, which are in satisfactory agreement with experiments on two-photon positron annihilation [2].

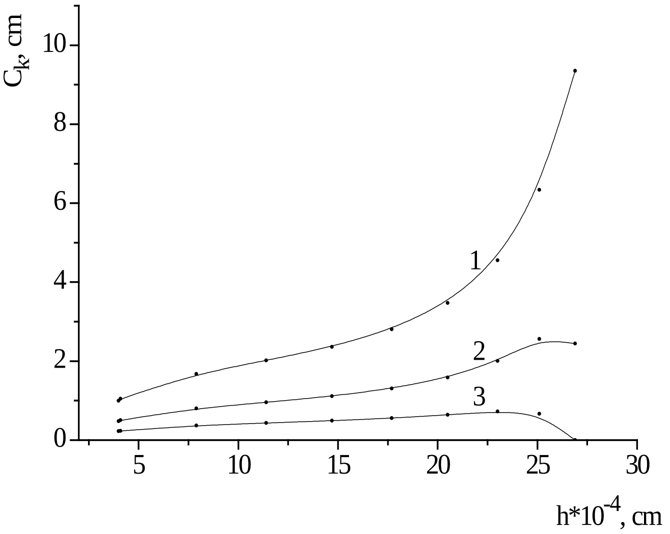

Fig. 6. Dependence of the vacancy clusters concentration on the penetration depth for alpha particles in molybdenum at E_0 = 10 MeV, E_C = 50, 100, 200 keV (1-3)

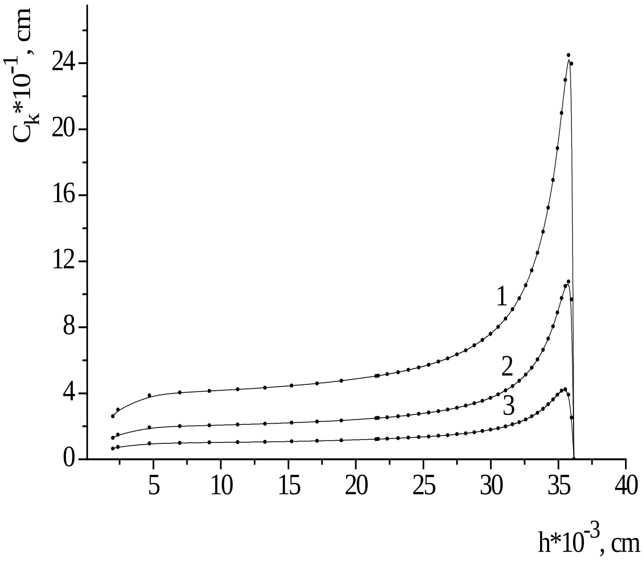

Fig. 7. Dependence of the vacancy clusters concentration on the penetration depth for alpha particles in molybdenum at E_0 = 50 MeV, E_C = 50, 100, 200 keV (1-3)

4. Conclusions

- The analysis of modified cross-sections and the calculation of cascade-probability functions for protons and alpha particles were carried out. It was shown that the correlation coefficients $\eta > 0.99$ (calculated and modified values), which is a good approximation.
- CPF was analyzed and its main properties were established. When k = 0, this function goes to the simplest CPF. There are inflection points and maxima. With increasing n, CPF increases, reaches a maximum, and further decreases. As h increases, the maxima of the curves shift to the right.

- The energy spectra of PKA in Mo were calculated. In a good approximation, we have $W(E_2) \sim 1/E_2$. With increasing depth, C_k increases slowly, reaches a maximum near the end of the path and drops sharply to zero. With increasing E_c, C_k decreases.

References

1. Agranovich VM, Kirsanov VV. Simulation problems of radiation defects in crystals. *Uspekhi Fizicheskikh Nauk*. 1976;118(1): 3-51.
2. Melker AI. *Dynamics of Condensed Matter, Vol. 2, Collisions and Branchings*. St. Petersburg Academy of Sciences on Strength Problems; 2010.
3. Aleksandrov OV, Visotskaya SA, Zhurkin VS. Model of charge of accumulation in MOS-transistors at ionizing irradiation. *Izvestiya St. Petersburg State Electrotechnical University «LETI»*. 2012;7: 20-27.
4. Bogatyrev YuV, Lastovsky SB, Soroka SA, Shwedov SV, Ogorodnikov DA. Influence of gamma radiation on MOS/SOI transistors. *Reports of BGUIR*. 2016;3(97): 75-80.
5. Melker AI. Creation and evolution of vacancy clusters in solids under irradiation. Theory and computer simulation. In: *AIP Conference Proceedings 303: Slow Positron Beams Technique for Solids and Surfaces*. Ottewitte E, Weiss AH. (Eds.) New York: American Institute of Physics; 1994. p.156-178.
6. Kharlamov VS, Kulikov DV, Lubov MN, Trushin YuV. Kinetic Modeling of the growth of copper clusters of various heights in subsurface layers of lead. *Tech. Phys. Lett.* 2015;41: 961-963.
7. Komarov FF, Milchanin OV, Skuratov VA, Mokhovikov MA, Janse A.van Vuuren, Neethling JN, Wendler E, Vlasukova LA, Parkhomenko IN, Yuvchenko VN. Ion-beam formation and track modification of InAs nanoclusters in silicon and silicon dioxide. *Proceedings of the Russian Academy of Sciences. Physical series*. 2016;80(2): 165-169.
8. Ivchenko VA. Atomic structure of cascades of atomic displacements in metals and alloys after different types of radiation. *IOP Conf. Series: Materials Science and Engineering*. 2016;110: 012003.
9. Velichko OI. Modeling of the transient interstitial diffusion of implanted atoms during low temperature annealing of silicon substrates. *Physica B*. 2012;407: 2176-2184.
10. Pogrebnjak AD, Yakushenko IV, Bondar OV, Sobol OV, Beresnev VM, Oyoshi K, Amekura H, Takeda Y. Influence of implantation of Au– ions on the microstructure and mechanical properties of the nanostructured multielement (TiZrHfVNbTa)N coating. *Phys. Solid State*. 2015;57(8): 1559-1564.
11. Kozlova OA, Zelenina MS. Ab initio simulation of two-dimensional MOS_2 with vacancy clusters using grid technologies. *Materials Physics and Mechanics*. 2014;20(1): 51-55.
12. Boos EG, Kupchishin AI, Kupchishin AA, Shmygalev YeV, Shmygaleva TA. *Cascade-probabilistic method. Solution of radiation-physical problems, Boltzmann equations. Connection with Markov's chains*. Almaty, Abay KazNPU, SRINCTaM al-Farabi KazNU, Kama LLP, 2015.
13. Kupchishin AI, Shmygalev EV, Shmygaleva TA, Jorabayev AB. Relationship between Markov Chains and Radiation Defect Formation Processes by Ion Irradiation. *Modern Applied Science*. 2015;9(3): 59-70.
14. Nelaev VV, Stempitsii VR. *Osnovy SAPR v mikroelektronike. Fizicheskoe modelirovanie tekhnologii i pribora: uchebnoe posobie*. Minsk: BSUIR; 2006.
15. Kupchishin AI, Voronova NA, Shmygaleva TA, Kupchishin AA. Computer simulation of vacancy clusters distribution by depth in molybdenum irradiated by alpha particles. *Key Engineering Materials*. 2018: 3-7.
16. Sogojan AV. Space Model. *M: MS University, Institute of Nuclear Physics*. 2007;2: 3-7.

17. Makhavikou M, Komarov F, Parkhomenko I, Vlasukova L, Milchanin O, Zuk J, Wendler E, Romanov I, Korolik O, Togambayeva A. Structure and optical properties of SiO_2 films with ZnSe nanocrystals formed by ion implantation. *Surface Coatings Technology*. 2018: 596-600.
18. Makhavikou M, Parkhomenko I, Vlasukova L, Komarov F, Milchanin O, Mudryi A, Zhivulko V, Wendler E, Togambayeva A, Korolik O. Raman monitoring of ZnSe and ZnS_xSe_{1-x} nanocrystals formed in SiO_2 by ion implantation. *Nuclear, Instruments and Methods in Physics Research Section B: Beam Interactions with Materials and Atoms.* 2018: 1-4.
19. Klimovicha IM, Komarov FF, Zaikova VA, Kuleshova AK, and Pilkob VV. Influence of Parameters of Reactive Magnetron Sputtering on Tribomechanical Properties of Protective Nanostructured Ti–Al–N Coatings. *Journal of Friction and Wear*. 2018;39(2): 92-98.
20. Boucard FA. Comprehensive solution for simulating ultra−shallow junctions: From high dose/low energy implant to diffusion annealing. *Mater. Sci. and Eng. B.* 2005;124-125: 409-414.

THE AUTHORS

Natalia A. Voronova
e-mail: nataliya.voronova@irb.rest
ORCID: -

Alexander A. Kupchishin
e-mail: -
ORCID: -

Anatoly I.Kupchishin
e-mail: ankupchishin@mail.ru
ORCID: 0000-0002-8872-3734

Tatiana A. Shmygaleva
e-mail: shmyg1953@mail.ru
ORCID: 0000-0001-6750-253X

Materials Physics and Mechanics. 2022;49(1): 145-152
Conference materials
http://dx.doi.org/10.18149/MPM.4912022_10

Emergence of topological defects in a bilayer of multiwalled carbon nanotubes irradiated by gamma-rays

H.V. Grushevskaya✉**, A.I. Timoshchenko, I.V. Lipnevich**

Physics Faculty, Belarusian State University, 4 Nezaleznasti Ave., Minsk, Republic of Belarus

✉ grushevskaja@bsu.by

Abstract. We have studied gamma-ray scattering on rolled graphene atomic layers of high-ordered multiwalled-carbon-nanotubes which organized a bilayer. Radiation high-energy topological defects of a type of pair "vortex-antivortex" in electron and hole densities have been revealed. We suppose that the fluxes of the vortex-antivortex pairs are produced by gamma-quanta in the graphene plane.

Keywords: carbon nanotube, gamma-ray scattering, radiation defect

***Acknowledgements**. No external funding was received for this study.*

Citation: Grushevskaya HV, Timoshchenko AI, Lipnevich IV. Emergence of topological defects in a bilayer of multiwalled carbon nanotubes irradiated by gamma-rays. *Materials Physics and Mechanics*. 2022;49(1): 145-152. DOI: 10.18149/MPM.4912022_10.

1. Introduction

Among applications of graphene-like materials in nuclear technologies, the development of radiation-resistant materials and of protective shielding nanostructured coatings are in great demand. Graphene is stable to irradiation because the knocked-on neutral carbon atoms reside on the graphene plane. The radiation resistance of graphene can be caused by an interaction of gamma-quanta with the graphene charge vortical carriers of the pseudo-Majorana type [1,2]. A mechanism of the interaction between gamma-quanta and the pseudo-Majorana charge carriers in the graphene plane leading to a Compton scattering on super-dense fluxes of the pseudo-Dirac charge carriers has been not ascertained yet.

In the paper, we will study gamma-ray scattering on rolled graphene atomic layers of high-ordered multiwalled-carbon-nanotubes (MWCNTs) which organized a bilayer. Our goal is to reveal radiation high-energy topological defects of a type of pseudo-Majorana pairs "vortex-antivortex" in graphene electron and hole densities.

2. Materials

MWCNT bundles were fabricated utilizing Langmuir-Blodgett (LB) nanotechnique. The carboxylated and stearic-acid-functionated MWCNTs under 2.5–5 nm in diameter have been decorated by nanocyclic complexes (Fe(II)DTP) of Ce and/or high-spin octahedral Fe with ligands being conducting oligomer of dithionylpyrrole series in the following way. As a preliminary, an alkyl hydrocarbon chain $C_{16}H_{33}$ was linked chemically to the oligomer. Chemical formula of the oligomer has the following form: 3-hexadecyl-2.5-di(thiophen-2-yl)-1H-pyrrole (H-DTP). A 5-monolayer graphene-like film of the nanocyclic organometallic complexes is fabricated by means of LB-nanotechnique. Then, inverse micelles of stearic acid

Publisher: Peter the Great St. Petersburg Polytechnic University

with MWCNTs inside are obtained by mixing stearic acid and MWCNTs in hexane by the ultrasound treatment, and the 2-monolayer MWCNT films fabricated from these micellar MWCNTs by the LB-nanotechnique are deposited on the nanocyclic-complex LB-cover.

We have used the planar capacitive sensor of interdigital-type on such glass-ceramic support as pyroceramics [3]. N_e pairs, N_e = 20, of aluminium electrodes of the sensors are arranged in an Archimedes-type spiral configuration. Every such pair is an "open type" capacitor. The dielectric coating of the electrodes represents itself nanoporous anodic alumina (AOA) with a pore diameter of 10 nm. The MWCNT LB-bundles decorated by organometallic complexes or the LB-films of nanocyclic organometallic complexes were deposited on the interdigital structure of aluminium electrodes, on the surface of which the AOA layer was previously formed.

3. Methods

Exposure to radiation and radiation spectroscopy. The standard low-intensive source of ionizing radiation (IRS) ^{137}Cs (CsJ) was utilized. A low-intensive beta-particles beam from IRS has been attenuated by a thin-film aluminium shield. The radiation source has the form of a drop with an average diameter of about d = 1.5 mm. An absolute IRS activity A_0 equal to 124.4 kBq on the date 1 April 1990 was quoted to about 1% precision. A sample with a diameter D = 4 mm is exposed through the lead collimator being of the order of 5 mm in diameter and L = 25, 50 mm long. The IRS is placed above the collimator. At the ratio $d/L = 0.03, 0.06$ the IRS can be considered a point source. Then an estimate of the fluence rate φ_0 for the primary gamma radiation within the irradiated sample gives $\varphi_0 = 8.5\ 10^3\ \text{m}^{-2}\text{s}^{-1}$ at $d/L = 0.03$ in supposing that the percentage of the emitted photons per one decay (quantum yield) is equal to 0.851 for the IRS ^{137}Cs. The fluence-increase factor is 24 for $d/L = 0.06$. A number of gamma quanta coincide with a number of 0.512 MeV electrons emitted by ^{137}Cs atoms in the decay process. Since the percentage of 1.174 MeV electrons is of 5.3 %, the fluence of beta-quanta with the energy 1.174 MeV is less than 485 $\text{m}^{-2}\text{s}^{-1}$ at $d/L = 0.03$. MWCNTs were exposed to radiation for 1 or 3 hours at $d/L = 0.03$ and 86 min at $d/L = 0.06$. Accordingly, we have registered approx 9200 events at $d/L = 0.06$. A graphene monolayer deposited on an insulator surface becomes conducting under action of β-radiation [4]. But, since in our case the intensity of the beta rays is very small due to aluminium shield, the doping of the MWCNT layer is negligible.

An analysis of secondary electrons spectra has been performed by a lab-quality radiation spectrometric facility "Nuclear Physics" (BSU, Minsk, Belarus). The scintillation crystal thallium-activated sodium iodide, NaI(Tl) (diameter of 25 mm, height of 40 mm)) was utilized as a detector crystal. A photoelectric-multiplier supply voltage U changes from 100 to 1000 V; the number of channels (a maximal pulse height) is 1024; the integral nonlinearity (transducer characteristic error) is less than 0.1%.

Impedance measurements. Electrophysical properties of the ultra-thin LB-films were studied by means of the impedance spectroscopy methods as a variation in dielectric polarization of a Helmholtz double electrically-charged layer formed at the interface between a surface of the fabricated electrochemical sensor and water. Electrochemical measurements were carried out in deionized water at room temperature.

The non-faradic impedimetric sensor operates on surface-polarization-decreasing effects originated by the conducting ultra-thin LB-layers screening the electrodes. The dielectric losses ε'' due to a dielectric-polarization relaxation process occur in a frequency range where the sensor capacitance C falls down. The ε'' is the imaginary part of the complex dielectric permittivity $\varepsilon = \varepsilon' + i\varepsilon''$, and, correspondingly, presents a resistivity because $\varepsilon'' = \Re e\, \sigma / \omega = \Re e\, (\sigma V)/(\omega V) \sim I/V$.

Here I and V are the electrical current and bias, respectively; σ is the conductivity. Then, as Figure 1 (at the left) shows, the discharging (charging) current I_{ch} emerges producing the bias

$$V \sim \varepsilon'' I_{ch}$$

in an RC oscillator. The V determines the energy $CV^2/2$ stored at (released from) the capacitance change C/T as

$$CV^2/2 \sim I_{ch}VT\ ,$$

where T is the charging-process duration. Substituting the expression for the V into the expression for the energy, one can assume that

$$\varepsilon'' \sim T/C\ .$$

The signal power W/T recorded by the Fourier analyzer is proportional to the dielectric dispersion ε' because W is the stored energy determined by the following equation:

$$W \sim T\vec{D} \times \vec{H}$$

with the electric displacement vector $\vec{D} = \varepsilon' \vec{E}$, where $\vec{E}$ and $\vec{H}$ are the electric and magnetic fields vectors, respectively.

Let us suppose that N dipole-polarization processes proceed inside of the Helmholtz layer emerging near the electrodes. It signifies that an equivalent circuit diagram of both the capacitor-charging (capacitor-discharging) and polarization processes consists of N+1 *RC* circuits. The equivalent circuit of the sensor is presented in Fig. 1 (at the right).

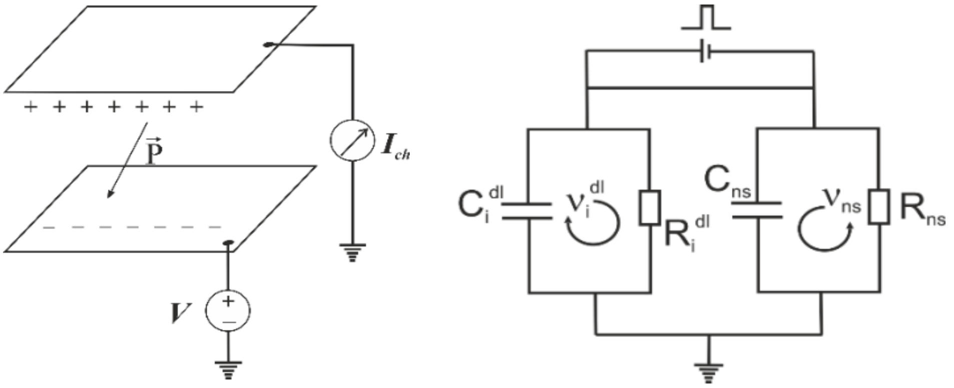

Fig. 1. Scheme of the sensor operation based on a dielectric-polarization relaxation process and an equivalent circuit diagram of the sensor. A square voltage pulse with a bias is applied to the sensor to excite the autooscillations; $\vec{P}$ is the polarization vector

As one can see in Fig. 1 (at the right), forced oscillations with a frequency ν_i can be generated in the i-th parallel circuit for which the double-layer resistance $R_i^{dl} \equiv R_i$ i=1,…, N is much less than the instrument resistance $R_{ns} = R_{N+1}$ in some frequency range $\nu_i \pm \Delta_i$. If $R_i < R_{ns}$ $i \neq 1,\ldots, N$, then the forced oscillations with a frequency $\nu_{ns} \equiv \nu_{N+1}$ are generated in the properly measuring (N+1)-th *RC* circuit. Thus, the dependence of T/C on WT will present N Cole-Cole plots and one Nyquist impedance plot for parallel connection of the capacitor to the instrument resistor R_{ns} (see Fig. 2).

To excite harmonic auto-oscillations of electric current (charge-discharge (charging) processes in the capacitors), the sensor was connected as the capacitance C into the relaxation resistance-capacitance oscillator (self-excited RC-oscillator) [5]. A self-excitation of an amplifier with positive feedback occurs in such RC-oscillator on quasiresonance frequencies. The capacitance change C/T of the sensor, entered measuring RC-oscillating circuit, has been calculated by the formula $C/T = 1/(2\pi R_{ns} f)$, where f is a quasi-resonance frequency.

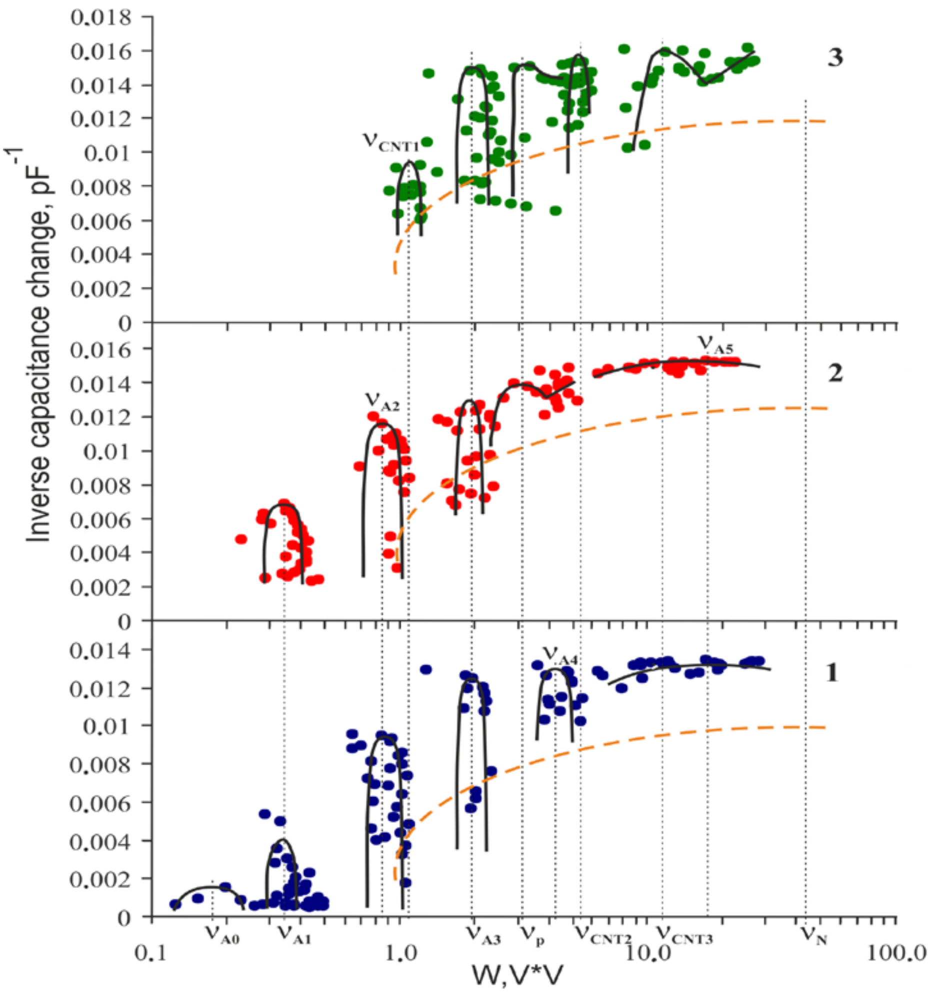

Fig. 2. Dielectric spectra: 1) for nanoporous AOA, 2) and 3) for nanoheterostructure based on Ce-containing nanocyclic compound Fe(II)DTP and on decorated MWCNTs, respectively. Quasiresonance frequencies ν of Cole-Cole plots in the spectra are marked as ν_{Ai}; $i = 0, \ldots, 5$ for AOA; ν_P for the organometallic compound and $\nu_{\mathrm{CNT}i}$; $i = 1,2,3$ for MWCNTs. Nyquist plot of impedance for the measuring circuit is marked by a yellow dash line with ν_N

4. Analysis of radiation spectra

Response functions of the detector with and without the absorber are shown in Fig. 3. The radiation spectrum of CsJ is a typical one recorded from the NaI(Tl) scintillation detectors. The IRS response function R_{Cs} feature peaks of photoelectric absorption (photopeak) and a characteristic X-ray at the lower and highest pulse heights respectively. The characteristic X-ray photons are emitted by free electrons filling non-occupied electron *K*-shells in atoms of the lead collimator. The photopeak appears at the energy of the original ^{137}Cs gamma-ray photon. A Compton scattering gives rise to a single Compton continuum of energies and multiple-Compton-scattering events in the IRS spectra. The multiple Compton scattering occurs due to the sufficiently large size of the detector crystal. One observes also a peak caused by the bremsstrahlung generated in stopping the beta particles by the IRS shield and the backscatter peak caused by photons Compton scattered at large angles in materials immediately surrounding the scintillator crystal (see Fig. 3a).

Radiation background has been subtracted from original distributions; the exposure lasted 86 min at $d/L = 0.06$. The backscatter peak, the photopeak, the characteristic X-ray peak, and the contribution from the bremsstrahlung are labeled by "BS", "Ph", "X", and "Brem", respectively; the absorber escape peaks of the pseudo-Majorana chiral, semichiral, nonchiral fermions, which are created at the interaction between graphene and gamma-ray, are designated as "V_{ch}", "V_{sc}", and "V_{nc}", respectively. The single Compton continuum and the area of multiple Compton scattering are labeled by "Single Compton" and "Multiple Compton", respectively.

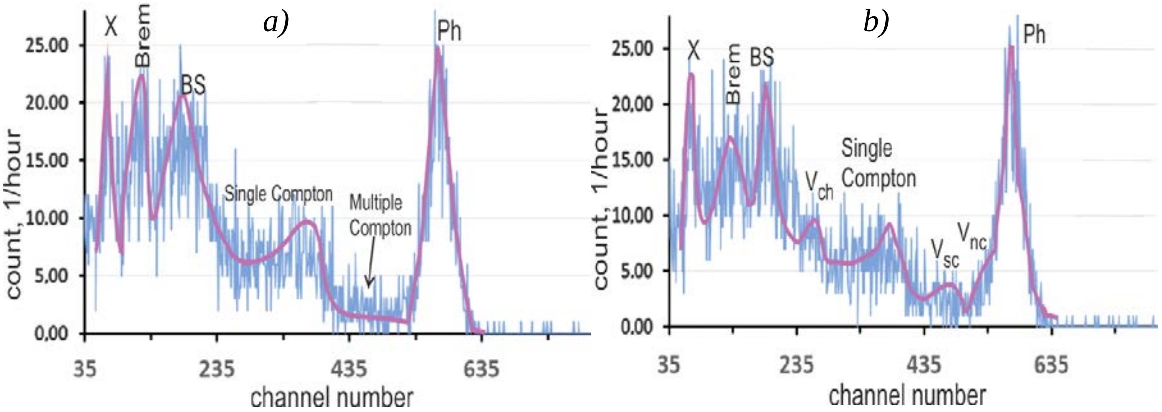

Fig. 3. Pulse height spectra R_{Cs} (*a*) and R_{CsG} (*b*) for photon beam incoming from IRS ^{137}Cs through the collimator without and with an absorber, respectively, and scattering on a detector crystal

Let us analyze MWCNT effects on the incoming ^{137}Cs gamma-quanta beam. After placing the electromagnetic-radiation absorber with the bilayer of ordered MWCNT bundles decorated by the organometallic compound into the collimator, three additional peaks reveal themselves in the ^{137}Cs-radiation spectrum of secondary electrons along with the photopeak, the single Compton continuum, the backscatter peak, the X-ray escape peak, and the bremsstrahlung. The spectra indicate narrowing of the ^{137}Cs-radiation peaks. The shape of the single Compton continuum of ^{137}Cs-radiation spectrum has a maximum being approximately in the 360th channel after placing the MWCNT sample into the collimator. Maxima of the three new peaks are approximately in the 260th, 460th, and 535th channels. It testifies that in creating pairs of charge carriers in graphene, the gamma-quanta escape from the detector. Collisions between the radiation defects of graphene and the photons of bremsstrahlung lead to decreasing the peak "Brem".

Now we will utilize the experimental data to elucidate a pseudo-Majorana nature of the graphene charge carriers. To do it, we offer the following mechanism of graphene radiation resistivity. The resistivity is generated by the creation of neutral vacancies V^0 with knocked-on neutral carbon atoms C^0 fixed on a graphene monolayer by radiation defects of a pseudo-Majorana type. The gamma-rays can escape from the detector crystal owing to the production of radiation-defect pairs. The pairs consist of topologically nontrivial defects of delocalized electron (hole) density in one part of the graphene plane and topologically nontrivial defects of hole (delocalized electron) density in another part.

The pseudo-Majorana vortex-antivortex pairs are created at the Compton scattering of the gamma-rays on the MWCNT graphene planes. The radiation defects decrease the energy deposited in the detector which results in the appearance of the additional peaks V_{ch}, V_{sc}, and V_{nc} in the response function R_{CsG} (see Fig. 3b). At colliding with carbon atoms the free pseudo-Majorana fermions are de-excited and confined by hexagonal symmetry near the Dirac touching valent and conductivity graphene bands. Meanwhile, the graphene pseudo-Majorana band structure has degenerated and the vortex pairs transit from the flat area to the conical one of the graphene band. It signifies that the branches of the vortex begin to move inconsistently. The vortex decay leads to the emergence of an electron-hole avalanche.

5. Impedance analysis

Dielectric spectra of non-exposed structures under investigation are presented in Fig. 2. Unlike graphene-like materials, the dielectric spectra of anodic alumina (AOA) do not have specific dielectric Cole-Cole plots with a diffuse element or Warburg impedance Z_W. Since the Warburg impedance is absent for AOA and, consequently, aluminium-electrodes oxidation does not happen, the fabricated nanoheterostructures are stable. The Cole-Cole plot for metal-containing dithionylpyrrole LB-films testifies both the Warburg impedance element Z_W of a diffuse layer, in which the electrochemical reactions with mass transfer proceed and an electric capacity of the Helmholtz double layer. For the dithionylpyrrole LB-films, this oxidation-reduction potential is stipulated by a change of molecular-group charge state which arises due to self-redox activity of pyrrole residue and electrical charge transport along the chain of conjugated double bonds According to the Cole-Cole plot of the spectrum with Z_W in Fig. 2, MWCNTs, as LB-DTP-films, are redox self-active. Changing the charge state of valleys $K(K')$ (Dirac points) of the graphene Brillouin zone in the momentum space is associated with the mass transfer that Kitaev-like chains with Majorana end states emerge. Meanwhile, the plasma oscillations of produced electron-hole pairs shield the electric field of charged electrodes.

The frequency dependences of electrical capacity for the two materials studied are shown in Fig. 4.

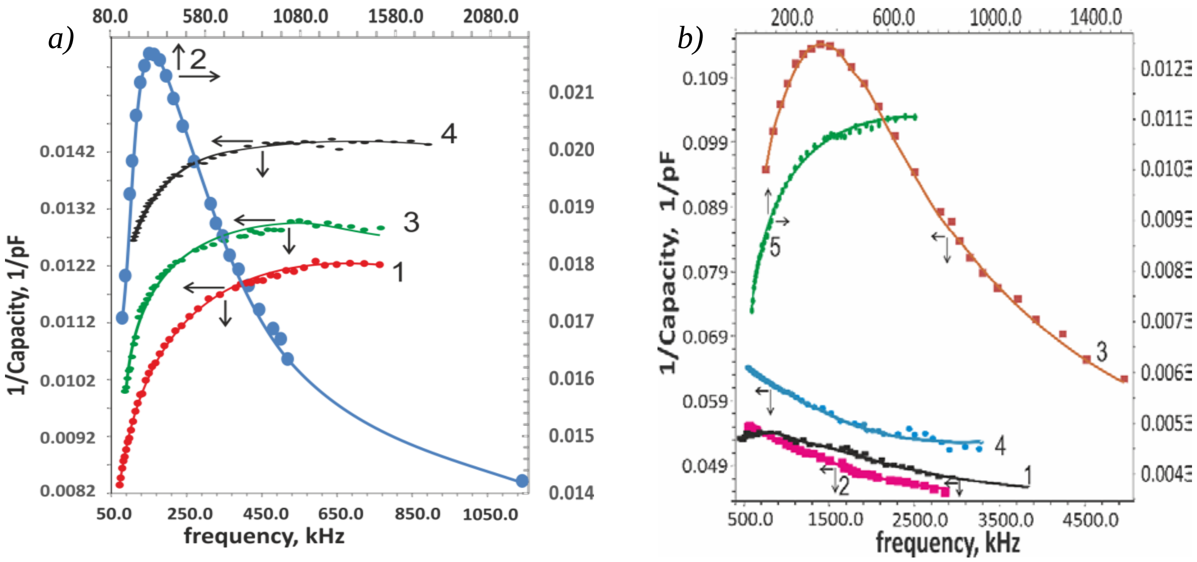

Fig. 4. Frequency dependences of electrical capacity.
(*a*) Fe-containing dithionylpyrrole LB-film:
1) immediately after irradiation, 2) in two weeks after irradiation, 3) in three months after irradiation, 4) before irradiation; the duration of irradiation was 1 hour at $d/L = 0.03$.
(*b*) MWCNTs decorated by nanocyclic complexes of Fe and Ce with dithionylpyrrole ligands.
1) immediately after irradiation, 2) in 24 hours after irradiation, 3) in three weeks after irradiation, 4) in four months after irradiation, 5) before irradiation; the duration of irradiation was 3 hours at $d/L = 0.03$

According to Bode capacity plots 1, 2, and 4 in Figure 4a for irradiated and non-irradiated organometallic-compound LB-films, the dipole relaxation of radiation-vacancy clusters is observed simultaneously with increasing the shielding degree two weeks after the irradiation by the weak gamma-ray fluence from IRS ^{137}Ce at $d/L = 0.03$. The sharp increase of shielding degree indicates that the number of free charge carriers enlarges extremely. Since the electron-hole pairs are charge carriers in graphene and graphene-like materials, the increase in the free charge carrier's density indicates the localization of holes or electrons from electron-hole pairs after irradiation. The incoming particles can collide with electrons only. Since the carbon atoms are knocked out, the holes (vacancies), localized in the Dirac points, remain. The charge density of vacancy ensemble has the form of atom-like density of localized holes surrounded by delocalized electron density. The dipole relaxation of these individual radiation-vacancy ensembles disappears for a long enough time about three months according to the comparison of dielectric spectra 2 and 3 in Fig. 4a. Emerging only two weeks later after the irradiation, the individual atom-like vacancy arrays indicate a decay of very large cluster of radiation vacancies into the small atom-like arrays (artificial atoms) in graphene-like monolayer plane during self-repairing processes.

We submit the following mechanism of emerging clusters of radiation vacancies. Since the gamma rays created by IRS possess high energy, the atom-like ensembles of radiation vacancies are produced in the excited state with non-occupied both valence and internal orbitals. Due to overlapping the external orbitals of such artificial atoms in an excited state, there arise large clusters of radiation vacancies. Hydrate complexes of atom-like structures formed by vacancies are appeared due to the transition of the latter into the ground state after two weeks, as it follows when the Bode plots 1 and 2, Fig. 4a, are compared. This is evidence that the external orbitals in the ground state are not overlapped. The decay of large radiation clusters into the separate artificial atoms (electrically confined quantum dots) is testified by the corresponding resonance at a frequency of 280 kHz for the metal-containing LB-film. The lifetime of an individual quantum dot is very large so the dots exist for one or two months.

Mobile interstitial carbon atoms, being near a monolayer plane, can form chemical cross-links with hydrocarbon alkyl chains. From the frequency dependencies 3 and 4, Fig. 4a, it follows that after the decay of the artificial atoms the sensor electric capacity of metal-containing dithionylpyrrole LB-films only slightly increases. The weak increase is stipulated by destroying the double-bound chains by the cross-links with near-lying alkyl hydrocarbon chains leads to an attenuation of the shielding effect.

The mechanism of MWCNT radiation resistivity is similar to that of metal-containing dithionylpyrrole LB-film. The dielectric spectra of irradiated and non-irradiated LB-films of MWCNTs decorated by nanocyclic complexes of Ce and octahedral high-spin Fe are presented in Fig. 4b. According to Bode plot 3, the dipole relaxation of hydrated atom-like clusters of radiation vacancies occurs at higher frequencies (about 1320 kHz) than in the dithionylpyrrole films. This is due to the restriction of the artificial atom size by the CNT diameter value. According to the Bode plots 1-4, Fig. 4b, the decay of excited radiation-induced artificial-atom aggregates occurs three weeks after irradiation, while the restoration of electrophysical properties of MWCNTs occurs in three months after the irradiation when quasi-stationary artificial atoms disappear. The shift of the maximum in frequency dependence 1, Fig. 4b, towards low frequencies is registered immediately after irradiation too. This shift indicates the formation of atom-like clusters of vacancies under the action of gamma-rays in the metal-containing dithionylpyrrole LB-monolayers decorating MWCNTs. Decreasing the electric capacity of non-irradiated MWCNTs from 85.2 to 18.5 pF is registered immediately after three-hour irradiation. Accordingly, the intensity increase in the Bode plot 1 in respect of plot 5 in Fig. 4b testifies to the high shielding efficiency of MWCNTs-network and, accordingly, its high electric conductivity. It signifies that in the addition to the radiation-resistivity mechanism for metal-containing dithionylpyrrole LB-film there are cross-connections between graphene monolayers of MWCNT and interstitial knocked-out carbon atoms through chemical bonds into a high-shielding network.

The shielding effect of the LB-films is revealed also as the intensity change of Compton scattering (see Fig. 3). Compare the single Dirac continuum in the detector spectrum in the presence of the absorber and without it. We observe a growth of the number of photons at the scattering angle θ = π. In accord with the Klein-Nishina formula [6], the number of photons scattered at θ = π grow with decreasing their energy [7]. Thus, as the quasi-relativistic graphene model predicts, the experimental study fulfilled discovered the existence of the Compton effect at irradiation of the graphene-like material.

6. Conclusions

Scattering the 661.7-keV gamma-rays in MWCNTs create pairs of topologically nontrivial radiation defects and antidefects. We assume that these high-energy graphene pairs of scattering centers are pseudo-Majorana vortical and antivortical fermions. Annihilating and scattering on carbon electron density, the pseudo-Majorana quasi-particles avalanche-likely produce electron-hole configurations of graphene charge density.

References

1. Grushevskaya H, Timoshchenko A, Avdanina E, Lipnevich I. Clustering artificial atoms induced by high-frequency electromagnetic radiation in graphene monolayers of multiwalled carbon nanotubes. *Int. J. Nonlinear Phenomena in Complex Systems.* 2020;23(3): 342-356.
2. Grushevskaya H, Krylov G. Vortex dynamics of charge carriers in the quasi-relativistic graphene model: high-energy kp approximation. *Symmetry*. 2020;12(2): 261.
3. Konstantinova TE, Lyafer EI. Hydrostatic compaction pressure influence on sintered spodumene pyroceramics properties. In: Trzeciakowski WT (ed.) *High Pressure Science and Technology*. Singapore: World Scientific Publishing; 1996. p.118-120.
4. Starodubtsev VA, Fursa TV, Zausaeva NN. Charge electrification of irradiated dielectrics and its effect on incident flux. *J. Electrostatics.* 1988;20(3): 341.
5. Abramov II, Hrushevski VV, Krylov GG, Krylova HV, Lipnevich IV, Orekhovskaja TI. A method of impedance calculation for impedimetric sensor with interdigital structure. *Petersburg Electronics J*. 2012;4(73): 59-67.
6. Krajewska K, Vélez FC, Kamiński JZ. Generalized Klein-Nishina formula. *Phys. Rev. A.* 2015;91(6): 062106.
7. Shafroth SM. (ed.) *Scintillation Spectroscopy of Gamma Radiation*. London: Gordon & Breach, Inc.; 1964.

THE AUTHORS

H.V. Grushevskaya
e-mail: grushvskaja@bsu.by
ORCID: 0000-0002-9527-9328

A.I. Timoshchenko
e-mail: TimoshchenkoAI@bsu.by
ORCID: -

I.V. Lipnevich
e-mail: lipnevich@bsu.by
ORCID: -

Materials Physics and Mechanics. 2022;49(1): 153-159
Conference materials
http://dx.doi.org/10.18149/MPM.4912022_11

Influence of temperature and load on mechanical properties of unirradiated and irradiated plexiglass

A.I. Kupchishin[1,2]✉, B.G. Taipova[1], M.N. Niyazov[1], D.C. Utepova[1], V.M. Lisitsyn[3], B.A. Tronin[1]

[1]Abai Kazakh National Pedagogical University, Dostyk, 13, Almaty, Kazakhstan

[2]Al-Farabi Kazakh National University, 71 Al-Farabi Ave., Almaty, Kazakhstan

[3]Tomsk National Research Polytechnical University, Tomsk, Russia

✉ ankupchishin@mail.ru

Abstract. Investigations of the mechanical, properties of unirradiated and irradiated plexiglass of various types have been carried out when tested for the flat straight bend. Exposure to temperature and radiation significantly affects the properties of the material. As a result of the research, the dependences of deformation on stress, length, and width of the specimens were obtained. The experimental curves are satisfactorily described by a linear model.

Keywords: bend, deformation, mechanical properties, plexiglass, radiation, stress

Acknowledgments. *This research has been funded by the Science Committee of the Ministry of Education and Science of the Republic of Kazakhstan (Grant No. AP08855701).*

Citation: Kupchishin AI, Taipova BG, Niyazov MN, Utepova DC, Lisitsyn VM, Tronin BA. Influence of temperature and load on mechanical properties of unirradiated and irradiated plexiglass. *Materials Physics and Mechanics*. 2022;49(1): 153-159. DOI: 10.18149/MPM.4912022_11.

1. Introduction

Thermoplastic materials are now widely used by both the academic research community and industrial sectors due to their good physical, mechanical, thermal, and optical characteristics [1-3]. Polymer materials have several advantages over traditional products. For example, they have excellent dielectric properties, ease of use, lightness, and simplicity of manufacturing methods. Among other things, polymers have improved thermal and mechanical properties. The automotive industry has recently been focusing on polymer-based composites instead of conventional steel products. They have high rigidity and a large pressure rate than metals, the strength of which additionally depends also on the geometry and shape [4,5]. Polyethylene, polyimide, polyethylene terephthalate, polytetrafluoroethylene, polymethylmetacrylate (plexiglass), epoxy resin, etc. are used in laboratory research as well-known homogeneous model materials for experiments. In particular, they are employed in systems whose mechanical properties are critical to aircraft designers and engineers [6]. These materials also find application as candidate ones, where loading with a high deformation rate is likely in many structures [7]. The mechanical properties of composites can change at high strain rates and after irradiation with high–energy particles [8-10]. Such materials will also vary their

Publisher: Peter the Great St. Petersburg Polytechnic University

properties with an increase in load. This makes it obligatory to take into account changes in the design and operation of structures operating in harsh conditions [11,12]. There are very few studies on the effects of temperature, irradiation, and mechanical load on polymer properties when tested in tension, compression, shear, bending and etc. This work is devoted to the comprehensive study of various types of unirradiated and irradiated plexiglass when tested for a flat straight bend.

2. Research methods

Two types of smooth and corrugated plexiglass (pyramids and stripes) were taken as the materials under study. Specimens of smooth plexiglass had thickness (h) of 1 mm and a width (b) of 5 and 10 mm and different working lengths (L) – 20, 30, 40, 50, 60, and 70 mm. For corrugated specimens, plexiglass thickness was 3 mm in the corrugations of the convex portion, the width – 5 mm, and length – 40 mm. The experiment was carried out at temperature of 20, 25, and 50°C. The relative humidity of the room was 50 %. Electron irradiation of corrugated plexiglass samples was carried out on an ELA-6 linear accelerator with an energy of 2 MeV in air. The radiation dose was 100 kGy. The thickness of the specimens was measured along the entire perimeter with a micrometer.

The experiments were carried out on a testing machine providing a uniform velocity v = 0.4 mm/s of the relative movement of the loading tip and supports, allowing measurements of the load with an error of ± 1%, and the deflection with an error of ± 2%. The impact took place at a constant rate. The specimens were loaded with one concentrated force applied in the middle of the specimen between the supports [13,14].

BI (bursting installation)-50 tensile testing machine was used for bending tests under various load conditions. It is the setup consisting of a loading device, a control panel, and rods connecting the loading device with a control panel. On the bottom of the device were a force sensor, a temperature chamber, and various supports. The test was carried out at an AC frequency of 9 Hz. Changing the frequency helps to control the speed of the loading crosshead of the installation.

3. Results and discussion

The dependences of deformation on stress, obtained for testing samples of smooth plexiglass of various sizes under flat straight bend, are shown in Figures 1 and 2. The figured points present the experimental results, and the lines display the calculation data. The physical and mechanical properties are displayed as functions ε (σ), because the dependence of σ on ε is incorrect, since σ is an argument, and ε is a function.

Figures 1 and 2 show that the dependence of deformation on stress is adequately described by a linear model for all sizes. Moreover, the maximum deformation of the specimens, depending on the sample length and the stress, varies in the range of 35 - 60%.

Figure 3 demonstrates the dependence of deformation on stress for unirradiated and irradiated specimens of corrugated plexiglass, in which plane bending occurs with and without taking into account the horizontal component (Fig. 3 a and b).

According to the results, when the stress increases, the relative elongation of the corrugated plexiglass specimens (both unirradiated and irradiated) grows by virtue of linear law. Furthermore, the striped-corrugated material has greater strength and a relative elongation than the pyramid-corrugated material. It can be seen that smooth plexiglass by mechanical properties is much better than corrugated (Figs. 1-4). Moreover, its strength properties are more than 5 times higher than those of corrugated plexiglass. After exposure to a dose of 100 kGy, the corrugated plexiglass specimens lose their plasticity by 20 and 40 % respectively compared to the unirradiated materials. The changes in the strength of materials after irradiation are insignificant. Visual analysis displays that the light transmittance (transparency) declines, while the specimens are painted brown.

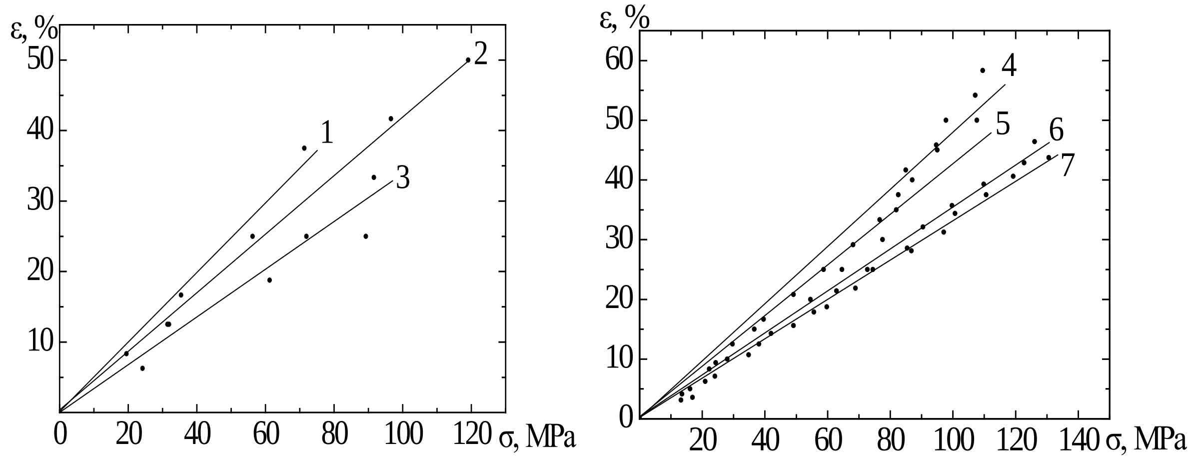

1 – 20; 2 – 30; 3 – 40; 4 – 50; 5 – 60; 6 – 70; 7 – 80 mm
figured points – experiment; lines – calculation

Fig. 1. Dependence of strain on stress for unirradiated specimens of smooth plexiglass 5 mm wide and different lengths at 20°C (room) temperature

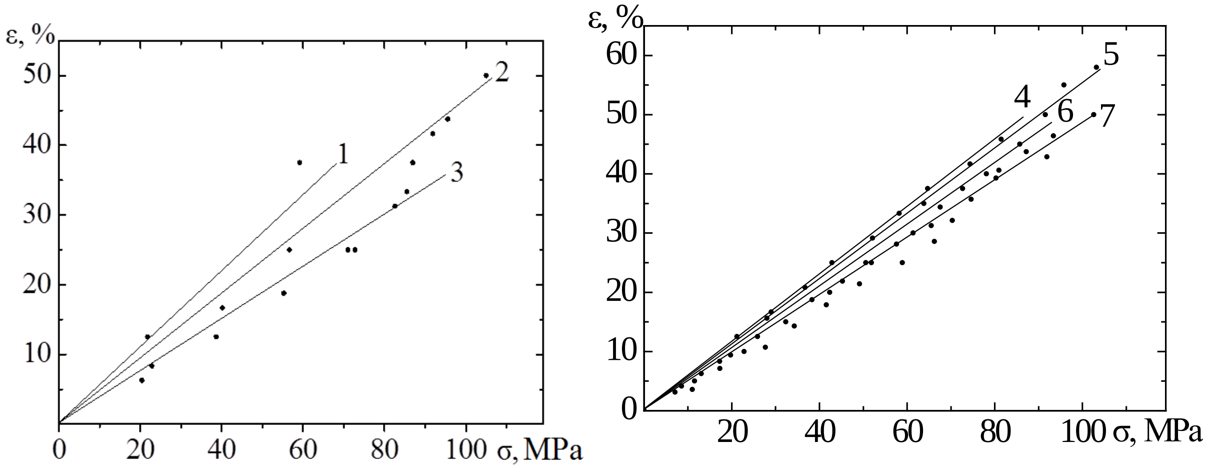

1 – 20; 2 – 30; 3 – 40; 4 – 50; 5 – 60; 6 – 70; 7 – 80 mm
figured points – experiment; lines – calculation

Fig. 2. Dependence of strain on stress for unirradiated specimens of smooth plexiglass 10 mm wide and different lengths at 20°C (room) temperature

The experimental data are described with good precision by a linear model, for both smooth and corrugated plexiglass of two types [15]

$\varepsilon = k\sigma$,

where *k* is the slope tangent. For unirradiated striped-corrugated glass *k*=0.14 and for pyramid-corrugated glass 0.2%/MPa. For irradiated materials *k*=0.1 and 0,13%/MPa, respectively. Figure shows that *k* ranges in the interval from 0.2 to 1.2%/MPa. In addition, it is the coefficient that is inverse to the modulus of elasticity, that is *k*=1/E.

Figure 4 illustrates the relationships between strain and stress for the plexiglass (PMMA) specimens 5 and 10 mm wide at a temperature of 25ºC. It can be seen that the curves are consistent with linear model calculations. As the width of the specimens rises, the deformation reduces. Strength characteristics also undergo considerable changes.

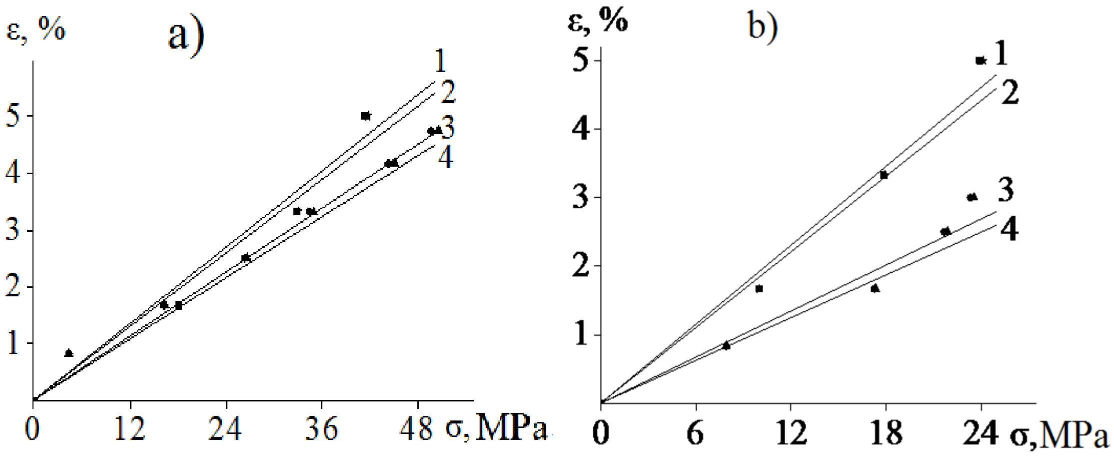

figured points – experiment; lines – calculation

Fig. 3. Dependence of strain on stress for unirradiated (1, 2) and electron irradiated (3, 4) specimens of striped – corrugated (a) and pyramid – corrugated (b) plexiglass, with plane bending, the horizontal component is taken into account (squares and asterisks) and without taking into account (points and triangles)

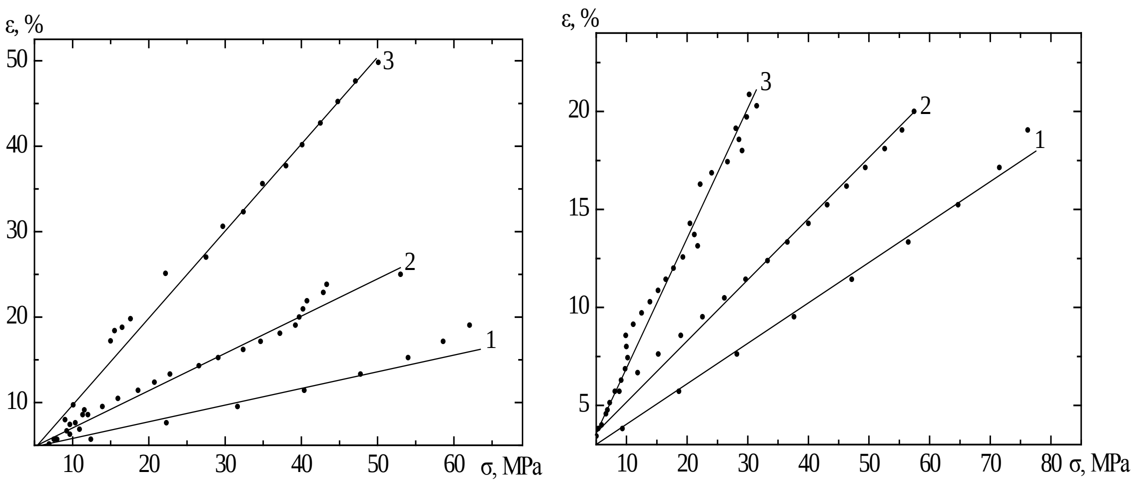

1 – 20; 2 – 40; 3 – 70 mm

Fig. 4. Dependence of deformation on stress for the plexiglass smooth specimens of 5 mm wide (left) and 10 mm (right) for bending at a temperature of 25°C

Figure 5 presents the dependence of deformation on stress for the plexiglass smooth specimens 5 and 10 mm wide in a temperature heating chamber. The device maintained a constant temperature of 50°C. With a further increase in temperature, the specimens begin to bend without load, which makes analyzing the material behavior difficult. It can be seen from the figures that a long sample has a greater deflection (regardless of the temperature) than a short one and breaks at a lower value of mechanical stress. With increasing the temperature, in the range of 20-50 degrees, the deformation increases by 20% for all the sizes of the material, and the strength characteristics deteriorate by 10-30%.

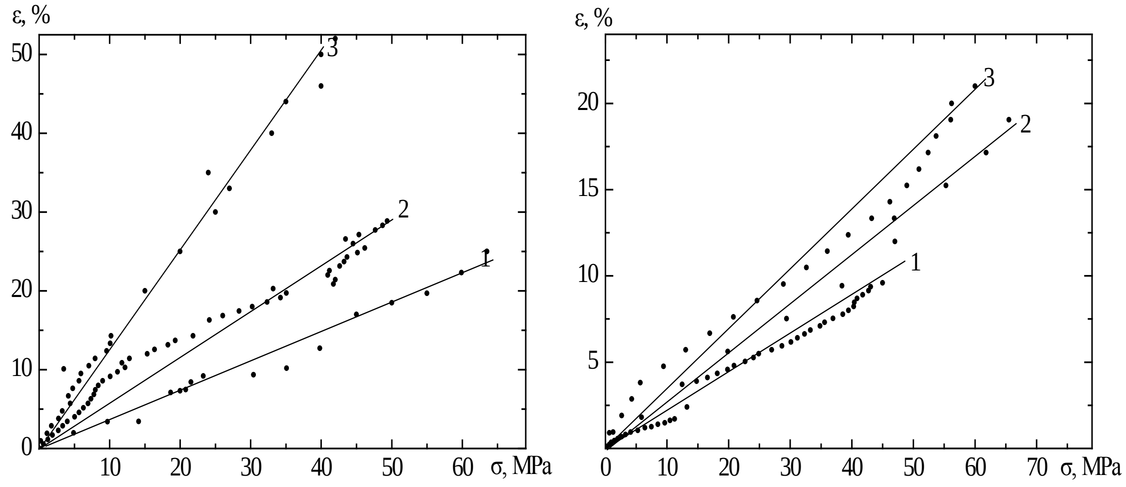

1 – 20; 2 – 40; 3 – 70 mm

Fig. 5. Dependence of deformation on stress for the plexiglass smooth specimens of 5 mm wide (left) and 10 mm (right) for bending at a temperature of 50°C

4. Conclusions

1. The experiments on the dependence of deformation on stress during flat straight bending testing of unirradiated and irradiated plexiglass specimens of various types in a temperature chamber have been carried out. It was found that the maximum deformation of specimens of different sizes varies in the range of 50-60%, depending on the stress, length, and width of the material.

2. It has been established that electron irradiation leads to a noticeable change in the deformation-strength characteristics of the material, manifested in a decrease in plasticity. The relative elongation of striped plexiglass after irradiation changes by 20%, and that of pyramidal – by 40%. At the same time, there is practically no change in strength.

3. With an increase in the temperature of the test specimen in the range of 20-50 degrees, an increase in deformation characteristics by 20% is observed for all sizes of the material, and the strength characteristics deteriorate by 10-30%.

4. The obtained curves of the dependence of ε on σ are satisfactorily described within the framework of a linear model.

References

1. Mousavi SS, Aliha MRM, Imani DM. On the use of edge cracked short bend beam specimen for PMMA fracture toughness testing under mixed-mode I/II. *Polymer Testing.* 2020;81: 106199.

2. Guduru RKR,. Shaik SH, Tuniki HP, Domeika A. Development of mono leaf spring with composite material and investigating its mechanical properties. *Materials Today: Proceedings.* 2020;45: 556-561.

3. Blumenthal WR, Cady CM, Lopez MF, Gray GT and Idar DJ. Influence of Temperature and Strain Rate on the Compressive Behavior of PMMA and Polycarbonate Polymers. *AIP Conference Proceedings.* 2002;620(1): 665-668.

4. Reis PNB, Gorbatikh L, Ivens J, Lomov SV. Strain-rate sensitivity and stress relaxation of hybrid self-reinforced polypropylene composites under bending loads. *Composite Structures.* 2019;209: 802-810.

5. Zhou W, Huang J, Huang W, Liu D. Dynamic fracture testing of polymethyl-methacrylate (PMMA) single-edge notched beam. *Polymer Testing.* 2020;91: 106833.

6. Kazemi M. Experimental analysis of sandwich composite beams under three-point bending with an emphasis on the layering effects of foam core. *Structures.* 2021;29: 383-391.

7. Jiang Y, Wu Q, Li Y, Peng Y, Gong J. Mechanical properties of low-temperature gaseous carburizated layer in 316L stainless steel based on nano-indentation and four-point bending tests. *Surface and Coatings Technology*. 2020;387: 125501.
8. Angelides SC, Talbot JP, Overend M. High strain-rate effects from blast loads on laminated glass: An experimental investigation of the post-fracture bending moment capacity based on time–temperature mapping of interlayer yield stress. *Construction and Building Materials*. 2021;273: 121658.
9. Qureshi Y, Tarfaoui M, Lafdi KK, Lafdi K. Development of microscale flexible nylon/Ag strain sensor wire for real-time monitoring and damage detection in composite structures subjected to three-point bend test. *Composites Science and Technology*. 2019;181: 107693.
10. Zhou J, Jiang W, Ao Y, Zeng W, Liu J, Mei J, Huang W. The three-point bending responses of carbon fiber composite sandwich beams with Y-frame cores at high and low temperatures. *Thin – Walled Structures*. 2021;162: 107595
11. Liu H, Liu J, Ding Y, Zhou J, Kong X, Harper LT, Blackman BRK, Falzon BG, Dear JP. Modelling damage in fibre-reinforced thermoplastic composite laminates subjected to three-point-bend loading. *Composite Structures*. 2020;236: 111889.
12. Cerbu C, Botis M. Numerical modeling of the Flax/Glass/Epoxy hybrid composite materials in bending. *Procedia Engineering*. 2017;181: 308-315.
13. Kupchishin AI, Niyazov MN, Voronova NA, Kirdiashkin VI, Abdukhairova AT. The effect of temperature, static load and electron beam irradiation on the deformation of linear polymers. *IOP Conf. Series: Materials Science and Engineering*. 2017;168: 1-4.
14. Kupchishin AI, Niyazov MN, Taipova BG, Khodarina NN, Shahanov KSh. The mechanical properties of the PCB and glass fiber under test on a flat straight bend. In: *Proceedings of the V International Scientific Conference "Contemporary Problems of Condensed Matter Physics, Nanotechnologies and Nanomaterials"*. 2018. p.209.
15. Kupchishin AI, Taipova BG, Voronova NA. Study of the influence of filler on the mechanical properties of composites based on polyimide. *Materials Science and Engineering*. 2016;168: 012015.
16. Kupchishin AI, Taipova BG, Kupchishin AA, Kozhamkulov BA. Study on the physical and mechanical properties of composites based on polyimide and polycarbonate. *Mechanics of Composite Materials*. 2015;51(1): 115-118.

THE AUTHORS

Anatoly I. Kupchishin
e-mail: ankupchishin@mail.ru
ORCID: 0000-0002-8872-3734

Buvkhan G. Taipova
e-mail: buv_7@mail.ru
ORCID: 0000-0003-1563-7189

Marat N. Niyazov
e-mail: marat--90@mail.ru
ORCID: -

Daniya C. Utepova
e-mail: utepova_daniya@mail.ru
ORCID: -

Victor M. Lisitsyn
e-mail: lisitsyn@tpu.ru
ORCID: 0000-0002-2075-4796

Boris A. Tronin
e-mail: troninboris@mail.ru
ORCID: -

Materials Physics and Mechanics. 2022;49(1): 160-172
Conference materials
http://dx.doi.org/10.18149/MPM.4912022_12

Rate-independent selection of slip patterns on grain and subgrain scales: state of the art

A.A. Zisman, N.Yu. Ermakova✉

Peter the Great St. Petersburg Polytechnic University, 29 Polytekhnicheskaya, St. Petersburg 195251, Russia

✉ ermakova@phmf.spbstu.ru

Abstract. To simulate the fragmentation of grains in cold deformed polycrystals, the underlying heterogeneity of crystal slip patterns should be quantified. Although it is understood that such patterns split owing to both the grain interaction and tendency to weaken the local strain hardening, properly justified numerical models for the considered effect are still wanted. This paper briefly surveys relevant extensions of rate-independent Taylor's theory and currently popular rate-sensitive formulations coupled with finite element modeling. Then, to exclude the limitations of such efforts, a novel rate-independent model is formulated that accommodates *macroscopic* deformation by the interfacial skeleton while suggesting specific slip patterns to keep the *local* strain compatibility across any grain boundary facet. Based on this approach, the fragmentation onset at grain junctions is predicted, and refinements of the model which should extend it to grain interiors are discussed.

Keywords: crystal fragmentation, dislocation boundary, plasticity, slip pattern, strain rate

Acknowledgements. *No external funding was received for this study.*

Citation: Zisman AA, Ermakova NYu. Rate-independent selection of slip patterns on grain and subgrain scales: state of the art. *Materials Physics and Mechanics*. 2022;49(1): 160-172. DOI: 10.18149/MPM.4912022_12.

1. Introduction

As shown by Rybin [1], the fragmentation of constitutive crystals into structural units separated by high-angle boundaries is a general regularity in polycrystals cold deformed to high strain degrees. Eventually detected on various metals [2-5], this effect attracts great attention because resulting ultrafine-grained structures provide extraordinary mechanical properties [4]. It is worth noting that piecewise uniform models extending the original Taylor's theory [6] still provide satisfactory predictions of the *overall* polycrystal texture even though they neglect the influence of the *local* orientation splitting [7]. Evidently, similar models average out related errors present on the grain scale; however, this simplification becomes irrelevant when the local grain fragmentation as such is considered.

It has been understood that the slip pattern and hence lattice orientation in deformed grains can split for two main reasons. First, this is the grain interaction effect indicated by TEM data [1] on triple grain junctions where deformation-induced dislocation boundaries nucleate and often branch toward grain boundaries. Similar behavior is also observed in the deformation of macroscopic tri-crystals [8]. A simplified 2D model [9] ascribes such events to the interaction of a primary slip system with various boundary facets that activates specific secondary systems. Another reason for the considered splitting is that simultaneous activity of many slip systems in the same local domain would significantly increase the strain hardening and, accordingly, the plastic work. Meanwhile, unlike the uniform flow by five slip systems of any crystal [6], it is possible to accommodate the given strain rate by a set of simpler slip patterns operating in its fragments [2,10]. Such a concept is supported by the prevailing dependence of slip patterns in constitutive grains on their own orientations [11], as well as by heterogeneity of orientation and plastic shearing in deformed single crystals [12,13] free of the grain interaction. A tendency to weaken the local hardening is also manifested by the single slip in shear microbands [14] and plastic accommodation of martensite laths splitting into partial simple shears of their constituents [15,16].

The present paper briefly surveys the potentiality of various models for crystal plasticity from the standpoint of fragmentation. A crucial issue, in this case, is that slip patterns of adjacent crystal domains determining their emerging disorientation should be selected *uniquely*. Unambiguity of slip patterns on the grain scale is conventionally ensured by the rate-sensitive plasticity [17] admitting in any crystal activity of all its slip systems. However, let alone computational difficulties due to the weak rate sensitivity in cold deformation, such an approach does not comply with actual patterns of neighboring fragments, each involving only a few slip systems. To select the latter, a rate-independent model is formulated in terms of the deformed interfacial skeleton that keeps local strain compatibility across grain boundaries. It properly predicts the crystal fragmentation onset at triple grain junctions, and further refinements are discussed which should extend the model to the orientation splitting into grain interiors.

2. Taylor-Bishop-Hill theory

Current rate-independent models of plastically deformed polycrystals are based on the classical formulation by Taylor [6] while refining the latter in a way to allow for the grain interaction and to select crystal slip patterns. Although such models ignore the fragmentation effect, it is advisable to recollect some of their terms and relationships applicable to local in-grain domains. According to [6], the arbitrary plastic strain rate $\boldsymbol{D}_g$ of any grain is accommodated by five slip systems:

$$\boldsymbol{D}_g = \sum_{k=1}^{5} \dot{\gamma}_k (\boldsymbol{b}_k \otimes \boldsymbol{n}_k + \boldsymbol{n}_k \otimes \boldsymbol{b}_k)/2, \tag{1}$$

where $\dot{\gamma}_k$ are the related shear rates, $\boldsymbol{b}_k$ and $\boldsymbol{n}_k$ are the shear directions and unit normal vectors to slip planes, respectively; ⊗ means the tensor product. The corresponding tensor of plastic rotation rate with respect to the invariant crystal lattice is

$$\boldsymbol{W}_g = \sum_{k=1}^{5} \dot{\gamma}_k (\boldsymbol{n}_k \otimes \boldsymbol{b}_k - \boldsymbol{b}_k \otimes \boldsymbol{n}_k)/2. \tag{2}$$

Thus, if the total material spin $\boldsymbol{W}_g^{(T)}$ of the grain is given, the lattice rotation rate is expressed by

$$\boldsymbol{W}_g^{(L)} = \boldsymbol{W}_g^{(T)} - \boldsymbol{W}_g. \tag{3}$$

To treat the grain interaction in the simplest way, it has been presumed that

$$\text{(a) } \boldsymbol{D}_g = \boldsymbol{D}, \text{ (b) } \boldsymbol{W}_g^{(T)} = 0, \tag{4}$$

where $\boldsymbol{D}$ is the deviator part of macroscopic strain rate; however, these presumptions can be refined while saving general Eqs. (1) to (3). A challenging problem in the considered approach is that five active slip systems are selected from a greater number of candidates as, for instance, twelve in FCC crystals. Accordingly, an enormous multiplicity of C_{12}^{5} selection variants should be checked. Moreover, although only combinations with the least amount of shear rates

$$\sum_{k=1}^{5} |\dot{\gamma}_k| = min \tag{5}$$

is admitted among them, the result remains *non-unique* and necessitates a random choice.

Corresponding to a certain shear resistance in all slip systems, Eq. (5) suggests the least plastic work on deformed grains and, as shown by Bishop and Hill [18], enables the model refinement in terms of the crystal yield surface. Facets of the latter correspond to the critical magnitude (CRSS) s of the resolved shear stresses (RSS)

$$\tau_i = \sigma_g : (\boldsymbol{n}_i \otimes \boldsymbol{b}_i) \tag{6}$$

in potential slip systems, where σ_g is the crystal stress tensor, and colon means the double scalar product. Thus, in the case of FCC lattice i=1, 2, …, 12 should be considered with Eq. (6). In this case, arbitrary $\boldsymbol{D}_g$ involves five slip systems from six or eight ones forming an apex of the crystal yield surface depending on the crystal orientation. As compared to Taylor's model, this diminishes the above-mentioned multiplicity to $\mathrm{C}_6^5 = 6$ or $\mathrm{C}_8^5 = 56$, respectively, although the previous non-uniqueness of the admitted selections is retained.

A principal origin of the considered ambiguity in the Tailor-Bishop-Hill (TBH) theory is Eq. (4a) which roughly extends an essentially *local* strain compatibility condition [19] to the interaction of whole finite crystals. The inaccuracy of this simplification is also evident in terms of the stress balance requirement. Indeed, contrary to the latter, any grain stress derived at a given $\boldsymbol{D}_g$ from the crystal orientation does not depend on stresses in neighboring grains. A natural way to improve the model in accordance with experimental data on cold deformed polycrystals is to allow for in-grain heterogeneity of plastic shearing. However, as considered in the next section, some approaches still provide a unique slip pattern while keeping uniformity of the crystal strain rate.

3. Unique selection of uniform slip pattern

To save the uniqueness of crystal slip patterns, different ways are used. The most popular one admits simultaneous activity of *all* potential slip systems depending on related RSS and thus avoids the selection multiplicity. Another approach refines constraint (5) excluding inactive slip systems in rate-independent models. We will consider below specific advantages and drawbacks of such expedients in application to crystal orientation splitting. A common complication of them is the cumbersome treatment of hardening in all (k=*1, 2, …, N*) slip systems. The general expression for time derivatives of related CRSS [20] is

$$\dot{s_k} = \sum_{n=1}^{N} h_{kn} |\dot{\gamma_n}|, \tag{7}$$

where $n = k$ and $n \neq k$ are due to the self-hardening and latent hardening, respectively. Let alone a great number $N^2$of h_{kn}, none of these coefficients is determined independently; instead, the whole set of them is fitted to the *macroscopic* stress-strain diagram that is hardly relevant to specific slip patterns of local in-grain fragments.

Rate-sensitive models. Following [17], the shear rate in whatever slip system number k is expressed by

$$\dot{\gamma_k} = \dot{\gamma_o} |\tau_k / s_k|^{1/m} sign(\tau_k), \tag{8}$$

where τ_k is its RSS, while m and $\dot{\gamma}_o$ are the rate sensitivity exponent and the reference strain rate, respectively. Suggesting activity of all slip systems in a stressed crystal, this expression provides its unique slip pattern. Moreover, since non-diagonal components (latent hardening) in matrix h_{kn} are generally higher [21], they weaken essentially formal contributions of systems with low RSS to the crystal strain and reorientation. Combined with the finite element method (FEM), this approach enables the modeling of heterogeneous plastic shearing in individual grains [13,22-24] while properly allowing for their interaction. At the same time, there are significant limitations as follows.

Eq. (8) is hard to apply in the case of cold deformation when m approaches zero [21]; this complicates the modeling on both the grain and in-grain scales. Computational expenses become enormous when the latter is treated in 3D by the crystal plasticity FEM. Indeed, an actual polyhedral grain has about 20 facets separating it from its next neighbors which should be allowed for to simulate the grain interaction. Furthermore, since typical fragments have submicron to micron dimensions [1-5], respective models should subdivide each grain or a more representative cluster into at least 10^5 finite elements. Hence, to utilize the potentiality of the considered approach, it would be highly desirable to decompose the modeling into *separate* constitutive crystals with properly predetermined boundary conditions.

Rate-independent selection. According to Anand [21], the unique slip pattern of a single crystal subject to a given strain rate can be derived from the consistency condition

$$\dot{s_k} = |\dot{\tau_k}| \qquad (9)$$

between time derivatives of CRSS, which change during the strain hardening, and those of respective RSS magnitudes, which follow both the variation of deforming stress and gradual reorientation of the crystal. Among virtual selections satisfying Eq. (9), the unique pattern found by a special algebraic approach suggests the least quadric norm of shear rates:

$$\sum_{k=1}^{N} \dot{\gamma_k}^2 = min, \qquad (10)$$

where the contributions of inactive slip systems are zero. Accordingly, the substitution of the latter norm for Eq. (5) could reduce the ambiguity of slip patterns in Taylor's theory. Although the physical sense of Eq. (10) wants clarification, the considered rate-independent model, as well as its modifications [25,26] can be used to avoid the slip pattern uncertainty in the piecewise-uniform approach to plastically deformed polycrystals. However, they still do not allow for crystal orientation splitting.

4. Local strain compatibility across interfaces

To refine the treatment of strain compatibility between grains, this constraint should be adjusted to each specific facet of a grain boundary. When applied to a planar interface with normal vector $\boldsymbol{N}$, the general compatibility equation [19] comes to

$$\boldsymbol{H}_N = \boldsymbol{N} \times (\boldsymbol{D}^+ - \boldsymbol{D}^-) \times \boldsymbol{N} = \boldsymbol{0}, \qquad (11)$$

where the strain rates $\boldsymbol{D}^+$ and $\boldsymbol{D}^-$ are due to the adjacent domains indicated by $\boldsymbol{N}$ and (-$\boldsymbol{N}$), respectively, and × means the vector product. According to Kröner [27], any plastic incompatibility $\boldsymbol{H}_N \neq \boldsymbol{0}$ is accommodated by an elastic strain field; in other words, the related boundary area becomes a two-dimensional source of internal stresses. Excluding the latter, Eq. (11) suggests equal planar projections of $\boldsymbol{D}^+$ and $\boldsymbol{D}^-$ i.e. similar strain rates of the boundary sides. This requirement applies to whichever *inelastic* strains. For instance [28], a collective effect of the lattice transformation and accommodative plastic shears in emerging martensite crystals is presumed to keep "invariant plane strains" for their habits. It is worth noting that a planar symmetric strain has only three independent components so that several components of tensor $\boldsymbol{D}^+ - \boldsymbol{D}^-$ do not affect the interfacial strain compatibility. Accordingly, the "relaxed constraint" of heavily flattened grains [29] enables their simplified slip patterns.

Along with the local influence of the grain interaction tractable by Eq. (11), another special constraint should be employed to accommodate the given *macroscopic* deformation of a polycrystal. As considered in the next section, simultaneous allowance for the two issues is provided by cluster models. Besides, to avoid their limitations and facilitate the modeling, a novel approach to the same problem will be introduced in Section 7.

5. Cluster models

Complying with Eq. (11), the simplest cluster model called LAMEL [30] accommodates macroscopic strain rate by any couple of plate-like grains separated by a boundary parallel to a rolling plane. To simulate the overall polycrystal texture at high degrees of thickness reduction, this rate-independent model treats one by one various virtual bicrystals whose orientation statistics correspond to the given initial texture. Unlike ten active slip systems in each couple according to Taylor's model, the partitioning of the imposed strain rate reduces their number to eight. Moreover, opposite shear rates of the two halves along the boundary, admitted by the interfacial compatibility, are selected to minimize the number of shear rates in the considered systems. The model has been eventually extended to admit various orientations of the planar interfaces [31] which gradually change their fractions following the grain shape. A more general approach of this sort [32] can involve the cluster whatever presumed number of constitutive grains.

As previously mentioned, statistical characteristics of the overall texture may implicitly allow for the in-grain orientation heterogeneity. Thus, a question appears of whether slip patterns splitting on the in-grain scale can be directly revealed in terms of the cluster concept. Such an effort [33] motivating the extension [31] of LAMEL model has been applied to thin bicrystals at the grain boundary facets, while a remaining part of the grain has been treated in terms of Taylor's model. As expected, the local slip patterns and resulting lattice orientations within the same crystal sharply split near triple junction lines. However, this interesting work still does not find any development because of some challenging issues. First, there is no rigorous criterion to select the thickness of the plate-like fragments. Second, it is not at all evident that their thin couples follow macroscopic strain rate. The latter issue gains in significance since the related disorientation strongly depends on the local distribution of plastic shearing. Finally, yet importantly, it is unclear how to extend this model to the eventual fragmentation of grain interiors.

6. Successive selection of active slip systems

It has been understood long ago [9,34] that the multi-slip gradually develops in disoriented constitutive crystals owing to their mutual plastic accommodation. There are two important aspects of this concept concerning crystal fragmentation. First, the local interaction of grains across their boundaries suggests a particular slip pattern at any interfacial facet; as considered in Section 7, such patterns trigger the orientation splitting near grain junctions. Second, each next slip system of a crystal is activated because of the strain mismatch and related reactive stress accumulated during the activity of the previous (incomplete) selection. We will make use of the successive activation events to quicken the selection of the final pattern. The algorithm does not follow the process in time; however, the whole sequence of its steps is explicitly reflected. As shown in the next section, simple combinations ($N<5$) of slip systems sought at the respective steps are relevant to local fragments near grain boundaries. Meanwhile, to better understand the formal grounds of this approach, it is reasonable to consider first a uniformly deformed crystal. For a case study, under consideration is the macroscopic strain rate tensor

$$\boldsymbol{D} = D\begin{pmatrix} 1 & 0 & 0 \\ 0 & -1 & 0 \\ 0 & 0 & 0 \end{pmatrix} \tag{12}$$

roughly corresponding to the rolling. Axes of related Cartesian system XYZ are parallel to the rolling, normal, and transversal directions, respectively. Table 1 numbers treated slip systems $\{111\}\langle 110\rangle$ of the FCC lattice.

Any local orientation is expressed by the rotation matrix $\boldsymbol{R}$ matching XYZ to the considered crystal domain; this matrix is derived as elsewhere from local crystallographic indices of the rolling plane (ND) and direction [RD]. Accordingly, normalized Burgers vectors $\boldsymbol{b}_i$ and normal vectors $\boldsymbol{n}_i$ to slip planes ($i = 1, 2, \ldots, 12$) are determined in terms of their reference counterparts corresponding to Table 1:

$$\boldsymbol{b}_i = \boldsymbol{R}\boldsymbol{b}_i^{(o)}, \boldsymbol{n}_i = \boldsymbol{R}\boldsymbol{n}_i^{(o)}. \tag{13}$$

The *active* slip systems are successively marked by subscripts $k = 1 \div 5$ which may differ from related numbers the table. Each of them is specified by the symmetric strain direction tensor

$$\boldsymbol{d}_k = (\boldsymbol{b}_k \otimes \boldsymbol{n}_k + \boldsymbol{n}_k \otimes \boldsymbol{b}_k)/2, \tag{14}$$

and the selection procedure makes use of Taylor's approximation (Eq. (4a) for the strain compatibility.

Table 1. Employed numeration of slip systems in FCC lattice

Number	1	2	3	4	5	6	7	8	9	10	11	12
Slip plane	(111)	(111)	(111)	$(\bar{1}11)$	$(\bar{1}11)$	$(\bar{1}11)$	$(1\bar{1}1)$	$(1\bar{1}1)$	$(1\bar{1}1)$	$(11\bar{1})$	$(11\bar{1})$	$(11\bar{1})$
Slip direction	$[01\bar{1}]$	$[10\bar{1}]$	$[1\bar{1}0]$	$[101]$	$[110]$	$[01\bar{1}]$	$[011]$	$[110]$	$[10\bar{1}]$	$[011]$	$[101]$	$[1\bar{1}0]$

The first active system is selected to provide the maximum contribution to $\boldsymbol{D}$ i.e.

$$|\boldsymbol{d}_1 : \boldsymbol{D}| = max\{|\boldsymbol{d}^{(i)} : \boldsymbol{D}|\}, \tag{15}$$

where superscript (i) the strain direction tensors of trial slip systems according to Table 1. In the case of several admitted variants, a random choice should be made, and the same rule remains valid at other steps ($k > 1$). The selection of slip patterns with the least deviation from $\boldsymbol{D}$ somewhat complicates the second to fourth steps. In algebraic terms, it suggests the maximum orthogonal projection of $\boldsymbol{D}$ on the linear space generated by the current set $\{\boldsymbol{d}_1, \dots, \boldsymbol{d}_k\}$ of direction tensors. To satisfy this condition, the procedure is repeated as follows at $k = 2, 3, 4$ with the same $\boldsymbol{p}_1 = \boldsymbol{d}_1$. Orthogonal to $\boldsymbol{d}_1, \dots, \boldsymbol{d}_{k-1}$, the virtual basic tensors

$$\boldsymbol{p}_k^* = \boldsymbol{d}_k^* - \boldsymbol{p}_1(\boldsymbol{d}_k^* : \boldsymbol{p}_1)/(\boldsymbol{p}_1 : \boldsymbol{p}_1) - \dots - \boldsymbol{p}_{k-1}(\boldsymbol{d}_k^* : \boldsymbol{p}_{k-1})/(\boldsymbol{p}_{k-1} : \boldsymbol{p}_{k-1}) \tag{16}$$

are determined first for all trial $\boldsymbol{d}_k^*$; next, acceptable $\boldsymbol{d}_k$, $\boldsymbol{p}_k$ and respective $\boldsymbol{D}_k$ are found to get

$$\boldsymbol{D}_k : \boldsymbol{D}_k = max\{\boldsymbol{D}_k^* : \boldsymbol{D}_k^*\} \tag{17}$$

where

$$\boldsymbol{D}_k^* = \boldsymbol{p}_1(\boldsymbol{D} : \boldsymbol{p}_1)/(\boldsymbol{p}_1 : \boldsymbol{p}_1) + \dots + \boldsymbol{p}_{k-1}(\boldsymbol{D} : \boldsymbol{p}_{k-1})/(\boldsymbol{p}_{k-1} : \boldsymbol{p}_{k-1}) + \boldsymbol{p}_k^*(\boldsymbol{D} : \boldsymbol{p}_k^*)/(\boldsymbol{p}_k^* : \boldsymbol{p}_k^*). \tag{18}$$

Since $\boldsymbol{d}_j : \boldsymbol{p}_m = 0$ at any $j < m$, the partial shear rates $\dot{\gamma}_m$ $(m = 1, 2, \dots, k)$ are simply expressed by

$$\dot{\gamma}_m = (\boldsymbol{D}_m : \boldsymbol{p}_m)/(\boldsymbol{d}_m : \boldsymbol{p}_m). \tag{19}$$

To further weaken ambiguity at intermediate steps $(2 \le k \le 4)$, one more constraint is applied:

$$\Gamma_k = |\dot{\gamma}_1| + \dots + |\dot{\gamma}_k| = min. \tag{20}$$

To exclude at $k \ge 3$ the slip systems geometrically dependent on previously selected ones, each

$$\boldsymbol{d}_k^* = \boldsymbol{p}_1(\boldsymbol{p}_1 : \boldsymbol{d}_k^*)/(\boldsymbol{p}_1 : \boldsymbol{p}_1) + \dots + \boldsymbol{p}_{k-1}(\boldsymbol{p}_{k-1} : \boldsymbol{d}_k^*)/(\boldsymbol{p}_{k-1} : \boldsymbol{p}_{k-1}) \tag{21}$$

is rejected.

At the last step, $\boldsymbol{D}$ can be accommodated by whatever available set of five slip systems. Among such patterns, only those with the least shear amount are admitted according to Eq. (5). Figure 1 shows the sequential selections at orientations $(\mathrm{ND})[\mathrm{RD}] = (23\bar{1})[115]$ and

$(\mathrm{ND})[\mathrm{RD}] = (123)[36\bar{5}]$. Note that some intermediate slip systems suggested by the least incompatibility criterion have been excluded because of additional requirements (20).

According to Eq. (6), the rate-independent approach [6,18] suggests RSS in active slip systems $m = 1 \div 5$ is equal to certain CRSS-s. Since the RSS depend only on the deviator σ' of the grain stress σ_g, the former can be derived from

$$\sigma' : \boldsymbol{d}_m = s \tag{22}$$

that comes to five simultaneous equations in five unknowns because $\sigma'_{33} = -\sigma'_{11} = \sigma'_{22}$. As soon as σ' is found, RSS in all remaining slip systems $(i \neq m)$ is determined by substitution of $\boldsymbol{d}^{(i)}$ for $\boldsymbol{d}_m$ and the sought τ_i for s in the same Eq. (22). In what follows, this enables the comparison of our algorithm with the Taylor-Bishop-Hill (TBH) theory.

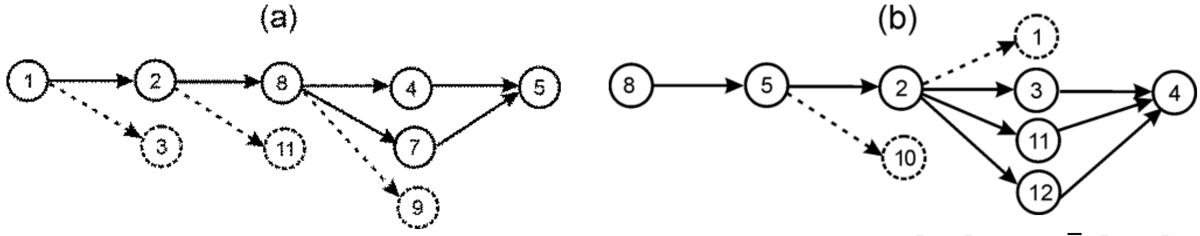

Fig. 1. Selection of active slip systems at crystal orientations (a) $(\mathrm{ND})[\mathrm{RD}] = (23\bar{1})[115]$ and (b) $(\mathrm{ND})[\mathrm{RD}] = (123)[36\bar{5}]$. Dash arrows indicate systems rejected because of excessive amount of shear rates at related steps

Table 2 represents numerical simulation results at orientation $(\mathrm{ND})[\mathrm{RD}] = (23\bar{1})[115]$; for brevity's sake, they are shown only for one of the two slip patterns (Fig. 1a) coinciding with Taylor's selections which have the least sum $\dot{\Gamma} = 2.829$ of shear rate magnitudes. In the second pattern slip system 7, previously *potentially* active ($|\tau|/s = 1$ but $\gamma = 0$), substitutes active system 4. Although in this case $\dot{\Gamma}$ remains the same, the underlying set of partial shear rates changes. According to Table 2, $|\tau|$ reaches s in *six* slip systems whereas, as considered below, another crystal orientation suggests *eight* ones. These findings comply with a specific property of FCC crystals according to the TBH theory where any apex of the yield surface [18] involves six or eight slip systems depending on the lattice orientations. Besides, as previously noted in [35], RSS in all *inactive* ($|\tau| < s$) slip systems of our crystals proved to vanish.

Table 2. RSS and magnitudes of related shear rates at orientation $(\mathrm{ND})[\mathrm{RD}] = (23\bar{1})[115]$

Slip system	Active*					Potential	Inactive					
	1	2	8	4	5	7	3	6	9	10	11	12
τ/s	-1	-1	1	1	1	1	0	0	0	0	0	0
$\lvert\dot{\gamma}\rvert/D$	0.872	1.134	0.674	0.086	0.062	0	0	0	0	0	0	0

*In order of selection

The simulation results shown in Table 3 are due to orientation $(\mathrm{ND})[\mathrm{RD}] = (123)[36\bar{5}]$ that suggests the yield surface apex formed by *eight* slip systems (active and potentially active) with $|\tau|/\tau_c = 1$. Unlike the previous $\mathrm{C}_6^5 = 6$, in this case, the TBH approach should check $\mathrm{C}_8^5 = 56$ sets of five slip systems. This is much more computationally expensive than our algorithm that compares steps 3 and 4 (Fig. 1b) with only $2 + 4 = 6$ potential variants of incomplete ($k < 5$) slip patterns. Thus, as the constitutive grains of the polycrystal generally have comparable fractions of both orientation types, the sequential selection enables much quicker simulations of the texture development. Although the algorithm finds almost all slip patterns of Taylor's type, the above-mentioned complex combinatorics some of them can be missed since they do not provide the least strain rate incompatibility in selection steps 2 to 4. For instance, the least $\Gamma = 4.199$ given by each of the found selections (Fig. 1b) is also the case when slip system 3 in the considered set is substituted by system 9 although the latter is excluded by our algorithm for the above-mentioned reason. To assess the statistical significance of such cases, it is advisable to consider related polycrystal textures.

Table 3. RSS and magnitudes of related shear rates at orientation $(\mathrm{ND})[\mathrm{RD}] = (123)[36\bar{5}]$

Slip system	Active*					Potential			Inactive			
	8	5	2	3	4	9	11	12	1	6	7	10
τ/s	-1	-1	1	1	-1	-1	-1	-1	0	0	0	0
$\lvert\dot{\gamma}\rvert/D$	2.030	0.770	0.630	0.700	0.070	0	0	0	0	0	0	0

*In order of selection

Both the TBH model and the present method have been applied with strain increments of 0.01 to predict the texture of an FCC polycrystal subject to the thickness reduction of 50% at $\boldsymbol{D}$ expressed by Eq. (12). A random distribution of 5000 crystal orientations was generated for the initial state, and the only difference between two approaches was in a way to select active slip systems of constitutive grains. Table 4 lists the resulting fractions of texture components calculated within angular deviations of 15° from the indicated orientations. As expected, the rare slip systems admitted in the TBH model, but excluded by our algorithm, affect the predicted results rather weakly. We do not display respective pole figures because it would be hardly possible to distinguish between them. Note that the likeness of these textures confirms the statistical similarity of related slip patterns even though at high strains each of the two approaches loses accuracy because the grain flattening is neglected. Limited to *uniform* crystals, the grain shape effect is tractable by extensions [29,30] of the original TBH theory; however, they are also unable to predict the fragmentation of plastically deformed crystals into disoriented parts.

Table 4. Predicted fractions of rolling texture components (per cent) in a FCC polycrystal at 50 % thickness reduction

Texture component	$\{110\}$ $\langle 001\rangle$	$\{110\}$ $\langle 112\rangle$	$\{211\}$ $\langle 111\rangle$	$\{123\}$ $\langle 634\rangle$	$\{100\}$ $\langle 001\rangle$
Present model	4.3	9.5	20.4	34.5	1.6
TBH model	4.0	9.4	20.0	33.8	1.6

To sum up this section, the considered approach quickens the selection of active slip systems while its essentially *geometrical* formulation avoids the poorly justified treatment of CRSS variations in strain hardening as well as specific limitations of rate-sensitive models. Although Taylor's problem of slip pattern ambiguity still has been retained, on the local scale at grain boundaries it can be resolved as demonstrated in what follows.

7. Model of deformed interfacial skeleton

While maintaining the *local* strain compatibility across grain boundaries considered in Section 4, a polycrystal should accommodate *macroscopic* deformation. To satisfy these two requirements at once, we will make use of a simple approximation. It presumes that the interfacial skeleton follows a macroscopic strain rate whichever in-grain heterogeneities and projection of $\boldsymbol{D}$ onto any boundary facet is accommodated at both its sides to keep the interfacial compatibility. Since a symmetric planar strain has three independent components, three slip systems in each of the two differently oriented crystalline domains will be sufficient to satisfy the latter condition.

Specific details of the proposed scheme are available elsewhere [36]; briefly, the previous tensor terms and related procedures minimizing the strain rate incompatibility are projected on planar boundary facets. According to Fig. 2, a trial simulation has been implemented at the perfect (120°) junction of three grain boundaries parallel to axis Z. Normal vectors to the considered facets are $\boldsymbol{N}_I = [-1/2, \sqrt{3}/2, 0]$ and $\boldsymbol{N}_{II} = [1/2, \sqrt{3}/2, 0]$ while the crystal orientation is specified by (ND)[RD] = $(123)[36\bar{5}]$. Respective planar projections of the macroscopic strain rate $\boldsymbol{D}$ are denoted in Fig. 2 by $\boldsymbol{S}_I$ and $\boldsymbol{S}_{II}$, and other terms correspond to local strain rates and underlying slip systems.

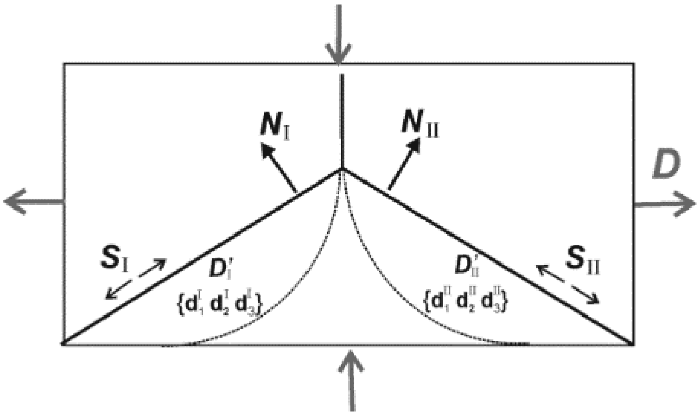

Fig. 2. Scheme to derive local slip patterns near grain boundary facets

Table 5 lists simulation results at $\boldsymbol{D}$ according to Eq. (12) for two adjacent domains of the same grain situated near the considered junction. $\boldsymbol{D}'$ and $\boldsymbol{w}'$ in this table are the local tensors of plastic strain rate and the vector of the plastic rotation rate, respectively; $\dot{\gamma}$ represents the shear rates in operating slip systems. It should be underlined that each of the predicted slip patterns proved to be *unique* although the number C_8^3 of potential variants was equal to C_8^5 in the case of Taylor's selection. Such a meaningful distinction is mostly due to one more constraint (orientation of a boundary plane) at the same strain rate and crystal orientation; besides, unlike five of Taylor's slip systems, the considered three suggest a lesser multiplicity of virtual selections.

Table 5. Simulation results for two neighboring domains of same grain (Fig. 2)

Domain	I	II
Slip systems	1 2 9	5 9 11
$\dot{\gamma}/D$	1.019 0.043 0.156	−0.735 −0.123 −0.733
$\boldsymbol{D}'/D$	$\begin{pmatrix} 0.211 & 0.455 & 0.099 \\ 0.455 & -0.211 & -0.171 \\ 0.099 & -0.171 & 0 \end{pmatrix}$	$\begin{pmatrix} 0.243 & -0.437 & 0.014 \\ -0.437 & -0.243 & 0.024 \\ 0.014 & 0.024 & 0 \end{pmatrix}$
$\boldsymbol{w}'/D$	$[0.072\ \ -0.235\ \ 0.481]$	$[0.192\ \ -0.387\ \ 0.066]$

To make use of $\boldsymbol{D}'$ and $\boldsymbol{w}'$ found in the considered fragments, respective increments of plastic strain and rotation during a small thickness reduction Δ expressed with Eq. (12) are kept in mind:

$$\boldsymbol{\varepsilon} = \boldsymbol{D}'\Delta/D, \boldsymbol{\omega} = \boldsymbol{w}'\Delta/D. \tag{23}$$

Given a plane (unit normal vector $\boldsymbol{N}'$) for a virtual dislocation boundary separating these two fragments, the corresponding increment of their disorientation vector is evaluated according to [37]:

$$\boldsymbol{\theta}' = \boldsymbol{N}' \times (\boldsymbol{\varepsilon}_{II} - \boldsymbol{\varepsilon}_{I}) \cdot \boldsymbol{N}' + \boldsymbol{\omega}_{I} - \boldsymbol{\omega}_{II} \tag{24}$$

where the dot indicates a scalar product. However, although a fresh boundary emerging near the grain junction may be revealed by means of electron microscopy; further refinements of the model are required to *predic*t $\boldsymbol{N}'$absent in Fig. 2.

To roughly assess the likelihood of the found patterns (Table 5), the contribution of $\boldsymbol{\omega}_I$ and $\boldsymbol{\omega}_{II}$ to $\boldsymbol{\theta}'$ has been calculated at $\Delta = 0.1$:

$$\boldsymbol{\theta}'_{\omega} = 2.6°[-0.262 \quad 0.332 \quad 0.906], \tag{25}$$

and its magnitude (angle) seems to be realistic for a dislocation boundary nucleating at the junction line. Next, a *virtual* boundary plane YZ (bisector of the lower grain in Fig. 2) has been presumed to assess the effect of plastic strain discontinuity. According to Eq. (24), it induces

$$\boldsymbol{\theta}'_{\varepsilon} = 5.1°[0 \quad 0.095 \quad -0.996] \tag{26}$$

whereas resulting disorientation vector

$$\boldsymbol{\theta}' = \boldsymbol{\theta}'_{\varepsilon} + \boldsymbol{\theta}'_{\omega} = 3.1°[-0.220 \quad 0.434 \quad -0.874] \tag{27}$$

still has a plausible magnitude.

To sum up, this work based on the least strain incompatibility criterion, a quick algorithm is formulated to select one by one active slip systems of a deformed crystal. When tested on virtually uniform slip patterns of whole grains, this approach generally finds Taylor's slip patterns with the least shear amount. When applied to the local domains at grain boundaries, it quantifies the related in-grain heterogeneity of plastic shearing and thus enables simulations of the crystal fragmentation onset.

8. Concluding remarks

The main limitation of the considered approach focused on local slip patterns near grain boundaries is that it ignores the orientation splitting into grain interiors. In principle, the problem is tractable by the crystal plasticity FEM; however, representative clusters of subdivided grains conventionally treated by this method suggest an excessive computational cost. Meanwhile, the interfacial skeleton concept seems to admit the model decomposition into separate constitutive crystals. Although this challenging issue is beyond the scope of the present paper, some expedients deserve discussion as follows.

Given CRSS s, the order tensor $\boldsymbol{C}^{-1}$of elastic compliance and grain boundary plane $\boldsymbol{N}$ prescribing a local slip pattern, the method of Lagrange multipliers enables the determination of related stress $\boldsymbol{\sigma}_N$. To this end, the density of elastic energy

$$e = \boldsymbol{\sigma}_N : \boldsymbol{C}^{-1} : \boldsymbol{\sigma}_N / 2 \tag{28}$$

should be minimized at constraint equalities ($k = 1, 2, 3$)

$$\boldsymbol{\sigma}_N : \boldsymbol{d}_k - s = 0 \tag{29}$$

due to the active slip systems Then, to mimic the interaction of grain with surroundings, specific forces (stress vectors)

$$\boldsymbol{f}_N = \boldsymbol{\sigma}_N \cdot \boldsymbol{N} \tag{30}$$

applied to its facets will provide boundary conditions enabling its *individual* modeling by the crystal plasticity FEM.

A remark should be made that these equations as well as the whole formulation are due to a *fixed* state of the deformed polycrystal whereas the fragmentation process develops over a rather wide strain range. Accordingly, the latter should be subdivided into small increments approximately keeping certain interfacial configurations, local crystal orientations, and respective slip patterns. It is easy to repeatedly upgrade grain shapes that follow macroscopic deformation; as to the lattice rotations accumulated in each increment at the fixed boundary facets, they can be quantified as in the case of constrained martensite crystals described elsewhere [16].

References

1. Rybin VV. *Large Plastic Strains and Fracture of Metals*. Moscow: Metallurgy; 1986. (In Russian)
2. Bay B, Hansen N, Hughes DA, Kuhlmann-Wilsdorf D. Overview No. 96: evolution of f.c.c. deformation structures in polyslip. *Acta Metallurgica et Materialia*. 1992;40(2): 205-219.
3. Humphreys FJ, Bate PS. The microstructures of polycrystalline Al–0.1Mg after hot plane strain compression. *Acta Materialia*. 2007;55(16): 5630-5645.
4. Valiev RZ, Korznikov AV, Mulyukov RR. Structure and properties of ultrafine-grained materials produced by severe plastic deformation. *Materials Science and Engineering: A*. 1993;168(2): 141-148.
5. Chen SF, Li DY, Zhang SH, Han HN, Lee HW, Lee MG. Modelling continuous dynamic recrystallization of aluminum alloys based on the polycrystal plasticity approach. *International Journal of Plasticity*. 2020;131: 102710.
6. Taylor GI. Plastic strains in metals. *Journal of the Institute of Metals*. 1938;62: 307-324.
7. Seefeldt M, Van Houtte P. Grain subdivision and local texture evolution studied by means of a coupled substructure-texture evolution model. *Materials Science Forum*. 2002;408-412: 433-438.
8. Rey C, Mussot P, Vroux AM, Zaoui A. Effects of interfaces on the plastic behavior of metallic aggregates. *Journal de Physique Colloques*. 1985;46(C4): 645-650.
9. Berveiller M, Bouaquine H, Fakri N, Lipinski P. Texture transition, micro shear bands and heterogeneous plastic strain in FCC and BCC metals. *Textures and Microstructures*. 1988;8-9: 351-379.
10. Ananthan VS, Leffers T, Hansen N. Characteristics of second generation microbands in cold-rolled copper. *Scripta Metallurgica et Materialia*. 1991;25: 137-142.
11. Zaefferer S, Kuo JC, Zhao Z, Winning M, Raabe D. On the influence of the grain boundary misorientation on the plastic deformation of aluminium bicrystals. *Acta Materialia*. 2003;51: 4719-4735.
12. Wert JA, Liu Q, Hansen N. Dislocation boundary formation in a cold rolled cube-oriented Al single crystal. *Acta Materialia*.1997;45(6): 2565-2576.
13. Wei P, Zhou H, Liu H, Zhu C, Wang W, Deng G. Investigation of grain refinement mechanism of nickel single crystal during high pressure torsion by crystal plasticity modeling. *Materials*. 2019;12(3): 351.
14. Zisman A, Nesterova E, Rybin V, Teodosiu C. Interfacial misorientations and underlying slip activity of a shear microband in mild steel: TEM analysis and numerical simulation. *Scripta Materialia*. 2002;46: 729-733.
15. Ball J, James R. Fine phase mixtures as minimizer of energy. *Archive for Rational Mechanics and Analysis*. 1987;100: 13-52.
16. Zisman A. Predictive micromechanical model for plastic accommodation and crystallography of martensite embryo. *International Journal of Engineering Science*. 2020;150: 103245.
17. Asaro RJ, Needleman A. Texture development and strain hardening in rate dependent polycrystals. *Acta Metallurgica*. 1985;33: 923-953.
18. Bishop JFW, Hill R. A theory of the plastic distortion of a polycrystalline aggregate under combined stresses. *Philosophical Magazine*. 1951;42: 414-427.

19. Navier M, Saint-Venant B. *Résumé des Lecons Données à École des Ponts et Chaussées sur l'Application de la Mécanique à l'Etablissement des Constructions et des Machines*. Paris: Dunod; 1864.

20. Hill R. Generalized constitutive relations for incremental deformation of metal crystals by multislip. *Journal of the Mechanics and Physics of Solids*. 1966;14: 95-102.

21. Anand L, Kothari M. A computational procedure for rate-independent crystal plasticity. *Journal of the Mechanics and Physics of Solids*. 1996;44: 525-558.

22. Knezevic M, Drach B, Ardljan M, Beierlein IJ. Three dimensional predictions of grain scale plasticity and grain boundaries using crystal plasticity finite element models. *Computational Methods in Applied Mechanics and Engineering*. 2014;277: 239-259.

23. Roters F, Eisenlohr P, Hantcherli L, Tjahjanto DD, Bieler TR, Raabe D. Overview of constitutive laws, kinematics, homogenization and multiscale methods in crystal plasticity finite-element modeling: Theory, experiments, applications. *Acta Materialia*. 2010;58: 1152-1211.

24. Li S, Donohue BR, Kalidindi SR. A crystal plasticity finite element analysis of cross-grain deformation heterogeneity in equal channel angular extrusion and its implications for texture evolution. *Materials Science and Engineering: A*. 2008;480(1-2): 17-23.

25. Petryk H, Kursa M. Incremental work minimization algorithm for rate-independent plasticity of single crystals. *International Journal for Numerical Methods in Engineering*. 2015;104(3): 157-184.

26. Orthaber M, Antretter T, Gänser H-T. On the selection of active slip systems in rate independent crystal plasticity. *Key Engineering Materials*. 2013;554-557: 1147-1156.

27. Kröner E. *Kontinuumstheorie der Versetzungen und Eigenspanungen (Ergebnisse der Angewandten Mathematik, 5)*. Berlin: Springer; 1958.

28. Bullough R, Bilby BA. Continuous distribution of dislocations: Surface dislocations and crystallography of martensitic transformation. *Proceedings of the Royal Society of London*. 1956;B69: 1276-1286.

29. Kocks UF, Chandra H. Slip geometry in partially constrained deformation. *Acta Metallurgica*. 1982;30: 695-709.

30. Van Houtte P, Delannay L, Samaidar I. Quantitative prediction of cold rolling textures in low carbon steels by means of the LAMEL model. *Textures and Microstructures*, 1999;31: 109-149.

31. Van Houtte P, Li S, Seefeldt M, Delannay L, Samaidar I. Deformation texture prediction: From the Taylor model to the advanced Lamel model. *International Journal of Plasticity*. 2005;21: 589-624.

32. Raabe D. Simulation of rolling textures of bcc metals considering grain interactions and crystallographic slip on {110}, {112} and {123} planes. *Materials Science and Engineering: A*. 1995;197: 31-37.

33. Evers LP, Parks DM, Brekelmans WAM, Geers MGD. Crystal plasticity model with enhanced hardening by geometrically necessary dislocation accumulation. *Journal of the Mechanics and Physics of Solids*. 2002;50: 2403-2424.

34. Budiansky B, Wu TT. Theoretical prediction of plastic strains of polycrystals. In: Rosenberg RM. (ed.) *Proceedings of the 4th U.S. National Congress on Applied Mechanics*. New York: ASME; 1962. p.1175-1185.

35. Clausen B, Leffers T, Lorentzen L, Pedersen OB, Van Houtte P. The resolved shear stress on the non-active slip systems in Taylor/Bishop-Hill models for FCC polycrystals. *Scripta Materialia*. 2000;42: 91-96.

36. Zisman A. Model for partitioning slip patterns at triple junctions of grains. *International Journal of Engineering Science*. 2017;116: 155-164.

37. Zisman AA, Rybin VV. Basic configurations of interfacial and junction defects induced in a polycrystal by deformation of grains. *Acta Materialia*. 1996;44(1): 403-407.

THE AUTHORS

Alexander A. Zisman
e-mail: azisman@spbstu.ru
ORCID: 0000-0002-9431-7097

Natalia Yu. Ermakova
e-mail: ermakova@phmf.spbstu.ru
ORCID: 0000-0002-1324-7112

Materials Physics and Mechanics. 2022;49(1): 173-181
Conference materials
http://dx.doi.org/10.18149/MPM.4912022_13

Analysis of the conditions of crack nucleation during lattice dislocations transition through grain boundary

V.N. Perevesentsev[1], S.V. Kirikov[1]✉, N.Yu. Zolotorevsky[1,2]

[1]Mechanical Engineering Research Institute of the Russian Academy of Sciences, 603024, Nizhny Novgorod, Russia

[2]Peter the Great St. Petersburg Polytechnic University, Polytekhnicheskaya 29, 195251, St. Petersburg, Russia

✉ ksv.kirikov@yandex.ru

Abstract. The formation of deformation facets at high-angle grain boundaries during their interaction with lattice dislocation pile-ups is accompanied by the appearance of wedge disclination dipoles disposed on the plane of the facets. Their elastic energy increases as the dislocations of pile-up penetrate the grain boundary and the deformation facet lengthens. A possibility was considered for the relaxation of elastic energy of the disclination dipole and the pile-up stored in the vicinity of the facet. A concept of the least possible length of the crack in a crystalline solid was introduced, and an energetic criterion of its nucleation was suggested. An analysis of conditions for the crack nucleation in configuration space of considered system parameters – the total Burgers vector of pile-up, the strength of disclination dipoles, and the value of external load – has been carried out.

Keywords: disclination, dislocation, dislocation pile-up, grain boundary, microcrack

***Acknowledgements**. The Russian Science Foundation supported this work, project №21-19-00366.*

Citation: Perevesentsev VN, Kirikov SV, Zolotorevsky NYu. Analysis of the conditions of crack nucleation during lattice dislocations transition through grain boundary. *Materials Physics and Mechanics*. 2022;49(1): 173-181. DOI: 10.18149/MPM.4912022_13.

1. Introduction

It is generally accepted that high local stresses, which are assumed to initiate fracture, relate to inhomogeneous plastic deformation [1]. Indeed, the strain inhomogeneity occurring within a grain ensemble leads to the appearance of plastic incompatibility at grain boundaries in the form of orientation misfit dislocations (OMDs) [2]. Under conditions of their sufficiently uniform distribution over the facets of grain boundaries, the OMDs can be conveniently described in terms of "mesodefects". The latter are planar defects of shear and rotational type – the uniform continual distributions of tangential and normal components of OMD Burgers vector, respectively [3,4]. Linear rotational defects and junction disclinations are formed at junctions and ledges of grain boundaries [5]. The strength of mesodefects and the intensity of elastic stresses generated by them increase during plastic deformation. If their relaxation owing to plastic accommodation is hampered, the only possible way of relaxation is the appearance of a crack. Conditions of the nucleation and characteristics of stable cracks formed under stresses generated by the mesodefects, such as a wedge disclination, a dipole of

Publisher: Peter the Great St. Petersburg Polytechnic University

wedge disclinations, combined shear-rotational mesodefects, and more complex systems of mesodefects, have been considered in many studies [6-12].

Under low homological temperature conditions, plastic deformation is characterized by its strong localization within separate slip planes of lattice dislocations. This, in its turn, leads to the appearance of planar dislocation pile-ups near grain boundaries. Conditions for the crack nucleation in the head of the pile-up hampered by an impenetrable barrier were considered in the classical Stroh model [13,14]. At that, grain boundaries were usually assumed to be such barriers. In this framework, a pile-up composed of a few hundred of dislocations is needed for the crack nucleation, however, so great pile-ups were not observed by electron microscopy. Moreover, generally, the grain boundaries are not impenetrable barriers. So, relaxation of the hampered pile-up can occur by way of lattice shear passing across the grain boundary. Various aspects of the process were considered earlier [15-20]. It has been shown [20] that the process depends on the lattice shear geometry, grain boundary misorientation, and the distance between a dislocation source and the boundary. The dislocations passing across the grain boundary can create extended grain boundary facets containing the planar mesodefects of rotational type in the form of biaxial dipoles of wedge disclinations. In its turn, these defects can generate cracks.

The aim of the present research is an analysis of conditions for the crack nucleation in the vertex of the deformation facet; the latter being formed by the lattice shear passing across a high-angle grain boundary.

2. Model description

Consider a pile-up of dislocations with Burgers vector $\mathbf{b_1}$, located in the first grain and pressed by the external load $\mathbf{P} = P\mathbf{n}$ ($\mathbf{n}$ is the unit vector along an axis of loading) to the high-angle tilt boundary with the misorientation $\boldsymbol{\theta} = \theta\mathbf{e_z}$, ($\mathbf{e_z}$ is directed at the right angle to the drawing plane, Fig. 1). Suppose that slip planes of these dislocations are oriented so that the resolved shear stress is maximal, that is $\angle(\mathbf{b_1}, \mathbf{n}) = \pi / 4$. For crossing the boundary, the dislocation of the first grain must dissociate into the dislocation of the second grains with Burgers vector $\mathbf{b}_2$ and orientation misfit dislocations (OMD) with the residual Burgers vector $\Delta\mathbf{b}$: $\mathbf{b}_1 = \mathbf{b}_2 + \Delta\mathbf{b}$. Because of these reactions and subsequent runaway of the dislocation $\mathbf{b}_2$ into the second grain, the OMD appear, which are associated with a ledge of height $\Delta l = b\cos\theta$ directed along the slip plane of dislocations of the first grain.

As dislocations $\mathbf{b}_2$ run away into the second grain, the pile-up is pressed by external stress to the grain boundary, and then the next dislocation crosses the boundary. Multiple repetitions of the process leads to the formation of the facet with the length of $l_f = n\Delta l$ (*n* is a number of dislocations gone away into the second grain) oriented along the slip plane of the first-grain dislocations. Resolving Burgers vector of OMDs $\Delta\mathbf{b}$ into the normal and tangential components relative to the facet plane, its defect content can be described as a superposition of two planar distributions of virtual dislocations.

The first distribution can be represented as a continual uniform distribution of sessile dislocations. It will be considered next as a biaxial dipole of wedge disclinations with an arm coinciding with the facet length l_f and strength $\mathbf{w_{dp}}$ equal to Burgers vector density of the sessile dislocations. Frank vector $\mathbf{w_d}$ of the disclinations constituting the dipole relates to $\mathbf{w_{dp}}$ as:

$$\mathbf{w_d}(\mathbf{r}_1) = \frac{\mathbf{w_{dp}} \times (\mathbf{r}_1 - \mathbf{r}_2)}{\| \mathbf{r}_1 - \mathbf{r}_2 \|}, \quad \mathbf{w_d}(\mathbf{r}_2) = \frac{\mathbf{w_{dp}} \times (\mathbf{r}_2 - \mathbf{r}_1)}{\| \mathbf{r}_1 - \mathbf{r}_2 \|}, \tag{1}$$

where $\mathbf{w_d}(\mathbf{r_1})$ and $\mathbf{w_d}(\mathbf{r_2})$ are the Frank vectors of the disclinations located in the points with radius-vectors **r₁** and **r₂**, respectively. Taking into account that $\mathbf{w_{dp}} = w_{dp}\mathbf{e_y}$, one can obtain $w_{dp} = -\tan\theta$.

It is worth noting that the sign of the disclination located in the head of the pile-up depends on the orientation of the dislocation slip plane in the second grain. We consider the most preferred for crack nucleation case, when a negative disclination generating tensile stress field is located in the head of the pile-up, which corresponds to values $\theta < 0$ (Fig. 1).

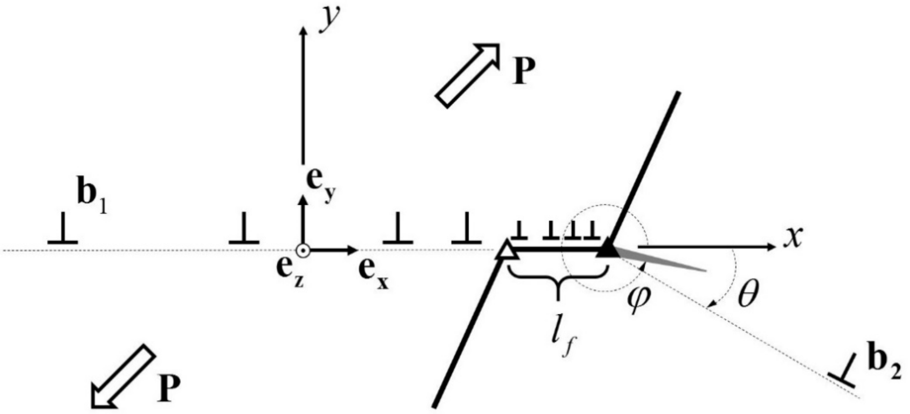

Fig.1. Schematic representation of dislocation pile-up crossing grain boundary

It is convenient for subsequent calculations to set parameters characterizing the system on every stage of the facet formation, namely, the total Burgers vector of dislocations in the pile-up $\mathbf{B} = (B, 0)$ and the facet length l_f. Let us choose Cartesian coordinate system *Oxyz* and the corresponding orthonormal basis associated with the facet as shown in Fig. 1; the origin of coordinates is set in the center of the pile-up. Since the disclination dipole is located in the facet plane oriented along the dislocation slip plane of the first grain and, hence, does not interact with the dislocations of the pile-up, the length of the pile-up *L* and the Burgers-vector-density distribution $\rho(x)$ are determined by the expressions [21]:

$$L = \frac{GB}{\pi(1-\nu)\tau_1}, \quad \rho(x) = \frac{2(1-\nu)\tau_1}{G}\sqrt{\frac{L/2+x}{L/2-x}}, \tag{2}$$

where $\tau_1 = \mathbf{e_y}\cdot(P\mathbf{n}\otimes\mathbf{n})\cdot\mathbf{e_x}$ is the shear stress in the slip plane of dislocations $\mathbf{b_1}$, G and ν are the shear modulus and Poisson coefficient, respectively. A drag force $f^{(dp)}$ acts from the disclination dipole on the dislocation going into the second grain. A value of the force increases as the dislocations cross the grain boundary and the facet lengthens. When the facet length reaches a certain value $l_f^{(dp)}$, this force balances the total force acting on the dislocation going into the second grain from the external stress $f^{(ext)}$ and the dislocation pile-up $f^{(p)}$. As a result, the process of a grain boundary crossing by the dislocations stops. A criterion for the stop of the facet lengthening can be written in the form:

$$\min_{x,y}\left(f^{(p)}(x,y) + f^{(ext)} + f^{(dp)}(x,y)\right) = 0. \tag{3}$$

Let **n₂** be the unit vector of the normal to the dislocation slip plane in the second grain. Thus, the forces acting on the going off dislocation:

$$f^{(p)}(x,y)=\mathbf{n}_2\cdot\left(\int\limits_{-L/2}^{L/2}\rho(x')\mathbf{G}(x-x',y)dx'\right)\cdot\mathbf{b}_2,$$
$$f^{(dp)}(x,y)=\mathbf{n}_2\cdot\left(\boldsymbol{\sigma}_{\mathbf{d}}(x-L/2+l_f^{(dp)},0)\right)\cdot\mathbf{b}_2,\quad f^{(ext)}=\mathbf{n}_2\cdot\left(P\mathbf{n}\otimes\mathbf{n}\right)\cdot\mathbf{b}_2, \tag{4}$$

where $\mathbf{G}(x-x',y)$ is the function of stress produced by the dislocation located in point (x', 0) with unit Burgers vector [21] oriented along axis Ox, $\boldsymbol{\sigma}_{\mathrm{d}}$ is a function of stress tensor from the positive disclination of the dipole (negative disclination does not produce shear stresses in the slip plane of dislocation $\mathbf{b}_2$ located in point $(L/2-l_f^{(dp)},0)$ [22]).

The action of the tensile stresses from the dislocation pile-up, the stresses from the negative disclination, and the external stress in the vicinity of the facet can lead to the formation of a crack. Usually, the crack nucleation is considered in the micromechanics of fracture in terms of an energetic approach. According to the approach, the crack nucleates if the interval of its length $(0,l_0]$ exists, in which the following condition is fulfilled:

$$\frac{\partial E}{\partial l}\le 0,\ \ \forall l\in(0,l_0], \tag{5}$$

where E is the energy of the system, and l_0 is the limit point, where condition (5) ceases to fulfil. At that, if $l_0<\infty$, then an equilibrium stable crack is generated. Otherwise, if $l_0=\infty$, then the main crack is produced. However, the application of this criterion for the model considered seems to be not quite justified. Actually, based on the earlier results [1] it can be shown that the relaxation of disclination elastic energy $\left(E_{el}^{\Delta}\right)_l'$ near point $l=0$ is infinitesimal. Consequently, the presence of the disclination dipole has no effect on the fulfillment of criterion (5). Nevertheless, it is quite apparent that a powerful tensile stress field from the negative disclination can facilitate significantly the crack nucleation in its vicinity. The disclination effect can be accounted for, if to suppose that the propagating crack does not pass through all intermediate states near point $l=0$, but rather opens up spasmodically to a certain finite length l_{nucl}. Based on physical consideration, the length equal to two periods of the crystal lattice, $l_{nucl}=2b$, can be taken as a minimal length of the crack. Thus the criterion of crack nucleation can be expressed using a finite increment of energy:

$$\Delta E=E(2b)-E_0\le 0, \tag{6}$$

where $E(2b)$ is the energy of the system with a crack of length $2b$, E_0 is the energy of the system without a crack. Assuming a negligible contribution of dissipative processes to the energy changing during crack nucleation, as well as the independence of the free surface of a crack tip from the crack length, one can obtain ΔE as:

$$\Delta E=\Delta E_{el}+\Delta E_{\gamma}=\Delta E_{el}+4\gamma b, \tag{7}$$

where γ is the specific energy of the free surface. At the same time, the change of potential energy E_{el} can be calculated as:

$$\Delta E_{el}=-\int\limits_0^{2b}F(l,\varphi)dl. \tag{8}$$

Here $F(l,\varphi)$ is the configurational force defined as the elastic energy released during crack propagation per unit length:

$$F(l,\varphi)=\frac{l}{8D}\left(\bar{\sigma}_{\varphi\varphi}{}^2+\bar{\sigma}_{r\varphi}{}^2\right), \tag{9}$$

where $D=G/[2\pi(1-\nu)]$, φ is the angle determining the crack orientation, $\bar{\sigma}_{\varphi\varphi},\bar{\sigma}_{r\varphi}$ are the averaged total stresses:

$$\bar{\sigma}_{\varphi\varphi}=\frac{2}{\pi l}\int_0^l \sigma_{\varphi\varphi}(r,\varphi)\sqrt{\frac{r}{l-r}}dr,\quad \bar{\sigma}_{r\varphi}=\frac{2}{\pi l}\int_0^l \sigma_{r\varphi}(r,\varphi)\sqrt{\frac{r}{l-r}}dr, \tag{10}$$

where $\sigma_{\varphi\varphi}$, $\sigma_{r\varphi}$ are the components of total stress produced by the biaxial dipole of wedge disclinations, the hampered pile-up, and the external load in the vicinity of the microcrack. We have used the polar system of coordinates, where the pole coincides with the location of the negative disclination of the dipole. Taking equation (8) into account, criterion (6) for the nucleation of the crack oriented along angle φ becomes (for given values of parameters l_f, B, P, w_{dp}):

$$\Delta E=4\gamma b-\int_0^{2b} F(l,\varphi)dl\le 0. \tag{11}$$

The most energetically preferred orientation of the nucleating crack is such direction $\varphi_{\max}$ that provides the maximal relaxation of the stress field:

$$\Delta E_{el}(\varphi_{\max})=\max_{\varphi}\int_0^{2b} F(l,\varphi)dl. \tag{12}$$

Naturally, the values of $\varphi_{\max}$ will differ for different sets of parameters l_f, B, P, w_{dp}. For given values of *B*, *P*, w_{dp}, the minimal facet length $l_f^{(cr)}$, for which the crack nucleation becomes possible, can be found in the equation:

$$4\gamma b-\int_0^{2b} F\left(l,\varphi_{\max}(l_f^{(cr)}),l_f^{(cr)}\right)\Big|_{B,P,w_{dp}} dl=0. \tag{13}$$

It is evident that, for $l_f>l_f^{(cr)}$, a direction always exists, in which the nucleation of the crack of length $l_0=2b$ becomes energetically preferable; but for $l_f<l_f^{(cr)}$, the crack does not nucleate according to this criterion. Hence, crack nucleation at a faceted boundary is possible only in the case when $l_f^{(cr)}\le l_f^{(dp)}$. Then, the functions $l_f^{(cr)}(B,w_{dp},P)$ and $l_f^{(dp)}(B,w_{dp},P)$ can be obtained by numerical calculations varying parameters B, P, w_{dp}.

3. Results of numerical calculations and discussion

The calculations were carried out for the following values of parameters: $G=45000$ MPa, $\nu=0.3$, $b=3\cdot 10^{-4}$ μm, $B\in[20b,50b]$, $\theta\in[-15^\circ,-30^\circ]$, $P=\{0.005G, 0.0075G\}$, $\gamma=Gb/8$. Figure 2 shows a typical view of the configurational force dependence on the crack length, calculated with $\varphi=300^\circ, B=40b$, $l_f=388.7b$, $w_{dp}=0.3$, $P=0.005G$.

Figure 3a and 3b show the dependencies of $l_f^{(dp)}/b$ and $l_f^{(cr)}/b$ on the total Burgers vector of the pile-up B normalized to b, calculated for fixed values of the disclination dipole strength w_{dp} and external load P. Intersection points of the curves $l_f^{(dp)}/b$ and $l_f^{(cr)}/b$

correspond to the threshold values of the total Burgers vector of pile-up B^*, at exceeding which the crack nucleates.

Figure 4 shows the dependencies of the threshold value of the total Burgers vector of pile-up B^*/b on the disclination dipole strength w_{dp} for the values of external load $P = 0.005G$ and $P = 0.0075G$.

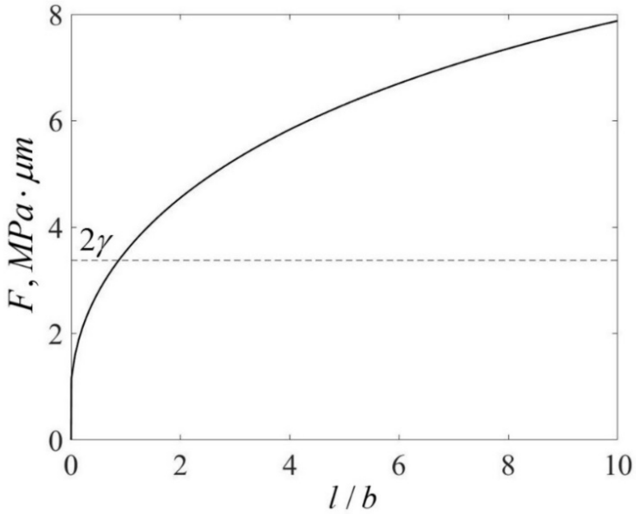

Fig. 2. Typical dependence of configurational force on a crack length

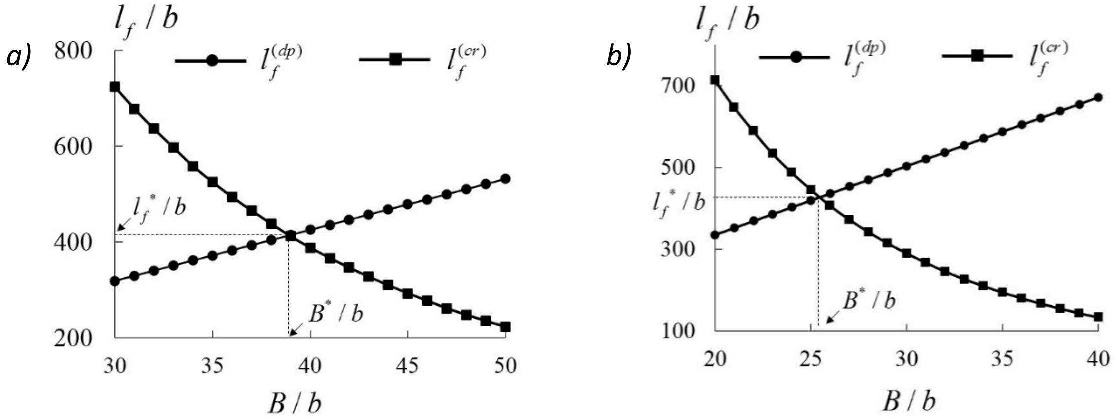

Fig. 3. Dependencies of $l_f^{(dp)}/b$ and $l_f^{(cr)}/b$ on the total Burgers vector of the pile-up B normalized to Burgers vector of a lattice dislocation b

One can see that the dependence of B^*/b on the disclination dipole strength is nonmonotonic. With increasing w_{dp}, that is, with increasing the misorientation of the original grain boundary, the value of B^*/b at first decreases and then grows. Such behaviour can be explained based on the following reasons. The fulfilment of the crack nucleation criterion with fixed external stress is provided owing to the growth of the stresses generated by the pile-up and the disclination dipole in the crack vicinity. At that, the disclination dipole has a dual role. Increasing the strength of the negative disclination leads to the growth of tensile stresses that it produces. Thus, all other things being equal, the less dislocations in pile-up is needed for the fulfilment of criterion (6). On the other hand, the greater the strength of the disclination dipole, i.e. the greater the misorientation angle of the original grain boundary, the smaller the arm of the dipole, i.e. the smaller the length of the facet, which is needed to stop boundary crossing by dislocations. Decreasing the length of the deformation facet and, hence, the arm of the dipole, enlarges, in its turn, the screening effect of the positive disclination on the elastic field of the negative one. Correspondently, more dislocations in pile-up are needed to fulfil criterion (6). The influence of those factors predetermines the occurrence of the minimum on the curves shown in Fig. 4. Taking into account the relation $w_{dp} = -\tan\theta$, from Fig. 4 it follows that the minimal number of dislocations in the pile-up, are needed for the crack nucleation, occurs when the dislocations cross grain boundaries with misorientation angles about 22°.

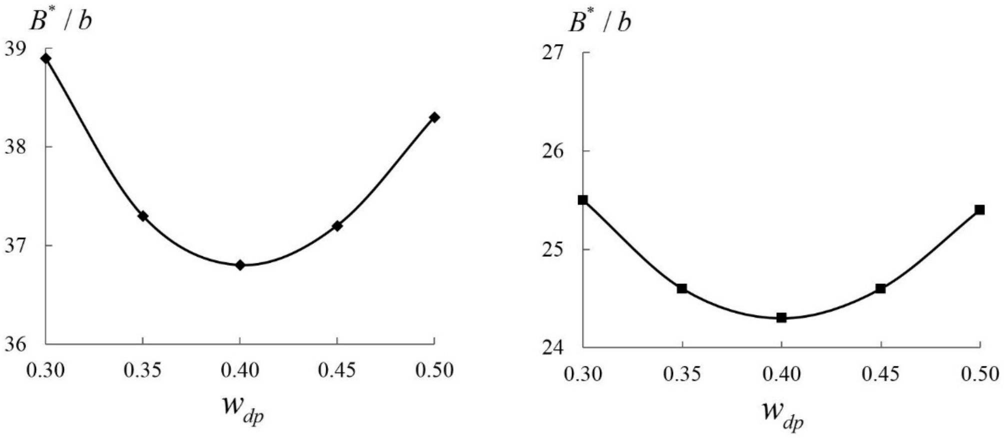

a) b)

Fig. 4. Dependencies of the threshold value of the total Burgers vector of the pile-up B^* / b on the disclination dipole strength w_{dp} (crack orientation is within the interval $\varphi_{\max} = [298°, 313°]$)

The dependence of the threshold length of deformation facet l_f^* / b on the disclination-dipole strength is illustrated in Fig. 5. One can see that the value of l_f^* / b decreases monotonically with increasing strength of disclination dipole, and depends weakly on an external load.

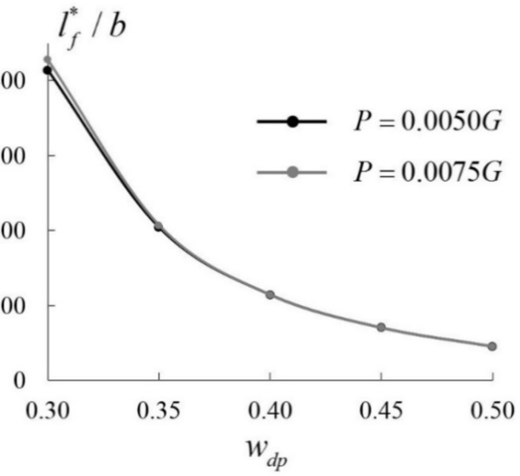

Fig. 5. Dependence of the normalized threshold length l_f^* / b of deformation facet on the strength of disclination dipole at external load $P = 0.005G$ and $P = 0.0075G$

4. Conclusion

We have shown that the formation of the disclination dipole due to grain boundary crossing by dislocations enables initiating fracture with less number of dislocations in pile-up (within the range from 25 to 40 dislocations) than in the framework of Stroh model. In the latter for coalescence of dislocations in the head of pile-up, it is needed ~150-200 dislocations (under external stresses considered in the present study). It should be emphasized that, in the framework of our study, the conditions for the nucleation of a crack and for its subsequent growth are fulfilled simultaneously. At that, the microcrack can transform into a stable one or open to the main crack, depending on particular parameters of the system considered and on the value of external stresses. For analysis of possible ways of its evolution, it is necessary to take into account dumping dislocations into the growing crack. This problem will be analyzed separately.

References

1. Indenbom VL. Fracture criteria in dislocation theories of strength. *Physics of Solid State*. 1961;3: 2071-2079. (In Russian)
2. Orlov AN, Perevezentsev VN, Rybin VV. *Grain Boundaries in Metals*. Moscow: Metallurgy; 1980.
3. Zisman AA, Rybin VV. Basic configurations of interfacial and junction defects induced in a polycrystal by deformation of grains. *Acta Materialia*. 1996;44(1): 403-407.
4. Kirikov SV, Perevezentsev VN. About the calculation of internal stresses from mesodefects accumulating at the boundaries during plastic deformation of solids. *Problems of strength and plasticity*. 2019;81(2): 212-221.
5. Rybin VV. Zisman AA, Zolotorevsky NY. Junction disclinations in plastically deformed crystals. *Acta Metallurgica et Materialia*. 1993;41(7): 2211-2217.
6. Wu MS. Energy analysis of Zener-Griffith crack nucleation from a disclination dipole. *International Journal of Plasticity*. 2018;100: 142-155.
7. Kirikov SV, Perevezentsev VN. Analysis of the conditions for the existence of stable microcracks in an elastic stress field from a rotational-shear mesodefect. *Letters on Materials*. 2021;11(1): 50-54.
8. Gutkin MY, Ovid'ko IA, Skiba NV. Effect of inclusions on heterogeneous crack nucleation in nanocomposites. *Physics of the Solid State*. 2007;49(3): 261-266.
9. Sarafanov GF, Perevezentsev VN. Conditions for the appearance of a stable microcrack in the elastic field of a screened disclination. *Russian Metallurgy (Metally).* 2016;2016(10): 889-894.
10. Ovid'ko IA, Sheinerman AG. Triple junction nanocracks in deformed nanocrystalline materials. *Acta Materialia*. 2004;52(5): 1201-1209.
11. Wu MS. Characteristics of a Zener crack wedged open by a disclination dipole. *Solid State Phenomena*. 2002;87: 277-300.
12. Zhou K, Wu MS, Nazarov AA. Continuum and atomistic studies of a disclinated crack in a bicrystalline nanowire. *Physical Review B: Condensed Matter and Materials Physics*. 2006;73(4): 1-11.
13. Stroh A. The formation of cracks as a result of plastic flow. *Proceedings of the Royal Society of London. Series A. Mathematical and Physical Sciences*. 1954;223: 404-414.
14. Stroh A. The formation of cracks as a result of plastic flow II. *Proceedings of the Royal Society of London. Series A. Mathematical and Physical Sciences*. 1955;232: 548-560.
15. Lee TC., Robertson IM., Birnbaum HK. TEM in situ deformation study of the interaction of lattice dislocations with grain boundaries in metals. *Philosophical Magazine A*. 1990;62(1): 131-153.

16. Guo Y, Collins DM, Tarleton E. Dislocation density distribution at slip band-grain boundary intersections. *Acta Materialia*. 2020;182: 172-183.
17. Zheng Z, Balint DS, Dunne FPE. Investigation of slip transfer across HCP grain boundaries with application to cold dwell facet fatigue. *Acta Materialia*. 2017;127: 43-53.
18. Schneider M, George EP, Manescau TJ, Záležák T, Hunfeld J, Dlouhý A, Eggeler G, Laplanche G. Analysis of strengthening due to grain boundaries and annealing twin boundaries in the CrCoNi medium-entropy alloy. *Int. J. of Plasticity*. 2020;124: 155-169.
19. Bieler TR, Alizadeh R, Peña-Ortega M, Llorca J. An analysis of (the lack of) slip transfer between near-cube oriented grains in pure Al. *Int. J. of Plasticity*. 2019;118: 269-290.
20. Perevezentsev VN, Kirikov SV, Svirina YV. Conditions of strain-induced facet formation during interaction between a lattice dislocation pile-up and a grain boundary. *The Physics of Metals and Metallography.* 2020;121(10): 929-935.
21. Hirth JP, Lothe J. *Theory of Dislocations*. New York: John Wiley & Sons; 1982.
22. Likhachev VA, Khayrov RYu. *Introduction to the Theory of Disclinations*. Leningrad, Leningrad University; 1975. (In-Russian)

THE AUTHORS

V.N. Perevesentsev
e-mail: v.n.perevezentsev@gmail.com
ORCID: 0000-0002-0437-8540

S.V. Kirikov
e-mail: ksv.kirikov@yandex.ru
ORCID: 0000-0002-5039-2271

N.Yu. Zolotorevsky
e-mail: zolotorevskii@mail.ru
ORCID: 0000-0002-0185-5452

Materials Physics and Mechanics. 2022;49(1): 182-192
Conference materials
http://dx.doi.org/10.18149/MPM.4912022_14

Modelling of composite materials with thermoplastic matrices, carbon fibres, and nanoparticles

A. Romashkina✉, **M. Khovaiko, A. Nemov**

Peter the Great St. Petersburg Polytechnic University, Polytechnicheskaya 29, St. Petersburg 195251, Russia

✉ zobacheva_ayu@spbstu.ru

Abstract. This paper reports a study regarding the modelling of the mechanical behaviour of a thermoplastic matrix/carbon fibre reinforced composite. It has been shown that the multiscale modelling approach, based on the submodelling technique, describes the material behaviour accurately enough. To simulate non-ideal adhesion, a series of composite material models were developed, the adhesion being modelled by introducing contact elements along with various parts of the fibre-binder interface surface. The introduction of contact interaction only affected the ultimate strength of the material. The introduction of the progressive damage process into the model allowed obtaining results close to those of full-scale tests.

Keywords: adhesion, carbon fibre, defect, finite element model, progressive damage, reinforced composite, submodelling, thermoplastic matrix

Acknowledgements*. The research is partially funded by the Ministry of Science and Higher Education of the Russian Federation as part of World-class Research Center program: Advanced Digital Technologies (contract No. 075-15-2022-311 dated 20.04.2022).*

Citation: Romashkina A, Khovaiko M, Nemov A. Modelling of composite materials with thermoplastic matrices, carbon fibers, and nanoparticles. *Materials Physics and Mechanics*. 2022;49(1): 182-192. DOI: 10.18149/MPM.4912022_14.

1. Introduction

The modelling of composite materials is a challenging area since it is impossible to model composite microstructures directly due to massive scales difference. For modelling composite materials, it is convenient to introduce the concept of macroscale (or macrolevel) to describe the behaviour of the whole composite structure, and microscale (or microlevel) to describe the behaviour on the scale of particular fibre reinforcement and binder material.

Numerous works have been devoted to solving the problem of modelling composite materials. Voigt and Reiss [1,2] describe simple approaches for calculating the effective elastic characteristics of structurally microhomogeneous media, which in modern terminology is commonly referred to as the homogenization problem. Hashin and Streichman proposed a variational method for determining effective moduli [3], which was further developed by Hill [4] and Hashin and Rosen [5] for fiber composite materials. Since the 1970s, homogenization methods based on the asymptotic analysis theory proposed for differential equations with rapidly oscillating coefficients [6-9] have been widely used. These methods provide tools for solving the inverse problem – calculating stresses at the microlevel from the results of solving the problem at the macrolevel – the so-called heterogenization problem. Further development of homogenization methods includes procedures based on solving problems with periodic boundary conditions [9], the method of direct homogenization [10], and the method of basic solutions [11]. These methods allow obtaining the most accurate solutions for composite materials with a periodic structure, or a structure that, within the framework of the approximations used, can be considered periodic. The combined application of homogenization and heterogenization methods allows calculations to be performed at several scale levels, i.e., for multilevel modelling of the mechanical behaviour of composite materials. In this case, "upward" movement along scale levels (from microscale to macroscale, or homogenization) is based on the direct homogenization method [10], and "downward" movement (from macroscale to microscale, or heterogenization) is based on the submodelling method [12].

In addition to direct modelling of the composite structure, modelling of various manufacturing defects is of particular interest. For example, Yan Lu et al. [13] investigate the influence of the manufacturing process parameters on the performance of the curved beams i.e., their macro- and micro-defects, interlaminate strength, and failure. In [14] Corveleyn et al. designed a model that accurately simulated the time-dependent mechanical behaviour of a short carbon fibre-reinforced PEEK. Dickson et al. [15] showed that the main cause of the failure is carbon-fibre pull-out and that the number of air inclusions, having a negative effect on the performance, increased with the fibre fraction. Adabi et al. [16] in the parametric study conclude that the level of fibre reinforcements and their orientation arrangement have significant effects on the structural performance of FRP 3D-printed composite sections. Caminero et al. [17] show that carbon fibre reinforced samples exhibit the best interlaminar shear performance with higher stiffness. According to Caminero et al. [17], the interlaminar shear strength grows when increasing the fibre volume fraction, but the increment is not proportional to the added fibres. The effect is most likely due to the increase in air gaps which have also been reported in other works.

This work is dedicated to a model of unidirectional composite, based on thermoplastic resin, reinforced with carbon fibres and nanoparticles, and obtained by a pultrusion process. Composites of this type are widespread in many industries (rocket and aircraft engineering, marine engineering, automotive engineering), since they are lightweight and, by varying the materials used, allow obtain the required properties, as well as to create more complex structural configurations.

2. Multilevel models

The specimens of unidirectional fibre composite material obtained by the pultrusion process were made on the basis of thermoplastic binder PEEK70 with three variants of reinforcing carbon fibres:

1. HTS45-12K-P12, a carbon fibre manufactured by Toho Tenax and apprehended by a thermoplastic;
2. SYT49-12K – carbon fibre produced by Zhongfu Shenying Carbon Fiber Co;
3. UMT45-12K-EP – carbon fiber of UMATEX Group production (JSC Khimpromengineering), deposited under epoxy resins.

The properties of carbon fibres are taken on the basis of the manufacturer's specifications, and the properties of the thermoplastic binder were determined by tensile test of the sample made of PEEK70. The elastic characteristics of the components of the composite material used in the simulations are presented in Table 1.

Table 1. Characteristics of the components of the composite material

	HTS45-12K-P12	SYT49-12K	UMT45-12K-EP	PEEK70
E , MPa	240 000	230 000	260 000	4682
ν	0.2	0.2	0.2	0.35

Fig. 1. Samples of the unidirectional thermoplastic-based composite

During the fabrication of the unidirectional composite samples, two configurations of equipment were used that differed in the shear forces induced in the fibres during impregnation, resulting in a difference in the mechanical characteristics of the samples (Fig. 1). We will refer to these two modes as configuration 1 (lower values of shear stresses during impregnation) and configuration 2 (higher values of shear stresses during impregnation). Since no significant geometrical differences in the microstructure of the samples obtained in this way were found, it was assumed that the additional forces applied to the fibres during impregnation influenced the quality of adhesion of the fibres to the binder. To analyse this assumption, a series of composite material models were developed at the mesolevel, based on the models developed earlier by the authors [19]. In these models, contact elements were introduced that allow modelling the non-ideal adhesion over various parts of the fibre-binder interface surface. Figure 2 shows an example of such a finite-element model in which non-ideal adhesion is accounted for on the part of the surface of one of the fibres present in the model. The diameter of a single fibre is accepted to be 7 μm based on the manufacturers' specifications. The volume fraction of fibres in the composite material is taken to be 55%.

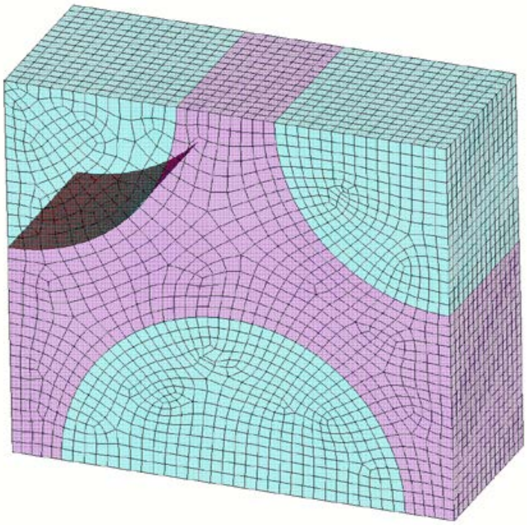

Fig. 2. Finite-element model of a unidirectional composite material at the mesolevel, taking into account the non-ideality of adhesion on a part of the fibre-binder interface

Virtual tensile and bend tests were performed to verify the developed models. Figure 3 shows the developed finite-element models at the macrolevel for tensile and bending tests for multilevel simulation. The dimensions of the samples have been defined according to the requirements of GOST 32656-2017 and GOST 57749-2017. The tensile and bending specimens have both thickness of 2mm and width of 10 mm, and the total length of tensile specimen is 150mm, and that of bending specimen is 64mm.

Fig. 3. Finite element models of a unidirectional composite material at the macro level. a) tensile test specimen; b) bend test specimen

Table 2. Effective elastic moduli

		E_1, GPa	E_2, GPa	E_3, GPa	υ_{12}	υ_{13}	υ_{23}	G_{12}, GPa	G_{23}, GPa	G_{13}, GPa
HTS45-12K-P12	case 1	15.46	15.44	134.02	0.435	0.0298	0.0297	6.194	12.03	2.12
	case 2	14.07	12.44	134.05	0.388	0.025	0.0216	3.574	9.682	0.531
	case 3	15.489	15.502	134.048	0.435	0.0298	0.0298	6.253	12.171	2.133
SYT49-12K	case 1	15.42	15.41	128.52	0.435	0.031	0.03	6.18	12.006	2.123
	case 2	14.04	12.41	128.56	0.387	0.026	0.022	3.567	9.664	0.531
	case 3	15.449	15.462	128.552	0.434	0.031	0.031	6.239	12.145	2.129
UMT45-12K-EP	case 1	15.53	15.51	145	0.436	0.0277	0.0277	6.218	12.07	2.136
	case 2	14.13	12.49	145.04	0.389	0.0232	0.0201	3.585	9.712	0.531
	case 3	15.56	15.573	145.04	0.436	0.0277	0.0277	6.277	12.218	2.142

3. Simulation tests

Effective characteristics of the composite material. The effective elastic characteristics of the composite material are calculated using a homogenization procedure based on the solution of boundary value problems for a periodicity cell. This section presents the results obtained under the assumption of orthotropic behaviour of the composite material. The results for configuration 2 (case 3) are obtained assuming perfect adhesion between the fibres and the binder, while for configuration 1, which exhibits lower effective elastic characteristics, the simulations were performed assuming no adhesion at the interface between the fibres and the binder. Two cases were considered: no adhesion on 1/8 of the surface of one of the fibres in the periodicity cell (case 1) and no adhesion on the surface of all fibres (case 2). The lack of adhesion, in this case, refers to the possibility of slippage of the fibres relative to the binder without the possibility of their detachment from each other. The results of the calculation of the effective elastic moduli of the macroscopic orthotropic composite material are presented in Table 2.

Tensile test. Virtual tests are performed by solving the problems of deformable solid mechanics on the mesoscale and the macroscale. The virtual tensile test of the experimental specimen is performed by stepwise application of tensile displacements u_x to the side faces of the specimen model. Since the sample is symmetrical, 1/8 of the sample is considered, and the symmetry conditions are applied on the corresponding planes (equality of zero displacements along the normal to the symmetry planes) (Fig. 4a). The specimen stresses, as in the experiment, are determined as the ratio of the total reaction force along the x-axis in the grips of the specimen to the cross-sectional area of the specimen.

In order to reconstruct the stresses and strains at the mesoscale, a submodelling procedure is used, in which the displacement fields defined at the macroscale are used as boundary conditions for the mesoscale model (Fig. 4b).

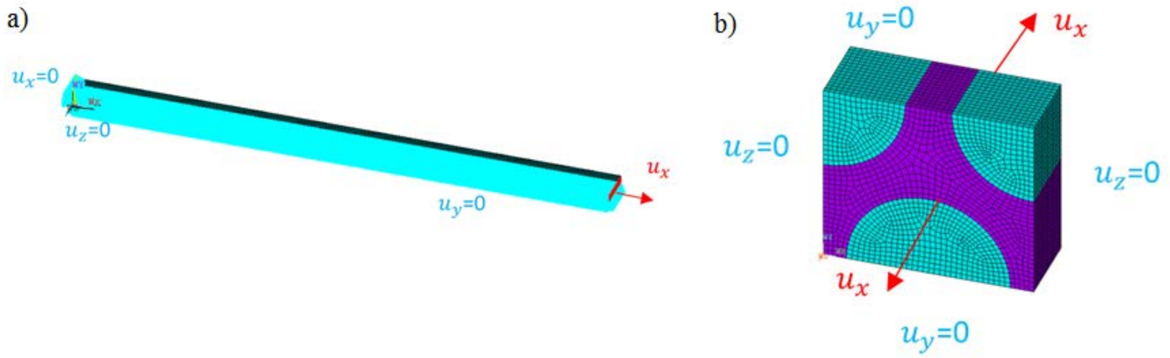

Fig. 4. Tensile test at: a) macrolevel, b) mesolevel

The mesolevel reconstruction is performed for each step of the macrolevel solution. So that the stress and strain in the fibres and in the binder are calculated for each value of displacements applied to the grips in the macrolevel model. When the tensile strength of the fibre/matrix is approached, the corresponding stress value is interpreted as the calculated tensile strength of the specimen [13].

In accordance with the presented formulation of the problem, the mechanical characteristics of the sample were calculated, using the obtained effective characteristics of the composite material. The comparison results for the three considered material types for Configuration 1 are shown in Fig. 5. According to the presented results, the composite material based on UMT45-12K-EP fibres has the highest tensile strength (1498 MPa) in Configuration 1. Similar calculations, performed for Configuration 2, showed that the difference in the mechanical characteristics of composite material calculated for both Configurations is less than 1%. The insignificant (less than 10%) difference in the mechanical characteristics of the considered materials is primarily related to the same binder for all materials.

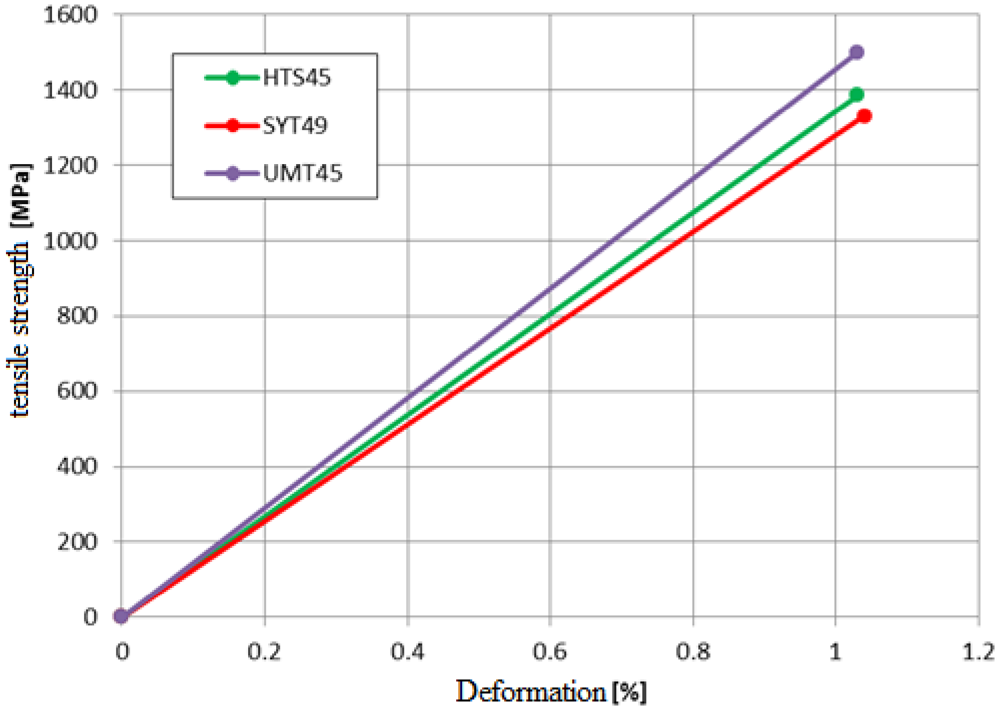

Fig. 5. Tensile test for 3 types of materials, Configuration 1

Bending test. Virtual three-point bend tests are performed by solving the problem of deformable solid mechanics at the meso- and macroscale. The virtual bend test of an experimental specimen is performed by applying the load P in the middle between the supports in stages (Fig. 6). The stresses in the sample, as in the experiment, are determined on the basis of the calculated total reaction force $F_{\max}$ by the formula $\sigma = \frac{1.5F_{\max}l}{bh^2}$ (b, h are the sample width and thickness, l is the distance between supports).

To reconstruct the stress and strain at the mesolevel, a submodelling procedure, similar to the above for tensile test, is used. Due to the availability of experimental results only for Configuration 1, a comparison is made only with them.

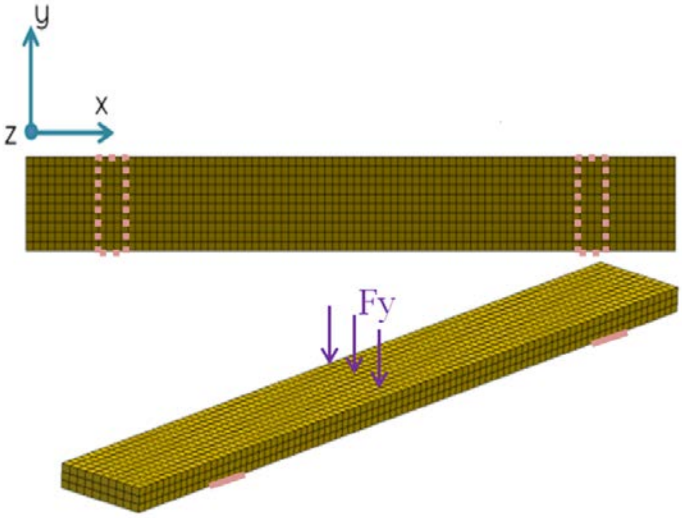

Fig. 6. FE calculation of the specimen for three-point bending at the macrolevel

Comparison of the modelling ways of adhesion between the fibres and the binder for three configurations is presented in Figure 7. The configurations are:

1) contact introduced in the periodicity cell at 1/8 of the circumference length of one fibre (ANSYS 1);

2) contact introduced in the periodicity cell at 1/4 of the circumference length of one fibre (ANSYS 2);

3) contact introduced in the periodicity cell along the entire circumference length of all fibres (ANSYS 3).

The calculations were made for the sample with HTS45-12K-P12 fibres. As can be seen from the graphs, introducing contact interaction affected only the material tensile strength.

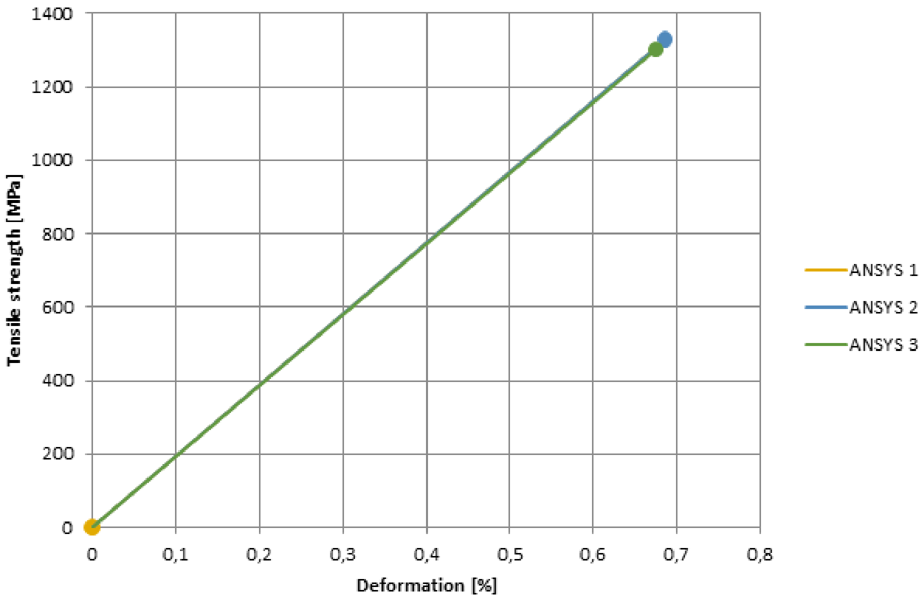

Fig. 7. Effect of non-ideal adhesion on mechanical characteristics at bending, Configuration 1

Figure 8 shows a comparison of strain curves for three different materials: UMT45-12K-EP, HTS45-12K-P12, and SYT49-12K, the contact being introduced in the periodicity cell along the entire circumference length of all fibres.

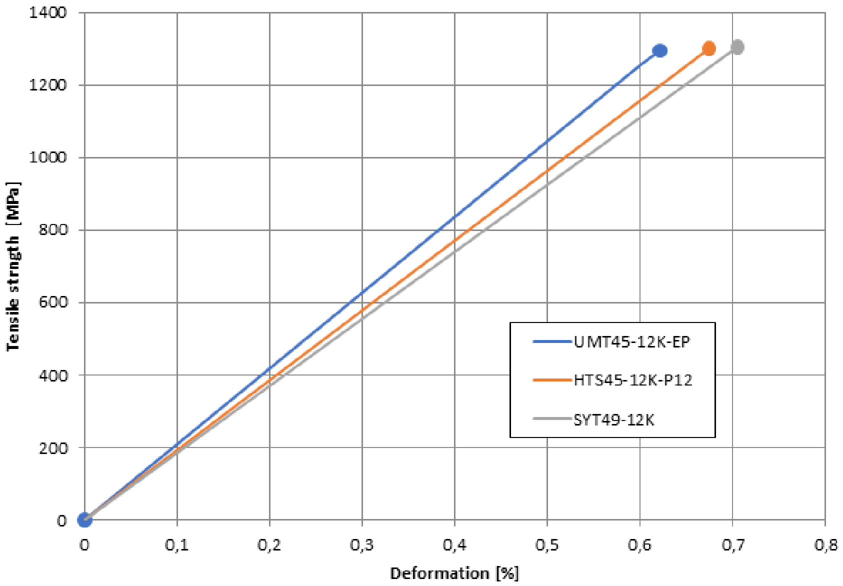

Fig. 8. Mechanical bending characteristics for 3 types of materials, Configuration 1

4. Validation of the experiments

Tensile. Comparison of the numerical solution (ANSYS) and experimental tests for material with UMT 45-12K-EP fibres is illustrated in Fig. 9. As can be seen, the difference between the numerically determined elastic modulus of the composite material and the results of full-scale tests is less than 10%. Nevertheless, the inaccuracy of determining the strength limit is 20-30%.

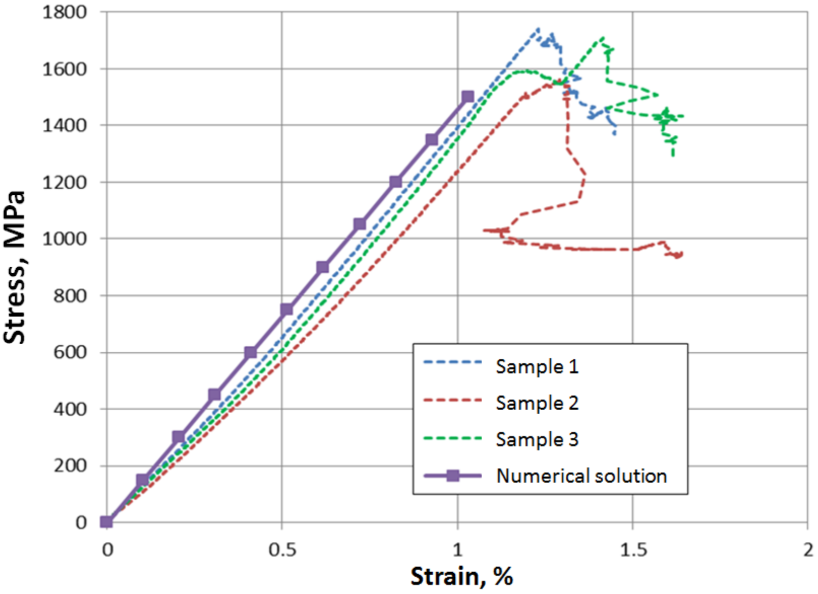

Fig. 9. Comparison of virtual and full-scale tensile test results

We assume that fracture begins in the fibre and the ultimate strength of the fibre is 3.4 GPa (Fig. 10). As can be seen from the presented graphs, the difference between the numerically determined strength of the composite material and the results of full-scale tests for specimens 1 and 3 is less than 10%.

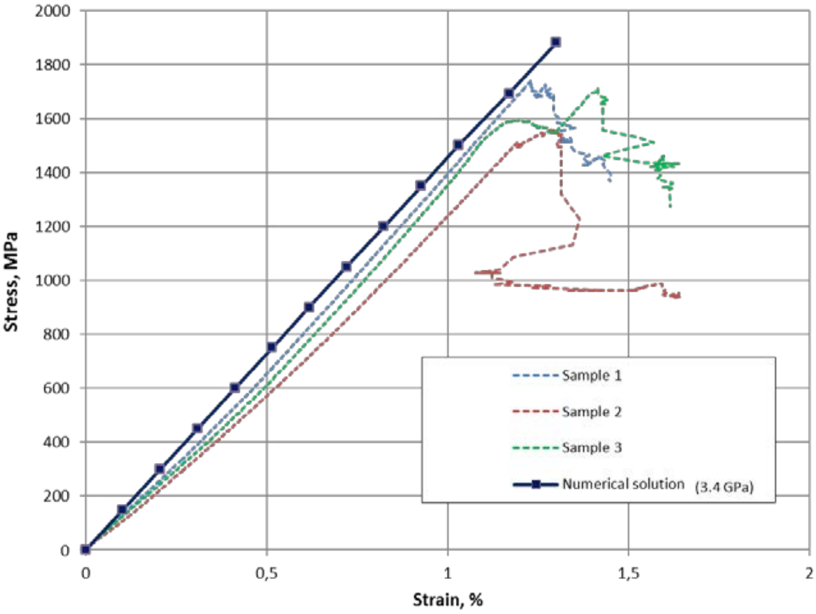

Fig. 10. Comparison of virtual and full-scale tensile test results. Elastic modulus correction

Bending. Figure 11 presents the results of the numerical solution (ANSYS) and full-scale tests for HTS45-12K-P12 material samples. The difference between the test results and the numerical experiment in terms of elastic modulus and ultimate strength is 20-40%.

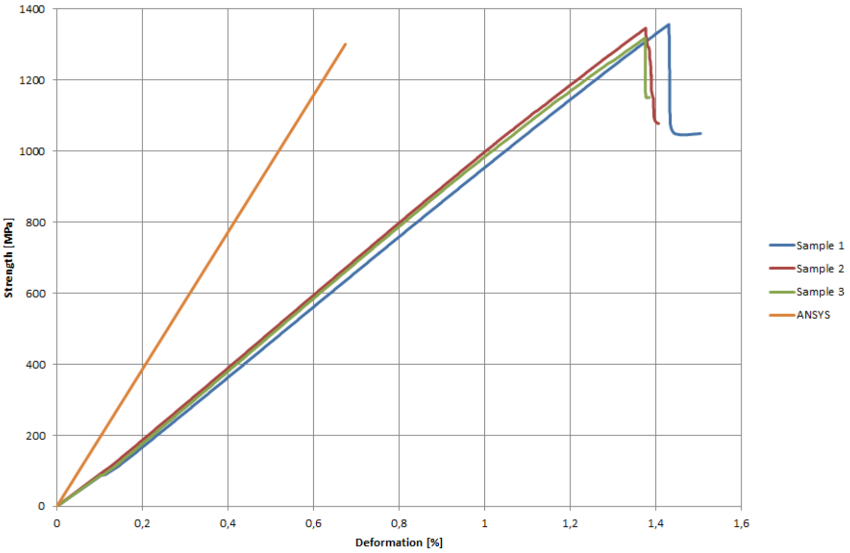

Fig. 11. Comparison of virtual and full-scale bending test results

To clarify the ultimate flexural modulus strength of the material, the model was adjusted to incorporate a progressive damage process [19]. In this case, there is a sharp failure of the specimen without prior weakening, both in the experiment and calculation. Comparison of the simulation with the experiment for one of the composite types is given in Fig. 12. The maximum load in the experiment and that of obtained in the simulation is different. In the experiment, the specimens collapsed at 1400 MPa, while in the simulation the maximum load was equal to 1640 MPa. Thus, the error in determining the modulus of elasticity is more than 20%.

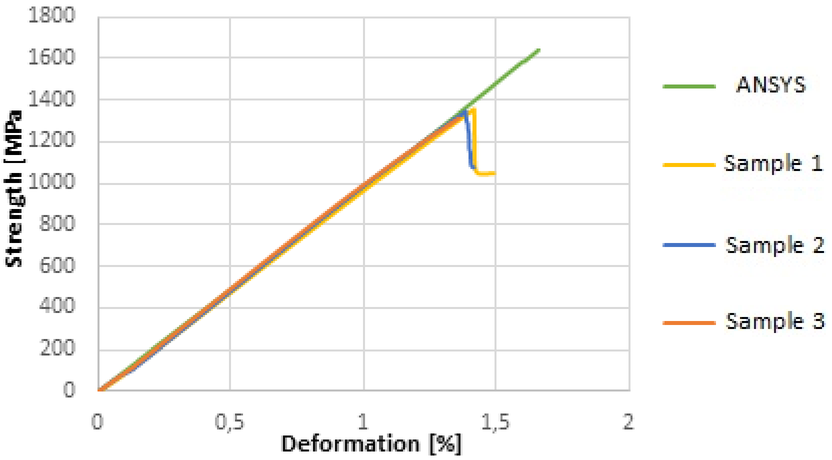

Fig. 12. Comparison of virtual and full-scale bending test results. Progressive damage

To improve the accuracy, the assumption was made that fracture would start in the fibre, and the ultimate strength was 3.4 GPa (Fig. 13). This assumption reduced the inaccuracy of determining the elasticity modulus to 2-3%.

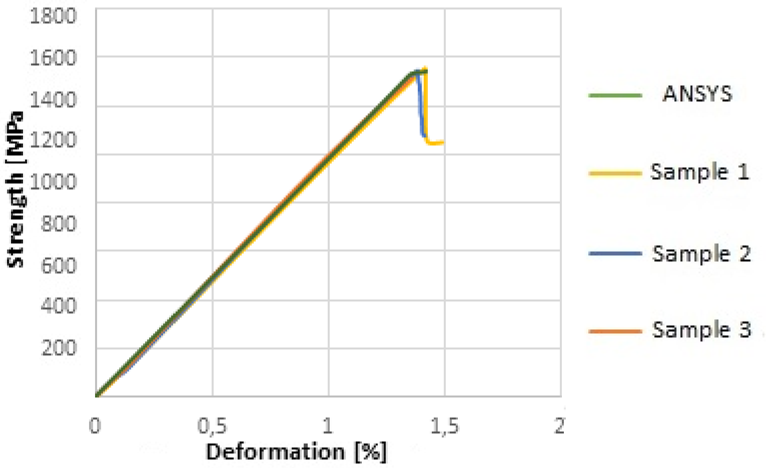

Fig. 13. Comparison of virtual and full-scale bending test results. Correction of elastic modulus

5. Conclusions

In this paper, a series of numerical calculations have been conducted to study the mechanical behaviour of thermoplastic matrix/carbon fibre reinforced composite. Modelling was realized using a multilevel approach based on the homogenization method and the submodelling method. The influence of non-ideal adhesion between fibres and matrix on the effective mechanical characteristics has been studied. In order to improve the material model to be more consistent with the full-scale experiment, the model was adjusted to incorporate a progressive damage process.

The results of the study showed:

- Consideration of non-ideal adhesion by introducing contact interaction between fibres and binder only affected the ultimate strength of the material. The insignificant (less than 10%) difference in the mechanical characteristics of the considered materials is primarily related to the same binder for all materials.
- The introduction of the progressive damage process into the model allowed obtaining results close to those of full-scale tests.
- The developed numerical models allow describing modern materials with sufficient accuracy (less than 10%).

References

1. Voigt W. Theoretische Studien über die Elasticitätsverhältnisse der Krystalle. *Abhandlungen der Königlichen Gesellschaft der Wissenschaften in Göttingen.* 1887;34: 3-51.

2. Reuss A. Berechnung der Fließgrenze von Mischkristallen auf Grund der Plastizitätsbedingung für Einkristalle. *Journal of Applied Mathematics and Mechanics.* 1929;9: 49-58.

3. Hashin Z, Shtrikman S. On Some Variational Principles in Anisotropic and Nonhomogeneous Elasticity. *Journal of the Mechanics and Physics of Solids.* 1962;10(4): 335-342.

4. Hill R. Theory of mechanical properties of fiber-strengthened materials. 1. Elastic behavior. *Journal of the Mechanics and Physics of Solids.* 1964;12(4): 199-212.

5. Hashind Z, Rosen W. The elastic moduli of fiber reinforced materials. *Journal of Applied Mechanics.* 1964;31(2): 223-232.

6. Bakhvalov NS. Averaging of partial differential equations with rapidly oscillating coefficients. *Sov. Math. Dokl.* 1975;16: 351-355.

7. Bensoussan A, Lions JL, Papanicolaou G. *Asymptotic analysis for periodic structures.* Amsterdam: North-Holland Publ. Comp; 1978.
8. Sanchez-Palencia E. *Non-homogeneous media and vibration theory.* Springer; 1980.
9. Bakhvalov NS, Panasenko GP. *Averaging processes in periodic media. Mathematical problems of mechanics of composite materials.* Moscow, Nauka; 1984. (In-Russian)
10. Borovkov AI. *Effective physical and mechanical properties of fiber composites*. Moscow: Viniti; 1985.
11. Palmov VA, Borovkov AI. Six fundamental boundary value problems in the mechanics of periodic composites. *Applied Mechanics and Materials.* 2006;5-6: 551-558.
12. Zobacheva AY, Nemov AS, Borovkov AI. Multiscale simulations of novel additive manufactured continuous fiber-reinforced three-component composite material. *Materials Physics and Mechanics.* 2017;32(1): 74-82.
13. Lu Y, Li Y, Zhang Y, Dong L. Manufacture of Al/CF/PEEK curved beams by hot stamping forming process. *Materials and Manufacturing Processes.* 2022. DOI: 10.1080/10426914.2022.2032140
14. Corveleyn S, Lachaud F, Berthet F, Rossignol C. Long-term creep behavior of a short carbon fiber-reinforced PEEK at high temperature: Experimental and modeling approach. *Composite Structures.* 2022;290: 115485.
15. Dickson AN, Barry JN, McDonnell KA, Dowling DP. Fabrication of continuous carbon, glass and Kevlar fibre reinforced polymer composites using additive manufacturing. *Additive Manufacturing.* 2017;16: 146-152.
16. Adabi HA, Thai H-T, Paton-Cole V, Patel V. Elastic properties of 3D printed fibre-reinforced structures. *Composite Structures.* 2018;193: 8-18.
17. Caminero MA, Chacón JM, García-Moreno I, Reverte JM. Interlaminar bonding performance of 3D printed continuous fibre reinforced thermoplastic composites using fused deposition modelling. *Polymer Testing.* 2018;68: 415-423.
18. Panina OA, Nemov AS, Zobacheva AY, Kobykhno IA, Tolochko OV, Yadykin VK. Numerical analysis of mechanical behavior of unidirectional thermoplastic-based carbon fiber composite for 3D-printing. *Materials Today: Proceedings*. 2020;30(3): 559-563.

THE AUTHORS

Romashkina Aleksandra
e-mail: zobacheva_ayu@spbstu.ru
ORCID: 0000-0002-0284-0527

Khovaiko Mikhail
e-mail: hovajko_mv@spbstu.ru
ORCID: 0000-0002-4756-1134

Nemov Alexander
e-mail: alexander.s.nemov@gmail.com
ORCID: 0000-0003-0431-4579

Submission of papers:

Manuscript should be submitted (**both MS Word and PDF**) by e-mail to: **mpmjournal@spbstu.ru**

After a confirmation of the paper acceptation, the authors should send the signed hard copy of the "Transfer of Copyright Agreement" form (available at http://www.mpm.spbstu.ru section "Authors") by regular post to "Materials Physics and Mechanics" editorial office:

Periodicals Editorial Office, Institute of Advanced Manufacturing Technologies, Peter the Great St.Petersburg Polytechnic University, Polytechnicheskaya, 29, St.Petersburg 195251, Russia.

The scanned copy of the signed "Transfer of Copyright Agreement" should be send by e-mail to: mpmjournal@spbstu.ru.

Filetype:

Authors are invited to send their manuscripts **as MS Word file with PDF format copy.**

MS Word file should be prepared according to the general instructions bellow; we are kindly asking the authors to look through the detail instruction at: http://www.mpm.spbstu.ru.

Length:

Papers should be limited to 30 typewritten pages (including Tables and Figures placed in the proper positions in the text).

Structure of the manuscript:

PAPER TITLE: CENTERED,
TIMES NEW ROMAN 14 BOLD, CAPITAL LETTERS

A.B. Firstauthor[1], C.D. Secondauthor[2*] - Times New Roman 12, bold, centered

[1]Affiliation, address, country - Times New Roman 10, centered

*e-mail: e-mail of the corresponding author - Times New Roman 10, centered

Abstract. Times New Roman 12 font, single line spacing. Abstract should not exceed 12 lines.
Keywords: please, specify paper keywords right after the abstract.

Paper organization. Use Times New Roman 12 font with single line spacing. Use *Italic* font in order to stress something; if possible, please, use **bold** for headlines only.

Page numbering. Please, do not use page numbering.

Tables, Figures, Equations. Please, see the sample file at http://www.mpm.spbstu.ru for more details.

References

References should be subsequently numbered by Arabic numerals in square brackets, e.g. [1,3,5-9], following the sample style below:

[1] Koch CC, Ovid'ko IA, Seal S, Veprek S. *Structural Nanocrystalline Materials: Fundamentals and Applications*. Cambridge: Cambridge University Press; 2007.

[2] Hull D, Bacon DJ. *Introduction to Dislocations*. 5nd ed. Amsterdam: Butterworth-Heinemann; 2011 Available from: https://www.sciencedirect.com/science/book// 9780080966724?via%3Dihub [Accessed 19th June 2018].

[3] Romanov AE, Vladimirov VI. Disclinations in crystalline solids. In: Nabarro FRN (ed.) *Dislocations in Solids*. Amsterdam: North Holland; 1992;9. p.191-402.

[4] Mukherjee AK. An examination of the constitutive equation for elevated temperature plasticity. *Materials Science and Engineering: A*. 2002;322(1-2): 1-22.

[5] Soer WA, De Hosson JTM, Minor AM, Morris JW, Stach EA. Effects of solute Mg on grain boundary and dislocation dynamics during nanoindentation of Al–Mg thin films. *Acta Materialia*. 2004;52(20): 5783-5790.
[6] Matzen ME, Bischoff M. A weighted point-based formulation for isogeometric contact. *Computer Methods in Applied Mechanics and Engineering*. 2016;308: 73-95. Available from: doi.org/10.1016/j.cma.2016.04.010.
[7] Joseph S, Lindley TC, Dye D. Dislocation interactions and crack nucleation in a fatigued near-alpha titanium alloy. To be published in *International Journal of Plasticity*. *Arxiv*. [Preprint] 2018. Available from: https://arxiv.org/abs/1806.06367 [Accessed 19th June 2018].
[8] Pollak W, Blecha M, Specht G. *Process for the production of molded bodies from silicon-infiltrated, reaction-bonded silicon carbide*. US4572848A (Patent) 1983.
[9] Brogan C. *Experts build pulsed air rig to test 3D printed parts for low carbon engines*. Available from: http://www.imperial.ac.uk/news/186572/experts-build-pulsed-test-3d-printed/ [Accessed 19th June 2018].

Правила подготовки статей:

Рукопись (**английский язык, MS Word и копия PDF**) должна быть направлена в редакцию журнала по электронной почте: **mpmjournal@spbstu.ru**.

После подтверждения принятия статьи в печать, авторы должны отправить подписанные:

1. Соглашение о передаче авторских прав (http://www.mpm.spbstu.ru, раздел «Авторам»);
2. Экспертные заключения о том, что материалы статьи не содержат сведений, составляющих государственную тайну, и информацию, подлежащую экспортному контролю; по адресу:

Россия, 195251, Санкт-Петербург, Политехническая, д. 29, Санкт-Петербургский политехнический университет Петра Великого, Институт передовых производственных технологий, Редакция периодических изданий.

Скан-копии подписанных документов просим направить по электронной почте: mpmjournal@spbstu.ru

Тип файла:

Редакция принимает **файлы MS Word с копией в формате PDF**. Статья должна быть подготовлена в соответствии с настоящей инструкцией, мы просим авторов также следовать более подробным инструкциям на сайте журнала http://www.mpm.spbstu.ru в разделе «Авторам».

Длина статьи:

Статья не должна превышать 30 страниц формата A4, включая Таблицы и Рисунки, размещенные непосредственно в соответствующих местах.

Общие правила оформления статьи:

НАЗВАНИЕ СТАТЬИ: ВЫРОВНЯТЬ ПО ЦЕНТРУ, ШРИФТ, TIMES NEW ROMAN 14 BOLD, ЗАГЛАВНЫЕ БУКВЫ

Автор(ы): **А.Б. Первыйавтор[1], В.Г. Автор[2*]** - шрифт Times New Roman 12, bold, по центру

[1]Наименование организации, адрес, страна - шрифт Times New Roman 10, по центру

* e-mail автора, представившего статью - шрифт Times New Roman 10, по центру

Аннотация. Аннотация статьи составляет не более 12 строк. Используйте шрифт Times New Roman 12, одинарный межстрочный интервал.

Ключевые слова: укажите ключевые слова после аннотации.

Как организовать текст статьи. Используйте шрифт Times New Roman 12, одинарный межстрочный интервал. При необходимости выделить какую-либо информацию используйте *курсив*. Используйте **полужирный** шрифт только для заголовков и подзаголовков.

Номера страниц. Пожалуйста, не используйте нумерацию страниц

Таблицы, Рисунки, Уравнения. Подробные правила оформления данных элементов статьи приведены в инструкции на сайте журнала http://www.mpm.spbstu.ru

Литература

Ссылки приводятся в тексте в квадратных скобках [1,3,5-9]. Стиль оформления ссылок:

[1] Koch CC, Ovid'ko IA, Seal S, Veprek S. *Structural Nanocrystalline Materials: Fundamentals and Applications*. Cambridge: Cambridge University Press; 2007.

[2] Hull D, Bacon DJ. *Introduction to Dislocations*. 5nd ed. Amsterdam: Butterworth-Heinemann; 2011 Available from: https://www.sciencedirect.com/science/book//9780080966724?via%3Dihub [Accessed 19th June 2018].

[3] Romanov AE, Vladimirov VI. Disclinations in crystalline solids. In: Nabarro FRN (ed.) *Dislocations in Solids*. Amsterdam: North Holland; 1992;9. p.191-402.

[4] Mukherjee AK. An examination of the constitutive equation for elevated temperature plasticity. *Materials Science and Engineering: A*. 2002;322(1-2): 1-22.

[5] Soer WA, De Hosson JTM, Minor AM, Morris JW, Stach EA. Effects of solute Mg on grain boundary and dislocation dynamics during nanoindentation of Al–Mg thin films. *Acta Materialia*. 2004;52(20): 5783-5790.

[6] Matzen ME, Bischoff M. A weighted point-based formulation for isogeometric contact. *Computer Methods in Applied Mechanics and Engineering*. 2016;308: 73-95. Available from: doi.org/10.1016/j.cma.2016.04.010.

[7] Joseph S, Lindley TC, Dye D. Dislocation interactions and crack nucleation in a fatigued near-alpha titanium alloy. To be published in *International Journal of Plasticity. Arxiv.* [Preprint] 2018. Available from: https://arxiv.org/abs/1806.06367 [Accessed 19th June 2018].

[8] Pollak W, Blecha M, Specht G. *Process for the production of molded bodies from silicon-infiltrated, reaction-bonded silicon carbide*. US4572848A (Patent) 1983.

[9] Brogan C. *Experts build pulsed air rig to test 3D printed parts for low carbon engines*. Available from: http://www.imperial.ac.uk/news/186572/experts-build-pulsed-test-3d-printed/ [Accessed 19th June 2018].

МЕХАНИКА И ФИЗИКА МАТЕРИАЛОВ

49 (1) 2022

Учредители: Санкт-Петербургский политехнический университет Петра Великого,

Институт проблем Машиноведения Российской академии наук

Издание зарегистрировано федеральной службой по надзору в сфере связи,

информационных технологий и массовых коммуникаций (РОСКОМНАДЗОР),

свидетельство ПИ №ФС77-69287 от 06.04.2017 г.

Телефон редакции

+7(812)552 77 78, доб. 224

E-mail: mpmjournal@spbstu.ru

Компьютерная верстка А.Ю. Ромашкина

Подписано в печать 31.08.2022 г. Формат 60x84/8. Печать цифровая
Усл. печ. л. 10,0. Тираж 100. Заказ____.

Отпечатано с готового оригинал-макета, предоставленного автором
в Издательско-полиграфическом центре Политехнического университета Петра
Великого. 195251, Санкт-Петербург, Политехническая ул., 29.
Тел.: +7(812)552 77 78, доб. 224.

MPM, Vol. 49, No. 1, 2022

MPM
SCIENTIFIC
JOURNAL